SLAC-236
UC-34d
(T/E/I)

A STUDY OF THE REACTIONS $\psi' \to \gamma\gamma\psi$

Mark Joseph Oreglia

Stanford Linear Accelerator Center
Stanford University
Stanford, California 94305

December 1980

Prepared for the Department of Energy

under contract number DE-AC03-76SF00515

Printed in the United States of America. Available from the National Technical Information Service, U.S. Department of Commerce, 5285 Port Royal Road, Springfield, VA 22161. Price: Printed Copy A11; Microfiche A01.

---

* Ph.D. dissertation.

ABSTRACT

A large solid angle array (the Crystal Ball detector) of NaI(Tl) crystals, together with spark and multiwire proportional chambers for charged particle tracking, is used to study the decays of the ψ' meson. Cascade reactions of the form $\psi' \to \gamma\chi$, $\chi \to \gamma\psi$, $\psi \to (e^+e^-$ or $\mu^+\mu^-)$ are used in this experiment to observe the intermediate χ states and to measure their spin by analyzing the angular correlations among the final-state particles. In addition, the multipole coefficients describing the individual radiative transitions are measured using the angular correlations. Values of J=2 and J=1 are obtained for the χ states with masses of 3.55 and 3.51 GeV, respectively. Radiative transitions to and from the χ states are found to be dominantly E1 in nature. The well-established J=0 $\chi(3.41)$ state is observed in a cascade reaction, with a branching ratio $BR(\psi' \to \gamma\chi \to \gamma\gamma\psi) = (0.06 \pm 0.02 \pm 0.01)\%$; the first error describes uncertainties arising from statistics and acceptance corrections, while the second error is systematic. Branching ratios of $(1.26 \pm 0.08 \pm 0.20)\%$ for $\chi(3.55)$ and $(2.38 \pm 0.12 \pm 0.38)\%$ for $\chi(3.51)$ are consistent with those obtained in previous experiments. Natural line-widths of (4±1) MeV for $\chi(3.55)$ and a full width consistent with the resolution of the apparatus for $\chi(3.51)$ are obtained.

An intermediate singlet-S state (the η_c') which has been reported by other experiments at masses of 3.46 and 3.59 GeV is not observed in a

cascade reaction by this experiment. A 90% confidence level upper limit of 0.04% is placed on the cascade braching ratio $BR(\psi' \to \gamma\eta_c' \to \gamma\gamma\psi)$.

The $\gamma\gamma(e^+e^-$ or $\mu^+\mu^-)$ final state is also found to result from the processes $\psi' \to (\eta$ or $\pi^0)\psi$, with branching ratios $BR(\psi' \to \eta\psi) = (2.18 \pm 0.14 \pm 0.35)\%$ and $BR(\psi' \to \pi^0\psi) = (0.08 \pm 0.02 \pm 0.01)\%$. Isospin symmetry is violated in the latter decay.

ACKNOWLEDGEMENTS

With sincere appreciation I thank Elliott Bloom for the years of guidance he has given me. The great satisfaction that I have enjoyed in the success of the Crystal Ball Project derives primarily from his efforts. The Crystal Ball Collaboration is as fine a one as ever I shall have the fortune to work with. Participation and enthusiasm have been of the highest caliber, and I must thank every member for their assistance.

Rich Partridge, Frank Porter, Charlie Peck (Caltech); Dikran Antreasyan, Wolf Kollmann, Mark Richardson, Karl Strauch, Klaus Wacker (Harvard); David Aschman, Toby Burnett, Matteo Cavalli-Sforza, Don Coyne, Hartmut Sadrozinski (Princeton); Bruce Beron, Ralf Eichler, Bob Hofstadter, Barrie Hughes, Ian Kirkbride, Herrmann Kolanoski, Kay Königsmann, Art Liberman, Jack O'Reilly, Bob Parks, Joe Rolfe, John Tompkins (HEPL-Stanford); Aaron Baumgarten, John Bernstein, John Broeder, Fatin Bulos, Ron Chestnut, John Gaiser, Gary Godfrey, Chris Kiesling, Bill Lockman, Thorwald van Hooydonk (SLAC).

A key role in the development and construction of the apparatus was played by the Harshaw Chemical Company. Russ Anderson, George Mataraza, Mike Mayhugh, Don Milliken, Erwin Schrader, Elmer Stewart, and a score of other Harshaw employees made it possible to enjoy a profitable, if not cold, residence at the Ohio plant during the winter of 1978.

During my first year at SLAC I benefitted from a training in theoretical physics under Sid Drell; I thank him for his patience, guidance, and support. Gary Feldman, Fred Gilman, and other faculty, staff, and visitors at SLAC have also been valued mentors. A proficiency in experimental physics was doubtless fostered during my researches as a Stanford undergraduate. I am grateful to Narinder Kapany, Arthur Schawlow, and the other members of the Schawlow group for the opportunities they provided me. Special thanks are due Ken Sherwin for sharing his wisdom and resources with me on so many occasions.

The years required to turn out a physicist have been costly. Without the financial aid from the state of California, the Department of Energy, and the Hertz foundation, I would not be in a position to write this acknowledgement. Edward Teller, in his administration of the Hertz awards, has spawned an appreciation of the excitement and impact of discovery, and of the role of the scientist in society; for this I applaud him.

I am fortunate to have friends and family with the patience to put up with me during several exceedingly taxing years; Jamie, Bruce, and my brother Robert have endured a regrettably sizeable dose. In this respect none have carried so great a burden as my parents. For their unfailing encouragement and support I dedicate this work to Augustine and Rita Oreglia, and to Joseph and Barbara Depuhl.

TABLE OF CONTENTS

Chapter I

THE DETECTOR

1.1 INTRODUCTION -- CHARMONIUM

Charmonium as devised in the celebrated model of Appelquist and Politzer[1] describes the meson system formed by a bound heavy quark-anti-quark pair. In direct analogy to positronium, the fundamental charmonium "atomic" system consists of 1^1S_0, 1^3S_1, 2^1S_0, 2^3S_1, 1^1P_1 and 1^3P_{012} states,[2] as shown in figure 1-1. The heavy charmed-quark masses (m_c=1.2 to 1.8 GeV/c^2) describe a reasonably non-relativistic system, thus inviting the use of a Schrödinger picture in obtaining the wave functions. Since the 2^3S_1 mass lies below that for two charmed mesons (i.e., c-u,d,s), the Okubo-Zweig-Iizuka rule enhances radiative decays in the fundamental system. In this experiment a photon-efficient, large solid-angle detector was used to study the ψ'-ψ radiative transitions in the fundamental system described above by identifying the cascade sequences $\psi' \rightarrow \gamma X, X \rightarrow \gamma \psi$, where X is a $^1S_0$ or 1^3P_j state. A search is made for new states in the charmonium system, an attempt is made to confirm the 2^1S_0 candidates, and the quantum numbers of the 1^3P candidates are determined.

---

[1] T. Appelquist and H. Politzer, Phys. Rev. Lett. 34, 43 (1975).

[2] In the notation employed here all the lowest L-states are denoted by 1L.

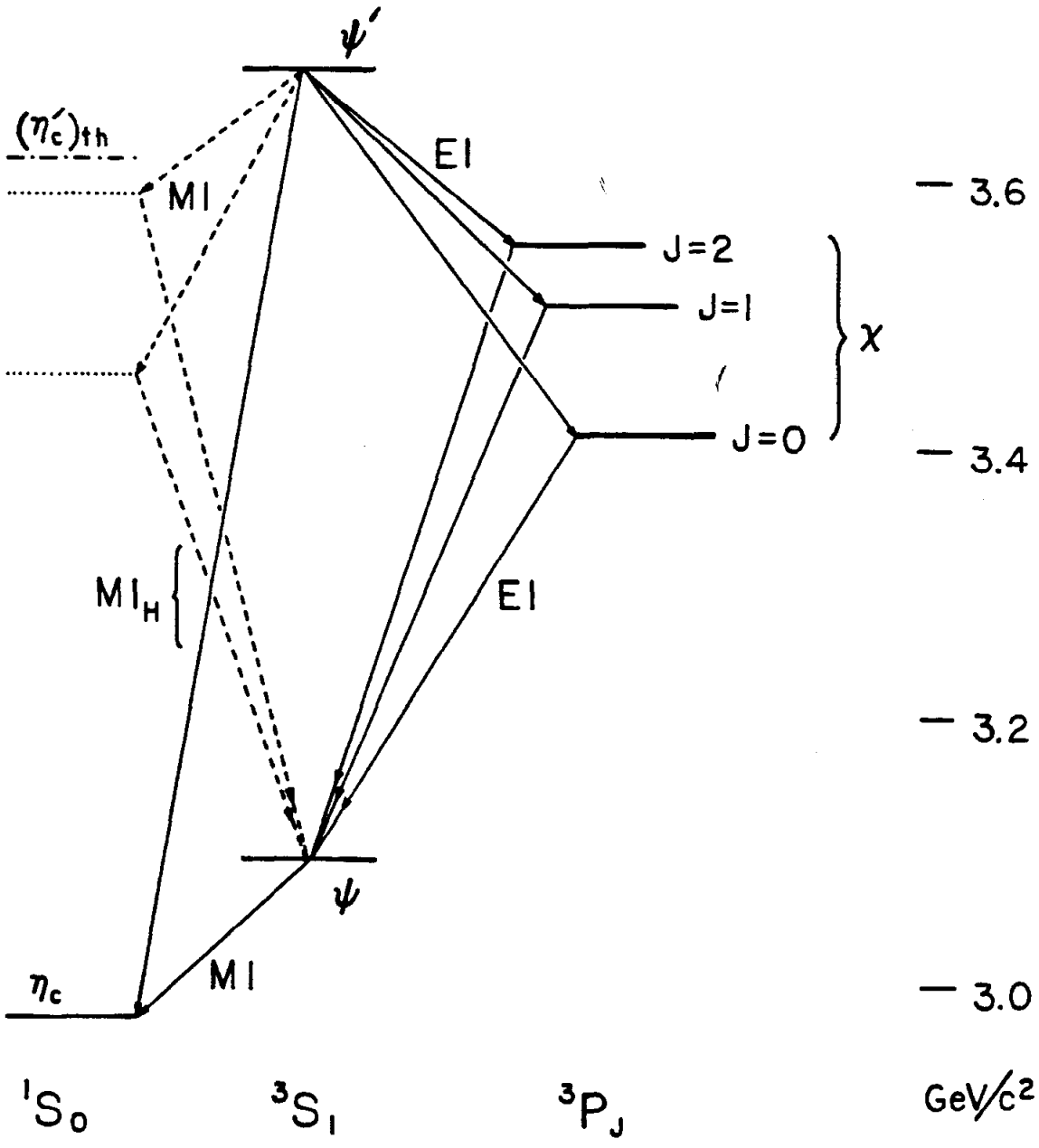

FIG..1-1 The charmonium levels. Putative levels and transitions not confirmed in this experiment are indicated by broken lines; (η_c')th denotes the level expected from the charmonium model. $M1_H$ denotes a hindered M1 transition.

Unlike the atomic model, the charmonium potential must have a long-range component in order to confine the quarks. If one assumes that the potential contains a Coulombic-like component and recalls that the 2S states are degenerate with the 1P states for a r^{-1} potential, then the addition of a confining potential imparts the largest energy to the more confined S states, breaking the degeneracy and placing the 1P states below the 2S states. Spin forces act to split the $^3P_{012}$ states (fine structure) and the ^1S-^3S states (hyperfine structure). Spin-parity considerations prevent radiative transitions between the $^3S_1$ and the $^1P_1$ state; therefore, the latter is not addressed in this study.

The $\psi'(3684)$ and $\psi(3095)$ are the well established[3] $^3S_1$ states, and candidates[4] for the 1^3P states have been observed in the expected mass region. A candidate for the 1^1S_0 state has been observed[5] and confirmed[6] at a mass of 2978 MeV/c^2; however, no information on its quantum numbers is currently available to firmly establish it as the 1^1S_0. Two candidates for the 2^1S_0 state have been reported at masses of 3455[7] MeV/c^2 and 3591(or 3180)[8] MeV/c^2, but have not fit well into the charmonium model.

---

[3]A. Boyarski et al., Phys. Rev. Lett. 34, 1357 (1975); V. Lüth et al., Phys. Rev. Lett. 35, 1124 (1975).

[4]J. Whitaker et al., Phys. Rev. Lett. 37,1596 (1976); W. Braunschweig et al., Phys. Lett. 57B, 407 (1975); G. Feldman et al., Phys. Rev. Lett. 35, 821 (1975).

[5]R. Partridge et al., Phys. Rev. Lett. 45, 1150 (1980).

[6]T. M. Himel et al., Phys. Rev. Lett. 45, 1146 (1980).

[7]J. Whitaker et al., op. cit.

[8]W. Bartel et al., Phys. Lett. 79B, 492 (1978).

Decays of the form $\psi' \to m\psi$, $m \to \gamma\gamma$ exhibit the same topology as the cascade reactions. A reasonably large number of such decays is provided by the η meson, which has a large (38%) branching ratio into diphotons; this process was studied carefully in order to separate it from the χ events. Additionally, the large rate for $\eta\psi$ production is surprising, suggesting either a charm component in the η or an unusually strong direct coupling -- these possibilities are discussed in chapter VI. The decay $\psi' \to \pi^0\psi$ is forbidden by isospin symmetry; however, violation of the symmetry at the 0.1% level has been observed in decays such as $\eta \to 3\pi$ and it may be responsible for the large value of $M_p - M_n$. A clear signal for the $\pi^0\psi$ decay was observed.

1.2 SPEAR

Data were obtained from decays of ψ' particles produced at SPEAR,[9] the e^+e^- annihilation storage ring at the Stanford Linear Accelerator Center. In the SPEAR ring[10] electrons and positrons, each in a single bunch of about 10^{11} leptons, are accelerated in opposite directions about the same orbit. These bunches therefore pass through each other at two diametrically opposite locations on the ring, with a period of 780×10^{-9} seconds. The collisions occured in the experiment "pits" shown in figure 1-2. All quantities at a point along the design orbit are expressed in terms of the SPEAR coordinates in which $\hat{y}$ is along the mag-

---

[9]This is the now inaccurate acronym first devised for the SLAC storage ring facility: Stanford Positron-Electron Asymmetric Rings.

[10]M. Sands, report SLAC-REPORT 121 (Stanford) (1970).

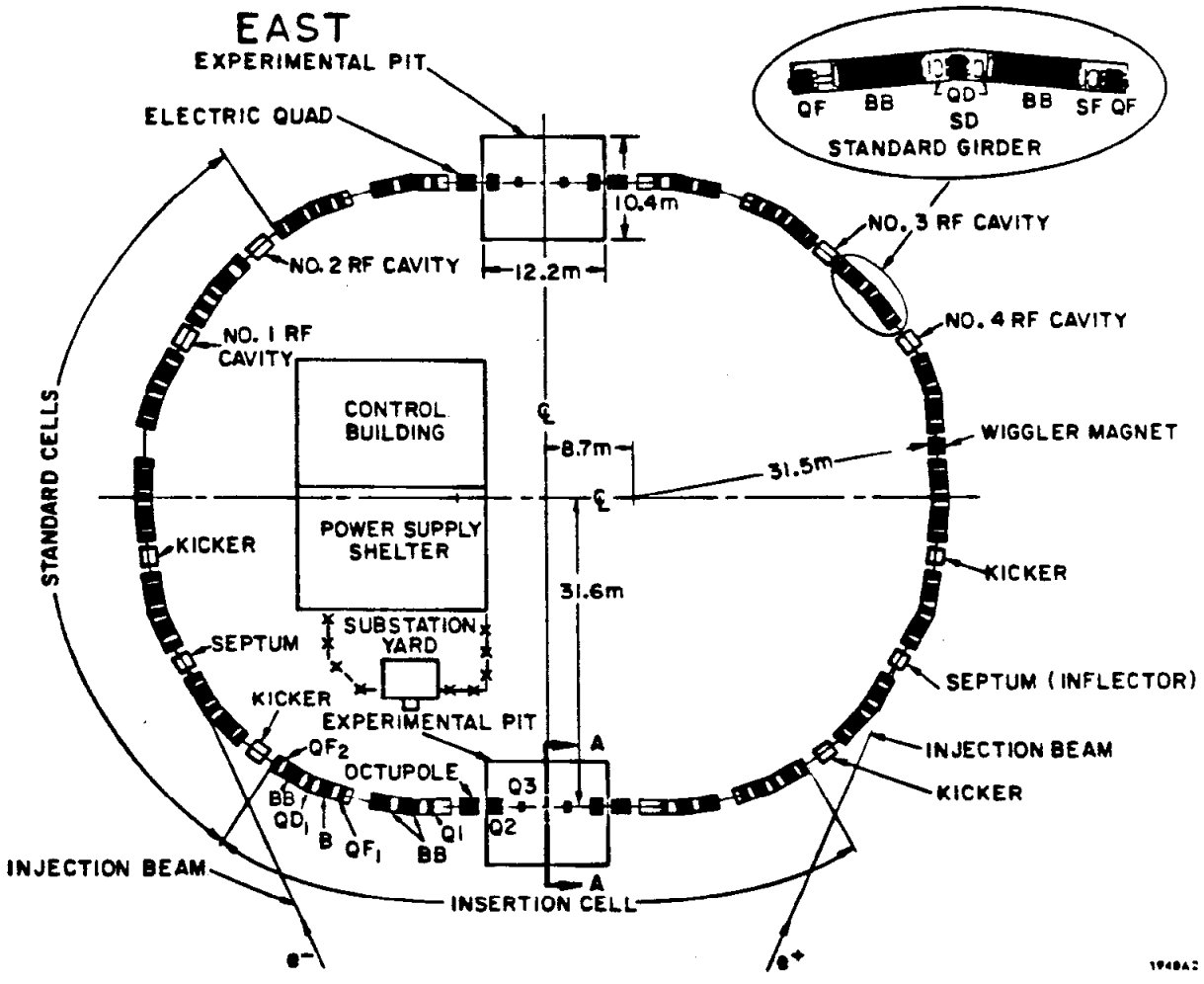

FIG. 1-2 The SPEAR layout. This experiment took place in the East Pit shown at the top of the figure.

netic bend field, $\hat{x}$ points toward the ring center, and $\hat{z}$ is tangent to the positron orbit.

Leptons are injected into the storage ring directly from the SLAC Linac, producing bunches of nearly a gaussian density distribution with σ_z=26 mm along the longitudinal dimension. The orbiting leptons lose energy due to the synchrotron radiation generated as they follow a curved path, and therefore SPEAR is equipped with four RF cavities to restore the radiated energy. As a result of the storage and acceleration/deceleration processes, oscillations ("synchrotron" and "betatron") are created about the ideal orbit intended for the leptons, with these oscillations most pronounced in the orbit (x-z) plane. The oscillations induce a transverse dimension to the bunches, with σ_x=0.50 mm and σ_y=0.03 mm at the ψ' energy E_b=1842 MeV. The storage process also introduces a chromatic dispersion to the beams, with $\sigma(E_b)\cong$1.2 MeV.

Beam position monitors around the ring recorded the actual orbit followed by the leptons, while fields in the bend magnets were monitored to an accuracy of 0.05% by a flip-coil located in a reference magnet; the latter was wired in series with the bend magnets. From a knowledge of the RF frequency, the orbit and the bend fields, the beam energy was calculated to an accuracy of 0.1%, or about 1.8 MeV at the ψ' energy. Since the e^+ and e^- energies are correlated, there is an uncertainty of $2\sigma(E_b)$ in the center-of-mass energy. The natural width of the ψ' resonance is 0.2 MeV, much smaller than the uncertainty in the beam energy or the beam width $\sigma(E_b)$. For this reason, the energy range about

E_b=1842.0 MeV was scanned at the beginning of each run cycle to insure that the ψ' was produced at the maximum rate. At the ψ' energy SPEAR achieved a maximum instantaneous luminosity of (1 to 2)$\times 10^{30}$ $cm^{-1}sec^{-1}$, corresponding to a ψ' production rate of 0.5 Hz maximum, or a practical realtime rate of about 0.3 Hz when injection time and other factors are taken into consideration.

High vacuum in the beam pipe is important in suppressing the background arising from collisions of beam electrons with residual gas molecules. Typically a vacuum of 10^{-9} Torr was achieved in the vicinity of the beam-beam interaction region. On occasions of beam-line repair and maintenance (occuring once during the 1978-1979 cycle) the vacuum remained at the 10^{-8} level for about a week following the access.

The beam pipe at the interaction region consisted of an aluminum tube 110 mm in diameter, and having a thickness of 0.065 inches. This thickness corresponds to 1.9% of a radiation length (L_{rad}) at normal incidence and 4.3% L_{rad} at $\cos\theta_z$=0.9 (the limit of the charge-tracking chambers).

1.3 GENERAL LAYOUT

The Crystal Ball apparatus resided in the East Pit at SPEAR (seen at the top of figure 1-2). To insure that the thallium-doped sodium iodide (NaI(Tl)) crystals, which are the heart of the detector, would not be damaged by atmospheric moisture, the entire detector rested in a special

enclosure called the "ballroom". The enclosure, measuring 18 ft. by 31 ft. by 21 ft. high and weighing 47 tons (excluding the iron absorbers for OHMS), moved together with the detector as a single unit. Air in the ballroom was cycled through a dehumidifier and a temperature control unit which maintained a dew-point of -42°C at a constant room temperature of (20±1)°C. Aside from the SPEAR beam line, only two elements of the experiment were located in the pit external to the ballroom. One of these was the spark chamber high-voltage system, shown on the right-hand side of figure 1-3; the other was a 500 KeV proton Van de Graaff accelerator located at the left of the figure. Mounted on rails and an elevator, the accelerator could insert its 14 foot beam-line into the center of the ballroom to calibrate the apparatus.

Inside the ballroom were the four elements of the detector. Rigidly mounted about the SPEAR beam pipe was a central tracking chamber system. Immediately surrounding these chambers were two arrays of NaI(Tl), each fastened to the ballroom foundations by means of an elevator system so that they could be separated to expose the chambers. Beyond the main NaI(Tl) arrays, and near the beam pipe, were smaller endcap arrays of NaI(Tl) and spark chambers, followed by the luminosity monitor counters. Finally, on either side of all these elements were the two arms of the Outer Hadron-Muon Separator (OHMS), which consisted of slabs of iron interspersed with proportional chambers and scintillation counters, covering 15% of the 4π solid angle. OHMS data were not necessary for the analysis presented in this study.

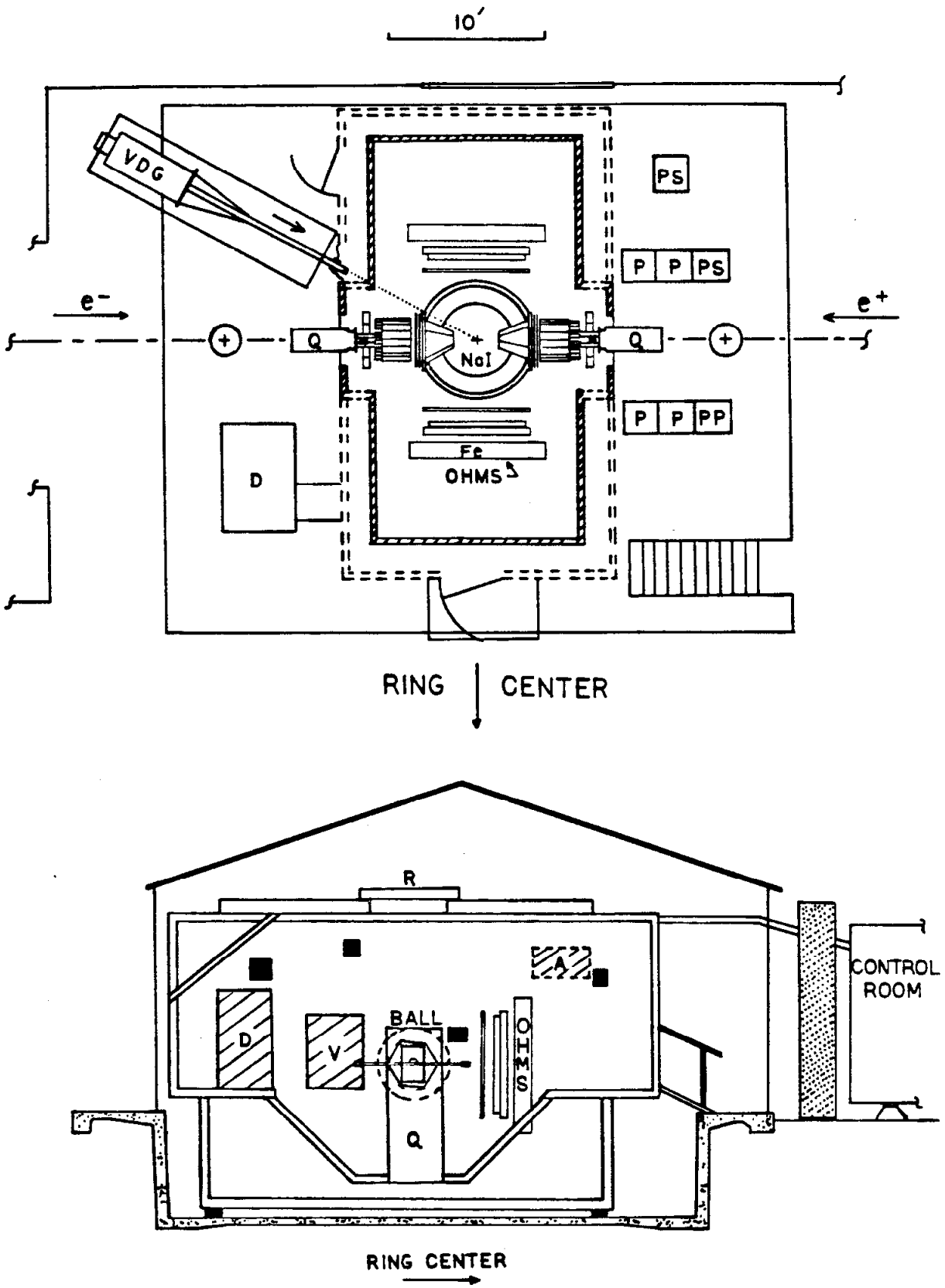

FIG..1-3 Layout of the East Pit. Key to upper figure: VDG = Van de Graaff system; D = dehumidifier; PS = power supply for MWPC or spark chambers; P = HV pulser, PP = prepulser for spark chambers; Q = quadrupole magnet. The double dotted wall denotes the upper stage of the ballroom. Key to lower figure: D = door; V = Van de Graaff port; A = dehumidifier port; Q = quadrupole magnet port. Shading indicates shielding concrete.

Signals from the detector were processed in the control room, where a PDP 11/T55 computer with four disk drives[11] and two magnetic tape units was located. All of the data processing electronics, the trigger system and the control console were located in the control room.

1.4 CRYSTAL BALL PROPER

Central to the Crystal Ball apparatus is the ball proper, a segmented spherical shell with an inner radius of 10 inches and an outer radius of 26 inches, consisting of 672 optically isolated NaI(Tl) crystals. Fabrication of the crystals was performed in collaboration with the Harshaw Chemical Company in their Solon, Ohio plant. A typical module (i.e., one crystal together with its phototube) is shown in figure 1-4. Each crystal was about 16 inches, or 15.7 L_{rad}, long and prismatic in shape, with a small end dimension of about 2 inches and a large end of about 5 inches; it was viewed by a two inch phototube[12] separated from the crystal by a glass window and a 2 inch air gap. The crystals were stacked to form two mechanically separate hemispheres, one upper and one lower. As demonstrated in figure 1-5, a 20-sided regular polyhedron, or icosahedron, forms the basis for construction of the two hemispheres. The major triangles of the icosahedron can be subdivided into four smaller minor triangles to form a more spherical object; the minor triangles in turn are subdivided into nine actual crystals, of which 720 would be

---

[11]The disk system consisted of two RK05j (2 megabyte) units, one RK06 (14 megabyte) unit, and one RK07 (28 megabyte) unit.

[12]C. Peck and F. Porter, Crystal Ball memo CB-NOTE 010 (1976).

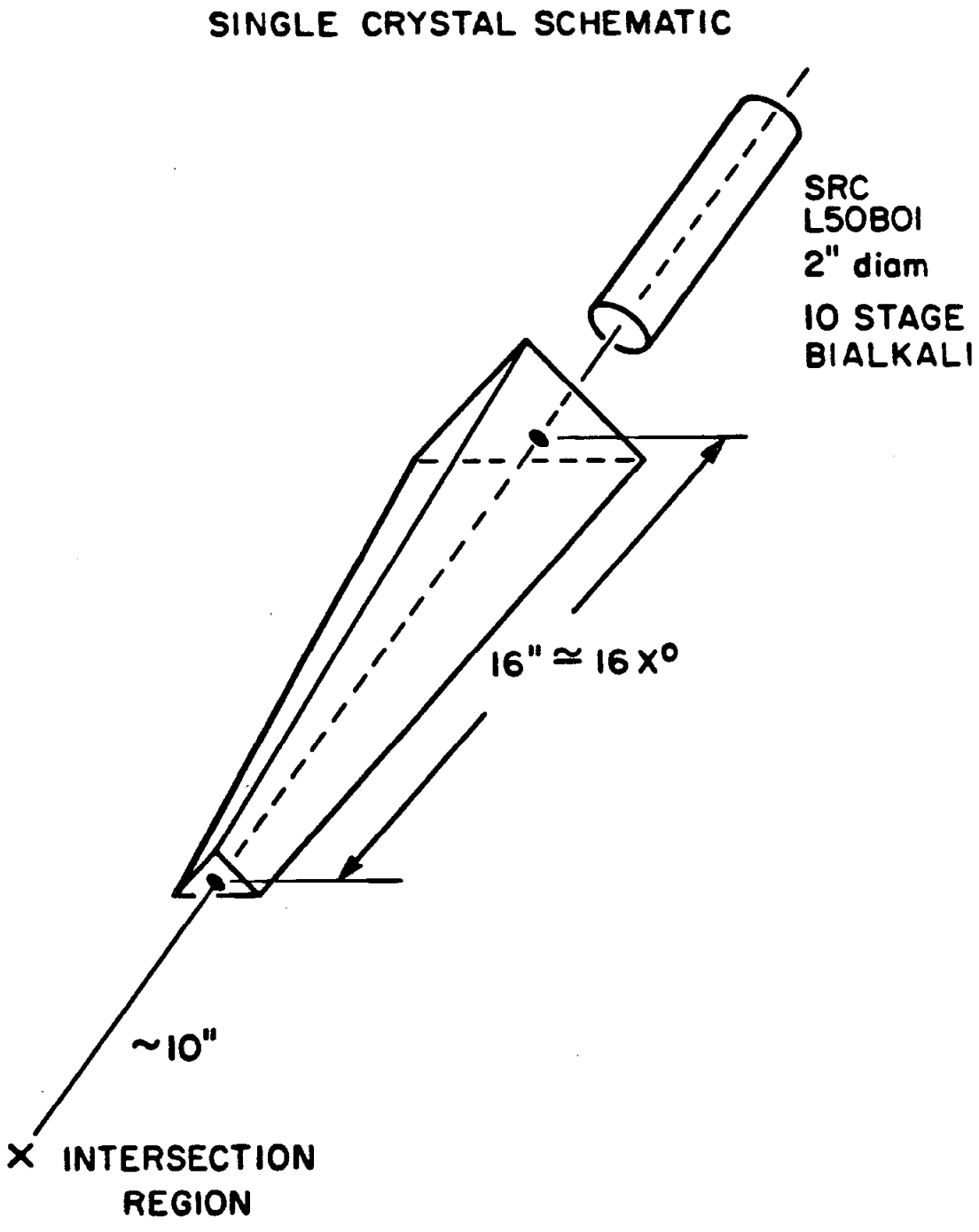

FIG..1-4 Schematic of a NaI(Tl) crystal/phototube module.

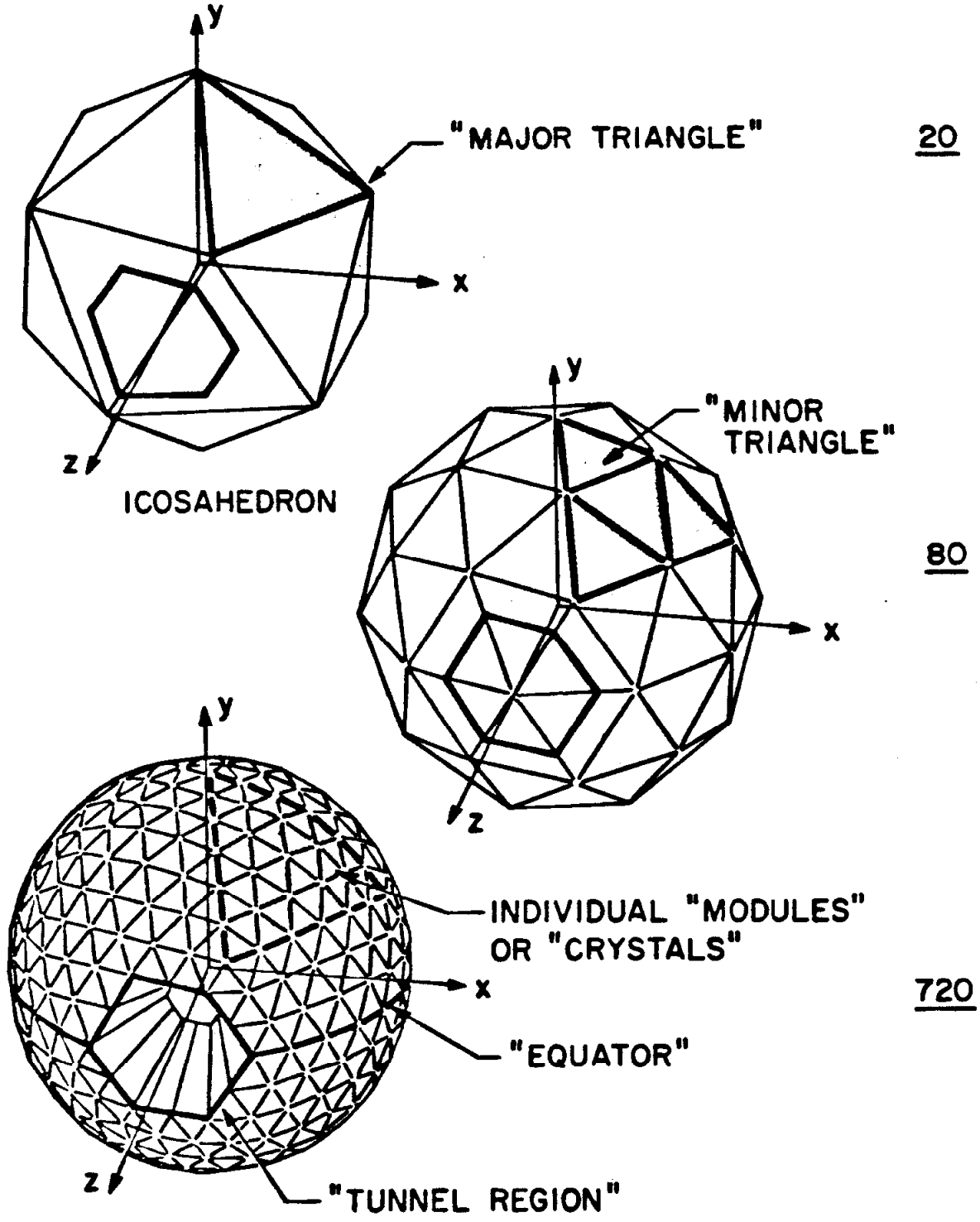

FIG..1-5 Development of the ball geometry and nomenclature.

needed to stack an entire sphere. In order to permit entry of the e^+ and e^- beams the 48 crystals nearest the +z and -z axes were removed, leaving 94% of the 4π solid angle covered. The "equator" shown in figure 1-5 demarcates the boundary of the two hemispheres; the "tunnel region" refers to the first layer of crystals surrounding the beam entries.

The analog sum of the modules comprising each minor triangle was available for trigger purposes. In particular, each minor triangle has a diametrically opposite partner, permitting a fast analog logic for back-to-back tracks. Major triangles were also useful for trigger logic, and they form the basis for a Mercator-like projection of the two hemisphere system; such a projection is shown in figure 3-3.

Crystals in each hemispherical stack were wrapped in reflector paper and aluminized mylar foil for optical isolation. Each stack was then hermetically sealed in an aluminium/stainless-steel can to protect the hygroscopic NaI from damage by water vapor in the atmosphere; the dehumidified ballroom served as a second line of defense. The cans, shown in figure 1-6, supported the phototubes which viewed each crystal. A dome of 1/16 inch stainless-steel (0.09 L_{rad}) formed the inner surface of each can. Construction details and stacking data can be found in appendix A. The upper and lower hemispheres were mounted in an elevator mechanism. Normally in contact during data acquisition, the hemispheres could be separated by up to 2 meters for maintenance and calibrations.

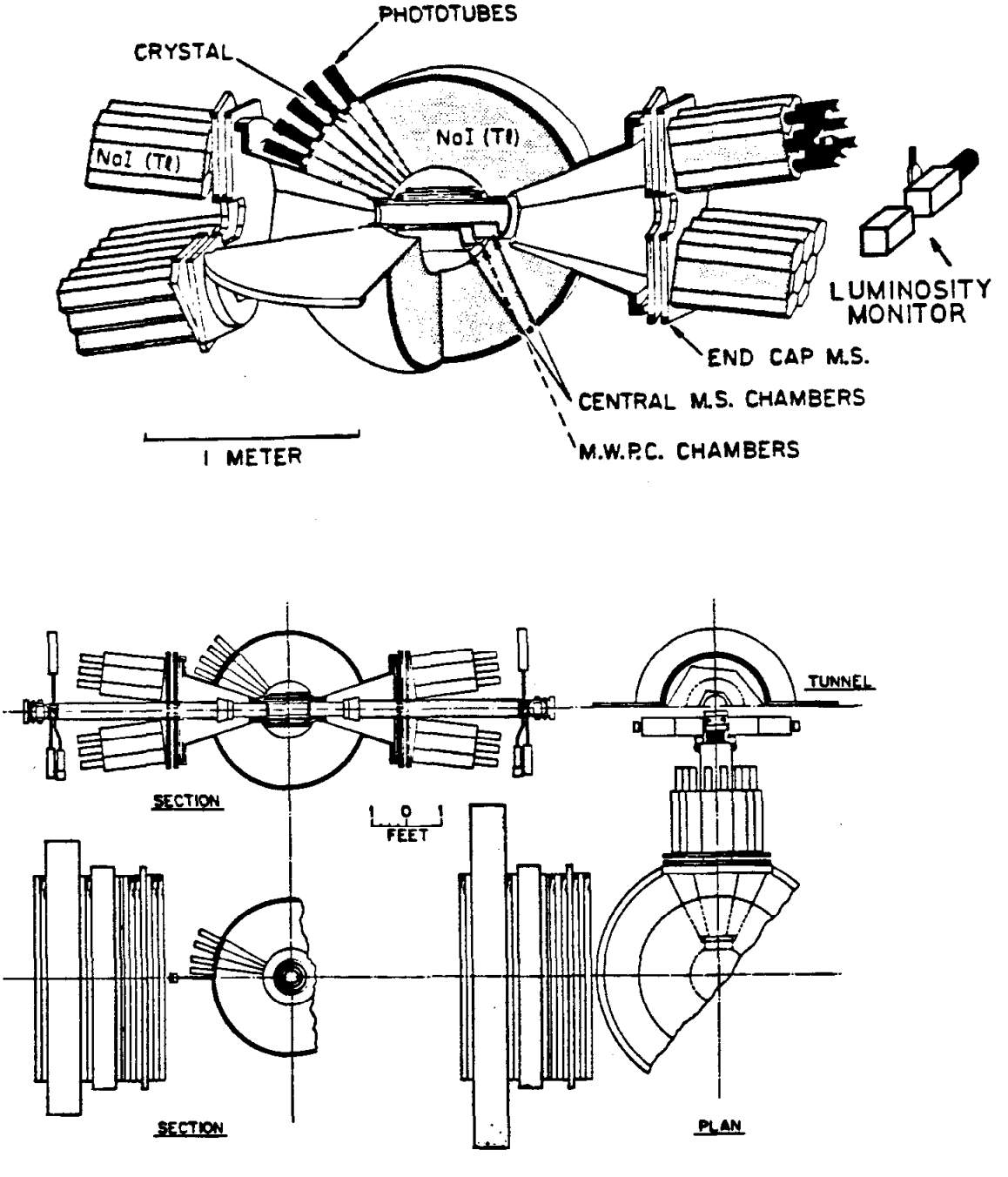

FIG..1-6 Schematic of the detector.

1.5 ENDCAPS

Also shown in figure 1-6 are the NaI(Tl) endcaps. These consisted of 60 hexagonal[13] crystals, typically 20 L_{rad} long (12 of them were 10 L_{rad}) and 6 inches across at the widest transverse dimension. Each endcap crystal was hermetically sealed in a stainless-steel can and viewed by a three inch phototube greased directly onto the rear window of the can. Four mechanical quadrants, each tilted 7° relative to the beam axis, describe the endcap array; the upper and lower pairs could be separated by an elevator system separate from that for the ball proper.

A perspective of the endcap and tunnel crystals, as projected from the interaction region onto the plane at the front face of the endcaps, is offered in figure 1-7. The endcaps brought the total NaI(Tl) solid angle coverage to 98% of 4π. In the analysis presented here the endcaps were not used to reconstruct tracks; rather, they served to detect the presence of photons over most of the 4π solid angle, and to reject events having any tracks beyond the tunnel region.

1.6 CHARGE TRACKING CHAMBERS

A four-stage system of charged particle tracking chambers augmented the NaI(Tl) portion of the detector. The system, indicated in figure 1-6, consisted of three cylindrical chambers about the beam pipe at the

---

[13]These hexagonal crystals are a standard Harshaw product, sold primarily for geographical explorations.

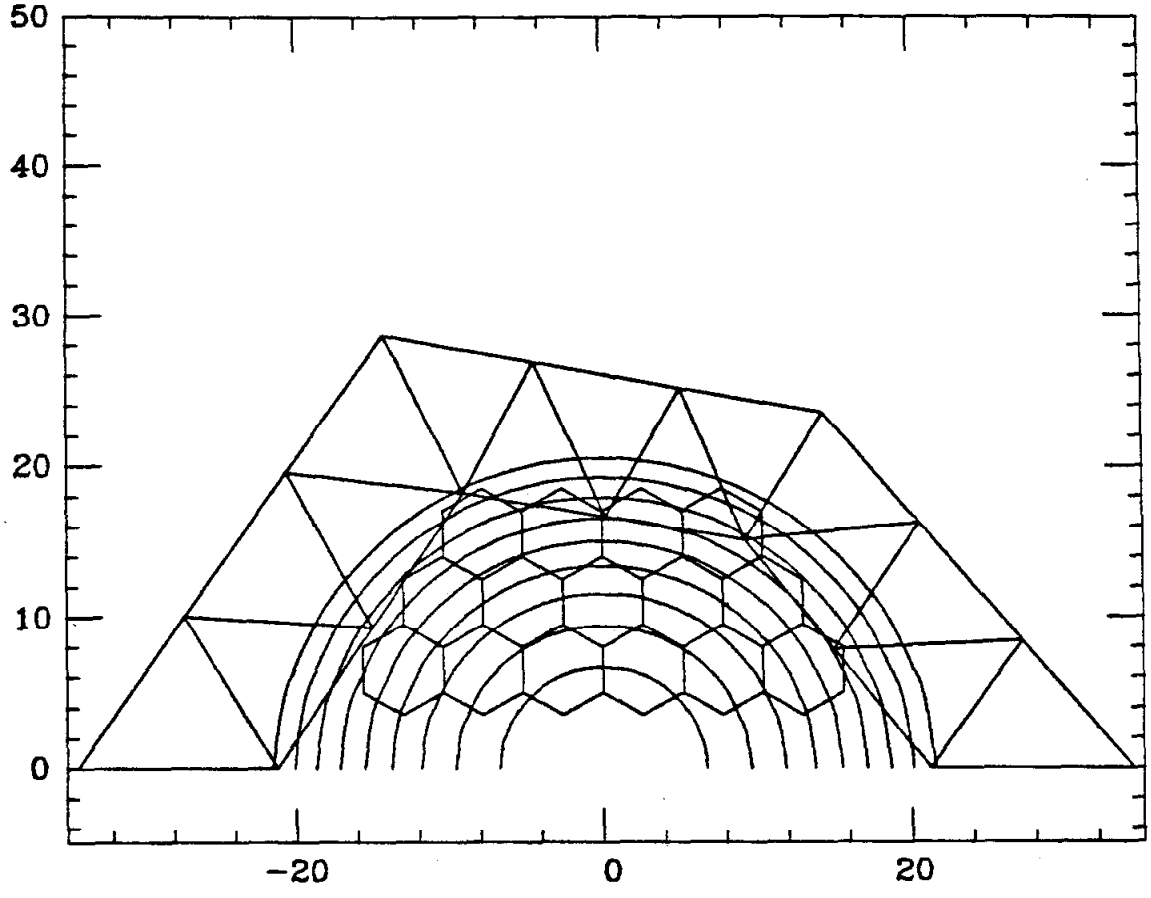

FIG..1-7 Projection of the tunnel modules from z=0 onto the plane at the front face of the endcaps. The circles are projections of cosθ from 0.91 to 0.99.

interaction region (the central chambers) and the planar endcap chambers. Working outward from the interaction region, a particle first traverses a spark chamber with magnetostrictive readout, followed by a multiwire proportional chamber, and finally another spark chamber. The proportional chambers were used only to identify a particle as charged after its trajectory had been reconstructed using the crystals, whereas the spark chamber system was capable of reconstructing charged track trajectories with greater accuracy than could the crystals.

The proportional chambers are shown schematically in figure 1-8. The unit appears as a cylindical shell with an inner radius of 90 mm, an outer radius of 115 mm, and an active length of 300 mm, corresponding to an effective coverage of 83% of 4π sr. Two separate chambers comprised the proportional chamber system. Each consisted of 144 gold-plated tungsten sense wires oriented along the beam axis, 0.02 mm in diameter and with an inter-wire spacing of about 4.5 mm. Separated from the wires by a 5 -mm gap were two cathode planes on either side of the wires; one plane was solid while the other consisted of 36 strips, each 7 mm wide and having a center-to-center spacing of 8 mm (9 mm) for the inner (outer) chamber. In the outer chamber the cathode strips were oriented 90° to the beam axis, while the inner chamber strips were oriented 62° to the beam. The two cathodes shared a common potential of about -1.7 KV relative to the sense wires, and a common gas supply of 90% Ar/10% CO_2 fed both chambers. Construction and performance details for the chambers can be found in reference 14.

---

[14]J. Gaiser et al., IEEE Trans. Nucl. Sci. NS-26 No.1, 173 (1979).

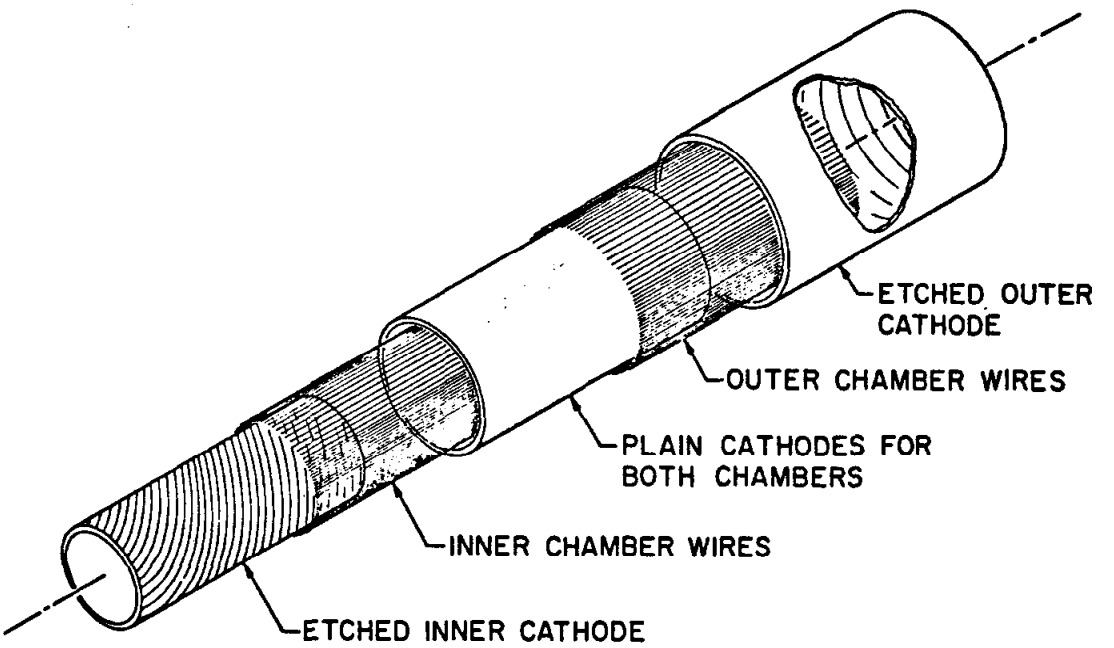

FIG..1-8 Exploded view of the multiwire proportional chambers.

Unlike the proportional chambers, the spark chambers were active only when the NaI(Tl) and proportional chambers had determined that an interesting event had occurred (a trigger). The two central spark chambers[15] each had two gaps and differed only in dimensions and orientation of the crossed-planes; they are shown schematically in figure 1-9. Solid angle coverage was 94% of 4π sr for the innermost chamber and 71% of 4π for the outermost chamber; since tracks in both chambers are required for a chamber-reconstructed trajectory, the latter acceptance applies to such reconstructions. A track perpendicular to the beam axis traveled through about 0.015 L_{rad} of chamber construction material before reaching the outermost spark chamber gap.

Endcap spark chambers,[16] also double-gapped, augmented the central units. These chambers were planar and resided just in front of the endcap crystals in the x-y plane. All the spark chambers were pulsed at about 9 KV and operated on a mixture of 90% Ne/10% He gas, with an ethanol doping for the endcap chambers only. A constant field of 10 volts was applied to the gaps to clear spurious ions and a pulsed ion-clearing field of 300 volts was applied after each firing of the chambers; the latter pulse required about 15 milliseconds to clear the gap.

---

[15]F. Bulos, Crystal Ball memo CB-NOTE 117 (1976).

[16]J. Tompkins, Crystal Ball memo CB-NOTE 232 (1977).

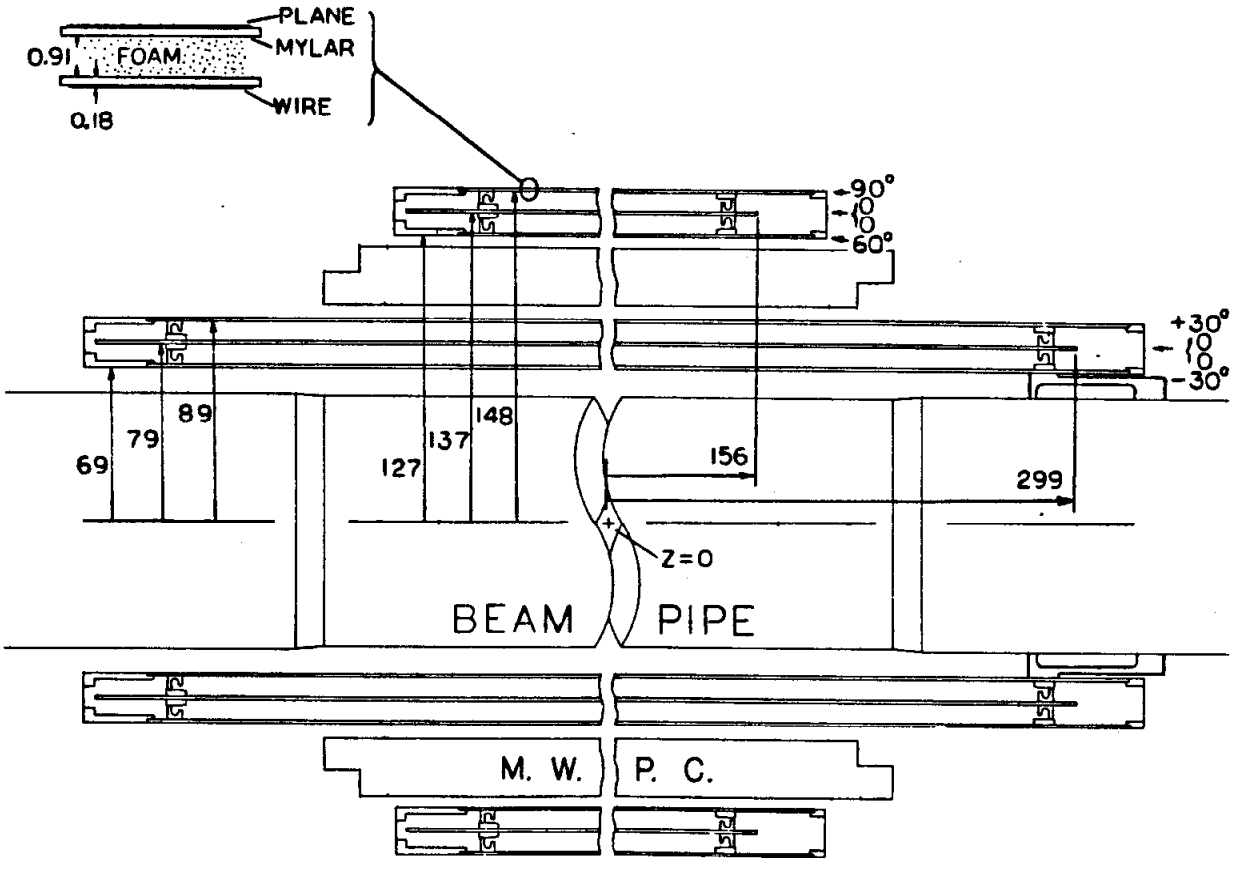

DISTANCES IN MM

FIG..1-9 Schematic of the central spark chambers.

1.7 LUMINOSITY MONITOR

A luminosity monitor[17] consisting of four counter elements centered at 4° relative to the beams is shown in figures 1-6 and 1-10. Each of the four elements was identical, consisting of three scintillation counters followed by a shower counter. The central Bhabha-defining counter subtended 4.2×10^{-4} sr, thus permitting a counting rate of 1.26 $E_b(GeV)^{-2}$ sec^{-1} at a luminosity of 10^{30} cm^{-2} sec^{-1}, corresponding to 0.4 Hz at the ψ' energy. Although the rate was too low for optimization of the SPEAR beams (the luminosity monitor in the SPEAR west pit, within 1.5° of the beams, had a much higher rate and therefore was used for this purpose), asymmetries in the four counting elements would indicate perverse beam orbits which were then corrected. An accuracy of better than 5% was achieved with the luminosity monitor; however, luminosity information is not used in the analysis.

---

[17] H. Kolanoski, Crystal Ball memo CB-NOTE 244 (1978).

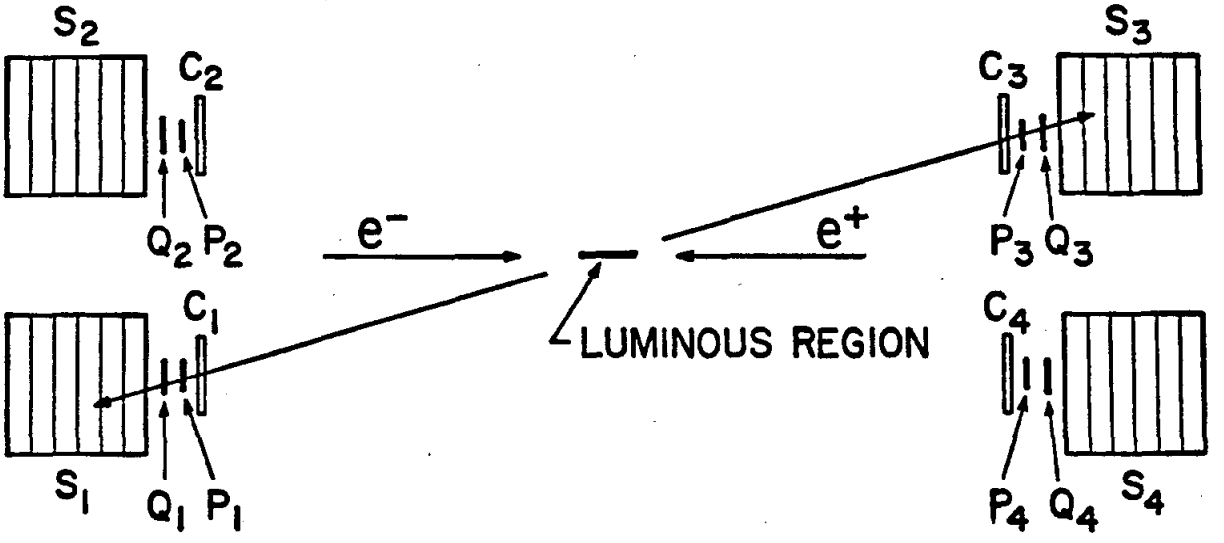

FIG..1-10 Schematic of the luminosity counters. Scintillation counters P (solid angle defining), Q, and C with shower counter S accept a hit if P and S fire together with C and S on the opposite side of the interaction region. Q is used as a diagnostic tool.

Chapter II

DATA ACQUISITION

2.1 SPEAR OPERATION

Data for the analysis were collected in four run periods totaling six weeks, from fall of 1978 through spring of 1979. During this time several of the storage ring parameters varied, such as vacuum in the beam pipe, status of the R.F. cavities, and current in the wiggler magnet. As a consequence, the machine energy resolution, luminosity, and backgrounds fluctuated over the run cycle.

For any particular machine configuration the beam orbit was adjusted to maximize the instantaneous luminosity, L, and to minimize the beam-related background seen by the detector. Beam noise arises from electrons which have unstable orbits and eventually deviate from the intended orbit sufficiently so as to strike the NaI(Tl) crystals or nearby structures in which they shower. Another background arises from the collision of beam electrons with residual gas in the beam pipe. The former background is minimized by using the occupancy of the endcap crystals as a monitor of the beam orbit quality, since the endcaps are located within inches of the beam pipe. Orbits were adjusted by the SPEAR operators so as to minimize the endcap rate.

During the injection of electrons into the storage ring the NaI(Tl) crystals experienced some radiation doses associated with the large fraction of injected electrons which are not captured into a stable orbit. It was extremely important to minimize the radiation, for it damages the NaI(Tl) crystal structure. A small ionization chamber mounted near the tunnel modules recorded the injection radiation, thus serving as a monitor of the injection quality. In particular, this monitor served to detect fill cycles in which injection kicker magnets were left on unnecessarilly.

An upper limit on the 1978-1979 radiation dose received by the NaI(Tl) arrays can be set at 100 to 300 Rads.[18] Measurements of the doses recorded by LiF thermoluminescent dosimeters mounted on various parts of the apparatus indicate that the brunt of the radiation was near the tunnel modules and the endcaps. Radiation-damage induced attenuation of light transmission in NaI has a characteristic length of one inch for a uniform dose of 50000 Rad; therefore, a 16 inch crystal uniformly irradiated with 100 Rad suffers a 3% decrease in its transmission coefficient. End-on radiation has a much smaller effect. No radiation damage was measured in the crystals (see appendix D).

Injection of positrons and electrons, together with orbit optimization, required 20 to 30 minutes on the average. The time lapse between fills was adjusted to maximize the ψ' yield over the fill cycle. Trial

---

[18] I. Kirkbride, Crystal Ball memo CB-NOTE 248 (1979).

and error was the actual method used to optimize the yield, with considerations for SPEAR-Linac schedules, machine reliability, and an idealized formula for the ψ' yield. A rough estimate of the yield is obtained from the naive (neglecting wall effects and assuming optimal coupling) relations:[19]

$$\begin{aligned} I_b &\sim I_0 \exp(-t/\kappa) \\ L &\sim L_0 I_b/\epsilon \\ \sigma(E_b) &\sim \sigma(E_b)\, I_b/I_0 \\ R_h &\sim \sigma(\psi')\, L/\sigma(E_b) \sim I_b/\epsilon \\ \epsilon &= \sigma_x\sigma_y = \epsilon_x{}^{\circ}\beta^*_x\beta^*_y\,(\beta^*_x+\beta^*_y)^{-1} \end{aligned} \qquad (2\text{-}1)$$

where R_h is the production rate of ψ' particles (the hadron rate), I_b the beam current, and I_0 the ceiling current. In practice, the emittance ϵ behaves as I^{α}, with $0<\alpha<1$ depending on the machine parameters. For a SPEAR configuration with no wiggler magnet and assuming a constant ϵ one obtains:

$$\int_0^T R_h\, dt = 1 - \exp(-T/\kappa)\ , \qquad \kappa \sim 500 \text{ minutes}. \qquad (2\text{-}2)$$

Optimizing over a fill cycle having a 20 minute injection yields:

$$\begin{aligned} &\frac{d}{dT}\,\frac{1-\exp(-T/\kappa)}{T+20} = 0 \\ &T = \kappa \exp(-T/\kappa) - (\kappa+20) \qquad (2\text{-}3) \\ &T(\text{optimum}) \sim 180 \text{ minutes} \quad . \end{aligned}$$

The calculated value of T(optimum) is a bit larger than the value of 120 to 150 minutes used during the actual run periods (those which did not utilize the wiggler magnet).

---

[19] M. Sands, SLAC report SLAC-121 (Stanford) (1970); and private communications from E.D. Bloom and H. Wiedemann.

The addition of a wiggler magnet in the late fall of 1978 made possible an increase in the beam current ceiling. Synchrotron radiation, produced as the electrons bend steeply in the wiggler magnet, worked to increase the transverse cross-section of the beam, thereby decreasing the beam-beam interaction. With the interaction diminished, more electrons could be stored in the bunch. However, the increased synchrotron radiation also increased the emittance and beam energy spread, as shown in figure 2-1. The dependence of ϵ and $\sigma(E_b)$ on the wiggler field B_W is:[20]

$$\frac{\epsilon(B_W)}{\epsilon(0)} = \frac{1 + 0.28\xi^3 \langle H_W\rangle/\langle H_0\rangle}{1 + 0.07\xi^2} \qquad (2\text{-}4)$$

$$\frac{\sigma(E_b)\big|B_W}{\sigma(E_b)\big|0} = \sqrt{\frac{1 + 0.28\xi^3}{1 + 0.07\xi^2}} \qquad (2\text{-}5)$$

where $\xi = B_W/E_b$ (Tesla/GeV) and H is a function of the machine magnet parameters. By measuring the luminosity at a fixed beam current of 8.5 ma, it was determined that $L(B_W=1.8T)/L(B_W=0) \sim 0.93$; the maximum wiggler field was 1.8 Tesla. The wiggler magnet's effect on the emittance appears to be negligible for $I_b > 8$ ma. Furthermore, we have observed the approximate behavior $R_h \sim I_b$ and $\sigma_h \sim (\text{constant} - I_b)$ for $B_W = 1.8T$ and beam currents in the range of 9 to 12 ma, which supports equation (1) with $\epsilon \sim$ constant. The expression for the ψ' yield then becomes:

$$\int R_h \, dt = \frac{I_0(B_W)\,[1-\exp(-T/K)]}{\sigma(E_b)\big|B_W} \qquad (2\text{-}6)$$

---

[20] H. Wiedemann, SLAC memo PEP NOTE-319 (1979).

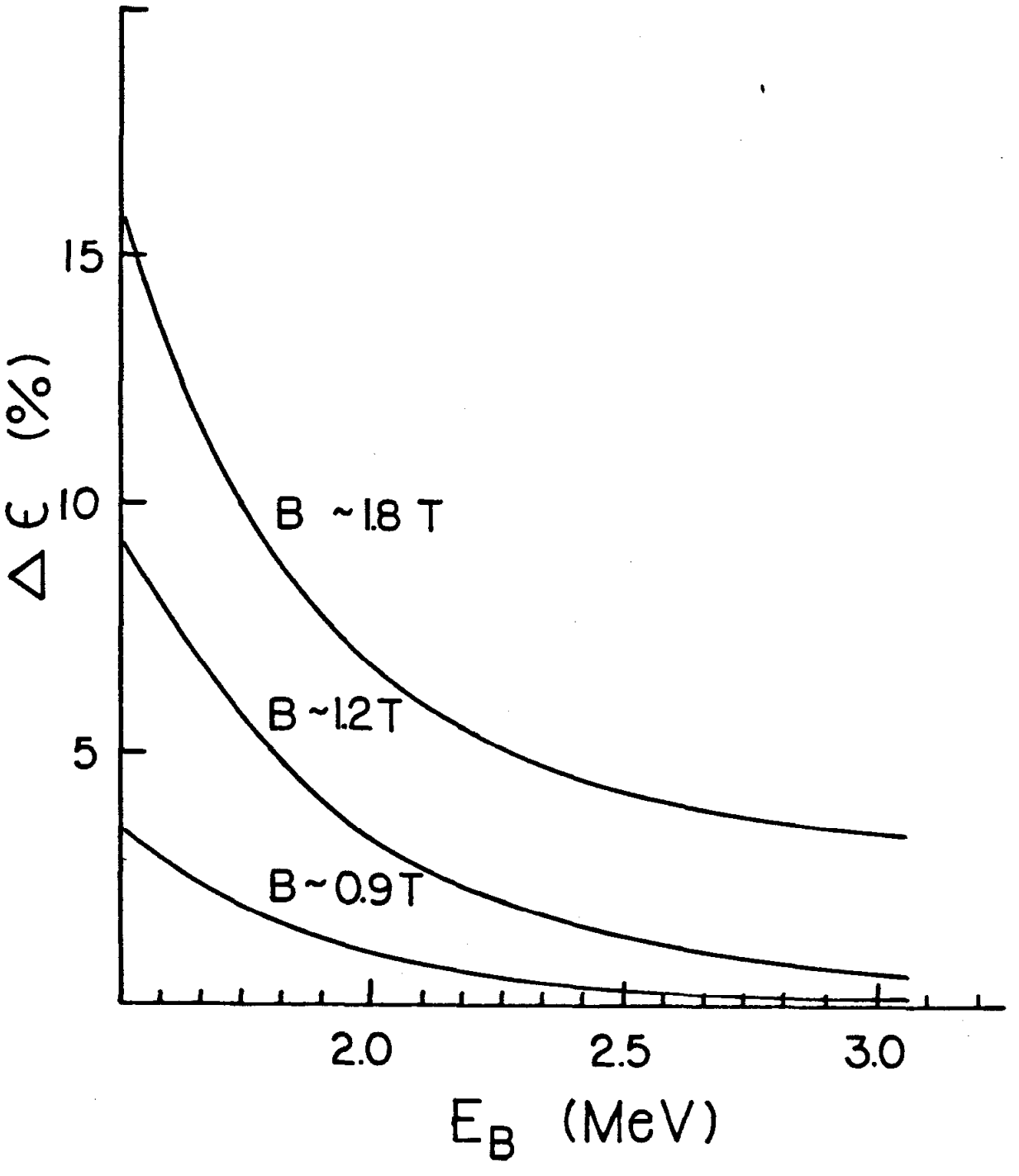

FIG..2-1 Effect of wiggler field (B, in Tesla) on the emittance.

where κ is now about 225 minutes for B_W=1.5T and 210 minutes for B_W=1.8T. The relative hadron yields as a function of wiggler current are roughly 1:1.5:1.3 for fields of 0:1.5T:1.8T . The run cycle was fixed at 120 minutes for B_W=1.5T and 100 minutes for B_W=1.8T; thus, the configuration with B_W=1.5T optimized the ψ' yield for the 1978-79 run cycles.

Since the wiggler magnet was a new device for which we had no prior experience, the 1978-79 cycle was used to experiment with the wiggler settings; the optimal configuration was therefore achieved over only a fraction of the total run period. Overall, 1623 nb^{-1} of ψ' data were accumulated, with 325 nb^{-1} taken with no wiggler field, 395 nb^{-1} with B_W=1.5T, and 903 nb^{-1} with B_W=1.8T. The chronological distribution for the acquired data is shown in figure 2-2.

2.2 TRIGGERS

Triggers for events recorded in the experiment all resulted from conditions which were satisfied in the hardware network of the apparatus. The overall trigger consisted of four independent systems designed to minimize acceptance of beam gas and cosmic ray events while still accepting all ψ' decays. Any one of the four elements was permitted to accept an event. In an effort to write data on tape at the reasonable rate of ~3 Hz maximum, each of the four trigger elements was adjusted to a level which would accomodate the maximum allowed rate. All rates listed in the following discussion are for an energy E_{cm}=3684 MeV, a current I_b=8 ma, and an instantaneous luminosity L=1.1 μb^{-1} sec^{-1}.

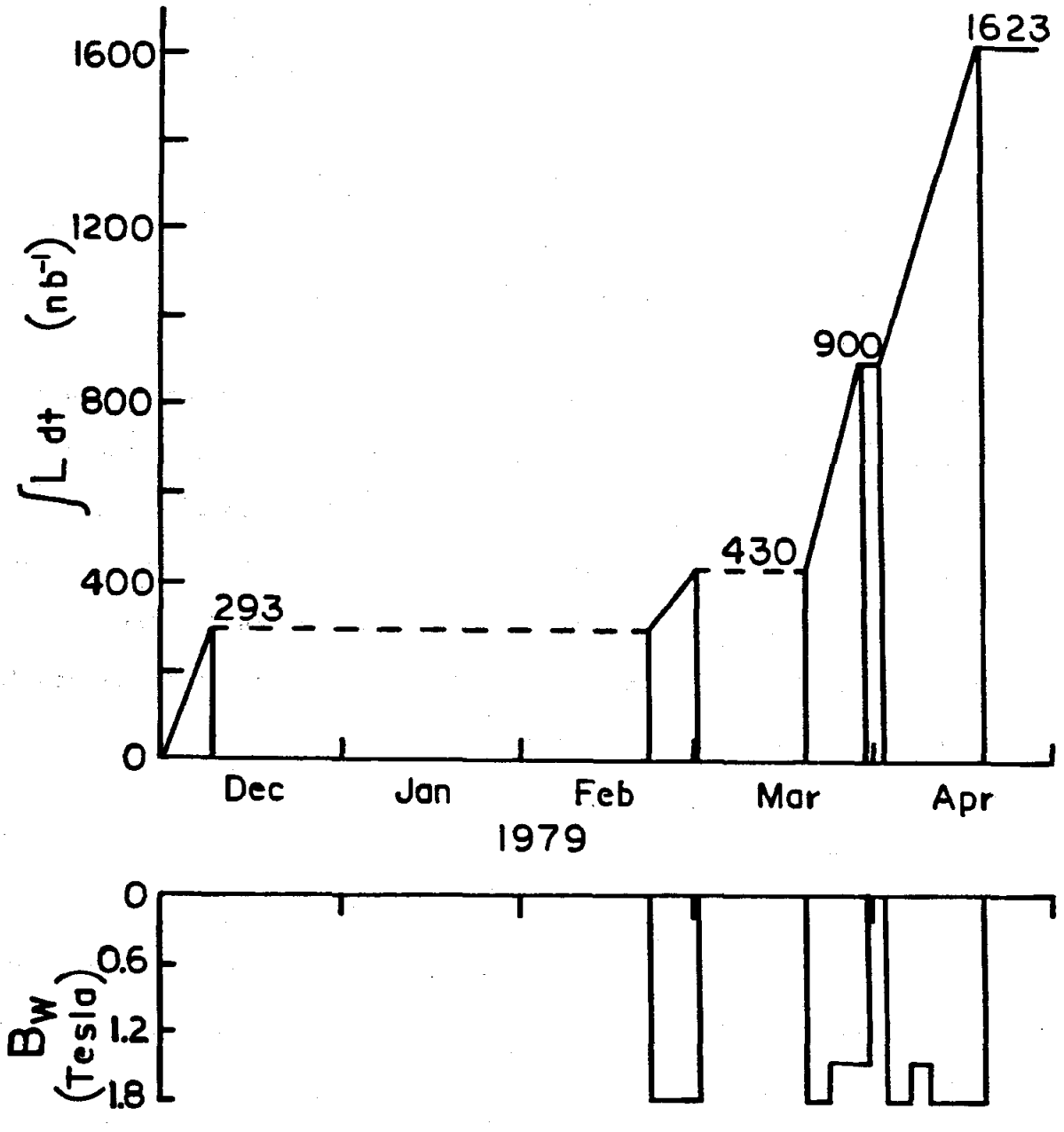

FIG..2-2 History of the 1978-79 SPEAR ψ' run. B_W is the wiggler field and L the luminosity.

Most general of the trigger elements was the Total Energy Trigger. This trigger was satisfied if the analog sum of the NaI(Tl) modules comprising the ball proper, but not the endcaps or tunnel modules, exceeded 30% of the beam energy. The solid angle over which the trigger was effective is 84% of 4π sr, and a contribution of about 0.9 Hz to the data rate was realized.

Fast Trigger is described in appendix B. This system examined the energy levels and timing of signals formed by the analog sum of crystals (including the tunnel modules but not the endcaps) in the top hemisphere of the detector, the bottom hemisphere, and the full ball. Each hemisphere was required to measure an energy exceeding 160 MeV, which safely corresponds to the lowest energy in the distribution of a minimum ionizing particle traversing 16 inches of NaI(Tl). The timing signal of the event in the full ball sum was required to occur within 8 ns of the beam-crossing signal.[21] Finally, the energy measured by the full ball sum was required to exceed 650 MeV -- the lowest energy threshold which could accomodate a 1.1 Hz contribution to the data rate and an overall data rate of 3 Hz. Cosmic rays dominated the trigger rate when the total energy threshold was much less than 650 MeV. The Fast Trigger system accepted the $\gamma\gamma\mu^+\mu^-$ final state with an efficiency of about 99.1% provided that all the particles were detected within the ball proper, an active solid angle of 92% of 4π sr; for this reason the full-ball energy threshold was set as low as possible.

---

[21] A pulse from the R.F. generators at SPEAR which corresponds to the instant that the e^+ and e^- beams collide.

Additional redundancy in the total trigger was supplied by the Multiplicity Trigger which required that two or more of the energy sums formed by crystals in a major triangle exceeded the minimum ionizing threshold. An additional requirement was at least one pair (a correlated inner and outer layer wire pair) of wires in the multiwire proportional chambers detecting a charged particle. The proportional chambers were used in this application because of their high efficiency and the ease in forming the hardware logic. The active solid angle for the system is limited to that covered by the proportional chambers -- about 80% of 4π sr, with this system responsible for a contribution of 1.5 Hz to the data rate. Circuit diagrams can be found in appendix B.

The last system in the redundant trigger hierarchy has the intriguing name of Quark Trigger. Here a signal for an energy exceeding 40 MeV had to be observed in back-to-back minor triangles; in addition, the total energy measured by all crystals, excepting tunnel modules and endcaps, had to exceed 140 MeV. This system was designed to respond to dE/dx signals in NaI(Tl) from high momentum heavy particles with a charge less than that of the electron. Since Bhabha electrons fulfilled the Quark trigger conditions, they were responsible for most of the rate observed in this system.

There was considerable overlap of the four trigger systems, so that the total data rate was much less than the sum of the four individual rates. The combined trigger efficiency for the $\gamma\gamma\mu^+\mu^-$ or $\gamma\gamma e^+e^-$ final state from $\psi' \to \gamma\gamma\psi \to \gamma\gamma l^+ l^-$ exceeded 99% provided that all particles were

detected within the central 90% of 4π sr solid angle away from the beam axis. The high efficiency is a consequence of the characteristics of the particular final state and the high efficiency of NaI(Tl) for measuring the energy of photons and electrons over a large energy range.

2.3 DATA ON TAPE

Data for each hardware trigger were written to magnetic tape with no intermediate software processing, save for the luminosity monitor events which were accumulated into 10-event buffers before being written to tape. The primary data tapes were written in PDP format with five types of data record being recorded onto tape:

1) calibration records, written at the beginning of each tape;
2) event records for physics events;
3) equipment status records, written every several minutes;
4) luminosity monitor records, written for every 10 such triggers;
5) xenon-flasher records (for calibration purposes), written in the same format as an event record, pulsed every 10 seconds to one of the hemispheres.

The calibration files recorded the high and low channel pedestals, the ^{137}Cs calibration slopes, and the high channel/low channel ratios for each NaI(Tl) module. These constants were updated on a weekly basis. Additional checks on the stability of the calibration for each module were obtained by periodically sending pulses of light from a xenon flashlamp to each phototube via fiber-optic cables. A xenon pulse was sent to all the phototubes of either the top or the bottom hemisphere,

including the endcaps. These events were then monitored offline to detect sudden changes in the gain of the phototubes. Also monitored periodically were the phototube high-voltage supplies, the luminosity monitor thresholds, and the SPEAR beam energy.

Each physics trigger was recorded on tape in a standard format, consisting of the tape, run, and event numbers, the date and the orbit-corrected SPEAR beam energy, followed by the raw measurements from the apparatus. The measured quantities included the high and low ADC channel number for each module, the fiducials and wand registers for the inner and outer magnetostrictive chambers, the wires registering hits in the multiwire proportional chambers, data from OHMS, channel numbers from the Fast Trigger ADCs and TDCs, and the identity of the trigger elements which were enabled for the run, as well as the identity of those which triggered for the event. Each event was written onto tape as a single record occupying about 3000 bytes, permitting about 7500 events to be stored on each PDP tape. Since the PDP can write tape at a maximum density of 1600 bpi, the PDP tapes were organized into groups of four, and copied onto a single tape of density 6250 bpi. The processing which created the "condense" tapes was accomplished using the Triplex (IBM 370/168) system at SLAC; and the original PDP format was preserved when creating the condense tapes.

2.4 DATA QUALITY CHECKS

Calibrations of the NaI(Tl) modules were performed frequently in order to guard against changes in the NaI(Tl) output (due to possible crystal degradation from hydration or radiation damage) and drift in the phototube gains or the electronics channels. "Hardware" calibrations, wherein a known source of photons was placed at the center of the ball and calibration data then recorded, were conducted weekly employing a ^{137}Cs source, and monthly using the Van de Graaff accelerator. The accelerator was employed to observe the 6.13 MeV line from the decay of ^{16}O*. The Cs calibration was performed within about two hours, while the Van de Graaff calibrations required about four hours to record data, which was then analyzed offline. In order to fine tune the calibration constants, Bhabha electrons accumulated during each week of running were used as a third calibration source. The average weekly drift in the calibration constants was about 1%, resulting in a total systematic uncertainty for energy measurements of about 2%.

During the course of each run a set of tests was performed automatically by the data acquisition system and a diagnostic message was printed by the online computer if the results of these tests fell outside of predetermined limits. These tests consisted of: a monitoring of the phototube high voltages, which had to remain constant to 0.1%; a monitoring of the SPEAR beam energy, constant to 0.02%; a realtime monitor of the calibration constants for each module, which computed the average pulse-height in each module for the xenon flashes over periods of approximately one hour; and, a system data acquisition monitor which detected errors on the CAMAC dataway and computer malfunctions.

In addition to the automated run tests a number of spot checks were made by the operators. The instantaneous luminosity of SPEAR and the beam position, as determined by the endcap noise monitor, were optimized throughout the run; the overall data rate was also monitored. Distributions of the timing of triggers, relative to the beam-crossing signal, were monitored to insure that the apparatus was triggering in coincidence with the real beam-crossing; additionally, side-bands on the timing distribution would indicate poor beam configurations. Proper operation of the charge tracking chambers was ascertained by observing the online reconstruction of Bhabha events. At the end of each run statistics on the luminosity monitor and the tracking chambers were inspected to insure that these were operating at the expected efficiencies.

Periodically during each 8-hour shift, the voltages of the CAMAC power supplies and the configuration of the enabled trigger elements were inspected. At the same time, the crystal environment was checked for adverse temperature, humidity or pressure conditions, and the gas systems for the tracking chambers were tested; gross deviations from safe levels were detected by electronic sensors.

Chapter III

DATA PROCESSING

3.1 INTRODUCTION

The raw measurements recorded on the condense tapes were processed on the SLAC Triplex (IBM 370/168) system in order to facilitate reconstruction of the events. At the same time, events which were obviously of no interest (cosmic rays and beam gas) were eliminated to some degree. Processing of condense tapes involved conversion of the PDP data format to IBM format, determination of energies, and reconstruction of tracks[22] -- a production tape resulted from each condense tape. Production tapes were then screened further to create a select-class datafile of the final states $\gamma\gamma l^+l^-$. A brief set of conditions was imposed on events put on the production tapes. The number of cosmic ray shower events was reduced by requiring the total energy of the ball-plus-endcaps to be less than 10 GeV. Demanding at least 20 MeV in both the +z and -z halves of the NaI(Tl) sphere and endcaps assisted in diminishing the highly asymmetric beam gas and degraded-electron backgrounds. Usually cosmic ray events failed to create more than one region of contiguous crystals, each crystal measuring more than 10 MeV[23] (about 30% of the time); ev-

---

[22]The word is used here to describe both neutral and charged trajectories.

[23]These are the "connected regions" discussed later.

ents with less than two such contiguous regions were therefore rejected. Lastly, if the number of reconstructed tracks exceeded 30, the event was rejected.

For the ψ' data acquired at SPEAR, 109 production tapes were reduced by 114 data summary jobs, followed by one kinematic fitting pass; some tapes or runs were not considered because of dubious equipment status -- these runs are documented in appendix C. A total computer expenditure of about 74 hours of CPU was realized.

3.2 ENERGY MEASUREMENT AND NEUTRAL TRACKING

Raw data from the crystals were recorded on tape in the form of two 13-bit ADC channels[24] ; the low channel recorded energies in the range 0-160 MeV, while the high channel was attenuated by a factor of 20 to cover the 0-3200 MeV range. Calibration of these channels consisted of determination of the pedestal for each channel, the low channel slope (dE/d(channel)), and the high channel/low channel slope ratio. Sources of monochromatic photons or electrons of several energies were required to calibrate the large dynamic range; the 0.66 MeV gamma line from ^{137}Cs, the 6.13 MeV gamma line from the decay of excited ^{16}O (obtained from the reaction $^{19}F(p,\alpha)^{16}O^*$ using 0.34 MeV protons from a Van de Graaff accelerator), and the high energy Bhabha electrons produced at SPEAR were employed for the calibration. The energy distribution for

---

[24] G. Godfrey, Crystal Ball memo CB-NOTE 121 (1976).

1.842 GeV electrons is shown in figure 3-1 for various stages of the calibration. The non-gaussian shape is primarily due to the energy line shape of the NaI(Tl); there is only a small contribution from electron bremsstrahlung. Details on the calibration procedure can be found in appendix D.

The direction cosines of a particle's trajectory were determined using the magnetostrictive spark or multiwire proportional chambers if it was charged, or by examining the patterns of energy deposited in the NaI(Tl) crystals[25] -- both of these methods are described in subsequent sections. Associated with the particle's trajectory is the particular NaI(Tl) module which it traversed, referred to as the "central module"; this crystal usually measured a larger energy deposition than any of the nearby modules.[26] Each central module was considered together with a set of its neighboring crystals to provide an energy sum which was related to the energy of the incident particle. Such a group of crystals defines an "energy cluster", or connected region. The geometry which describes the stacking of the crystals naturally forms clusters of one, four, or 13 crystals with which one can measure the energies; these clusters are indicated in figure 3-2. In figure 3-3 is a Mercator-like projection of all the modules comprising the ball proper, with the measured energy appearing for all modules measuring more than 0.5 MeV. The figure demonstrates the clusters of 13 crystals associated with each major energy de-

---

[25]These patterns are referred to as the shower "profile".

[26]Shower fluctuation and hadronic interactions sometimes cause neighboring modules to measure a larger energy than the central module.

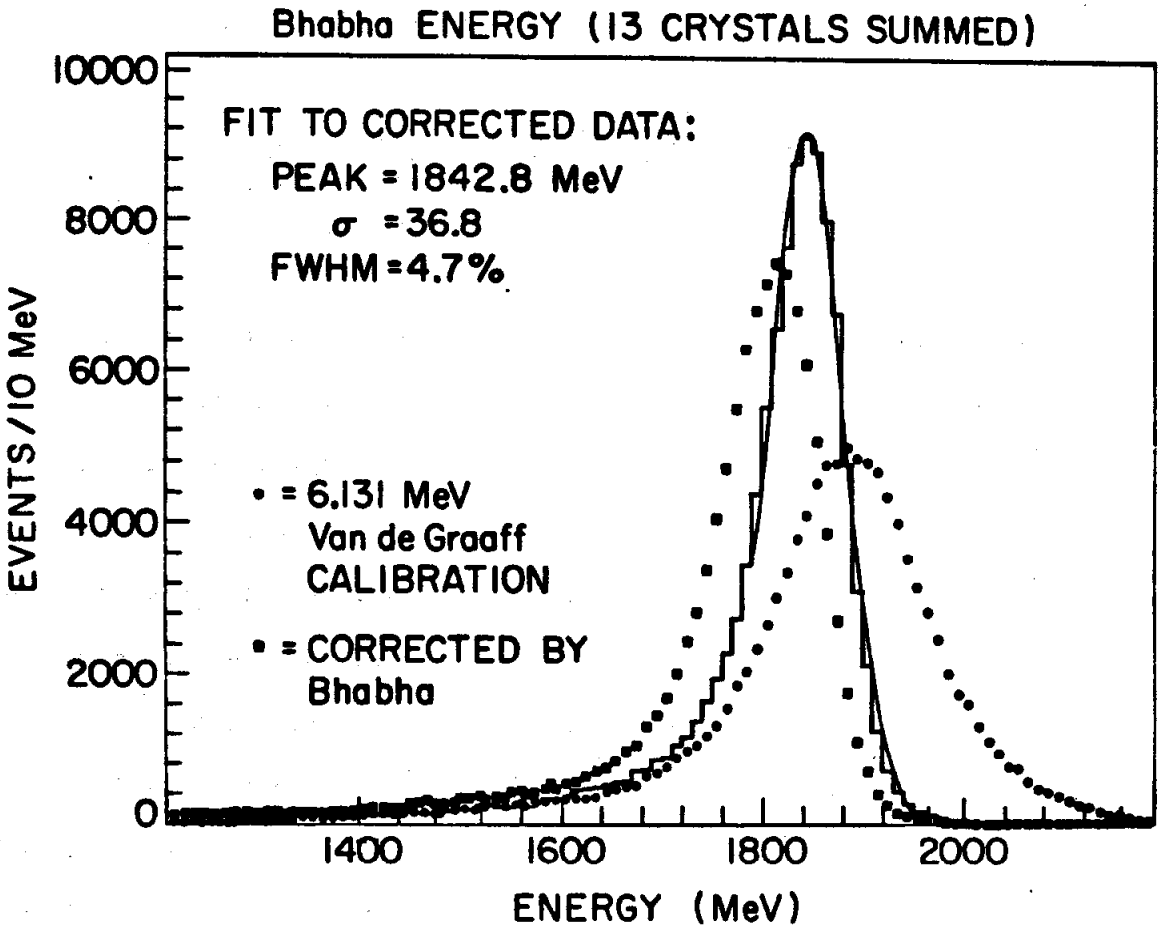

FIG..3-1 Line shape produced by the $\sum 13$ energies for Bhabha electron events at the ψ' energy. Dots indicate a calibration solely from sources up to 6 MeV; squares show the correction using the Bhabha electrons to calibrate; the histogram is obtained when position dependence in the crystal is considered (appendix D).

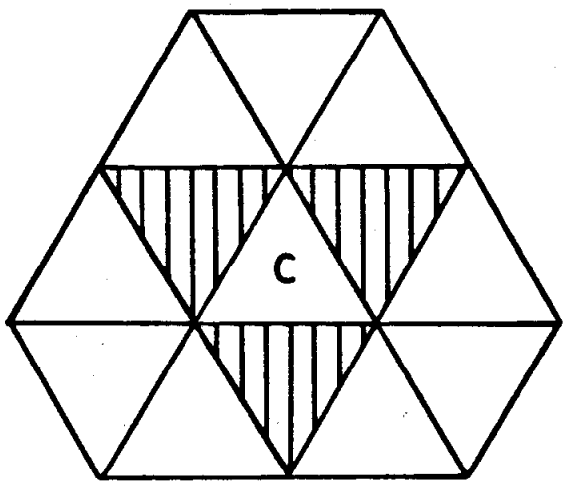

FIG..3-2 Energy measurement geometries. C denotes the central module ($\sum 1$); C together with the shaded crystals produces the $\sum 4$ energy; all crystals shown contribute to the $\sum 13$ energy.

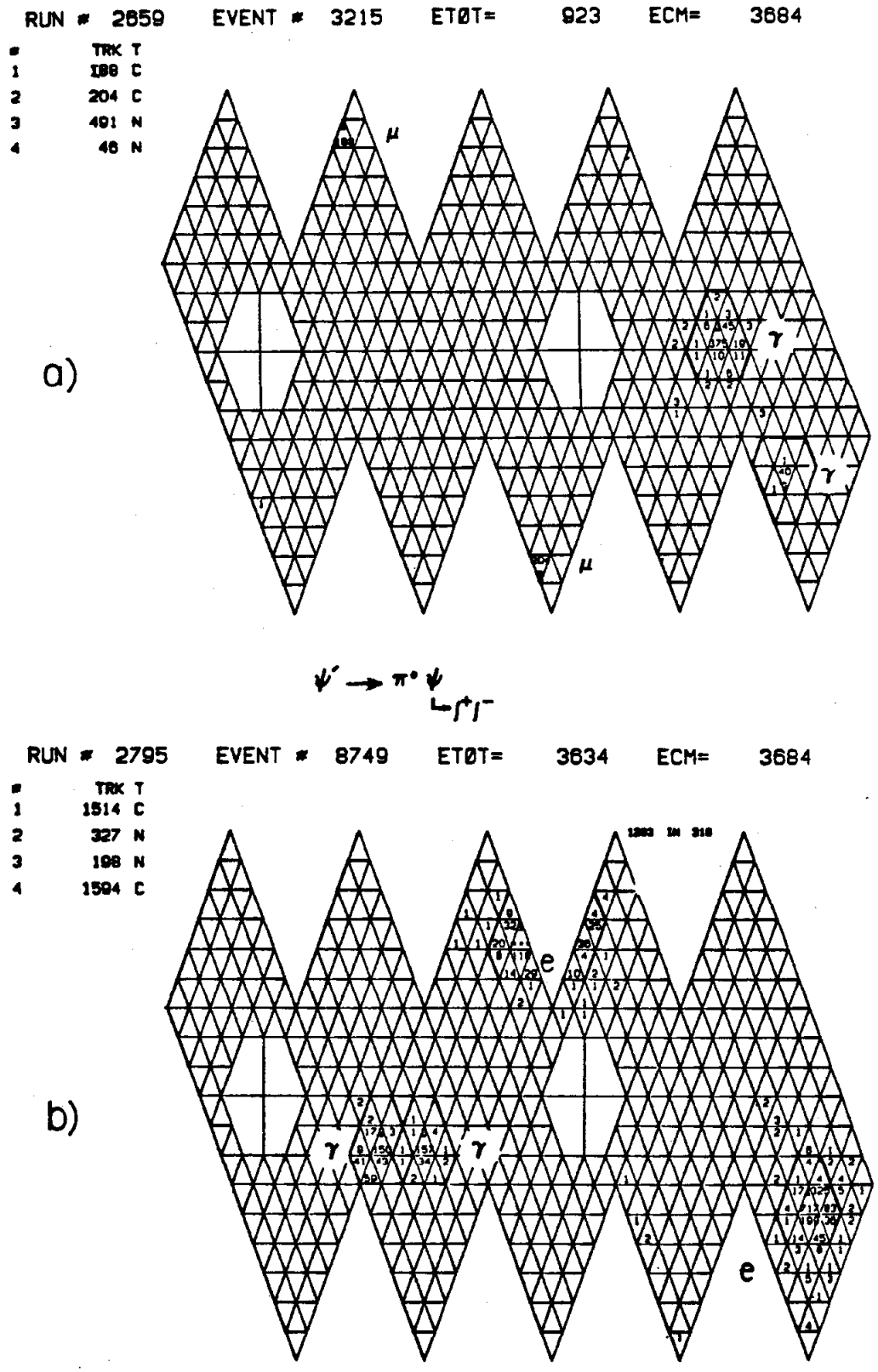

FIG..3-3 Event projection for $\psi' \to \pi^0 \psi$ events.

position zone in the ball proper; the clusters, which comprise the standard energy measurement configuration (the $\sum$13 energies) used in the analysis, subtend 1.8% of the 4π solid angle. The projections in figure 3-3 are shown for some events from the decay $\psi' \to \pi^0 \psi \to \gamma\gamma l^+ l^-$. The π^0 has the average kinematically allowed energy in figure 3-3a and the maximum allowed energy in figure 3-3b. One observes a slight overlap of the photon tracks in the latter figure, although the photons are still clearly resolved. For overlaps worse than the 26° ($\cos\theta_{\gamma\gamma} = 0.9$) case, fluctuations of the electromagnetic shower make it difficult to measure the individual energies accurately. Also apparent in figure 3-3b is a fake track caused by a fluctuation in the shower of an energetic electron. Muon tracks in figure 3-3a are seen to be much cleaner than the electron tracks. Note that the tunnel modules cannot contain the central crystal of a track for which a $\sum$13 energy is desired; the solid angle covered by the ball proper, excluding the tunnel region, is 85% of 4π.

Interactions of the incident particle in NaI(Tl) are divided naturally into three classifications: particles which always deposit their total energy; particles which deposit minimum ionizing energy; and, particles which deposit ill-defined dE/dx energy or suffer hadronic interactions in the NaI(Tl). Since the crystals have a length of 16 radiation lengths, light electromagnetically interacting particles (i.e., $e^{\pm}$ and γ) produced at SPEAR energies deposit virtually all of their energy in the NaI(Tl). The $\sum$13 configuration reliably measures 97.5% of the shower energy with a resolution $\sigma = 0.028 \times E^{3/4}$ GeV (see appendix E). Typically, the central module contains more than 50% of the total track en-

ergy. Then, since a 10 MeV threshold has been applied to all crystals when searching for energy clusters (see below), all tracks which are reconstructed on the production tapes must have an energy exceeding 20 MeV.[27] By examining the shower profile the position of an electromagnetically showering track can be determined to much better than the size of the central module, though fluctuation of the shower limits the accuracy of angles determined in this manner. The Crystal Ball has achieved a resolution σ=1.5° to 2°, with a slight energy dependence on the result (appendix E).

Heavy charged particles with momenta greater than 200 MeV/c (such as the muons from the ψ decay) deposit energy in NaI(Tl) via the process of dE/dx and thus form minimum ionizing tracks, imparting an average energy of about 208 MeV after traveling the full length of a single crystal. Particles of lower momenta tend to deposit more than minimum ionizing energy in material; indeed, if they are of sufficiently low energy (e.g., a kinetic energy less than 218 MeV for pions), they will stop in the NaI(Tl). Minimum ionizing tracks provide an outstanding signature in that only a single crystal will illuminate[28] if the track is fully contained in the one crystal (i.e., there is no shower). Tracks originating at a displaced interaction vertex will not traverse the ball radially and may illuminate up to 3 crystals. In addition, there is some multi-

---

[27]This threshold must not be confused with another threshold of 40 MeV, which is imposed to select events of high quality later in the analysis.

[28]The term is used to refer to a module which measures more than 0.5 MeV.

ple scattering, so that up to 5 crystals may be illuminated by a high-momentum muon. Figure 3-4 shows the results of a study of muons from the decay $\psi' \to \gamma\chi(3510), \chi \to \gamma\psi, \psi \to \mu^+\mu^-$. Note that 5-crystal illumination seldom occurs. The distribution in energy exhibits a long (Landau) tail on the high energy side, the result of atomic ("knock-on") electrons scattered by the heavy charged particle, which in turn shower in the NaI(Tl). Since all of this shower energy is measured, the net measured heavy particle energy exceeds the minimum ionizing value. The process also contributes to a small sharing of energy with the neighboring crystals. The muons from the decay of the ψ have very high momentum; hence, the muon identification algorithm is:

1) track energy = 150 → 280 MeV

2) 1 → 4 crystals register an energy greater than 10 MeV each

3) the track is charged

Slower muons and a variety of other particles ($\pi^{\pm}$, $K^{\pm}$, p, $\bar{p}$, etc.) deposit a wide range of energies in NaI(Tl) by the process of dE/dx and by hadronic interactions with the nuclei in the crystal lattice. Energy profiles from these reactions are quite unpredictable, producing large energy deposition regions of irregular shape and density. Lacking the well defined behavior of electromatic showers, the strong interaction tracks are easily identified by hand scanning the events. Figure 3-5

---

[29]M. Suffert, $\bar{p}$-LEAR NOTE No. 41 (CERN) (1979).

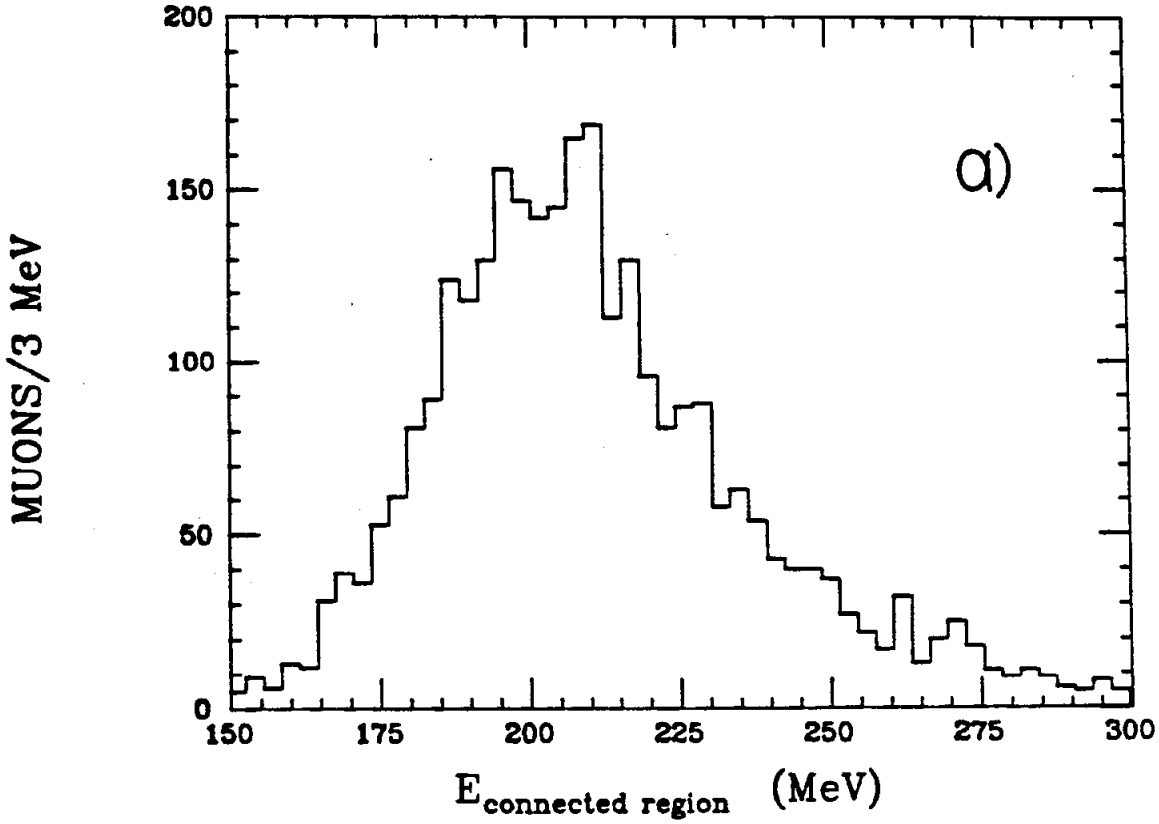

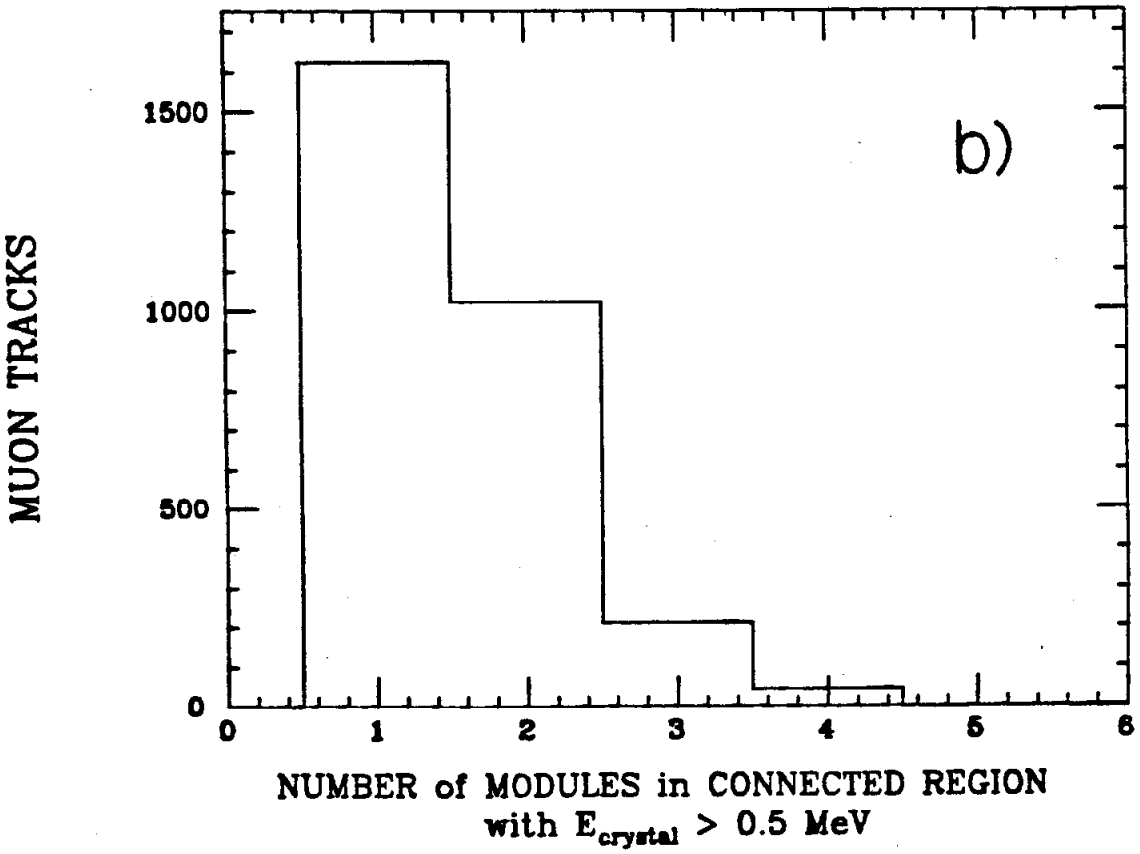

FIG..3-4 Study of muon characteristics from $\psi' \to \gamma\chi(3.51) \to \gamma\gamma\mu^+\mu^-$.

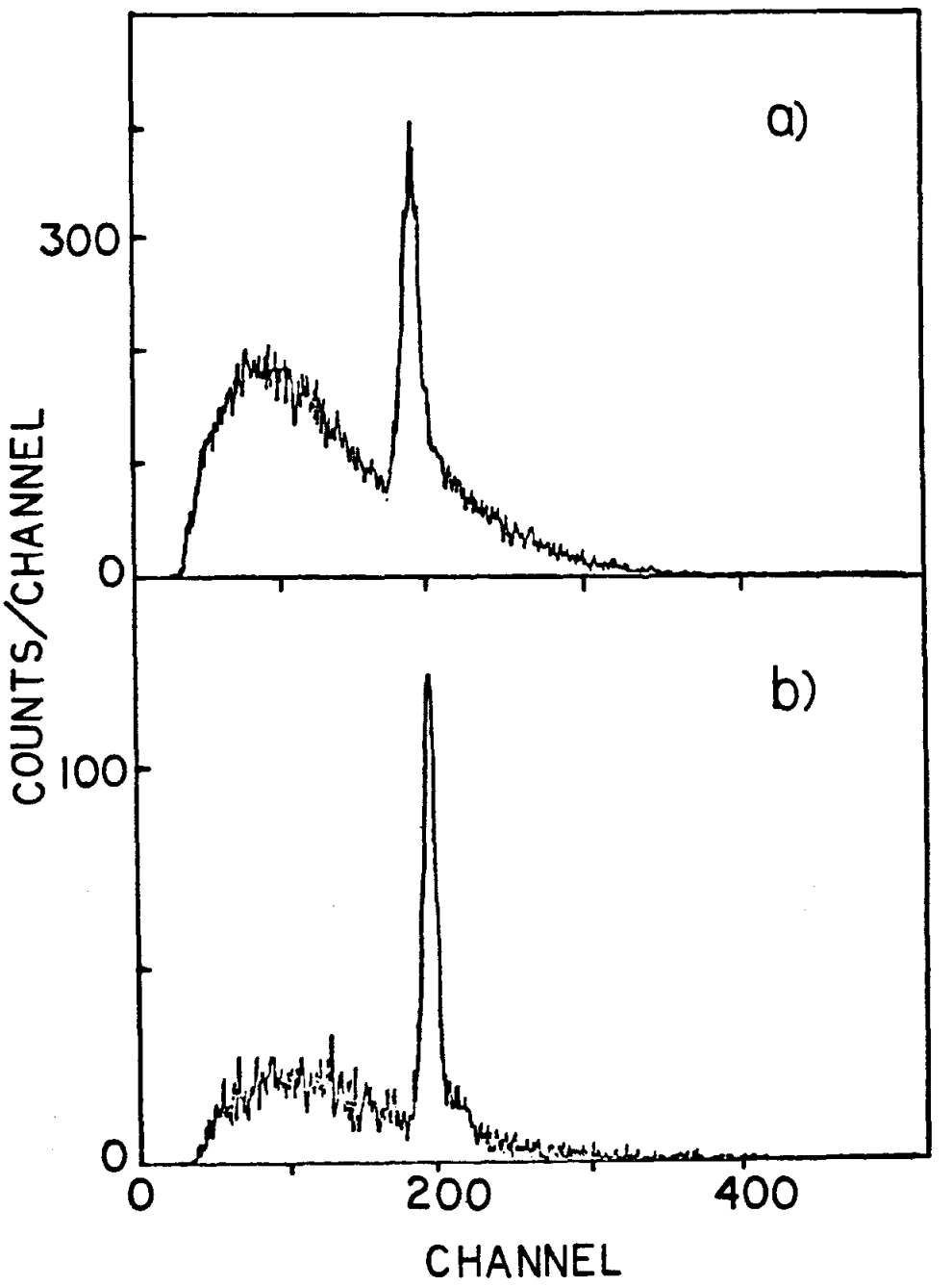

FIG..3-5 Spectrum of 200 MeV/c charged pions in a cluster of 54 Crystal Ball crystals (from Suffert et al.). Negative pions in a) and positive pions in b). The peaks (at ~120 MeV) are caused when the low energy pions range out and by muons in the beam. One crystal length corresponds to about one nuclear absorption length. The continuum results from π+N→X.

shows the energy distributions for 200 MeV/c charged pions[29] impinging on a small array of Crystal Ball crystals. The interaction is an important one to consider, as pions provide the primary background to the ψ' decays. Minimum ionization does not occur regularly for the low energy pions; these pions can range out in the NaI(Tl), producing the large peak corresponding to their kinetic energy. Positively charged pions eventually decay into a muon and a neutrino, the muon decaying generally too late (~2μs) for detection. Negative pions interact with the NaI(Tl) nuclei after stopping, imparting more of their decay energy in detectable form. An example of $\psi' \rightarrow \pi^+\pi^-\mu^+\mu^-$ is shown in figure 3-6.

Tracking of neutral particles requires isolation of the energy clusters created by each particle. It is often the case that these clusters overlap, and therefore an algorithm was needed to examine the energy profile over the entire ball and identify the clusters from each incident particle. The recognition algorithm was accomplished in two steps: first, the isolated "connected regions" of all contiguous crystals, each crystal measuring more than 10 MeV, were identified; then each connected region was scanned for structure which indicated the presence of overlapping clusters. Significant structures in a connected region are called "bumps"; each bump corresponded to one incident particle. Finally, the trajectory of each bump-producing particle was reconstructed using the energy profile in the bump. If the track constructed in this manner coincided with one reconstructed using the spark chambers, or matched a "hit" in the spark/multiwire-proportional chamber system, the particle was flagged as charged. Details concerning the connected region, bump, and neutral tracking routines are to be found in appendix E.

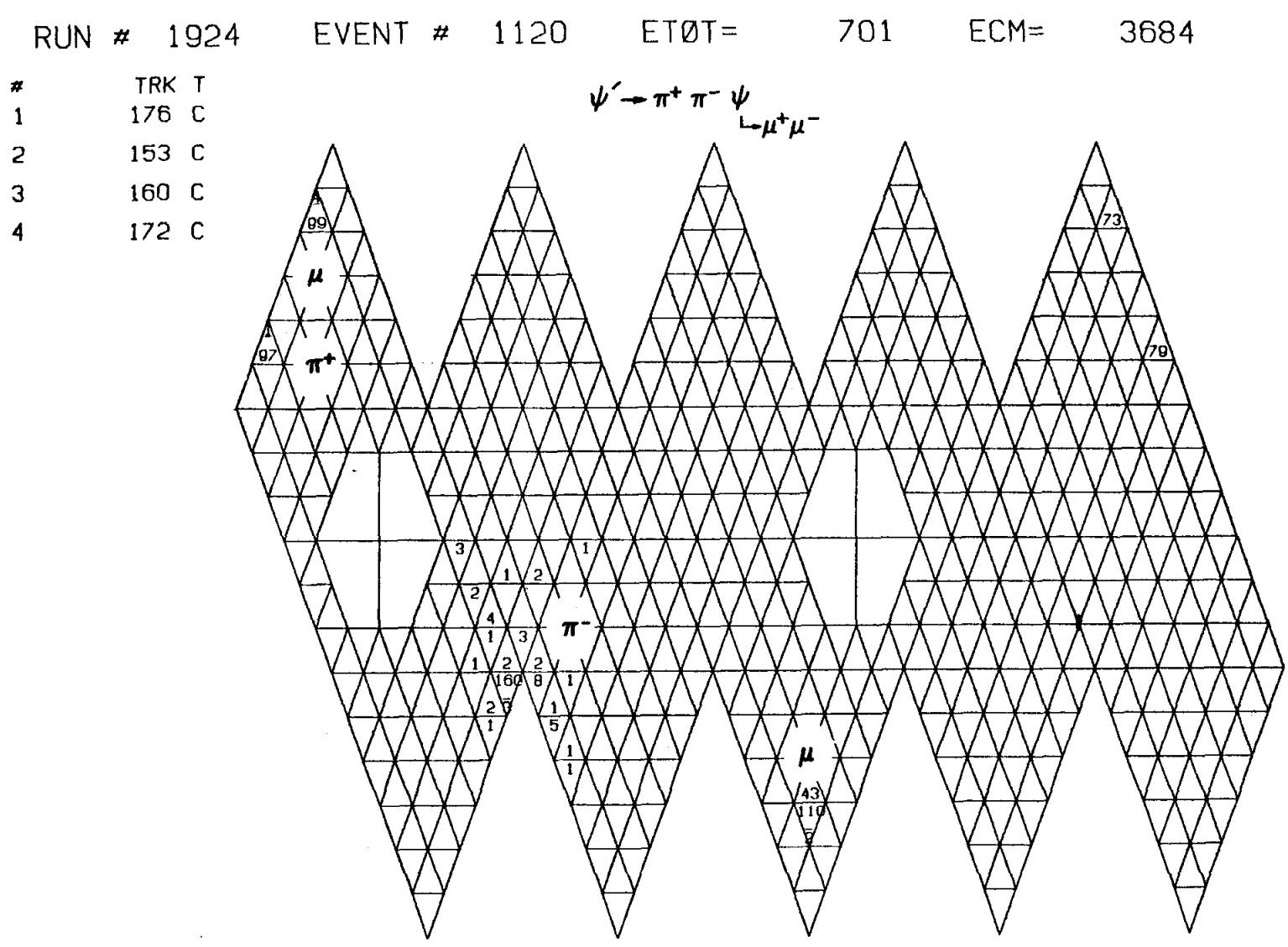

FIG..3-6 Hadronic event projection.

3.3 CHARGED TRACKING

Reconstruction of the charged particle trajectories was only performed if information from both the inner and outer spark chambers was available; charged tracking therefore covered 71% of the 4π solid angle. Tracks were reconstructed using the algorithm described in appendix F and were generally accurate to about 1° (σ). Because of the spread in z of the interaction region (the measured vertex distribution is shown in figure 3-7), 14% of the leptons from the decay of a ψ did not traverse the outer spark chamber. In these cases the $e^{\pm}$ were tracked with a resolution of 1.5° using the neutral tracking technique; the non-showering $\mu^{\pm}$ were tracked with a poorer resolution of 3.2° (essentially the inscribed cone for a single crystal).

3.4 TAGGING

Both leptons had to be identified as charged in order to accept events in the $\gamma\gamma l^+l^-$ sample. For leptons not tracked by the spark chambers, a charge assignment[30] was made based on poorer information from the spark and multiwire-proportional chambers; such an assignment is termed a "tag". Trajectories of tagged tracks were reconstructed using the energy profile technique -- the tagging algorithm is described in appendix F. Charge identification of the dual lepton tracks, both by tagging and by full charged track reconstruction, had an efficiency of

---

[30]The sign of the charge is not determined.

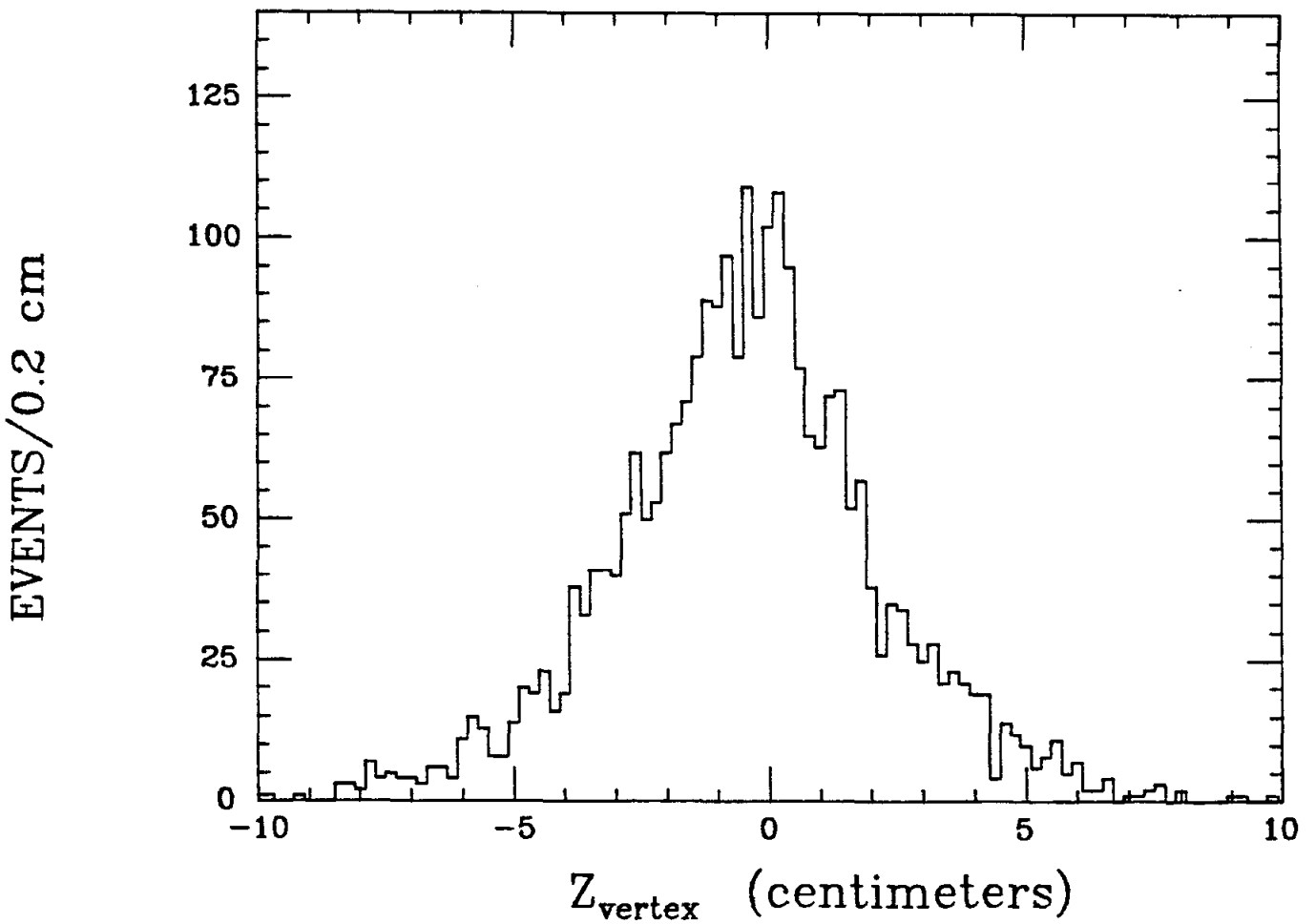

FIG..3-7 Distribution of reconstructed vertices for $\gamma\gamma l^+l^-$ events. The distribution yields $\langle z \rangle = 3 \pm 1$ mm and $\sigma = 26$ mm.

0.96. In addition, 5% of the $\gamma\gamma l^+l^-$ events were lost when one or both of the photons converted in the 0.03 L_{rad} of material preceding the outermost spark chamber. The overall charge identification efficiency as a function of cosθ is shown in figure 3-8. Here the efficiency is shown for each charged track in events which have two final state electrons and two photons.

3.5 MERGING

Extreme fluctuation of the shower created by an energetic photon or electron sometimes created an energy profile which appeared to result from two particles rather than one; "merge" is the routine that was used to recombine the "split-off" track with the parent track. After studying the problem with a Monte Carlo simulation of such showers, it was found that tracks with an energy exceeding 40 MeV virtually never arise as a result of a split-off type fluctuation (also verified experimentally). Neutral tracks of less than 40 MeV were suspect if they appeared reasonably close to an energetic (defined as having more than 900 MeV) electron shower. A cut on the opening angle ($\theta_{e\gamma}$) between the electron and the suspect track of $\cos\theta_{e\gamma} > 0.85$ -- the angle corresponds to 32°, or about three crystal widths -- proved to define a reasonable zone of suspicion for the photon; if the apparent photon was in the zone and had an energy less than 40 MeV, its track was eliminated from the event and its measured energy was added to that of the nearby $e^{\pm}$. Figure 3-9 depicts a typical merge candidate.

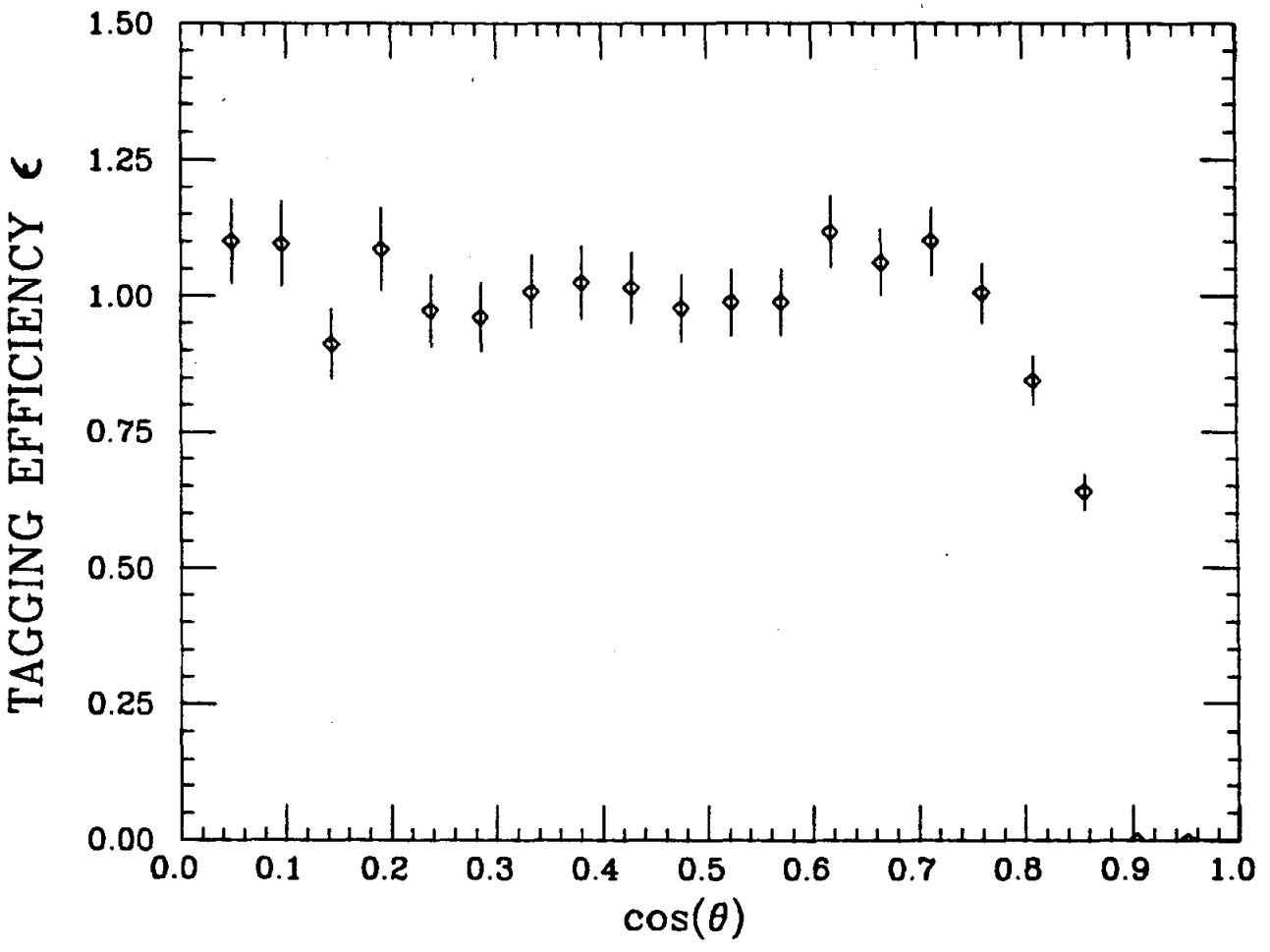

FIG..3-8 Relative tagging efficiency as a function of geometry. Efficiency shown is for each track in events having two prongs.

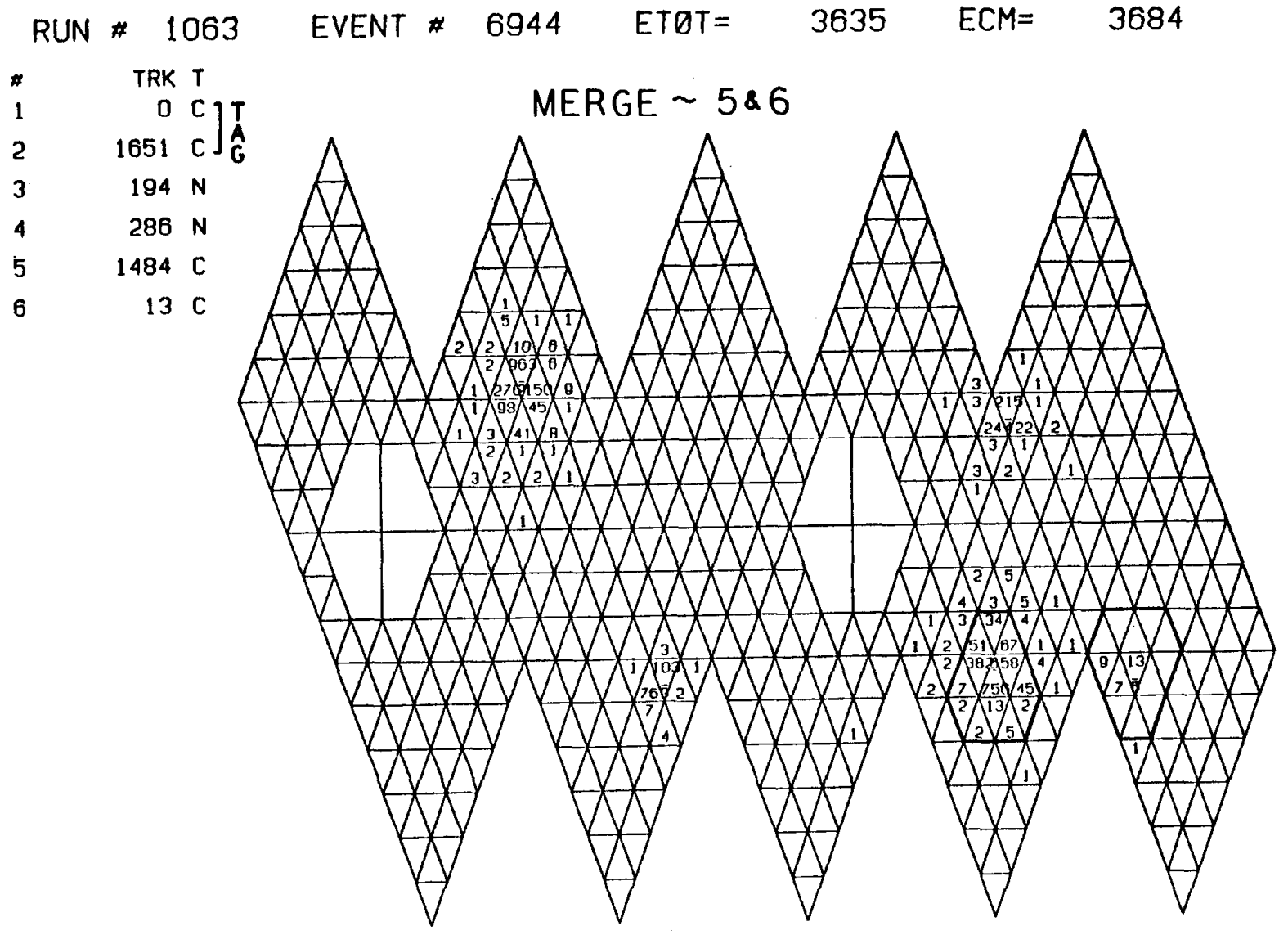

FIG..3-9 Example of an event with a fake split-off track.

3.6 CHARACTERISTICS OF THE $\gamma\gamma L^+L^-$ FINAL STATE

In the decays

$$\psi' \rightarrow \gamma\gamma\psi,\ \psi \rightarrow e^+e^- \text{ or } \mu^+\mu^- \qquad (3\text{-}1)$$

the two photons originate from the decay of an η or π^0, or from the cascade decay via an intermediate χ state; thus, the calculated opening angle between the leptons must exceed 158° since the ψ has a maximum momentum of 589 MeV. For the reaction containing electrons the final state is fully comprised of electromagnetically showering particles and complete measurement of all energies is possible. On the other hand, the muonic final state deposited only about 320 to 560 MeV from the minimum ionizing particles, and about 550 MeV from the two photons. The gamma energy range was safely smeared by 15% when formulating the total energy acceptance windows given below.

In addition to the phenomenon of split-off, electron bremsstrahlung potentially can increase the number of tracks observed in the crystals. The overwhelming majority of radiative photons are emitted at very small angles relative to the radiating electron trajectory; thus, the two shower patterns overlap sufficiently to be recognized as one by the bumps routine.

3.7 PRELIMINARY CUTS

Candidates for the reaction (3-1) were required to have a total measured energy of 792 to 1100 MeV for muonic and 3300 to 4200 MeV for

electronic final states. Figure 3-10a shows the total energy distribution of events from the production tapes, and indicates both the energy acceptance windows and the trigger thresholds. The first peak at about 400 MeV apparent in the figure is caused by minimum ionizing particles accepted by the Multiplicity trigger; the second "peak" at about 650 MeV indicates the Fast trigger threshold for the total event energy. Figure 3-10b shows the e^+e^- mass distribution of accepted events just prior to kinematic fitting. The tails in figure 3-10b are smooth and not significantly truncated by the choice of energy window.

In order to insure charged particle detection, events with tracks in the extreme foreward and backward cones defined by $|\cos\theta|>0.9$ were rejected (θ is the polar angle with respect to the incident electrons). Tracks at the limits of the acceptance region had passed through the inner spark chambers and had a central module that was fully surrounded by at least one layer of crystals, thus permitting reliable energy detection. Events with too small an opening angle were also rejected, for if $\cos\theta_{ij}<0.9$ (θ_{ij} is the opening angle between particles i and j) the showers overlap enough so as to prevent accurate energy determination and neutral tracking.

Once the merge routine had been applied to the data, only four tracks, each having a measured energy greater than 40 MeV, were permitted in the event, and two of them must have been flagged as charged. The $E_\gamma>40$ MeV cut was imposed to insure that the photon energies were not corrupted by spurious energy in the ball. The cut had no effect on

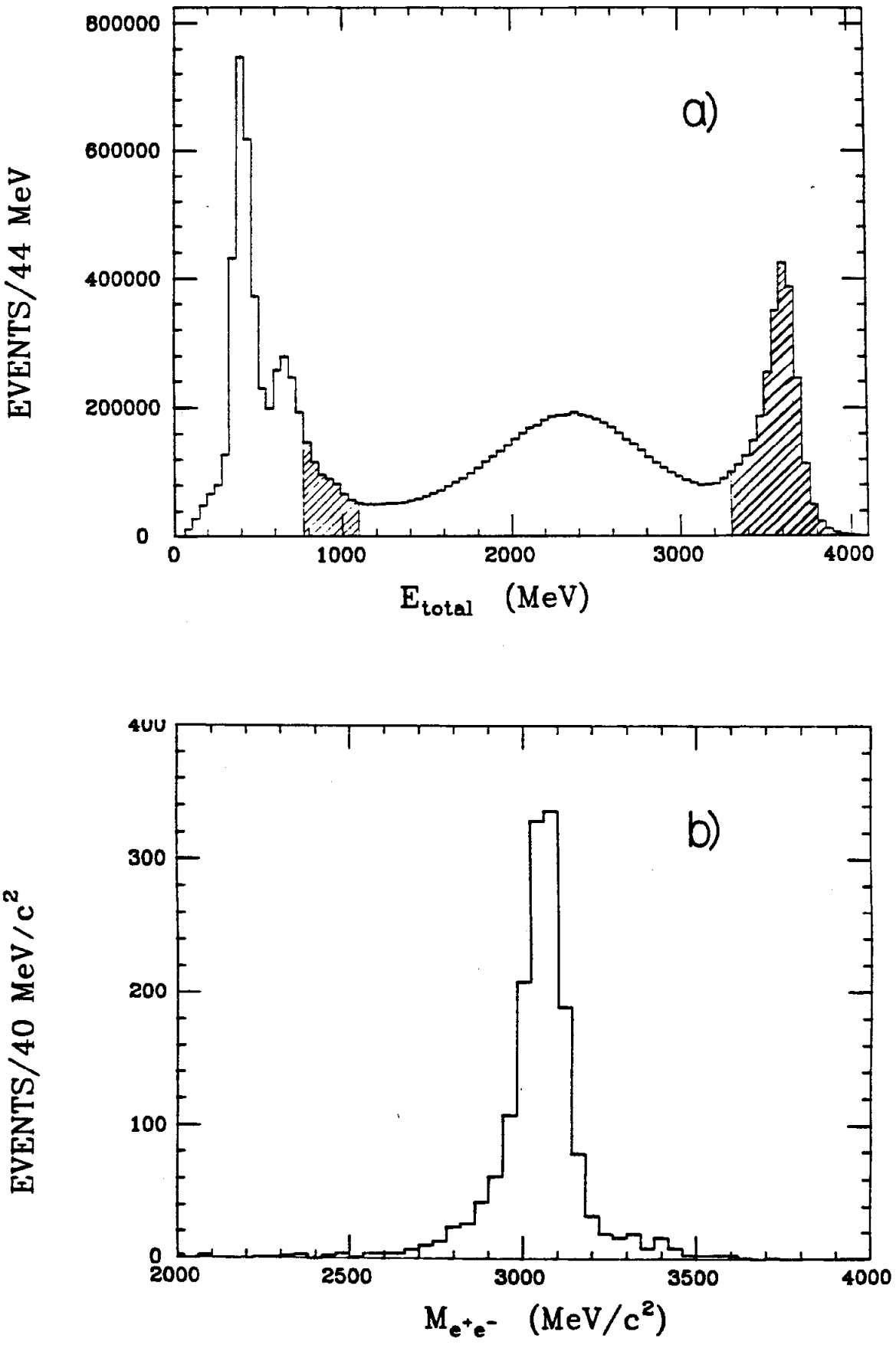

FIG..3-10 Energy windows. a) shows the total energy distribution of events before cuts and the cuts (shading) for μ and e samples. b) shows the electron mass for the final events.

the acceptance for χ or η events; however, it excluded 8% of the π^0 events. If the event had any tracks with $20<E_{track}<40$ MeV it was rejected; this cut was important for the elimination of backgrounds (chapter IV). A lepton opening angle cut was imposed at 120° so that errors in tracking would not introduce additional inefficiency.

The acceptance cut mentioned above required that no particle be allowed in the region $|\cos\theta|>0.9$. The endcaps were used to identify extraneous particles and thus served as a veto to reject unwanted events. There was a negligible impact on good events when the endcap energy was required to be less than 8 MeV (some energy is expected in the endcaps from spray and shower fluctuations). Figure 3-11 shows the endcap energy for events passing the initial total energy cut. Events in the long tail have been hand scanned to insure that the 8 MeV cut did not eliminate more than 2% of the good events.

The time between the beam-cross signal and the detection of an event in the apparatus was used as a final test of each event. The timing distribution for all events on a production tape and for the final $\gamma\gamma l^+l^-$ candidates is shown in figure 3-12. None of the final candidate events fell outside of the 13 ns wide peak (the wings consist primarily of cosmic ray events). More timing distributions can be found in appendix B.

Tables 3-1 and 3-2 summarize the cuts and demonstrate the effect of each one. Some efficiences for the $\pi^0\psi$ final state which are not in-

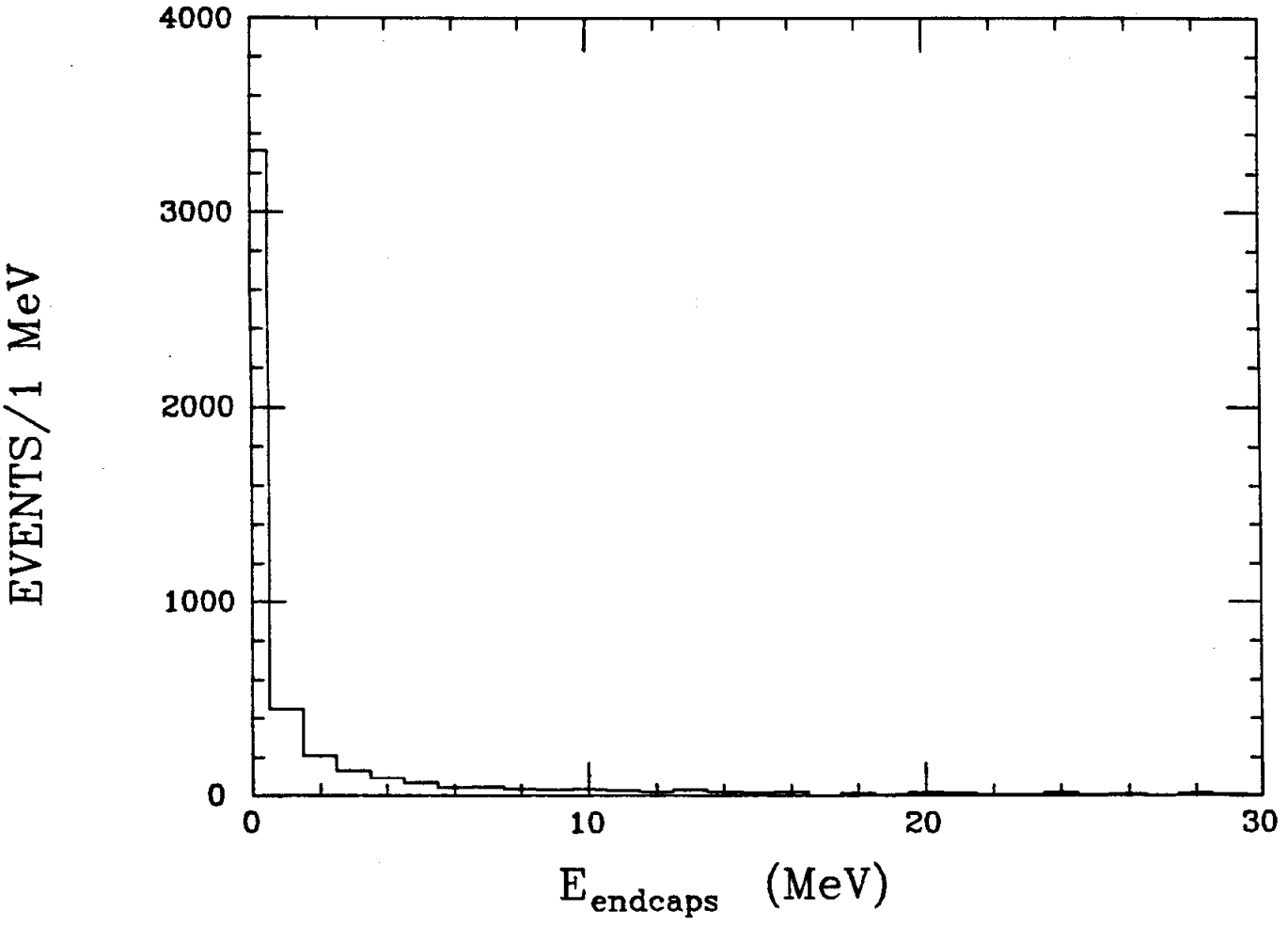

FIG..3-11 Endcap total energy distribution after preliminary cuts.

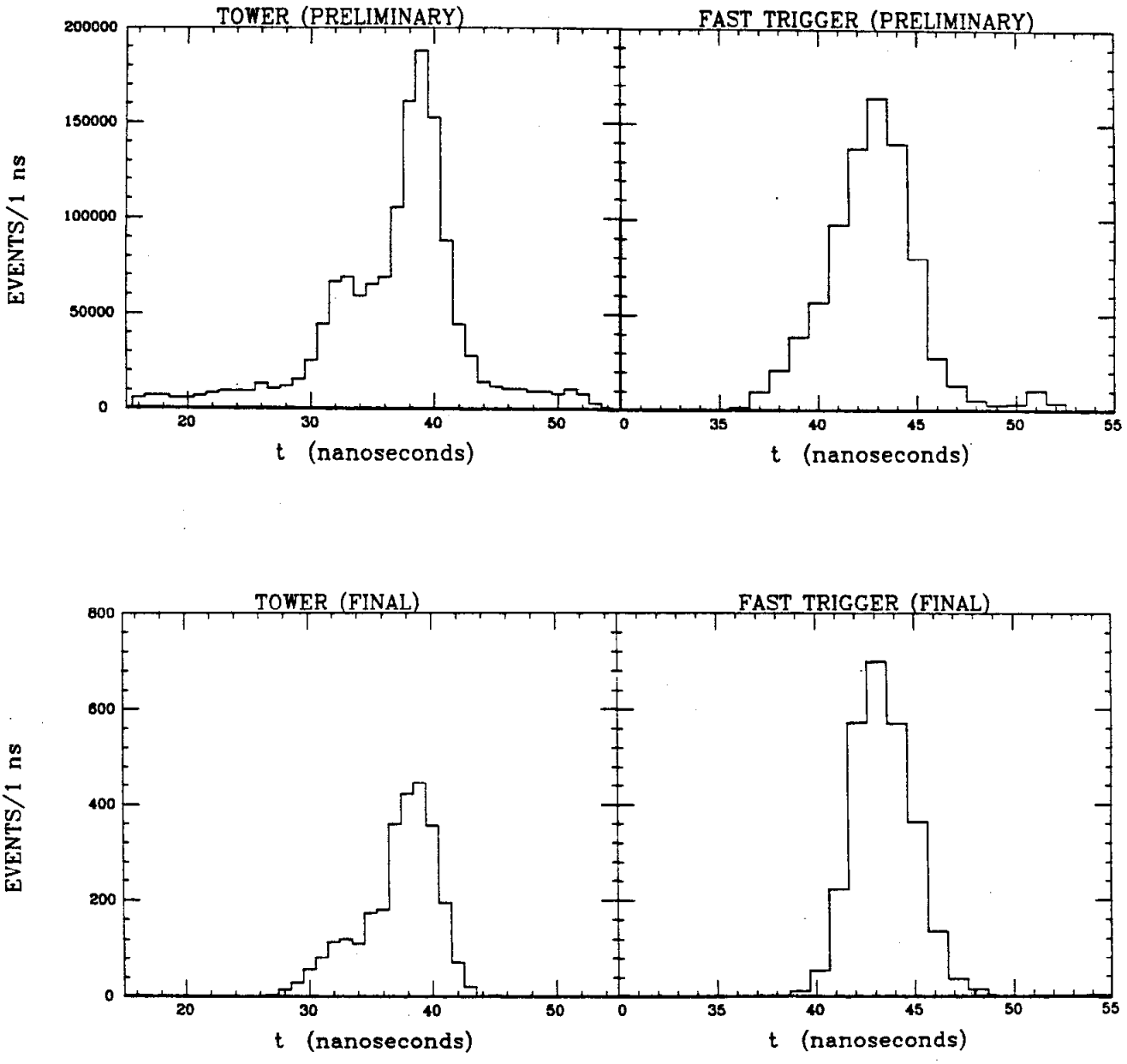

FIG..3-12 Timing distributions for initial and final events.

cluded in Table 3-2 are: ϵ(opening angle cut)=0.93; $\epsilon(E_\gamma>40$ MeV)=0.92; $\epsilon(M_{\gamma\psi}=3530\pm60, 3411\pm5$ and $m_{\gamma\gamma}=135\pm25)=0.70$. All energies in Table 3-2 are given in MeV.

TABLE 3-1

CUT	NUMBER OF EVENTS REMAINING	EFFECT
Production	3×10^6	73% pass
E_{total}	7×10^5	23% pass
e/μ pattern (retain Bhabhas)	5.7×10^5	82% pass
Reject Bhabhas	5452	1% pass
Require two charged tracks	4750	87% pass
------ first summary tapes complete ------		
$E_{endcap}<8$ MeV	4433	93% pass
Merge	185 tracks absorbed	
Acceptance cut: $\lvert\cos\theta\rvert<0.9$	3281	74% pass
Require that the "photons" are not tagged	3276	99.8% pass
Overlap cut: $\cos\theta_{ij}<0.9$	3063	93% pass
------ second summary tape complete -------		
Kinematic fit	2747	90% pass
Require unfitted $E_{neutral}>490$MeV	2415	88% pass
C.L.>0.005 and hand scan	2228	92% pass

TABLE 3-2

EFFICIENCIES FOR VARIOUS CUTS

STATE		$\lvert\cos\theta\rvert<0.9$	$\lvert\cos\theta\rvert<0.9$ $\cos\theta_{ij}<0.9$ $E_{track}>40$ MeV $E_{ec}<8$ MeV Chamber-Geometry	$\lvert m_{\gamma\gamma}-135\rvert$ <25 MeV/c^2	$m_{\gamma\gamma}<525$	C.L.>0.005	TOTAL
$\chi(3.55)$	e	0.47	0.42	0.93	1.00	0.94	0.370±0.015
	μ	0.53	0.47	0.93	1.00	0.94	0.408±0.016
$\chi(3.51)$	e	0.53	0.45	0.95	0.97	0.93	0.387±0.011
	μ	0.61	0.50	0.95	0.97	0.93	0.425±0.012
$\chi(3.41)$	e	0.42	0.39	0.96	0.83	0.94	0.295±0.007
	μ	0.49	0.44	0.96	0.83	0.94	0.333±0.008
$\chi(3.59)$	e	0.48	0.40	0.92	1.00	0.92	0.338±0.008
0^-	μ	0.54	0.45	0.92	1.00	0.93	0.380±0.009
$\chi(3.46)$	e	0.45	0.39	0.97	0.87	0.94	0.306±0.007
0^-	μ	0.51	0.43	0.97	0.87	0.94	0.344±0.008
η	e	0.53	0.48	1.00	0.00	0.94	0.455±0.010
	μ	0.60	0.53	1.00	0.00	0.93	0.497±0.011
π°	e	0.47	0.39	0.88	1.00	0.94	0.254±0.007
	μ	0.52	0.41	0.88	1.00	0.94	0.276±0.007

3.8 KINEMATIC FITTING

Once an event passed the cuts just described it was a candidate for the decays (3-1). The validity of the hypothesis was tested by investigating the degree to which energy and momentum were conserved in the event; the conservation laws also served to improve on the measurements of energies and angles once the hypothesis was trusted. All variables in the electronic final state were measured, leading to four implementable

constraint equations (the conservation of a four-vector). Muonic final states lacked an accurate energy measurement for two of the four tracks, thereby eliminating two of the constraints. Kinematic fitting to the decay hypothesis required that the initial-state four vector be well known (indeed the ψ' mass is well established and the beam energies in the SPEAR collider are known to better than 2 MeV). Furthermore, an intermediate mass ($M(\psi')$) in the decay chain was known, so there existed an additional constraint on the dilepton mass. The last constraint was quite successful in making up for the lack of measured muon energies. Thus, a total of five constraints in the fitting of e^+e^-, and three in the fitting of $\mu^+\mu^-$ final states, was used.

False hypothesis events which passed all tests in the fit routine (primarily from the decays $\psi'\rightarrow\pi\pi\psi$) populated the relevant scatterplots more or less uniformly -- the important thing to understand is that these events were not forced to the kinematic borders (which would create misleading features). The Monte Carlo simulation described in appendix G proved that false (i.e., background) events which had survived the fitting process (and they were few in number) had confidence levels confined to exceedingly small values -- typically less than 0.0001 . Additionally, the slightly non-gaussian energy distribution of NaI(Tl) (see appendix D) caused a preponderance of events in the low C.L. bins. The fitted candidates were cut at a confidence level of 0.005, which effectively eliminated more than 95% of the $\pi\pi$ contamination; other backgrounds were likewise eliminated.

Chapter IV

DATA ANALYSIS

4.1 INTRODUCTION

Past studies of the $\gamma\gamma\psi$ final state resulting from the reaction

$$\psi' \rightarrow \gamma' \chi, \quad \chi \rightarrow \gamma\psi \tag{4-1}$$

have presented data in the form of a scatterplot of the $\gamma\psi$ masses. The kinematic boundaries and the appearance of relevant states on the scatterplot are illustrated in figure 4-1a. The outermost envelope of the scatterplot contains any state between the ψ' and ψ which is detected via two photons and the ψ.[31] Doppler broadening of the photon cascading to the ψ causes the mass pairs to occupy either horizontal or vertical bands between the kinematic boundaries. The intrinsic resolution of the measuring apparatus smears the kinematically allowed regions, while the constraints imposed during kinematic fitting of the data restore the outer envelope. Decays of the form

$$\psi' \rightarrow m\psi, \quad m \rightarrow \gamma\gamma \tag{4-2}$$

where m represents an η or π^0 for instance, reside on diagonal curves recessed from the envelope borders, with the η and π^0 masses (indicated in the figure) very near the extremes; the density along these mass traces is nearly uniform.

---

[31] Two masses may be formed with the ψ and either one of the photons, the higher energy photon yielding a higher mass solution than its partner.

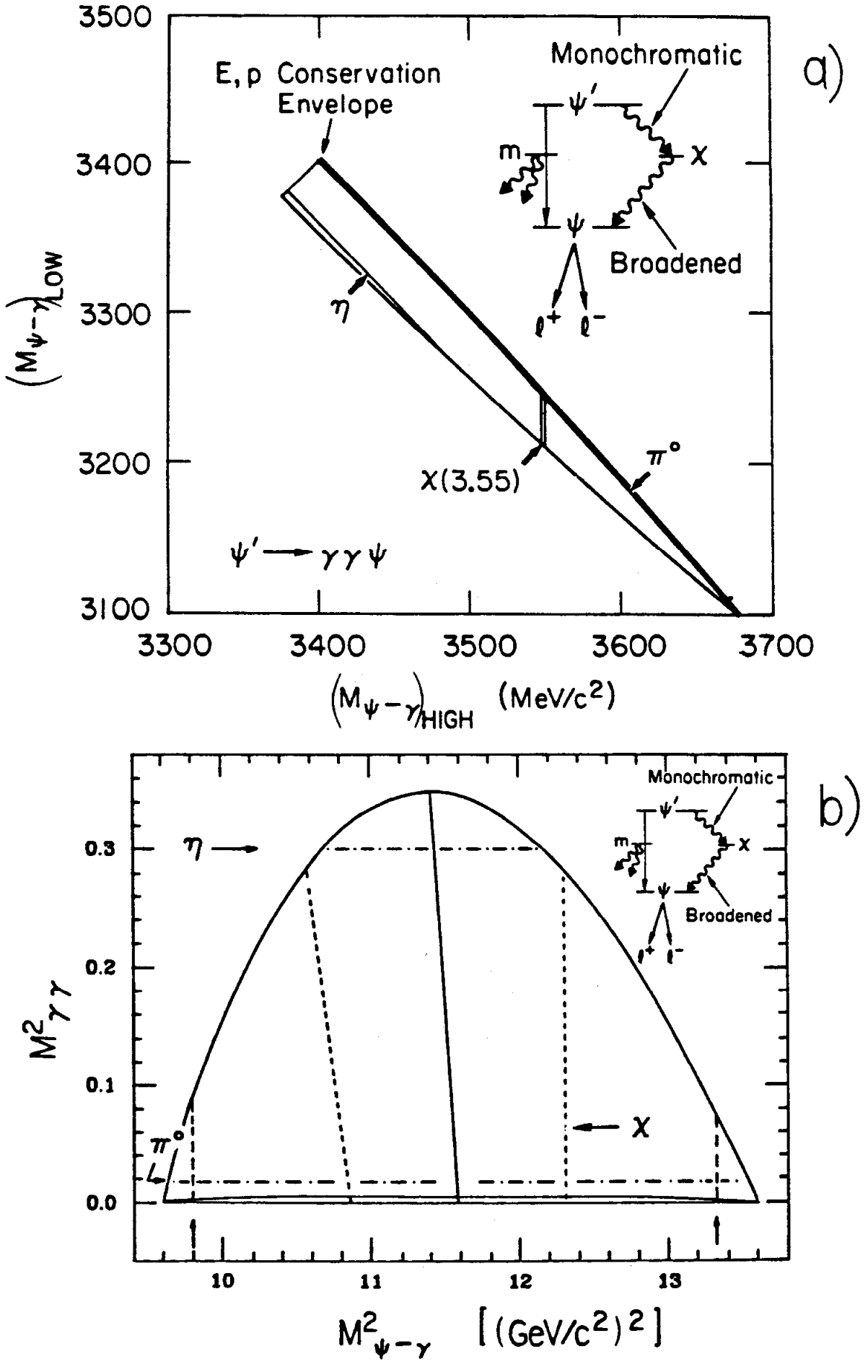

FIG..4-1 Kinematic boundaries for $\psi' \to \gamma\gamma\psi$.

Identification of the Doppler broadened and true masses of χ states is difficult on the mass scatterplot because of an apparent broadening arising from the NaI(Tl) energy resolution. The problem is alleviated by presenting the data on a Dalitz plot ($m_{\gamma\gamma}^2$ vs. $M(\gamma\psi)^2$) on which each event is plotted twice, once for each $\gamma\psi$ mass. Such a Dalitz plot contains information that is more easily interpreted than that in the $M(\gamma\psi)$ scatterplot; the Doppler-shift broadening is separated from the resolution effect by observing the characteristic slope $d(m_{\gamma\gamma}^2)/d(M(\gamma\psi)^2)=1$ for the Doppler-shifted mass. The kinematic boundaries for the Dalitz plot, subject to all the cuts described in chapter III, are shown in figure 4-1b. The Dalitz plot exhibits all the relevant structure of the decay matrix elements -- data from this experiment is therefore displayed in the $M(\gamma\psi)$ format primarily for purposes of comparison with previous studies.

4.2 FEATURES APPARENT IN UNFITTED DATA

The two stronger χ states and the η band (which is actually a box in the upper left corner) clearly appear in the $M(\gamma\psi)$ scatterplots of the unfitted e^+e^- and $\mu^+\mu^-$ final states (figures 4-2a,b). Though elongation of the χ states would suggest Doppler broadening (and indeed they are stretched along the correct direction), the observed broadening is primarily a resolution effect.

The e^+e^- and $\mu^+\mu^-$ subsets of the data are similar in number and in distribution on the scatterplot. The decays

$$\psi' \rightarrow \pi^0\pi^0\psi, \quad \pi^0 \rightarrow \gamma\gamma \tag{4-3}$$

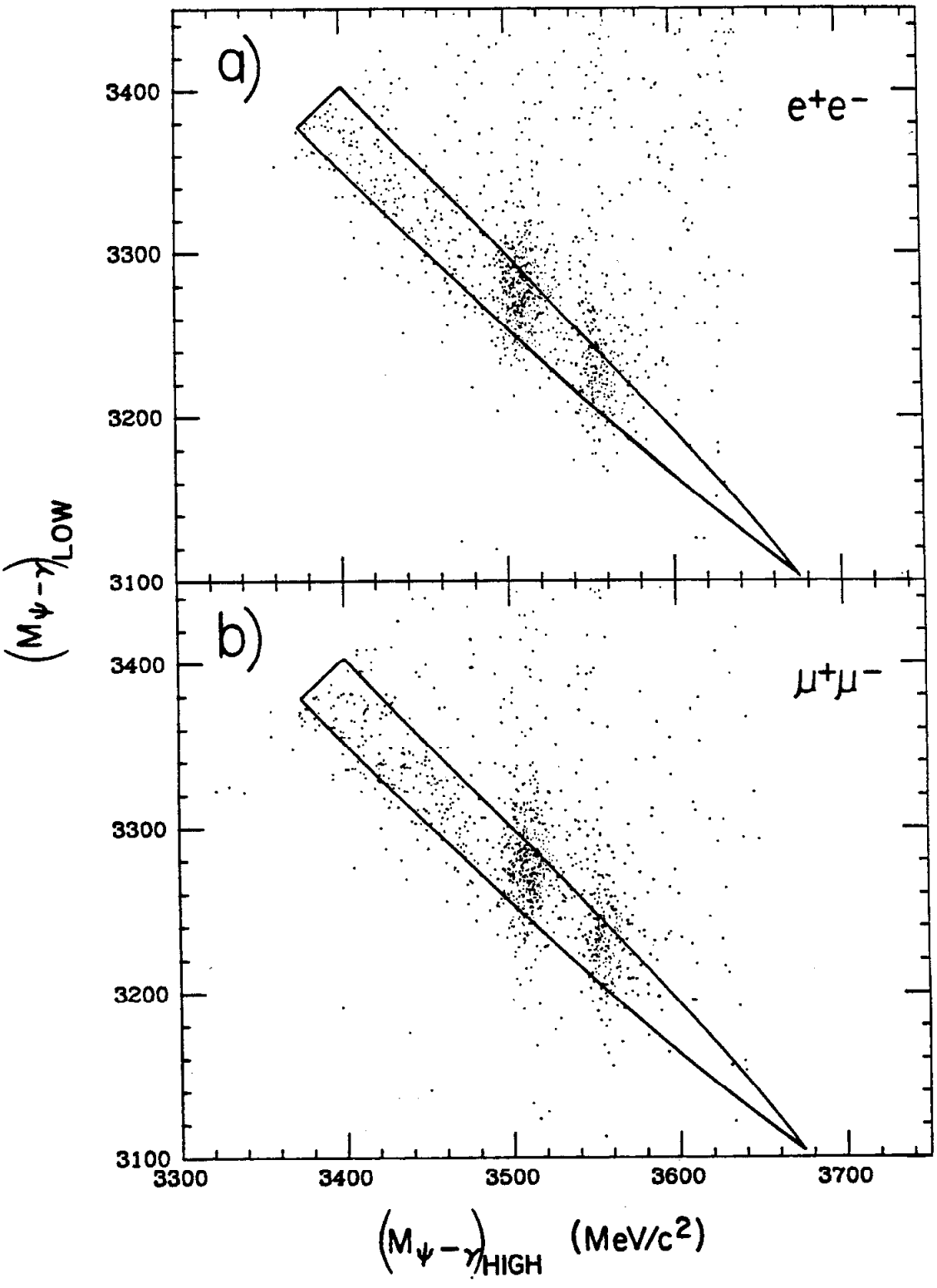

FIG..4-2 Unfitted preliminary event sample.

in which two photons have been lost (or have energies less than 20 MeV) dominate the background and tend to populate the region of the η band more than any other. The measured distributions of $M_{\pi\pi}$ for $\psi' \to \pi^0\pi^0\psi$ and $\psi' \to \pi^+\pi^-\psi$ are shown in figure 4-3.[32] Since the ψ and ψ' have isospin 0, the $\pi\pi$ system can have only an I=0 amplitude, and therefore the $\pi^+\pi^-$ and $\pi^0\pi^0$ distributions must have the same shape; the data in figure 4-3 support the isospin argument. Because of the better statistics on the Mark-II measurement of the $\pi^+\pi^-$ distribution, their $M_{\pi\pi}$ distribution was used in the Monte Carlo simulation of $\pi^0\pi^0$ background. Chiral dynamics[33] and the $\epsilon(1400)$ resonance[34] both offer theoretical models which account for the peculiar shape of the observed mass spectrum.

QED radiative contamination results from the process $e^+e^- \to \gamma\gamma e^+e^-$,[35] the probability of each radiation behaving as E_γ^{-1}. Thus, the background is found primarily in the low photon energy (high $M(\gamma\psi)$) region of the mass scatterplot. Consistency of e^+e^- and $\mu^+\mu^-$ plots therefore indicates that the radiative background is very small.

Another background arises from the decays

$$\psi' \to \pi^+\pi^-\psi, \ \psi \to l^+l^- \qquad (4\text{-}4)$$

---

[32]The $\pi^+\pi^-$ data was obtained from T. M. Himel; the mass distribution shown is obtained by dividing the observed mass spectrum by the efficiencies given in his Ph.D. thesis (SLAC-report 223 (1979)). F. Porter is responsible for the $\pi^0\pi^0$ Crystal Ball data in this plot.

[33]N. Byers, preprint UCLA/75/TEP/10 (UCLA) (1975); L. Brown and R. Cahn, Phys. Rev. Lett. 35, 1 (1975).

[34]J. Schwinger, K. Milton, W. Tsai and L. DeRaad, Phys. Rev. D12, 2617 (1975).

[35]The QED process with final state muons contributes much less.

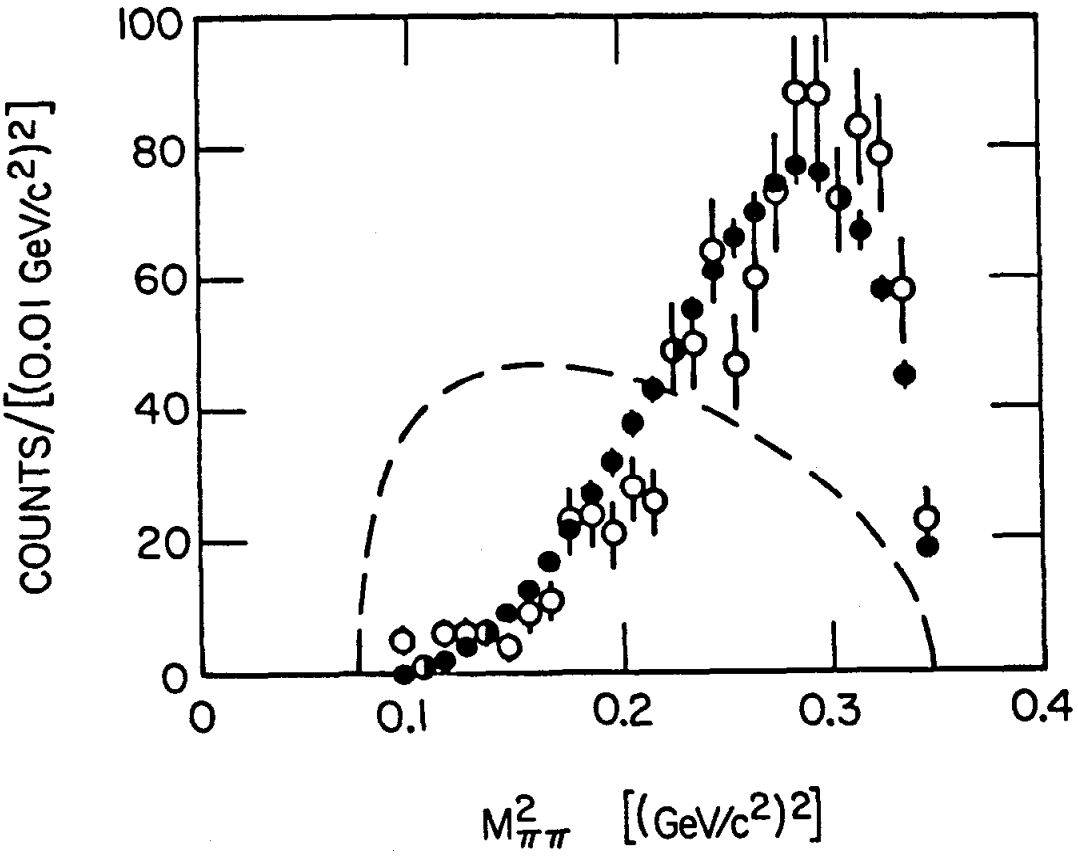

FIG..4-3 Distributions in $\psi' \to \pi\pi\psi$. The solid line is the phase space distribution; solid circles are Mark-II $\pi^+\pi^-$ measurements while open circles are Crystal Ball $\pi^0\pi^0$ measurements. All curves are normalized to equal data.

and

$$\psi' \rightarrow \pi^+\pi^-\pi^0,\ \pi^0 \rightarrow \gamma\gamma \quad , \tag{4-5}$$

though the latter decay is exceedingly rare. Pions from reaction (4-4) may appear as photons due to charge detection inefficiency; these pions do not have sufficient energy to produce minimum ionizing signals and therefore populate a broad region of the scatterplot in the high $M(\gamma\psi)$ areas.

By plotting $m_{\gamma\gamma}$ vs. $p_{\gamma\gamma}$ (figure 4-4a) the relative contributions of neutral and charged pion backgrounds (reactions (4-3) vs. (4-4)) can be measured. The strip along the π^0 mass band for $p_{\gamma\gamma}<450$ MeV results when both lost photons from the decay (4-3) originate from the same pion; the frequency of mixed gamma losses (i.e., each pion contributes one photon) is several times greater, with the $\pi^0\pi^0$ background occupying broad regions of the scatterplot.

A dense cluster corresponding to a mass of 0.55 GeV/c^2 in figure 4-4a can be attributed to $\psi' \rightarrow \eta\psi$. The projection on the $m_{\gamma\gamma}$ axis (figure 4-4b) shows the NaI(Tl) resolutions (FWHM before kinematic fitting) of 16% obtained for a slow π^0 and 6% for an η arising from the process (4-2). The photon energy is measured quite well, while neutral tracking provides an anglular resolution of about 2° (σ). Since the pion opening angle is small, the large angular error contribution in $m_{\gamma\gamma}^2 = 2EE'(1-\cos\theta_{\gamma\gamma})$ means that kinematic fitting will have little effect in sharpening the mass resolution. Photons from the η on the other hand are emitted nearly back-to-back, so kinematic optimization dramatically improves the mass resolution.

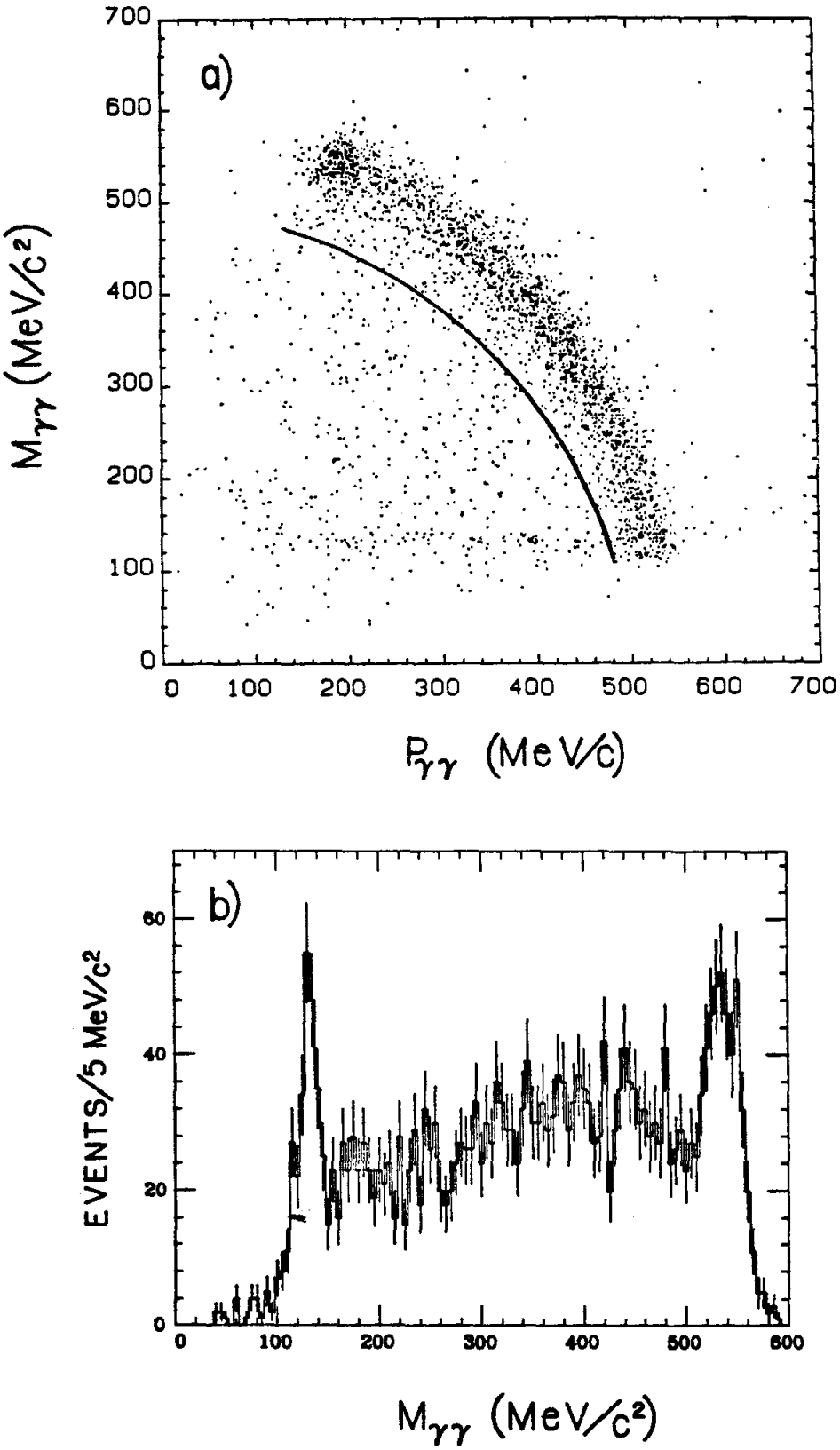

FIG..4-4 Diphoton momenta and mass distributions for preliminary candidates. The solid line denotes $E_{neutral}$=490 MeV. The peak in b) at the pion mass is attributed to events with a diphoton momentum less than ~450 MeV/c.

The neutral energy for the decays (4-1) or (4-2) is kinematically confined to the range $542<E_{neutral}<589$ MeV. The requirement $(E_{\gamma'}+E_{\gamma})>490$ MeV therefore removes most of the background but does not affect good events. The effect of the cut in eliminating backgrounds is demonstrated in the $m_{\gamma\gamma}$-$p_{\gamma\gamma}$ scatterplot (figure 4-4a). Data passing the neutral energy requirement is presented on the Dalitz plot in figure 4-5. The kinematically allowed region for the data in this plot is limited by the $E_{\gamma}>40$ MeV cut and the overlap cut on opening angles. The real and Doppler-shifted[36] solutions for $\chi(3.51)$ and $\chi(3.55)$ are apparent in the Dalitz plot of unfitted data, as are the η and π^0 decays.

The remaining background tends to separate from the $m_{\gamma\gamma}=135$ MeV/c^2 region, clustering primarily in the $M(\gamma\psi)=3.4$ GeV/c^2 area. This behavior is consistent with the Monte Carlo simulation of background from $\pi^0\pi^0$ events. The simulation of the $\pi^0\pi^0$ background to the decays (4-1) and (4-2) shows a strong dependence on the distribution of $M_{\pi\pi}$ in reaction (4-3). A Dalitz plot of the Monte Carlo $\pi^0\pi^0$ simulation is shown in figure 4-6. After normalizing to the data sample, the Monte Carlo simulation of the $\pi^0\pi^0$ background predicts 140 background events after the $E_{neutral}>490$ MeV cut, none having $m_{\gamma\gamma}<200$ MeV/c^2; such behavior is consistent with the distribution of background events in the Dalitz plot (figure 4-5).

---

[36]The Doppler-shifted solutions appear broader than their monochromatic partners because the broadened photons have a higher energy in the cases of $\chi(3.51)$ and $\chi(3.55)$; the NaI(Tl) resolution varies as $E(GeV)^{3/4}$.

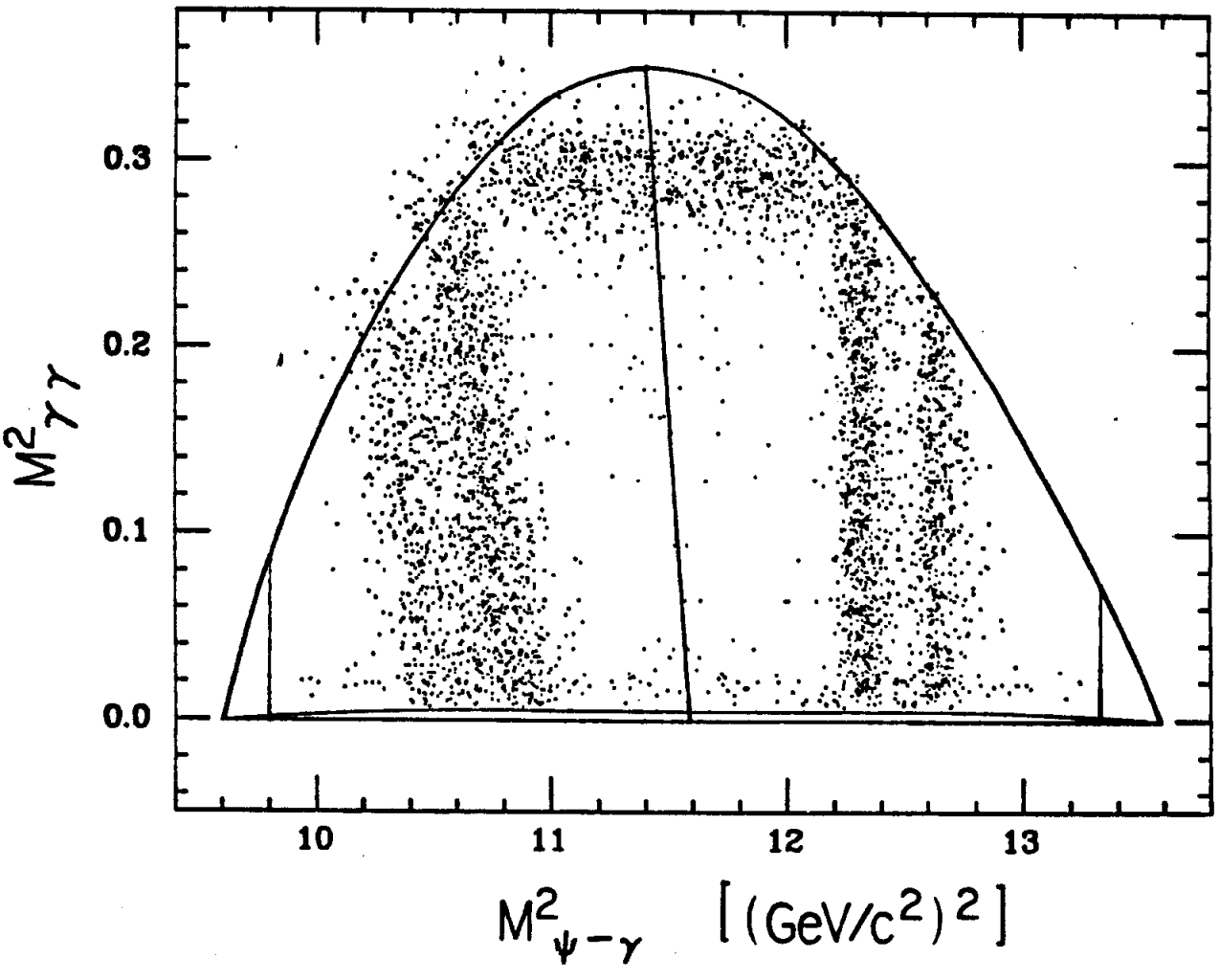

FIG..4-5 Final sample prior to kinematic fitting.

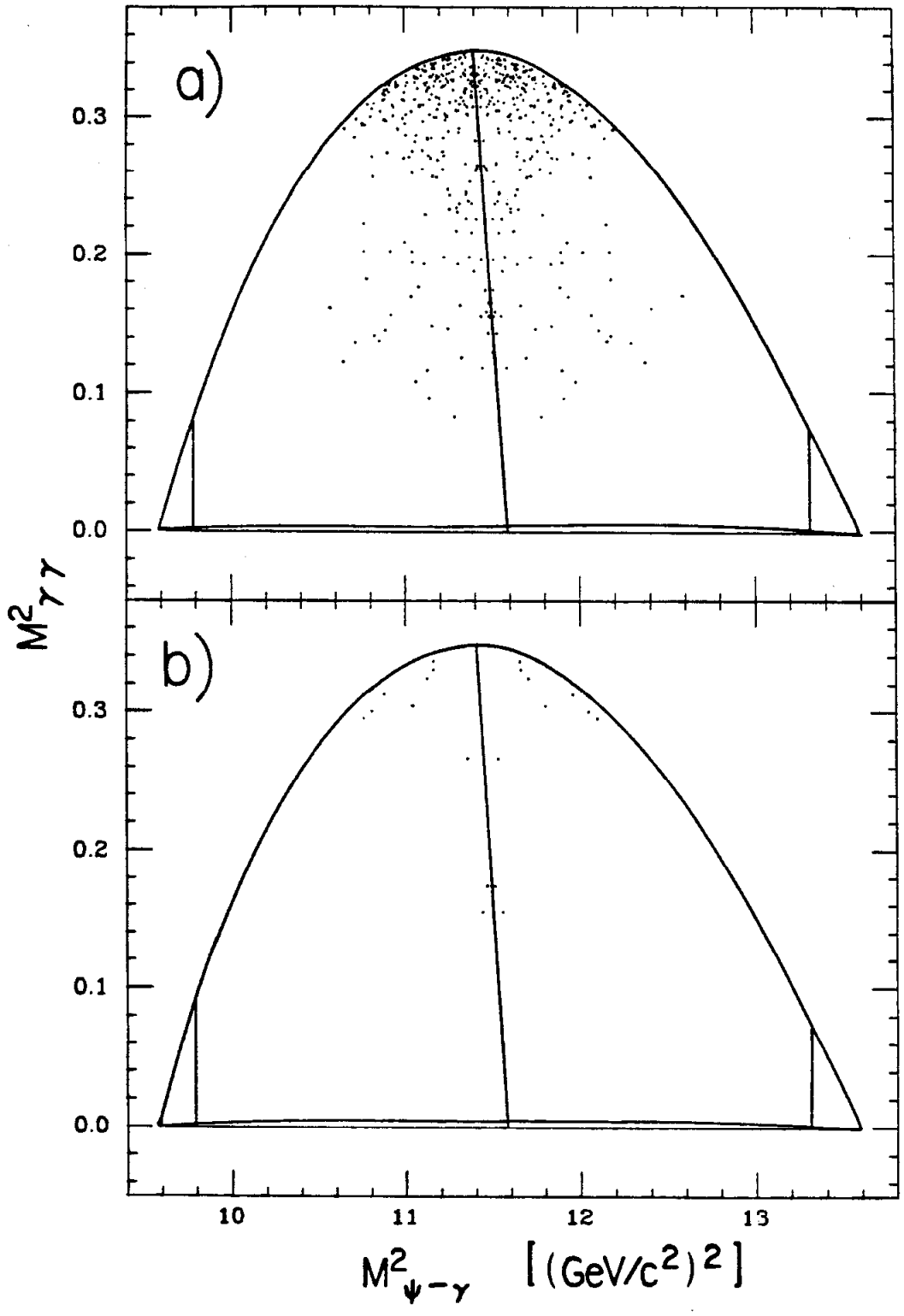

FIG..4-6 Monte Carlo simulation of $\pi^0\pi^0$ background. All survivors (after all cuts and fitting) of 10^6 generated pionic decays are shown in a), while b) showns the approximate level expected in this experiment.

4.3 FITTED DATA

Events are plotted on the M($\gamma\psi$) scatterplot (figure 4-7a) and the Dalitz plot (4-7b) after they have been kinematically fit to the hypothesis that they arise from $\psi' \to \gamma\gamma\psi$; the fitting restricts all events to fall within the envelope illustrated in figure 4-1a. Confidence level distributions returned from the fitting of the e^+e^- (a 5C fit) and the $\mu^+\mu^-$ (3C) final states are shown in appendix H. Both the e^+e^- and the $\mu^+\mu^-$ confidence level distributions are flat for C.L.>0.005; the requirement is imposed on all fitted data. Doppler broadening of the lower $\gamma\psi$ masses for $\chi(3.51)$ and $\chi(3.55)$ is somewhat clearer in figure 4-7b than in the unfitted plot (figure 4-5) since the kinematic fitting improves the absolute energy errors of the higher energy photons to those of the lower energy photons (FWHM=18 MeV). As explained in the previous section, the η band is sharpened dramatically by the fit while the π^0 mass band shows no improvement over that for the unfitted data. Imposing a cut on the confidence level returned from the fit removed most of the background, leaving the high high-mass solution region particularly clean.

After kinematic fitting the events were hand-scanned as a final quality control, since a small fraction of the hadronic decays of the ψ' will satisfy the software algorithm which identifies the $\gamma\gamma l^+l^-$ final state. Upon inspection of the energy distribution over the crystals, events with hadronic interactions in the NaI(Tl) were easily identified by the existence of widespread and erratic shower energy patterns (see

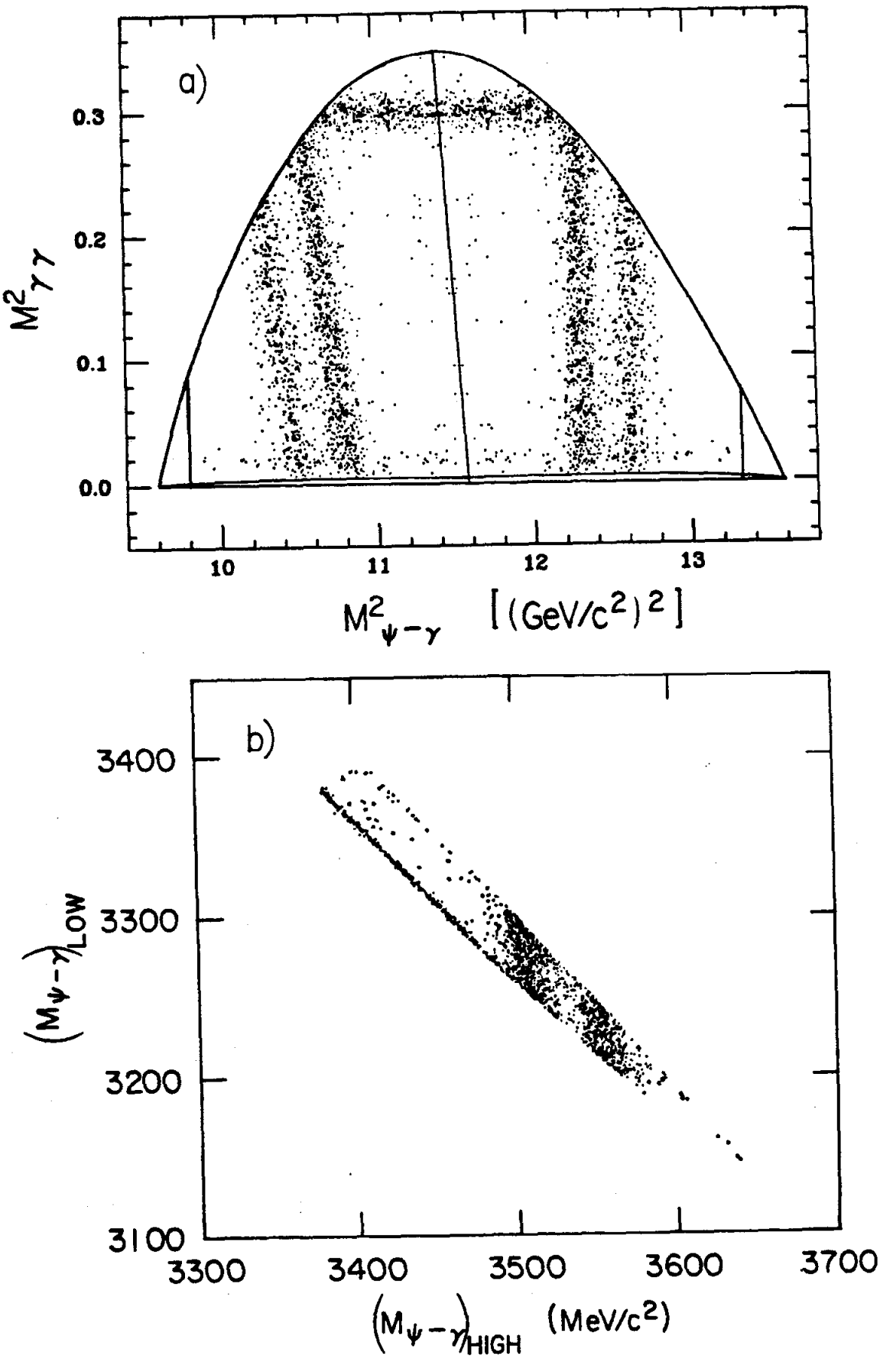

FIG..4-7 Events after kinematic fitting.

chapter III and examples in appendix C). An examination of events in this manner identified 6 hadronic background events -- these events are subtracted from the final event sample and are documented in appendix C.

The electronic and muonic subsets of the data are in complete agreement (e.g., comparable numbers of events are observed in the χ, η and π^0 regions of the plots), save for 6 events in the region of $(M(\gamma\psi))_{high}$=3.46 GeV/c^2 which all arise from the e^+e^- final state. In these events there is considerable overlap of low energy photon clusters with the fringe zones of high energy electron clusters. Furthermore, these events are consistent with a tail emanating from the $\chi(3.51)$. These 6 events are also displayed in appendix C. After all cuts are applied, 2048 events remain in the $\gamma\gamma\psi$ data sample. The scanned and π^0/η subtracted plots appear in figure 4-8.

4.4 THE η TRANSITION

The $m_{\gamma\gamma}$ distribution for all fitted events is shown in figure 4-9a. The η events are separated from χ and π^0 events by using the cut $m_{\gamma\gamma}>525$ MeV/c^2, which loses no real η events but does admit some $\chi(3.51)$ events into the η sample. The Monte Carlo simulation for χ events (normalized to the χ sample size) indicates that 21 $\chi(3.51)$ events are included in the η sample. On the basis of another Monte Carlo simulation, 5 $\pi^0\pi^0$ background events are also expected to be included in the η sample. Including the predicted background, 412 events comprise the η data sample.

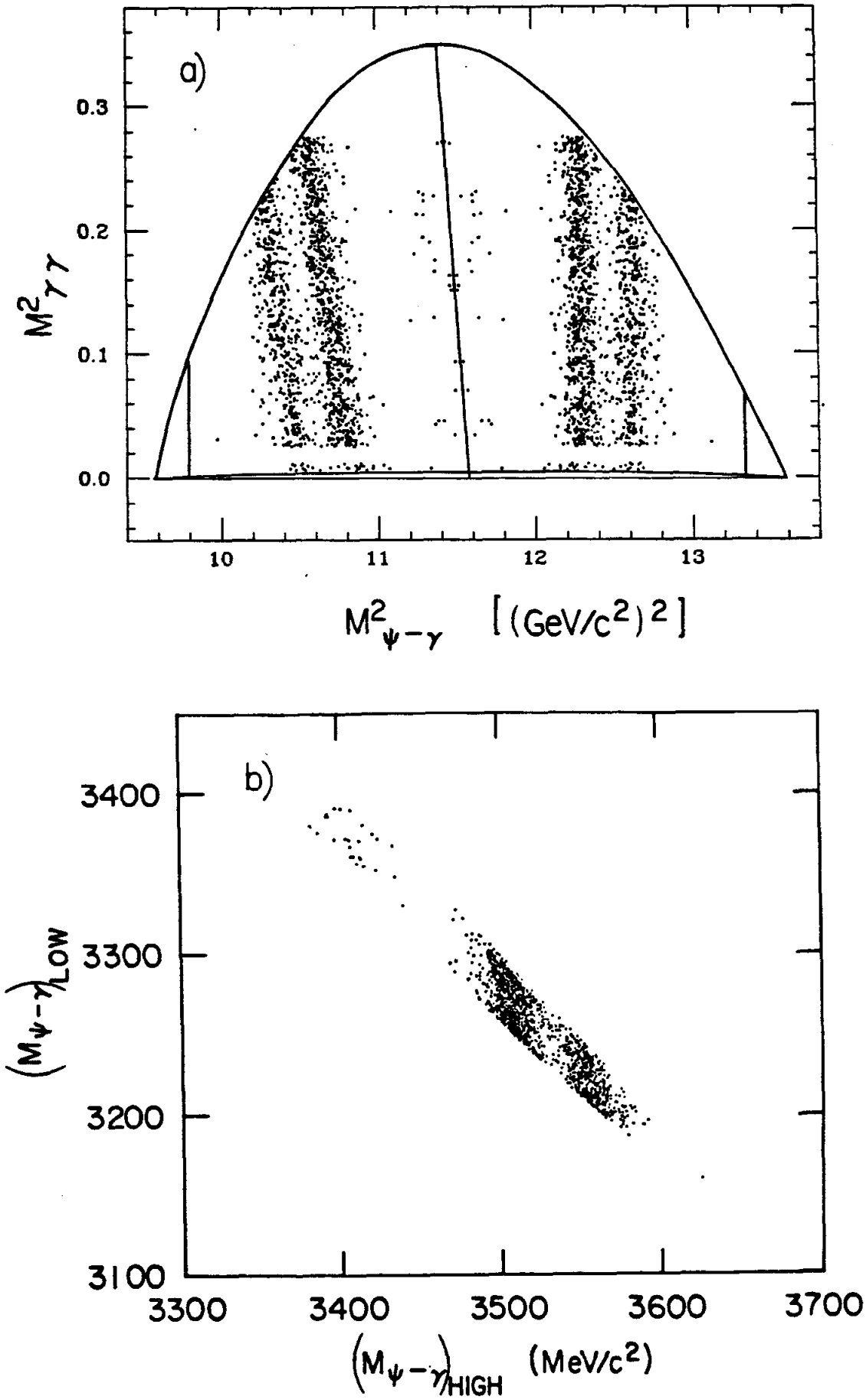

FIG..4-8 Fitted events after hand scanning and subtraction of events with diphoton masses in the ranges 135±25 or >525 MeV/c^2.

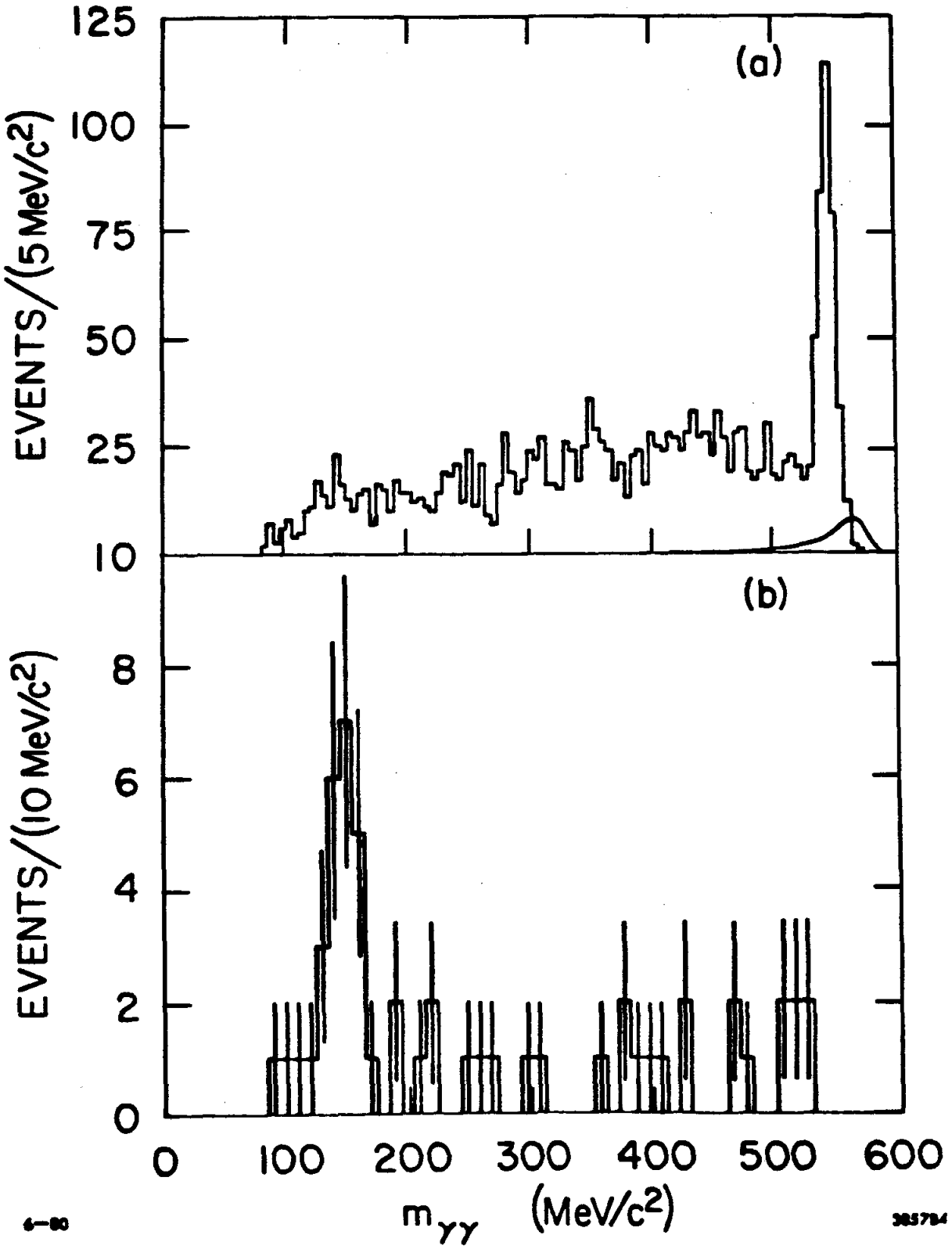

FIG..4-9 Diphoton masses of fitted events. The solid line in a) is the expected $\pi^0\pi^0$ background magnified by 10. In b) events have been removed from a) if the high $\gamma\psi$ mass fell in a χ region.

Photons from decay of the η have an average energy of 260 MeV, thereby permitting checks on general acceptances of the apparatus and especially verification that the algorithm for identification of minimum ionizing particles is not cutting out real photons. Figure 4-10a displays the expected box for the photon energy distribution; NaI(Tl) energy resolution rounds the corners with the $E^{3/4}$ variation in energy resolution rounding the high energy side more than the low energy side. The companion plot (figure 4-10b) of the angular distribution of the η relative to the incident positrons demonstrates that the events assumed to contain η have the correct $1+\cos^2\theta$ angular distribution. Although the $\pi^\circ\pi^\circ$ contamination is strongest in the η mass region, its effective diphoton angular distribution peaks at $\cos\theta=0$; the Monte Carlo simulation of this distribution has been subtracted from the data in the plot. The agreement between the data and the simulated distribution in figure 4-10b therefore checks that such $\pi^\circ\pi^\circ$ contamination is treated correctly in the Monte Carlo and is of the expected low level.

The η mass distribution is shown separately for e^+e^- and $\mu^+\mu^-$ final states in figure 4-11. The Monte Carlo simulation for $\pi^\circ\pi^\circ$ background indicates that $\pi^\circ\pi^\circ$ contamination of electronic final states is equal to that for the muons when the $E_\gamma>40$ MeV cut prevails; consistency of the tails and the small number of events observed in them also supports the low number of background events predicted by the $\pi^\circ\pi^\circ$ background Monte Carlo simulation.

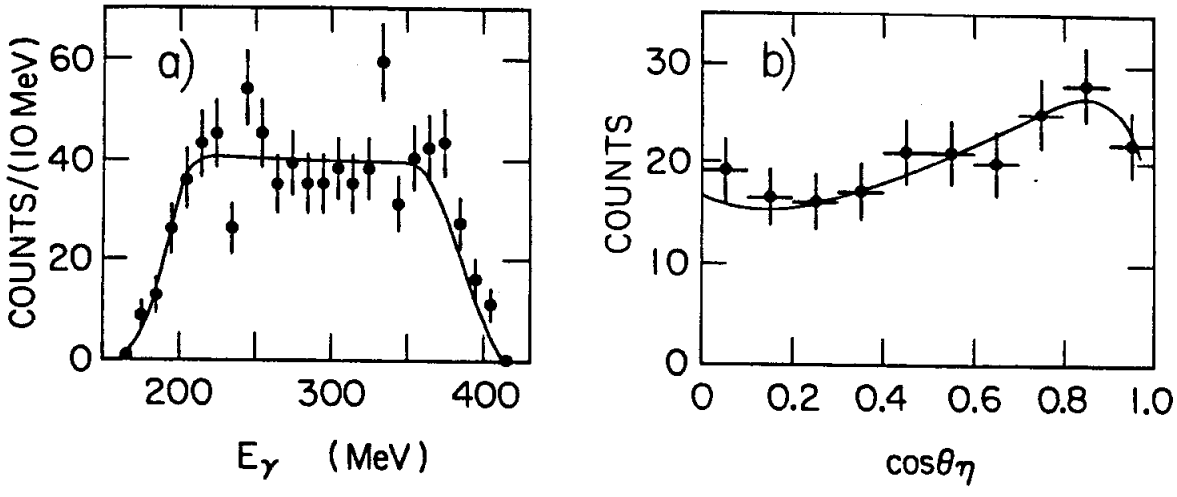

FIG..4-10 Distributions for $\psi' \to \eta\psi$. a) distribution of photon energy from $\eta \to \gamma\gamma$ (solid line is a Monte Carlo simulation). b) Polar angle of the reconstructed η with Monte Carlo simulation for a $1+\cos^2\theta$ (solid line) distribution.

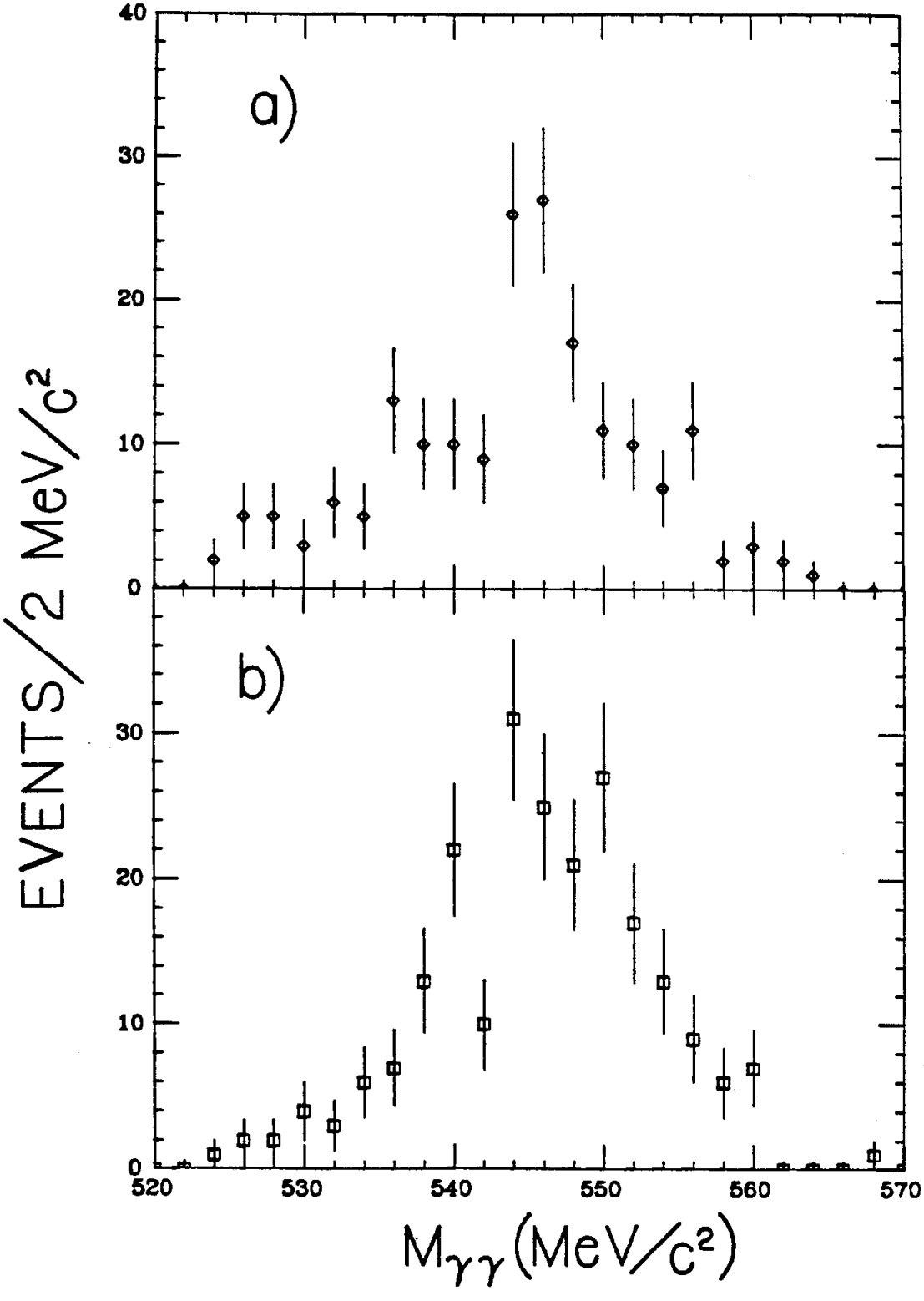

FIG..4-11 Reconstructed η masses for e^+e^- (a) and $\mu^+\mu^-$ (b) samples.

After kinematic fitting the mass distributions appear slightly non-gaussian in shape owing to the non-gaussian energy line shape of NaI(Tl). For this reason an error (i.e., uncertainty in knowledge of the NaI(Tl) line shape) is introduced on the fitted mass, which is estimated from Monte Carlo studies to be ± 0.5 MeV/c^2. For mass states arising from reaction (4-2) there is an additional error on the fitted mass which is intrinsic to the fitting program (see appendix H). The latter error arises from the uncertainty in the difference between the ψ and ψ' masses.[37] The value $m_\eta = 547.3 \pm 0.5 \pm 0.9$ MeV/c^2 is obtained from the fitted data, where the first error is statistical and the second error covers the uncertainties described above. In the Particle Data Tables the value for the η mass is 548.8 ± 0.6 MeV/c^2. This implies a preferred value for the ψ-ψ' mass splitting from the results of this experiment of 590.1 ± 1.0 MeV/c^2. The gaussian fit yields a width $\sigma = 1.2\%$ on m_η for the kinematically fitted data.

4.5 THE π° TRANSITION

Existence of the transition $\psi' \to \pi^\circ \psi$ is apparent in the Dalitz plots of both fitted and raw data (figures 4-5,4-7); observation of the decay at this level indicates violation of strong isospin symmetry (discussed in

---

[37] The Particle Data Tables quote 588.6 ± 0.8 MeV/c^2 for the ψ-ψ' mass splitting; the values 3095.0 and 3684.0 MeV/c^2 were used for the ψ and ψ' masses, respectively, in the fitting program.

[38] It should be stressed that T. Himel of the Mark-II collaboration noticed the π° transition in data acquired during the same SPEAR cycle of 1978-1979 -- see reference 32.

chapter VI). The first experimental indication[38] of the decay was seen in the plot of $p_{\gamma\gamma}$ (figure 4-12), where the sharp peak at high momentum occurs in the position of the expected momentum for a π^0 from the decay (4-2). To observe the signal in the diphoton mass plot it is sufficient to remove the dominant background from cascade photons by cutting on the $\gamma\psi$ masses. A subtraction of events from the $m_{\gamma\gamma}$ plot (figure 4-9a) with $(M(\gamma\psi))_{high}$ in the ranges 3410±5 and 3530±60 MeV/c^2, and $m_{\gamma\gamma}$>525 MeV/c^2, results in the distribution shown in figure 4-9b.

The data in figure 4-9b in the mass range 0 to 525 MeV/c^2 have been fitted to a gaussian peak with a quadratic background distribution. The fit yields 23 events above background in the π^0 peak, with 8 fitted background events having $m_{\gamma\gamma}$<200 MeV/c^2. A value of 136.1±2.5±3.4 MeV/c^2 is obtained for the location of the peak (the first error is statistical and the second arises primarily from the ψ-ψ' mass difference uncertainty), with a mass resolution σ=(7.7±1.2)%; the value of σ is consistent with the expected value of 6.8% for a π^0 from reaction (4-2). For $m_{\gamma\gamma}$<200 MeV/c^2 and with the χ cuts described above, the Monte Carlo simulations predict a total of 5 background events. Less than one background event from the process (4-3) is expected in this mass region.

It is not possible for the observed pion events to result from reaction (4-3) when one π^0 escapes detection. This mechanism implies a missing energy of more than 135 MeV -- the kinematic fitting program will not meet the convergence criteria in these cases. Moreover, the pulls generated from the kinematic fitting of the π^0 events are not bi-

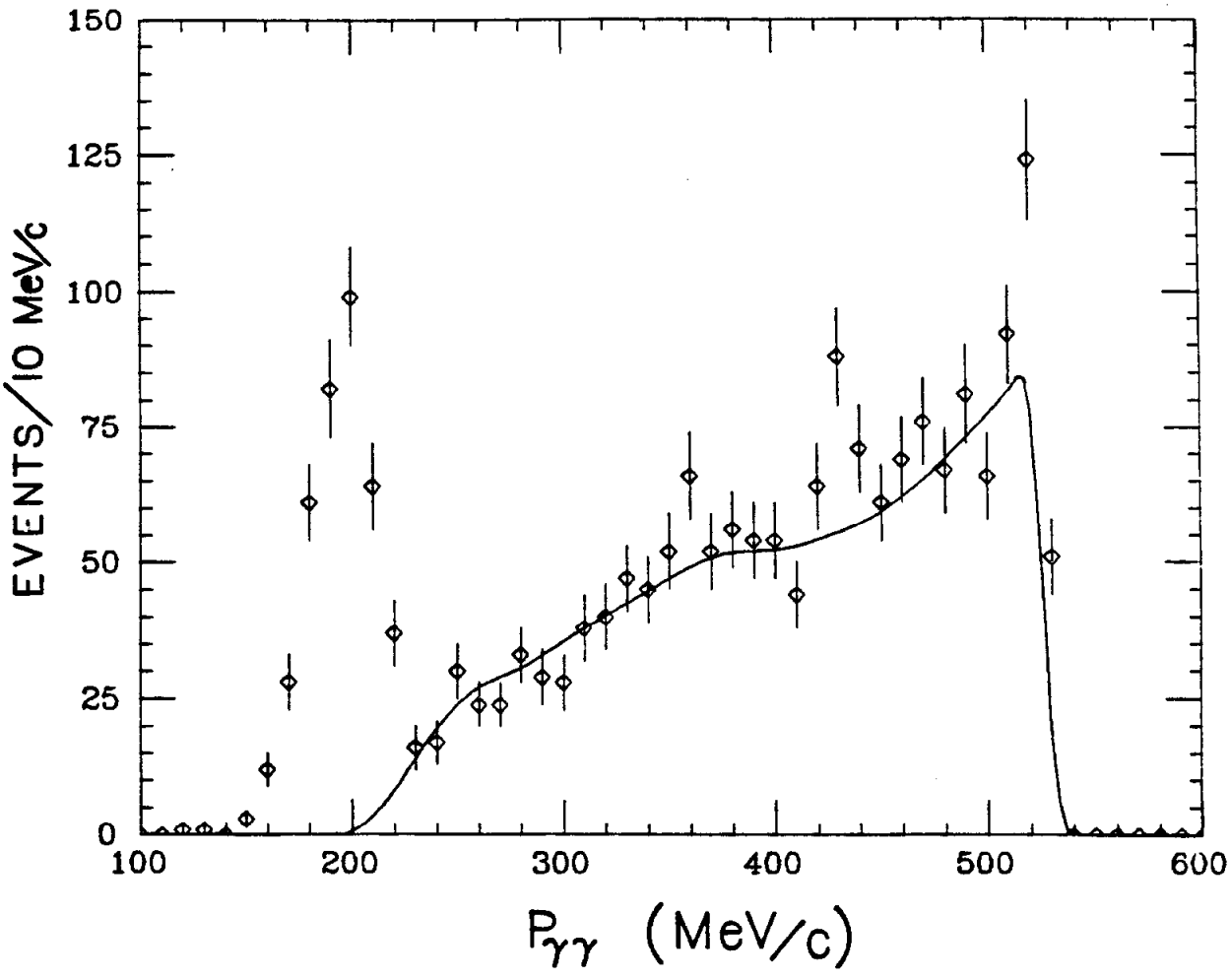

FIG..4-12 Diphoton momenta of fitted data. Solid line is Monte Carlo simulation of background from χ events.

ased, as would be the case if false hypothesis events had been pulled into the pion region. Final lepton states for the pion transition are divided equally between electrons and muons (12 and 11, respectively).

There is some concern that the non-resonant process $e^+e^-\to\pi^0\psi$ (an electromagnetic process which does not violate isospin symmetry) may be responsible for the $\pi^0\psi$ events observed. The hypothesis is tested by searching for a similar transition at E_{cm}=3772 MeV (ψ''). An analysis[39] of 1772 nb^{-1} worth of data produced only one candidate for $e^+e^-\to\pi^0\psi$, $\psi\to e^+e^-$, giving a 90% C.L. upper limit cross section of 0.06 nb. Non-resonant production should scale as 1/s, implying variation of 5% for the rate of the process between the ψ' and ψ'' energies. Then, at most 3.3 of the 23 π^0 events observed may have non-ψ' parentage.[40]

4.6 THE CASCADE STATES

Individual Dalitz plots for the e^+e^- and the $\mu^+\mu^-$ final states are shown in figures 4-13a,b, after the application of all cuts and after events arising from reaction (4-2) have been subtracted by requiring $m_{\gamma\gamma}<525$ MeV/c^2 and $|m_{\gamma\gamma}-135$ MeV/$c^2|>25$ MeV/c^2. The distribution of both lepton datasets on the $(M(\gamma\psi))_{high}$ axis is shown in figure 4-13c. The

---

[39]R. Partridge of the Crystal Ball collaboration is responsible for this analysis.

[40]This corresponds to a 90% C.L. value of $BR(e^+e^-\to\pi^0\psi)$ at E_{cm}=3684 MeV of 0.01%. For the analogous non-resonant $\eta\psi$ production, one expects the p-wave extrapolation $BR(e^+e^-\to\eta\psi) < (0.01\cdot m_\pi^2/m_\eta^2)\%$, which represents a trivial correction to the resonant $\eta\psi$ branching ratio.

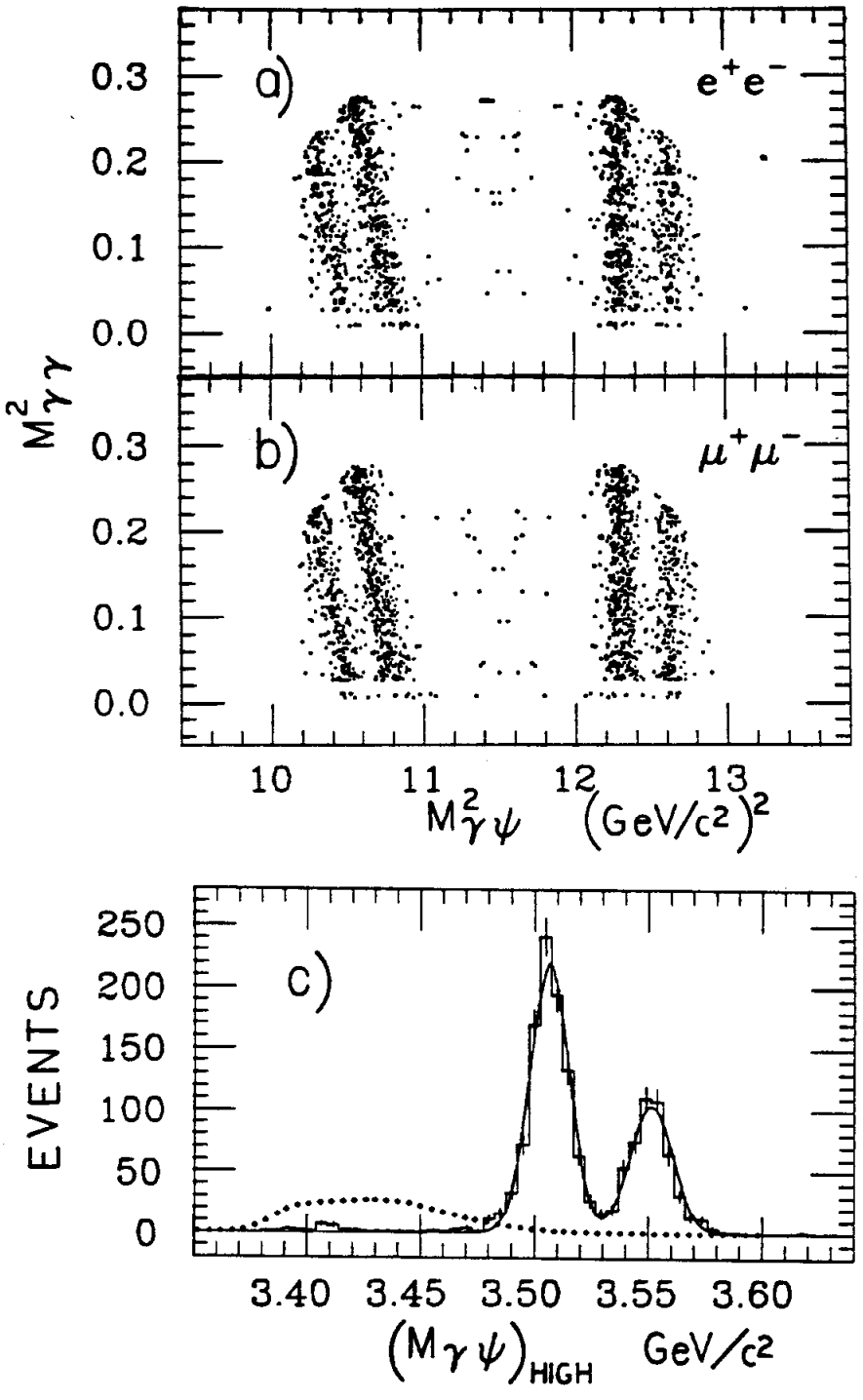

FIG..4-13 Final χ samples, π^0 and η subtracted. In c) is the projection of both datasets on the higher $\gamma\psi$ mass axis. The dotted line is the $\pi^0\pi^0$ background magnified 100 times.

populous states at $\gamma\psi$ masses of 3.55 and 3.51 GeV/c^2 fit reasonably well to a gaussian line shape, yielding 479 and 943 events, respectively. A gaussian line fit to the state at 3.41 would not be reasonable, as 3 of the 20 events are expected to come from $\pi^0\pi^0$ contamination. Furthermore, the position of $\chi(3.41)$ is near enough to the kinematic limit that the projection suffers a fold-over effect (at the $E_\gamma' = E_\gamma$ boundary) which alters the line shape.

A cluster of 6 events centered at $(M(\gamma\psi))_{high}$=3.465 GeV/c^2 (all coming from electron final states) does not exhibit a reasonable NaI(Tl) line shape; rather, it resembles a tail from the large peak at 3.51 GeV/c^2. Corresponding to a photon energy slightly higher than expected for a $\chi(3.51)$, the tail results from overlap of $\sum 13$ clusters from the monochromatic photon with abnormally widespread electron showers, or from the inclusion of spray[41] into the photon clusters (see appendix E for more discussion). The spray contribution in particular is difficult to Monte Carlo, and one must therefore consider these 6 events when computing the upper limits on a state at 3.455 GeV/c^2. The E_γ>40 MeV cut restricts $M(\gamma\psi)$ to the range 3129 to 3644 MeV/c^2. In this region there is no evidence for a fourth χ state.

The energy distributions for the primary photon in the cascades of $\chi(3.51)$ and $\chi(3.55)$ are shown in figure 4-14a fitted to a NaI(Tl) reso-

---

[41]This refers to extreme shower fluctuation, or secondary electrons and photons arising from showers in other parts of the apparatus.

[42]The precise form is $\sigma \propto E^3/((E-E_0)^2+\Gamma^2/4)$.

lution folded with a non-relativistic Breit-Wigner line shape.[42] Resolution of the $\chi(3.51)$ is consistent with the NaI(Tl) resolution function described in appendix D.[43] There is little improvement of these resolutions by kinematic fitting, for the low energy photons have such a small lever arm in adjusting energy-momentum conservation when compared to the high energy leptons. The function $\chi^2(\Gamma)$ for the fit to the line shape is shown in figure 4-14b. From the functions one obtains:

$$\Gamma(\chi(3.51)) < 2.6 \text{ MeV (90\% C.L.)}$$

$$\Gamma(\chi(3.55)) = (4.1 \pm 0.9) \text{ MeV}$$

The resolution function used in these fits is assumed to have the $E_0^{3/4}$ behavior; for an evaluation of the uncertainty here, see the discussion in appendix D.

4.7 BRANCHING RATIOS

Implementing all the cuts used to obtain the final data samples, the Monte Carlo described in appendix H has been used to calculate efficiences for the states observed, as well as for the putative $J^{PC}=0^{-+}$ states with masses 3.455 and 3.591 GeV/c^2. Spin assignments used in the Monte Carlo simulation of χ states are assumed to be the conventional ones, with the results described in the next chapter supporting our choices of $J^{PC}=0^{++}$, 1^{++}, and 2^{++} for $\chi(3.41)$, $\chi(3.51)$, and $\chi(3.55)$, respectively. Results of the peak fitting and acceptance correction are summarized in Table 4-1.

---

[43] The resolution function is comprised of a gaussian distribution with $\sigma=0.027E_0^{3/4}$ which has a low-energy tail $(E_0-E)^{-3.5}$ beginning at $E=E_0-1.8\sigma$.

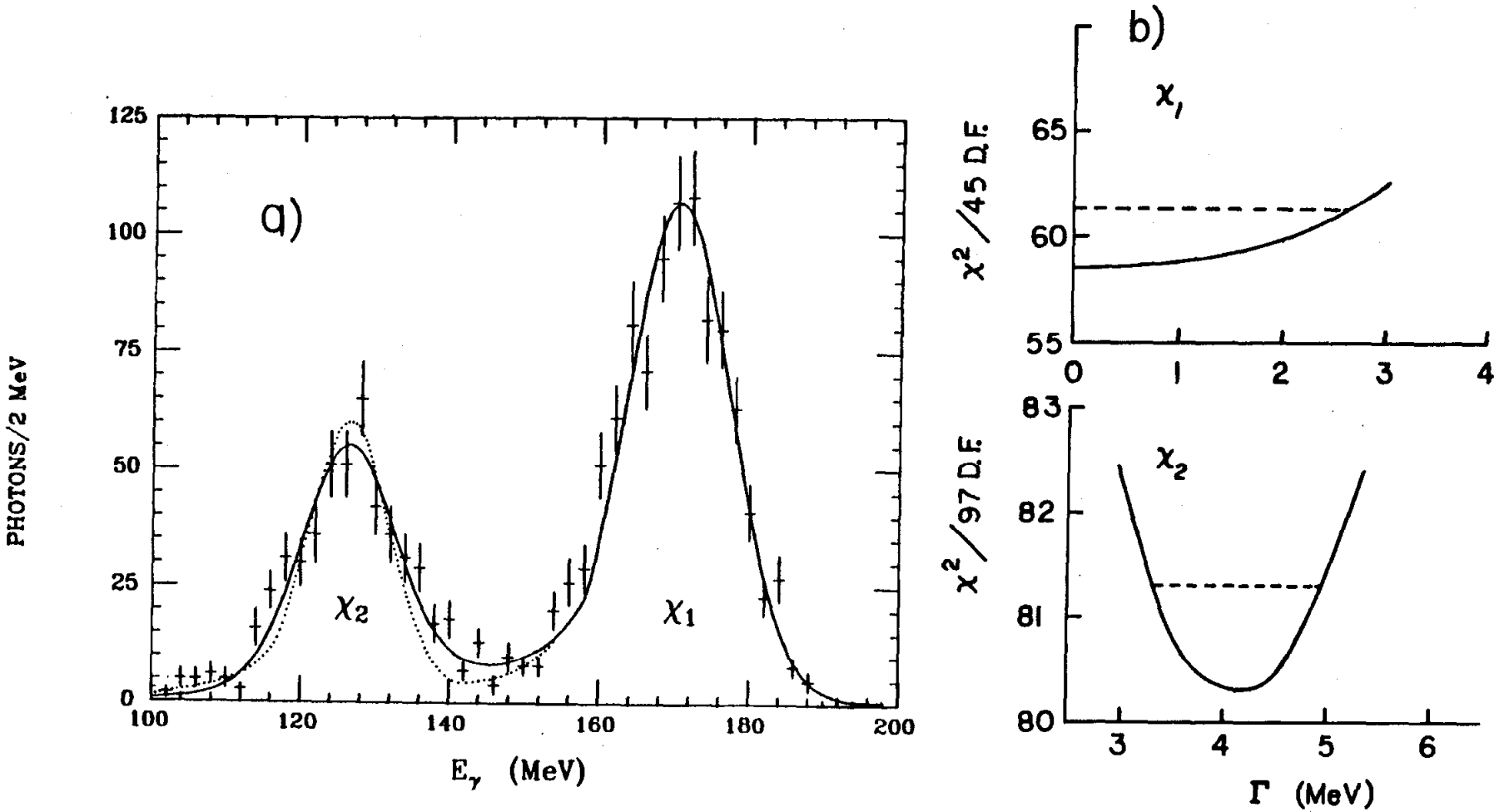

FIG..4-14 Spectrum of monochromatic photons. The dotted line in a) is the NaI(Tl) shape for the detector; the solid line is the best fit obtained by folding in an intrinsic χ width. Confidence level as a function of the intrinsic full width (Γ) is shown in b). Horizontal bars are the 90% C.L. level for χ_1 and the one standard deviation level for χ_2.

TABLE 4-1

MASS (MeV/c^2)		N (observed)	N (corrected)	ERROR (%)
3553.9±0.5±4	e	231	1351±90	6.7
	μ	248		
3508.4±0.4±4	e	442	2545±132	5.2
	μ	501		
3413 (see text)	e	7	61.5±15.7	25.5
	μ	10		
547.3±0.5±0.9	e	170	887±56	6.3
	μ	216		
136.1±2.5±3.4	e	11	90±20	21.2
	μ	12		
3455	e	<10.7	<36.2	3.8
	μ	< 2.3	< 7.8	3.8
3591	e+μ	< 5.8	<18.6	3.8

The mass of χ(3.41) is well established as 3412.9±0.6±4 MeV/c^2 from its hadronic decays.[44] Numbers reported for the putative states not observed in this experiment are 90% confidence level upper limits; the accompanying error applies to the acceptance factor only. Error on the masses obtained for χ(3.51) and χ(3.55) is dominated by the 4 MeV/c^2 uncertainty in M_ψ. Aside from this error, kinematic fitting establishes the χ masses quite precisely; the process is described in appendix H. The first error on M_χ in Table 4-1 covers uncertainties arising from statis-

---

[44]T.M. Himel, report SLAC-REPORT 223 (Ph.D. thesis) (Stanford) (1979).

tics, the NaI(Tl) energy line shape, and on our knowledge of the ψ-ψ' mass splitting. For the π^0 and η masses in the table, the first error describes the statistical uncertainties while the second error arises from uncertainty in the ψ-ψ' mass splitting and in the NaI(Tl) line shape correction.

In order to test the ability of the Monte Carlo simulation to incorporate the true geometry of the apparatus and predict shower extent and fluctuation, the corrected number of $\chi(3.51)$ has been computed for several values of the general acceptance cut on $|\cos\theta|$. The results of the study are summarized in figure 4-15.

To facilitate computation of final branching ratios one requires knowledge on the number of ψ' produced. Hadrons produced from the ψ' decays were counted directly; therefore, the analysis relies heavily on the ability of the Crystal Ball to detect hadrons reliably and on the large solid angle covered by the NaI(Tl) detector. Sources of background arise from cosmic rays in time with the beam-cross signal, and beam-gas collisions. Of these two classes, the cosmic ray background may be further categorized as muons which pass through the void in the center of the NaI(Tl) ball, muons which traverse a single continuous path through NaI(Tl), and cosmic electron showers which tend to deposit energy throughout the entire ball. The second and third classes produce a highly asymmetric event pattern. An attempt was made to identify such backgrounds by comparing the total energy deposited in the NaI(Tl) with the asymmetry[45] of the event. Figure 4-16 depicts the comparison for

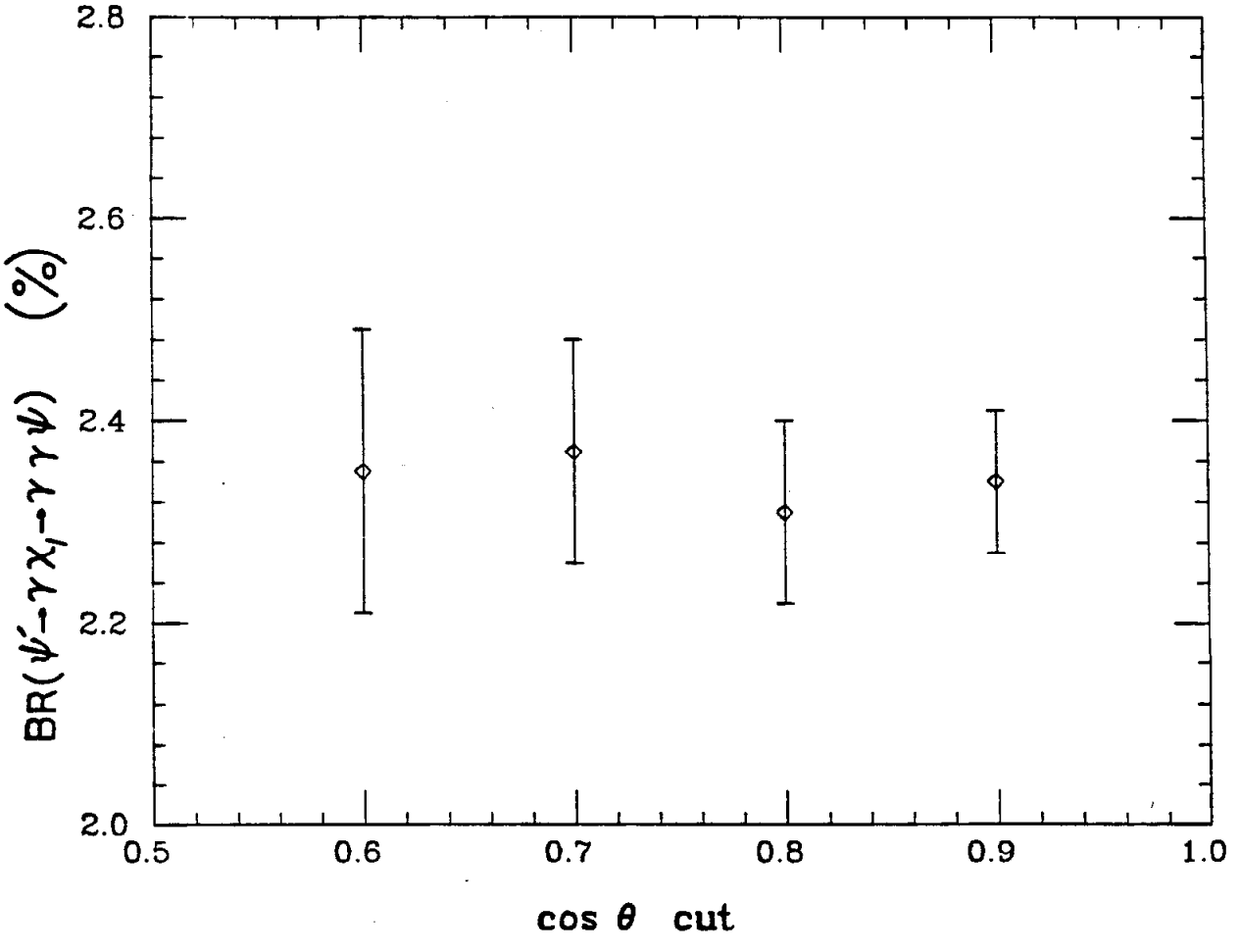

FIG..4-15 Branching ratio obtained for the $\chi(3.51)$ cascade as a function of the acceptance cut.

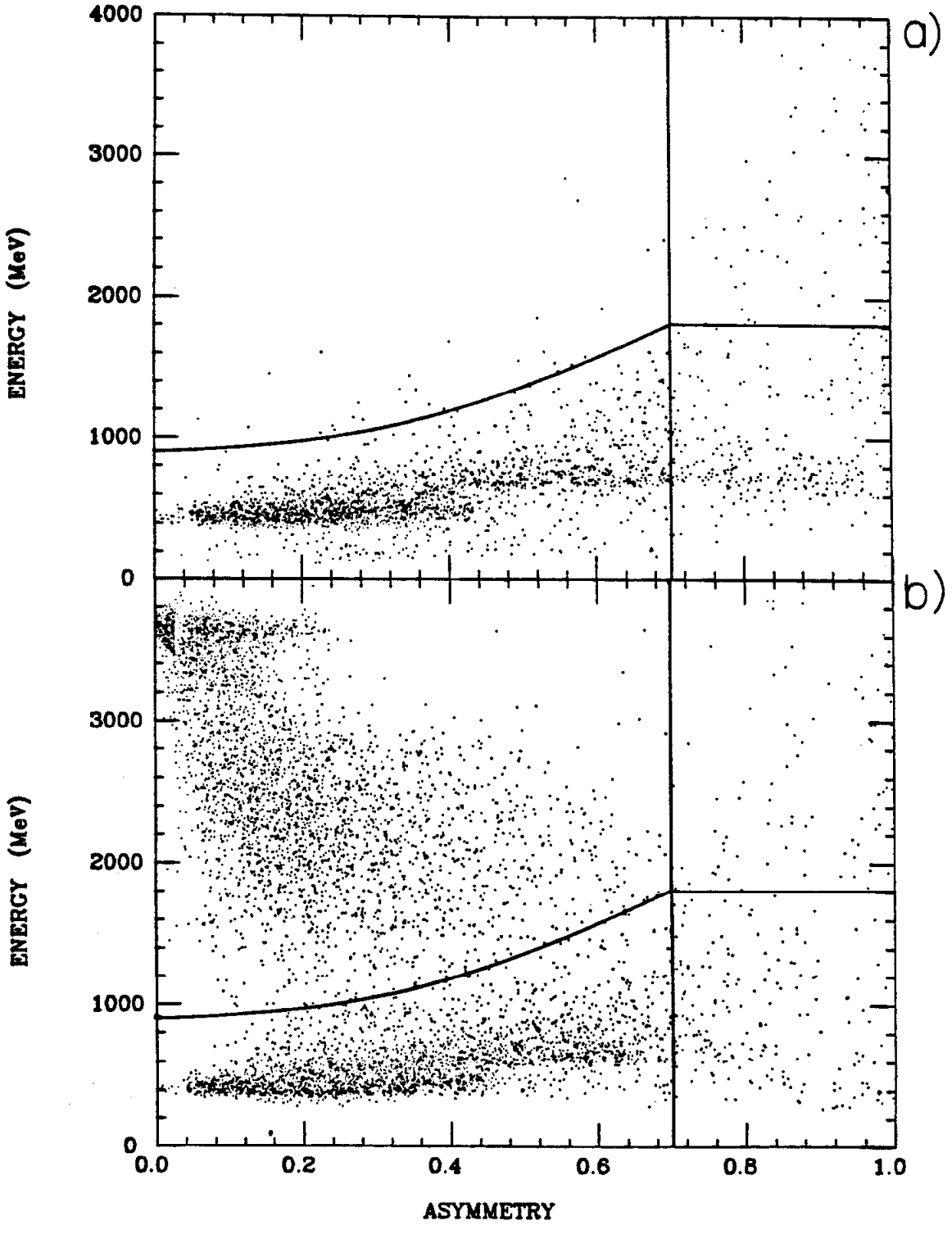

FIG..4-16 Total event energy/asymmetry plots for separated (a) and colliding (b) beams.

both separated and colliding beam runs. Central cosmics traversing the void appear quite symmetric and tend to deposit about 400 MeV in the NaI(Tl), accounting for the high density cluster in the lower left portion of the plots. Cosmic rays of the second class traverse more crystalline material and therefore deposit about 600 MeV. These events are fairly asymmetric and account for the cluster just above the previous one. Roughly 10% of the cosmics rays shower; such events have ill-defined energies and tend to be extremely asymmetric. The total energy of a beam gas event may not exceed the single beam energy, and while one would naively expect symmetry to be poor, it is actually possible to realize relatively uniform illumination of NaI(Tl) because of the tendency to create large numbers of randomly directed nuclear fragments.

A separation of hadronic events from the backgrounds is observed in figure 4-16b. The boundary shown in the figure defines the hadron dataset (the upper left region). Leakage across the boundary is less that 1% for the backgrounds, and is estimated to be similarly small for hadrons. The latter estimate comes from a comparison of colliding beam data with separated beam runs; a conceivable change of nature in the beams after separation dictates the conservative 10% uncertainty ascribed to the leakage correction.

The 900 MeV threshold of the hadron-defining boundary in the high symmetry region of figure 4-16b has been shown by a Monte Carlo study to

---

[45] Asymmetry is defined as $|\sum E_i|/E_{tot}$ for tracks i.

exclude about 3% of the known ψ' decays. The overall correction factor on the number of hadrons observed is 1.02±0.10. In calculating the number of parent ψ', one must subtract the number of hadrons produced non-resonantly from the process $e^+e^-\rightarrow$hadrons. The number is given by

$$N_{nr} = R\ \sigma[\mu^+\mu^-]\ \int Ldt = (2.5\pm0.2)\ 6.45\ (1600\pm100) = 25818\pm10\%$$

Then, since there are 786,422 hadrons counted in figure 4-16b,

$$N_{\psi'} = 786422\cdot1.02 - 25818 = 776332\pm10\% \quad .$$

The branching ratio for the decay of the ψ into dileptons is taken as[46] $BR(\psi\rightarrow l^+l^-)= 2\cdot(0.069\pm0.09)$; it is the dominant systematic error (13%) in this experiment. Combined in quadrature with the normalization uncertainty, an overall systematic error of 16% is realized. The branching ratios shown in Table 4-2 are thus obtained for the processes (4-1) and (4-2); the confidence levels shown there are computed incorporating all of the uncertainties involved, a la appendix I. A comparison of the results in Table 4-2 with previous experiments can be found in chapter VI.

---

[46]A. Boyarski et al., Phys. Rev. Lett. 34, 1357 (1975).

TABLE 4-2

MASS (MeV/c^2)	BR (%)	ERROR stat.+acceptance		systematic	
	$BR(\psi' \to \gamma\chi \to \gamma\gamma\psi)$				
3553.9±0.5±4	1.26	±	0.08	±	0.20
3508.4±0.4±4	2.38	±	0.12	±	0.38
3413 (see text)	0.059	±	0.015	±	0.009
3455 (0^-) e+μ	< 0.04				90% confidence level
μ	< 0.02				
3591 (0^-)	< 0.04				
	$BR(\psi' \to m\psi)$				
547.3±0.5±0.9	2.18	±	0.14	±	0.35 ($\eta \to$ all)
136.1±2.5±3.4	0.08	±	0.02	±	0.01 ($\pi^0 \to$ all)

Chapter V

MULTIPOLE ANALYSIS

5.1 THEORY OF MULTIPOLES

Application of the radiative cascade sequence (4-1) to determine the spin and parity of nuclei has been a routine practise for more than twenty years. Nearly the same scheme lends itself well to the study of heavy quark-antiquark spectroscopy, especially when one considers the photon dominance in the ψ-ψ' system (owing to the OZI rule). Our cascade analysis is limited by the lack of a photon polarization measurement. Electric and magnetic multipole amplitudes for the radiative transitions are interchanged by the transformation $\vec{E}\to\vec{H}$, $\vec{H}\to-\vec{E}$ which leaves the Poynting vector $\vec{E}\times\vec{H}$ unaltered.[47] Parity information is forfeited because the left and right circular polarization of the photons is not differentiated; an angular distribution analysis therefore measures only the spin of the intermediate particle.

Focussing on each element of the cascade independently,

$$e^+e^- \to \psi' \qquad (5\text{-}1a)$$

$$\psi' \to \gamma'\chi \qquad (5\text{-}1b)$$

$$\chi \to \gamma\psi; \qquad (5\text{-}1c)$$

$$\psi \to l^+l^- \quad , \qquad (5\text{-}1d)$$

---

[47] H. Frauenfelder and R. Steffen, in Alpha-, Beta-, and Gamma-Ray Spectroscopy, ed. by K. Siegbahn, North-Holland, Amsterdam, 997 (1965).

computation of the angular distributions of the final state particles entails first a rotation describing ψ' decay, a boost to the χ frame followed by a rotation describing its decay, a boost to the ψ frame, and finally a rotation for the last decay. Furthermore, the helicity formalism requires that two rotations accompany each boost so that a particle boosts with the helicity axis along its trajectory. It is difficult to express the angular distribution in terms of quantities which are all measured in the laboratory frame, although this is possible in approximation.[48] Indeed, the χ and ψ particles are massive compared to the photon energies in (5-1). This approximation for the analogous ψ',χ, and ψ rest frames is common in the nuclear physics cases where β is typically less than 0.01; however, high energy systems do not adapt as well to this approximation since β has a maximum value of 0.2. One avoids the need for such approximation by boosting the measured laboratory angles appropriately.

The particles participating in the sequence (5-1) define the frames described in figure 5-1. The sign of the outgoing lepton charges is not measured in the non-magnetic detector, thereby necessitating a random charge assignment in both the data and in the Monte Carlo simulations of data. Knowledge of the sign of the lepton charge would only be required for a measurement of the χ parity; since the polarization information is not available anyway (thus preventing determination of the parity) the analysis is not impaired by the lack of lepton charge identification.

---

[48] One assumes equivalence of all the frames (i.e., a negligible χ recoil.)

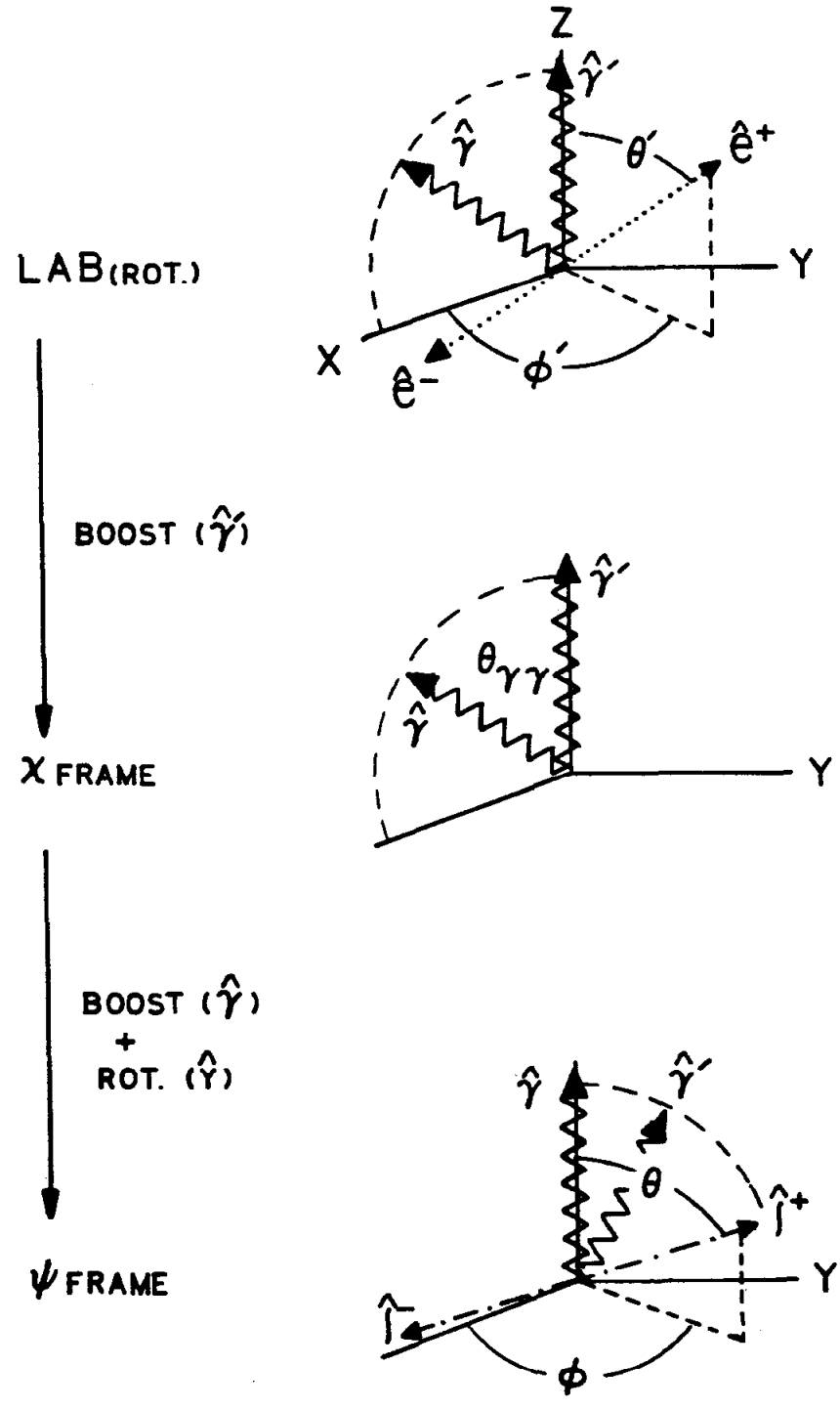

FIG..5-1 Vectors and frames describing the cascade reaction.

The ψ' is produced in a helicity state λ' [49] (which has only two projections owing to the extreme relativistic nature of SPEAR electrons), and then proceeds to decay as follows:

$$\psi'(\lambda') \to \gamma'(\mu')\ \chi(\nu'),\ \lambda' = \pm 1 = \mu' - \nu' \qquad (5\text{-}2)$$

$$\mu' = \pm 1$$

$$\nu' = -J_x \to J_x$$

with amplitude $B_{\nu'\mu'}$

$$\chi(\nu) \to \gamma(\mu)\ P(\lambda), \qquad \lambda = 0, \pm 1 \qquad (5\text{-}3)$$

$$\mu = \pm 1$$

$$\nu = -J_x \to J_x$$

with amplitude $A_{\nu\mu}$

A parity transformation gives $A_{-\nu-\mu} = (-)^{J_x} P_x A_{\nu\mu}$ and likewise for the first amplitude, permitting the definitions

$$A_\nu \equiv A_{\nu 1} \qquad B_\nu \equiv B_{\nu 1} \qquad (5\text{-}4)$$

with a form for the angular distribution:

$$W(\cos\theta', \phi', \cos\theta_{\gamma\gamma}, \cos\theta, \phi; \underset{\sim}{p}) = \qquad (5\text{-}5)$$

$$\sum_{\substack{\nu'\tilde{\nu}';\ \mu'=\pm 1 \\ \nu\tilde{\nu};\ \mu=\pm 1}} \rho^{(\mu'-\nu',\,\mu'-\tilde{\nu}')}(\theta', \phi') B_{|\nu'|} B_{|\tilde{\nu}'|} d^J_{-\nu',\nu}(\theta_{\gamma\gamma}) d^J_{-\tilde{\nu}',\tilde{\nu}}(\theta_{\gamma\gamma}) A_{|\nu|} A_{|\tilde{\nu}|} \rho^{*(\nu-\mu,\,\tilde{\nu}-\mu)}(\theta, \phi)$$

where $\underset{\sim}{p}$ represents the parameter vector describing the spin of the χ particle and the multipole structure of the radiative transitions (5-1b) and (5-1c), and ρ is the density matrix for the leptons:

---

[49] The conventions and formulae are those established in a paper by G. Karl, S. Meshkov and J. Rosner, Phys. Rev. D13, 1203 (1976).

$$\rho = \begin{pmatrix} \frac{1+\cos^2\theta}{2} & \frac{\sin\theta\cos\theta\, e^{-i\phi}}{\sqrt{2}} & \frac{\sin^2\theta\, e^{-2i\phi}}{2} \\ \rho_{10}^* & \sin^2\theta & -\rho_{10} \\ \rho_{1-1}^* & -\rho_{10}^* & \rho_{11} \end{pmatrix} \qquad (5\text{-}6)$$

The d-functions in (5-5) are given in standard references.[50]

The angular distribution function W is described by the five measured angles shown schematically in figure 5-1. The polar angles of e^+ in the rotated lab frame are denoted by θ' and ϕ', with the polar axis taken along the γ' direction, and with $\hat{y}$ orthogonal to the two photon directions. Similarly, θ and ϕ describe l^+ (or an average over l^+ and l^-) in the ψ rest frame, with $\hat{z}$ along the direction of γ; $\hat{y}$ is not altered by the boost to the ψ rest frame.[51] The angle between the photons in the χ rest frame is $\theta_{\gamma\gamma}$. Vectors used to obtain these angles are measured in different frames accordant with the calculation for W; they can be defined using the unit vectors $\hat{e}^+$ (the incident positron) and $\hat{\gamma}'$ in the ψ' rest frame; $\hat{\gamma}_\chi'$, $\hat{\gamma}$ in the χ rest frame; and $\hat{l}^+$ (the final positive lepton) and $\hat{\gamma}_\psi$ in the ψ rest frame. Then,

$$\cos\theta' = \hat{e}^+ \cdot \hat{\gamma}' \qquad \tan\phi' = \frac{\hat{e}^+ \cdot (\hat{\gamma}_\chi' \times \hat{\gamma})}{\hat{e}^+ \cdot ((\hat{\gamma}_\chi' \times \hat{\gamma}) \times \hat{\gamma}')}$$

$$\cos\theta_{\gamma\gamma} = \hat{\gamma}_\chi' \cdot \hat{\gamma} \qquad (5\text{-}7)$$

$$\cos\theta = \hat{l}^+ \cdot \hat{\gamma}_\psi \qquad \tan\phi = \frac{\hat{l}^+ \cdot (\hat{\gamma}_\chi' \times \hat{\gamma})}{\hat{l}^+ \cdot ((\hat{\gamma}_\chi' \times \hat{\gamma}) \times \hat{\gamma}_\psi)}$$

---

[50] Review of Particle Properties, Rev. Mod. Phys. 52, (1980).

[51] All boosts are taken in the x-z plane, thereby leaving all y quantities unaltered.

The helicity amplitudes may be written in terms of multipole coefficients:[52]

$$A_{|\nu|} \sim \sum_j a_j \sqrt{\frac{2j+1}{2J_x+1}} \langle j,1,1,|\nu|-1 \,|\, J_x,|\nu| \rangle \quad , \tag{5-8}$$

a_j being the multipole amplitudes normalized by

$$\sum_{j=1}^{J_x+1} (a_j)^2 = 1 \tag{5-9}$$

The explicit forms of A_ν are given in reference 49. The proportions of the various a_j, in addition to the overall J_x, can be measured. In the helicity notation the parameter vector is written as $\underset{\sim}{p}=(J_x,\underset{\sim}{a}',\underset{\sim}{a})$.

5.2 PARITY TRANSFORMATIONS

The data is analyzed by means of a histogram over the five measured angles, a technique which facilitates the use of goodness-of-fit tests after the optimal values for p have been determined. It has been pointed out by Tanenbaum[53] that the statistics for each histogram bin are enhanced if parity conservation is used to restrict the range of some variables. Each of the four decays (5-1) involved in the cascade conserves parity in the appropriate rest frame. The transformations

---

[52]Actually the normalization is $\Gamma(\chi\to\gamma\psi) \propto \sum (A_\nu)^2 = \sum (a_j)^2$ Then, if $P_x=+$, a_1 corresponds to an E1 transition, a_2 to M2, and a_3 to E3.

[53]W. Tanenbaum et al., Phys. Rev. D17, 1731 (1978).

a) $\hat{\gamma}' \rightarrow -\hat{\gamma}'$, ψ' rest frame

$\hat{\gamma} \rightarrow -\hat{\gamma}$, χ rest frame

$\hat{l} \rightarrow -\hat{l}$, ψ rest frame

b) $\hat{\gamma} \rightarrow -\hat{\gamma}$, χ rest frame

$\hat{l} \rightarrow -\hat{l}$, ψ rest frame (5-10)

c) $\hat{e} \rightarrow -\hat{e}$, ψ' rest frame

d) $\hat{l} \rightarrow -\hat{l}$, ψ rest frame

all leave the angular distribution unchanged. In terms of the measured quantities, the effect of the parity transformations is:

a) $\cos\theta' \rightarrow -\cos\theta'$

$\phi' \rightarrow \pi-\phi'$

$\cos\theta_{\gamma\gamma} \rightarrow +\cos\theta_{\gamma\gamma}$

$\cos\theta \rightarrow +\cos\theta$

$\phi \rightarrow -\phi$

c) $\cos\theta' \rightarrow -\cos\theta'$

$\phi' \rightarrow \pi+\phi'$

$\cos\theta_{\gamma\gamma} \rightarrow +\cos\theta_{\gamma\gamma}$

$\cos\theta \rightarrow +\cos\theta$

$\phi \rightarrow +\phi$

(5-11)

b) $\cos\theta' \rightarrow +\cos\theta'$

$\phi' \rightarrow \pi+\phi'$

$\cos\theta_{\gamma\gamma} \rightarrow -\cos\theta_{\gamma\gamma}$

$\cos\theta \rightarrow +\cos\theta$

$\phi \rightarrow \pi-\phi$

d) $\cos\theta' \rightarrow +\cos\theta'$

$\phi' \rightarrow +\phi'$

$\cos\theta_{\gamma\gamma} \rightarrow +\cos\theta_{\gamma\gamma}$

$\cos\theta \rightarrow -\cos\theta$

$\phi \rightarrow \pi+\phi$

Given values for the five measured variables in a particular event, 1 of 16 combinations[54] of the 4 principle transformations may be applied to the data to produce a set of variables in which $\cos\theta'$, $\cos\theta_{\gamma\gamma}$, $\cos\theta$, and ϕ' all have positive values and the distribution W is left unaltered. The decision to choose ϕ as the variable with full-range values was arbitrary.

5.3 SPIN ANALYSIS

The goal of the multipole analysis is to compare the data (binned in 5 angles) with similar histograms produced by a Monte Carlo simulation of the experiment. A Monte Carlo simulation of the cascade decay for a specific χ state requires the χ spin and the cascade multipole parameters ($\underset{\sim}{p}$) as input parameters; the best value of $\underset{\sim}{p}$ is the one which maximizes a likelihood function obtained from a comparison of the real and Monte Carlo simulated data. Certain projections of the five dimensional space are particularly revealing and can provide information on the spin of the χ states. Studies for the spin hypotheses 0,1,2 and several multipole configurations have determined that $\cos\theta'$ and $\cos\theta$ are useful in this manner. Figures 5-2a,b show data for the $\chi(3.51)$ and $\chi(3.55)$ with suitably normalized Monte Carlo curves[55] for the three spin hypotheses. The two Monte Carlo simulations for spin 1 and 2 yield distributions of

---

[54] The order in which the transformations (5-11) are performed is important.

[55] For this comparison the helicity amplitudes in the Monte Carlo simulations were fixed assuming lowest order multipole dominance.

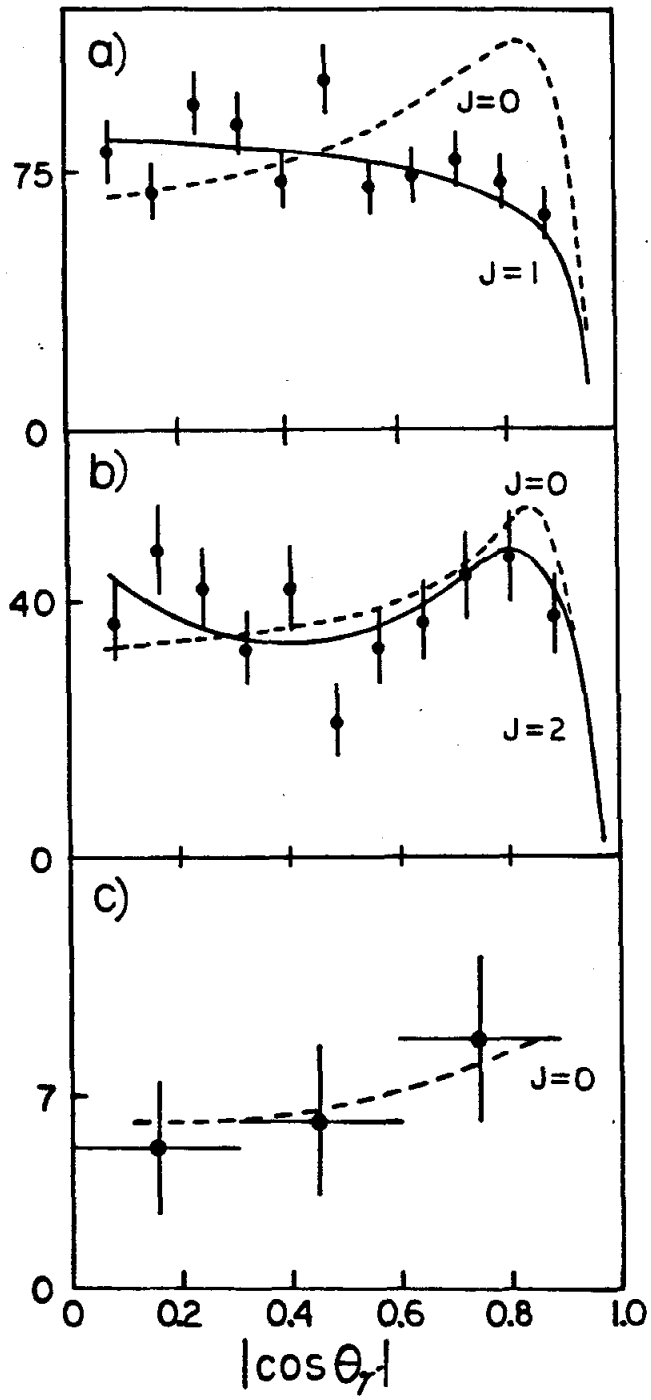

FIG..5-2 Projections of cosθ′. a) χ(3.51) data. b) χ(3.55) data. c) χ(3.41) data. Lines are Monte Carlo simulations for the indicated spin hypotheses.

$\cos\theta'$ with opposite second derivatives, thus establishing the spin for $\chi(3.51)$ quite well. Although the $\chi(3.55)$ data fits a spin 0 curve rather poorly, the evidence from the projection does not present an overwhelming case for an assignment of spin 2. The maximum likelihood fit over all variables enables one to combine the information from all projections, thereby establishing spin assignment with far greater accuracy. The distribution for $\chi(3.41)$ shown in figure 5-2c demonstrates only that the $\cos\theta'$ projection for the 20 $\chi(3.41)$ events seen in the cascade mode has a distribution not inconsistent with $1+\cos^2\theta'$; within the limited statistics, the distribution is not flat (as it would be if the events resulted from $\pi^0\pi^0$ background -- cf. Section 4.4). The poor statistics here yield a confidence level of 0.22 for the fit of the data to a χ_0 Monte Carlo simulation, as opposed to a value of 0.03 for a fit to a $\pi^0\pi^0$ simulation.

5.4 MULTIPOLE ANALYSIS

For a χ with spin J_χ there are $J_\chi+1$ multipole amplitudes which describe the radiative decays (5-1b) and (5-1c). Given the standard charmonium model,[1] one expects that the low order multipole amplitudes dominate. Therefore, the octupole coefficient possible in the spin 2 case was ignored initially; it would have been considered had the quadrupole amplitude proven significant. The five dimensional histogram over $\cos\theta'$, ϕ', $\cos\theta_{\gamma\gamma}$, $\cos\theta$, and ϕ was formed by dividing the variables with only positive ranges into three equal bins, and ϕ into 6 bins; a total of 486 bins resulted, which represents a practical maximum for the 921 $\chi(3.51)$ and 441 $\chi(3.55)$ in the sample.

Each spin-multipole hypothesis $\underset{\sim}{p}$ required calculation of a binned Monte Carlo simulation which was acceptance corrected and constrained to have a total number of events equal to that in the experimental data sample. Such a constraint on the normalization required that a binomial probability density function be used in describing the probability for observing a given number of events in any particular bin.[56] The likelihood function therefore had the form:

$$L(\underset{\sim}{p}) = N! \prod_{i=1}^{486} \frac{\langle n_i(\underset{\sim}{p}) \rangle^{n_i}}{n_i!} \quad , \quad N \equiv \sum_{i=1}^{486} n_i \quad , \tag{5-12}$$

where n_i is the number of events measured in bin i, and $n_i(p)$ is the number expected in the bin if the hypothesis $\underset{\sim}{p}$ correctly describes the data. Appendix I (statistics) elaborates on the techniques used here. The quality of a fit obtained by maximizing L over $\underset{\sim}{p}$ may be examined with a likelihood ratio test. It is remarked in reference 56 that, in the instance of small bin populations, the ratio test provides a more reliable goodness-of-fit check than the more common Pearson χ^2 test. A suitably transformed likelihood ratio variable has a distribution approaching χ^2 for large data samples (N>100); the constraint of normalization must be subtracted from the number of bins. In obtaining the confidence levels quoted for the fits to various hypotheses, bins with one count or fewer were not considered in (5-12).

---

[56] W. Eadie et al., Statistical Methods in Experimental Physics, North-Holland, Amsterdam (1971).

The data for the χ states was separated from the other $\gamma\gamma\psi$ data by applying the η and π^0 cuts described in chapter IV. The individual χ states were then separated by cutting on $M(\gamma\psi)_{high}$ with 95% and 90% windows for $\chi(3.509)$ and $\chi(3.554)$, respectively; 921 events for the $\chi(3.51)$ and 441 events for the $\chi(3.55)$ then comprised the individual data samples. The acceptance cuts and efficiencies of the apparatus were taken into account when forming the Monte Carlo simulation histograms. The e^+e^- and $\mu^+\mu^-$ final states were treated separately, and then the electron and muon Monte Carlo histograms were added together when the likelihood function was calculated. The experimental data was therefore binned directly, without weighting for acceptance.[57]

The results from the likelihood fit are presented in Table 5-1. The stability of these results has been tested by altering various parameters in Monte Carlo simulations of the likelihood fit, as well as by intentionally smearing the experimental data in a gaussian manner. The study supported the values for the quoted errors on the multipole intensities. The notation of reference 53 is adopted in describing the dipole-quadrupole mixing in (5-1b) and (5-1c):

D pure dipole, $a_2(a_2') = 0$

Q pure quadrupole, $a_2(a_2')=1$

D+Q equal mixture with positive sign, $a_2(a_2') = +1/\sqrt{2}$

D-Q equal mixture with negative sign, $a_2(a_2') = -1/\sqrt{2}$

---

[57]An acceptance correction to the data creates difficulty in the handling of empty bins.

TABLE 5-1

HYPOTHESIS	CONFIDENCE LEVEL	a_2'	a_2
$\chi(3.51)$ data:			
$J_x=1$	0.13	$+(0.077\ {}^{+0.050}_{-0.045})$	$-(0.002\ {}^{+0.020}_{-0.008})$
$J_x=2$	0.02		
$J_x=0$	$<10^{-6}$		
$\chi(3.55)$ data:			
$J_x=2$	0.11	$+(0.132\ {}^{+0.098}_{-0.075})$	$-(0.333\ {}^{+0.292}_{-0.116})$
$J_x=1$	0.01		
$J_x=0$	5×10^{-4}		

Plots of the likelihood function and its logarithm, for the optimal spin assignments, are shown in figures 5-3 and 5-4. The normalization of the multipole amplitudes limits the range of a_2 (or a_2') to $[-1 \rightarrow +1]$ (an overall sign of ±1 is is contained in the quadrupole amplitude). Likelihood products for large data samples behave gaussianly in the region of peaks; it is therefore informative to plot contours of the likelihood function at $L_{max}\cdot\exp(-n^2/2)$ intervals, with each level below the main peak representing a successive 1σ departure from optimization. These contour levels form the grids in figures 5-3 and 5-4; the contour maps are shown in figure 5-5. The apparent degeneracy (the main peak is actually preferred by 5σ) in the log-likelihood plot for spin 1 is due to the viewing angle of the pictorial representation.

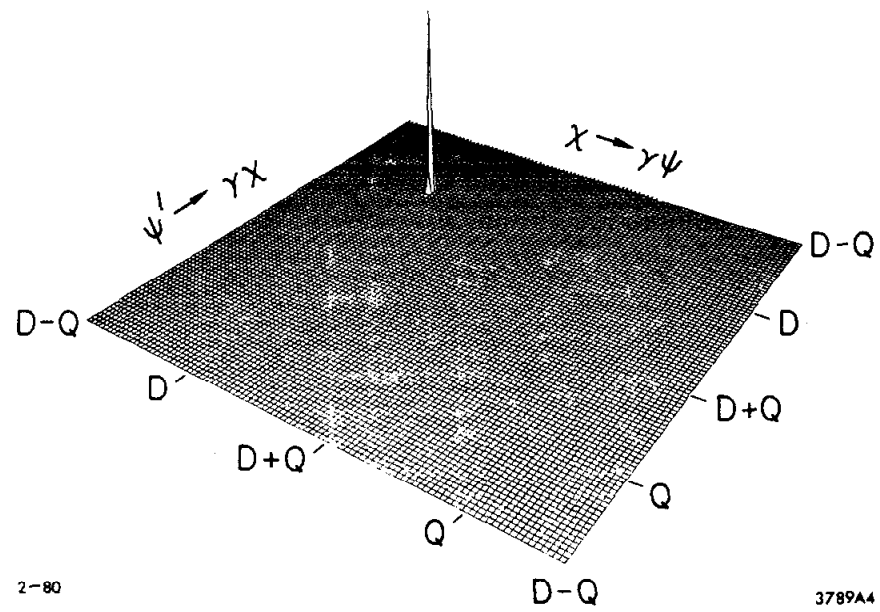

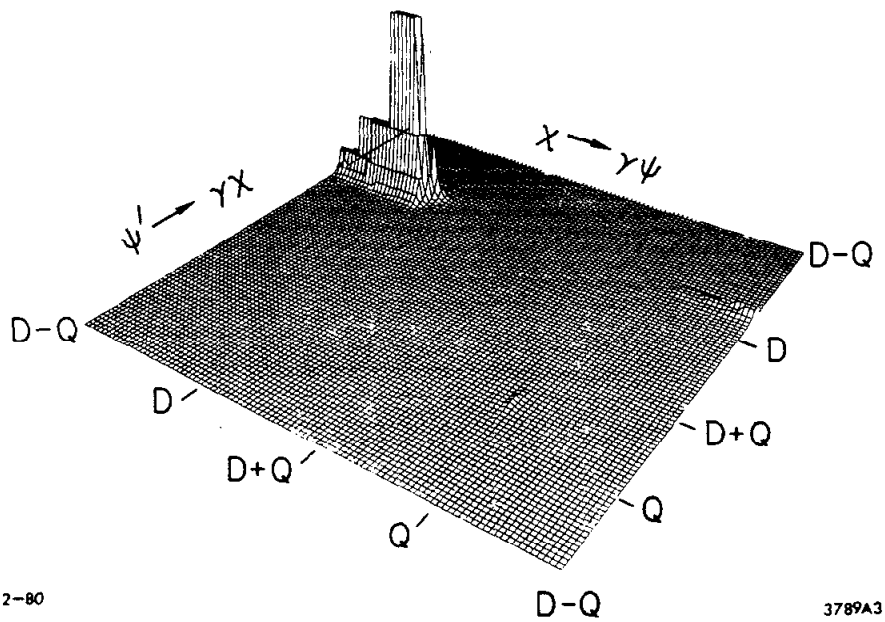

FIG..5-3 Likelihood function. Upper figure is $\chi(3.51)$ data and J=1 hypothesis. Lower figure is $\chi(3.55)$ data and J=2 hypothesis. Vertical contours are plotted at gaussian deviations from the maximum value (see text).

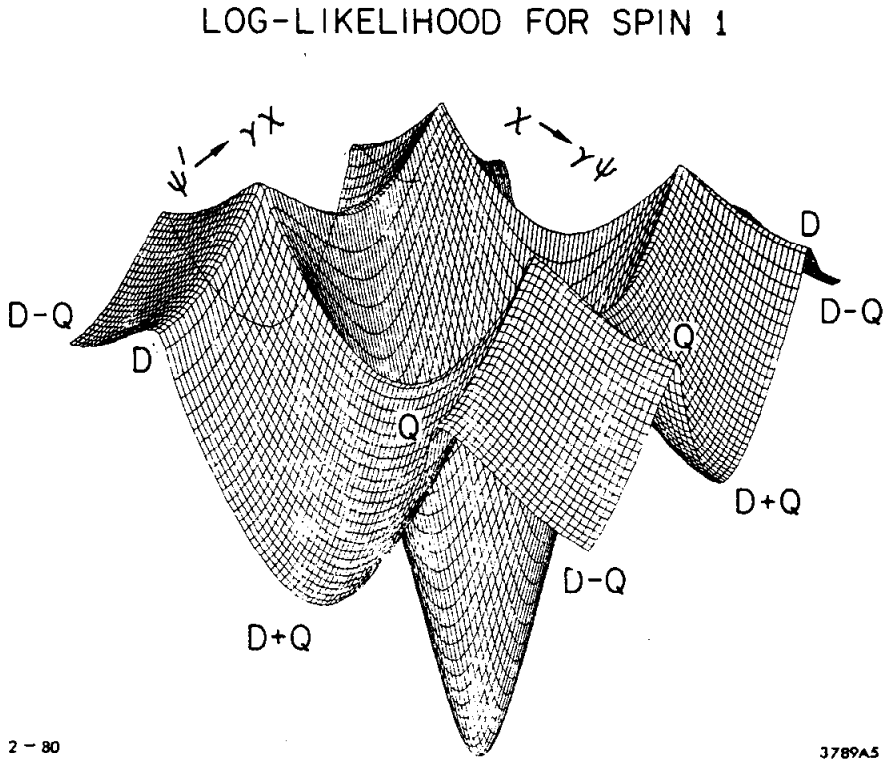

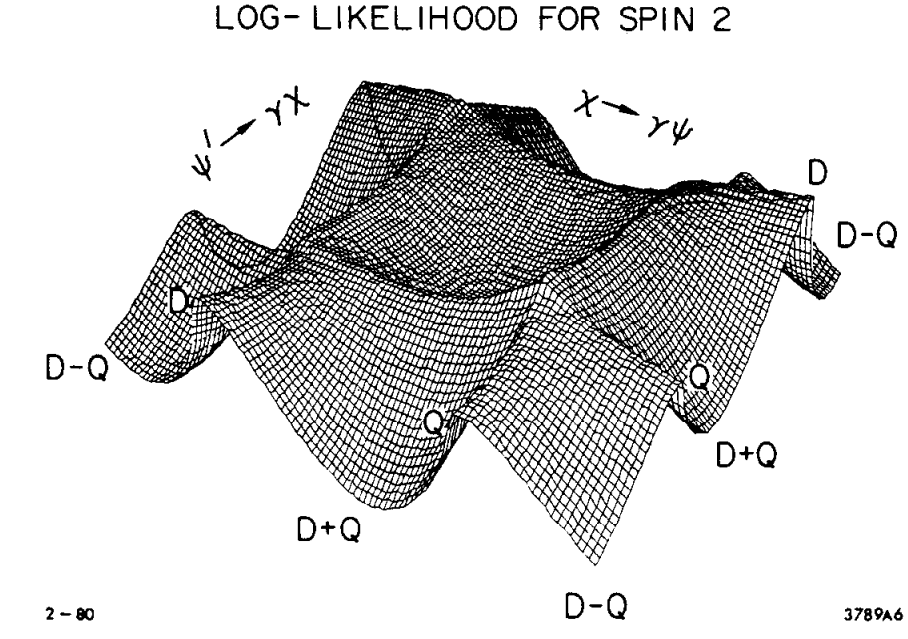

FIG..5-4 Logarithm of the likelihood functions in figure 5-3.

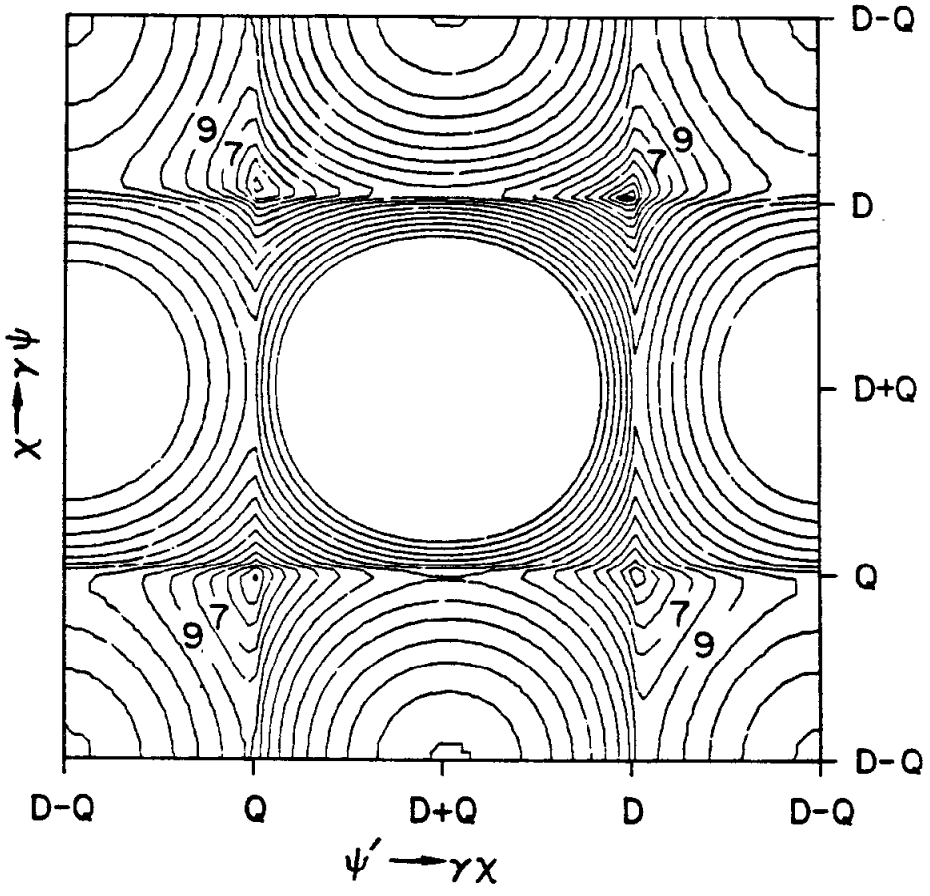

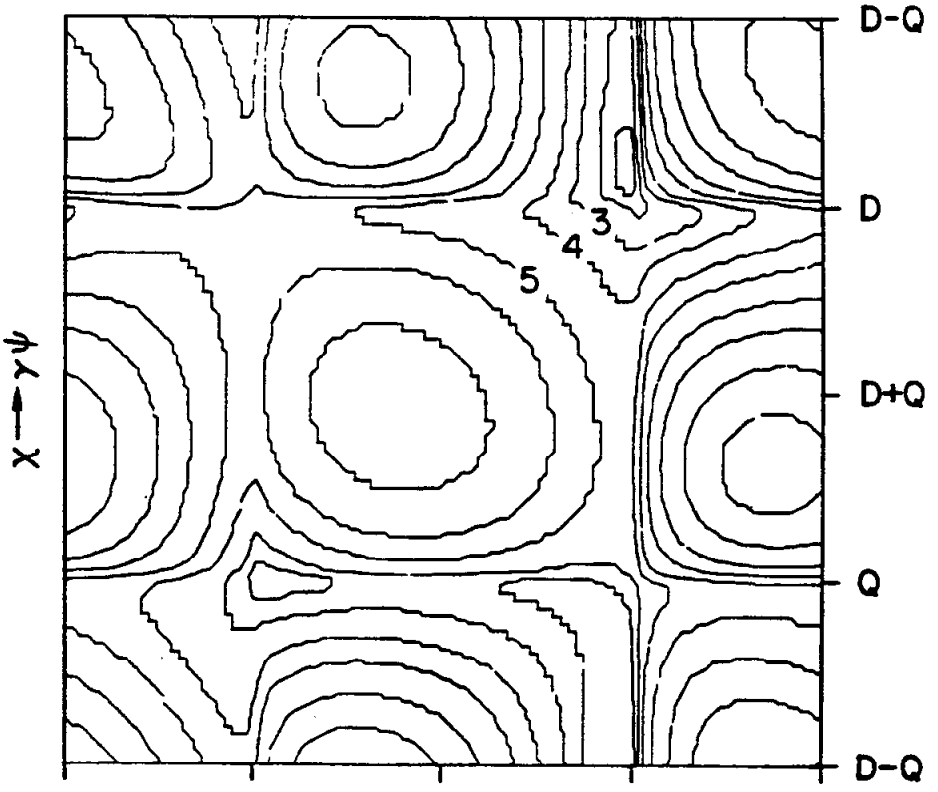

FIG..5-5 Contour levels indicated in figure 5-3. Contour 0 is taken at the maximum value of L.

5.5 CONCLUSIONS

Examination of the hadronic decay modes of the χ states is required in order to determine their parity; it also furnishes some spin information. In particular, it is observed that $\chi(3.55)$ and $\chi(3.41)$ decay frequently into $\pi^+\pi^-$ and K^+K^- while $\chi(3.51)$ does not.[58] Since both these decay products are pseudoscalar ($J^P=0^-$), one concludes that $\chi(3.55)$ and $\chi(3.41)$ have $J^{PC}=0^{++},(1^{--})$, or 2^{++}. The negative C-parity candidate must be eliminated since χ states are created along with a single photon from the ψ' decay. Failure of the $\chi(3.51)$ to decay into two pseudoscalars suggests an unnatural spin-parity $(0^-,1^+,2^-)$. Furthermore, this χ state is observed to decay into $\pi^+K^-K_s$[59] (three pseudoscalars) so 0^+ is not a possible assignment. The angular distribution of γ' is not compatible with $1+\cos^2\theta'$, eliminating 0^{-+} as a possible assignment. Thus 1^{++} and 2^{-+} are left as possibilities for the J^{PC} assignment for $\chi(3.51)$.

The hadron decay information is augmented by the evidence that $\chi(3.41)$ has an angular distribution behaving like spin 0 $(1+\cos^2\theta')$ while the other states do not appear to.[60] One can therefore summarize the previous knowledge of the χ quantum numbers:

---

[58] Reference 53

[59] Reference 44

[60] Reference 53

$\chi(3.55) \sim (0^{++}$ unlikely) 2^{++}

$\chi(3.51) \sim 1^{++}, 2^{-+}$

$\chi(3.41) \sim 0^{++}$

Information from the cascade analysis is necessary in order to assign spin values for the two higher mass states.[61] Only one previous experiment has reported a spin analysis using the cascade reaction,[62] and in fact only $\chi(3.51)$ was considered because of a small data sample. The earlier investigation did report a dipole-dominant multipole configuration for the hypothesis of spin 1; however, the overall maximum likelihood solution favored spin 2 by only 1.5σ.

The data from the analysis in this new study yield high confidence levels for the spin and multipole assignments preferred in the standard charmonium model; spin 2 for $\chi(3.51)$ is ruled out. Using the results of Table 5-1, the status of the spin-parity assignments for the χ states may be summarized[63] as:

$\chi(3.55) \sim 2^{++}$, -- 0^{++} ruled out at 6.3 σ level

$\chi(3.51) \sim 1^{++}$, -- 2^{-+} ruled out at 5.7 σ level

---

[61] An angular distribution of $1+\cos^2\theta$ for $\chi(3.55)$ has been rejected at less than a 2σ level.

[62] Reference 53.

[63] The significance of the fits are given in terms of gaussian σ: $n = \sqrt{2}(\ln[L_{max}/L])$.

Chapter VI

CONCLUSIONS

6.1 THE CHARMONIUM MODEL

Qualitative agreement between the standard charmonium model[1] and the experimentally observed psionium states is good. The 1^3P_{012} states have all been identified and lie in the expected mass region. A comparison of the branching ratios determined in this experiment with earlier values can be found in Table 6-1.

TABLE 6-1

STATE (MeV/c^2)[67]	Crystal Ball	Mark-II[64]	Mark-I[65]	DESY-Heidelberg[66]
		$BR(\psi' \to \gamma\gamma\psi)$ (%)		
χ(3553.9±0.5)*	1.26±0.22	1.1±0.3	1.0±0.6	1.0±0.2
χ(3508.4±0.4)*	2.38±0.16	2.4±0.6	2.4±0.8	2.5±0.4
χ(3412.9±0.6)†	0.06±0.02	< 0.56	0.2±0.2	0.14±0.09
χ(3455)	< 0.02	< 0.13	0.8±0.4	< 0.25
χ(3591)	< 0.04	------	-------	0.18±0.06
		$BR(\psi' \to m\psi)$ (%)		
η	2.18±0.38	2.5±0.6	4.3±0.8	3.6±0.5
π^0	0.09±0.03	0.15±0.06	-----	-------

---

[64]T.M. Himel et al., Phys. Rev. Lett. 44, 920 (1980).

[65]J. Whitaker et al., Phys. Rev. Lett. 37, 1596 (1976).

[66]W. Bartel et al., Phys. Lett. 79B, 492 (1978).

The two candidates for the 2^1S_0, which had masses much too low to fit easily into the model, have not been confirmed in this sensitive experiment. Models for the hyperfine splitting are discussed later and predict[68] a 2^1S_0 mass of 3616 MeV/c^2, with a cascade branching ratio less than 2×10^{-5} provided that 2978 MeV/c^2 is the correct 1^1S_0 mass.[5] This cascade branching ratio is an order of magnitude below the sensitivity of the experiment.

Initially a phenomenological $c\bar{c}$ potential of the form $V(r) = -kr + r/a^2$ [69] was used to describe the charmonium system. Using the 1^3S_1, 2^3S_1 and 1^3P_j masses as input parameters, models with either linear or logarithmic confining terms give an average quark velocity of $\langle\beta^2(1^3S_1)\rangle \simeq 0.14$ and $\langle\beta^2(2^3S_1)\rangle \simeq 0.25$, thus supporting the non-relativistic treatment.[70] A beautiful form for the potential with better predictive power is due to Richardson.[71] Here one observes that the potential, in momentum space, should have Coulombic properties at short distances, while the long distance confinement is suggested by the form of the running coupling constant α_s:

---

[67] C.B. ~ *, Mark-II ~ †; there is an additional 4 MeV/c^2 error on all the masses.

[68] C. Quigg in Proc. 1979 Int. Symp. on Lepton and Photon Interaction at High Energy, Batavia, Illinois, ed. by T. Kirk and H. Abarbanel, p. 239 (1979).

[69] J. Kang and H. Schnitzer, Phys. Rev. D12, 841 (1975); E. Eichten et al., Phys. Rev. Lett. 34, 369 (1975); B. Harrington et al., Phys. Rev. Lett. 34, 706 (1975); J. Kogut and L. Susskind, Phys. Rev. Lett. 34, 767 (1975); R. Barbieri et al., Nucl. Phys. B105, 125 (1976).

[70] E. Eichten et al., Phys. Rev. D17, 3090 (1978).

[71] J.L. Richardson, Phys. Lett. 82B 272 (1979).

$$V(q^2) = \frac{\alpha_s(q^2)}{q^2} = \frac{4\pi\ \alpha_s(\Lambda^2)}{1+(11-2N_f/3)\ \alpha_s(\Lambda^2)\ \ln(q^2/\Lambda^2)} \qquad (6\text{-}1)$$

where N_f is the number of quark flavors. Consequently, the potential has the form

$$V(r) = \begin{cases} r \to \infty & \\ r \to 0 & \frac{1}{r\ \ln(\Lambda r)} \end{cases} \qquad (6\text{-}2)$$

Using only the 1^3S_1 and 2^3S_1 masses as input parameters, this model predicts the center-of-gravity[72] of the 1^3P states to be 419 MeV/c^2 above the ψ mass, compared to our experimentally observed value of (428.1±0.4) MeV/c^2.

6.2 FINE STRUCTURE AND THE ANOMALOUS MAGNETIC MOMENT

Fine structure in the ^3P_j states is not straightforward to model since the Lorentz structure of the spin interactions at large distances remains unknown for heavy $q\bar{q}$ systems. Formalisms stemming from lattice gauge models[73] produce spin dependent forces which are exponetially damped at large distances; a first-order Bethe-Salpeter expansion[74] leads to forces which diminish less rapidly with increasing r. Schnitzer[75] has calculated the spin-dependent (Breit-Fermi) Hamiltonian

---

[72]This is defined as COG = $(1/9)\cdot\sum_J((2J+1)\cdot Mj) - M(1^3S_1)$.

[73]K. Wilson, Phys. Rev. D10, 2445 (1974); J. Kogut and L. Susskind, Phys. Rev. D11, 395 (1975).

[74]H. Schnitzer, Phys. Rev. D13, 74 (1976).

[75]H. Schnitzer, Phys. Lett. 65B, 239 (1976).

for Lorentz 4-vector structure of the spin forces, incorporating a possible c-quark anomalous magnetic moment.[76]

$$H = H_0 + V(r) \qquad (6\text{-}3)$$

$$+ \frac{3+2\kappa}{2m^2}\,\frac{1}{r}\,\frac{dV(r)}{dr}\,\vec{L}\cdot\vec{S} \qquad \text{spin-orbit}$$

$$+ \frac{(1+\kappa)^2}{6m^2}\,\vec{\sigma}_1\cdot\vec{\sigma}_2\,\nabla^2V(r) \qquad \text{Breit-Fermi}$$

$$+ \frac{(1+\kappa)^2}{12m^2}\,[3\vec{\sigma_1}\cdot\hat{r}\vec{\sigma_2}\cdot\hat{r}-\vec{\sigma_1}\cdot\vec{\sigma_2}]\,\frac{d^2V(r)}{dr^2} - \frac{1}{r}\,\frac{dV(r)}{dr} \qquad \text{tensor}$$

The labels 1 and 2 refer to the quarks, and the quark mass is taken to be $m=1.84\ \mathrm{GeV}/c^2$.[77] This Hamiltonian is compared to data by means of the mass ratio

$$R_1 \equiv \frac{M(1^3P_2) - M(1^3P_1)}{M(1^3P_1) - M(1^3P_0)}\ , \quad R_{1\,exp} = 0.48\pm0.01 \qquad (6\text{-}4)$$

For $\kappa=0$ the pure $\vec{L}\cdot\vec{S}$ term in H gives $R_1=2$, while the tensor force gives $R_1=-2/5$.[78] It is conceivable that κ is small at short distances, growing with r so as to shield μ at large distance. For this reason Schnitzer has calculated R_1 using (6-3) and only the linear potential to obtain:

$$R_{1\,lin} = \frac{1}{5}\,\frac{14 + 8\kappa - \kappa^2}{2 + 2\kappa + \kappa^2/2} \qquad (6\text{-}5)$$

In order to agree with the experimental value, $\kappa = -1.4$ or $+2.8$.

---

[76]The anomaly is defined to be κ in the formula $\mu=\mu_{dirac}(1+\kappa)$.

[77]E. Eichten et al., Phys. Rev. D21, 203 (1980).

[78]Reference 68

Henriques et al.[79] obtain a value $R_1=1/2$ in a model with no anomalous magnetic moment. In this calculation both the Coulombic and long-range linear parts of the potential are used to obtain 1^3P_{012} masses of 3.42, 3.50 and 3.54 GeV/c^2; the potential is damped by a factor of exp(-r), which possibly mimics shielding of the linear confining potential by qq pairs. The success of this model strongly supports the notion that κ is small.

Using a similar Hamiltonian, Karl, Meshkov, and Rosner[80] have calculated the effect of κ on the multipole coefficients for the $^3S_1$-^3P_j radiative transitions. In the notation of chapter V the quadrupole M2 amplitudes are given by:

$$a_2 \simeq \xi \frac{E_\gamma}{4m}(1+\kappa)\begin{bmatrix}\sqrt{9/5}, & J=2\\ 1, & J-1\end{bmatrix} \qquad (6\text{-}6)$$

where ξ=-(+) for $2^3S_1\rightarrow\gamma 1^3P_j$($1^3P_j\rightarrow\gamma 1^3S_1$). This calculation was performed retaining only terms to order E_γ/m in the Hamiltonian and using the lowest order multipoles in the expansion of $\exp(i\vec{k}\cdot\vec{r})$. For the radiative transitions kr ranges from 0.3 to 1.2[81] and thus one must be wary of the retardation effects; the next higher order retardation term is of order $(kr)^2/40$.[82] Retardation effects thus create an estimated 10% uncertainty

---

[79]A. Henriques et al., Phys. Lett. 64B, 85 (1976).

[80]G. Karl, S. Meshkov and J. Rosner, Phys. Rev. Lett. 45, 215 (1980).

[81]K. Gottfried, preprint CLNS 80/465 (Cornell) (1980).

[82]See, for instance, V. Novikov et al., Phys. Rep. 41, 1 (1978).

[83]I thank R. McClary and N. Byers for pointing this out to me.

in formula (6-6). Using the virial theorem,[83] $E_\gamma/m = (E_f-E_i)/m = v^2$, where v is the average quark velocity in the charmonium center-of-mass frame. The expansion parameter is therefore of the same order as the relativistic corrections which have been neglected in the calculation. In addition, there is the uncertainty due to the use of Lorentz 4-vector structure for the spin interactions. With these caveats in mind, the predicted value of κ for this model is obtained using the values for a_2 obtained in chapter V. The likelihood plots of $1+\kappa$ obtained from the two 1^3P_{12} cascades are shown in figure 6-1; χ^2 on these plots is obtained from a likelihood function which is distributed like the Pearson χ^2 and is valid for the statistics of this analysis (see appendix I). The smaller statistics sample of 1^3P_2 cascades has a shallow minimum which does not establish κ well but is consistent with the value obtained from the higher statistics 1^3P_1 cascade. Using only the latter cascade sample, a value of

$$\kappa_{exp} = \begin{matrix} +0.72 \\ -0.07 \\ -0.63 \end{matrix} \qquad (6\text{-}7)$$

is obtained for κ. This value for κ supports the Henriques picture which emphasizes the effect of the Coulombic part of the potential.

When the retardation, relativistic, and ψ'' mixing corrections are applied to Karl, Meshkov, and Rosner's formula for the rates, Byers and McClary have determined that the correction can be quite large. A cor-

---

[84] R. McClary and N. Byers, preprint UCLA/80/TEP/20 (UCLA) (1980); and a private communication.

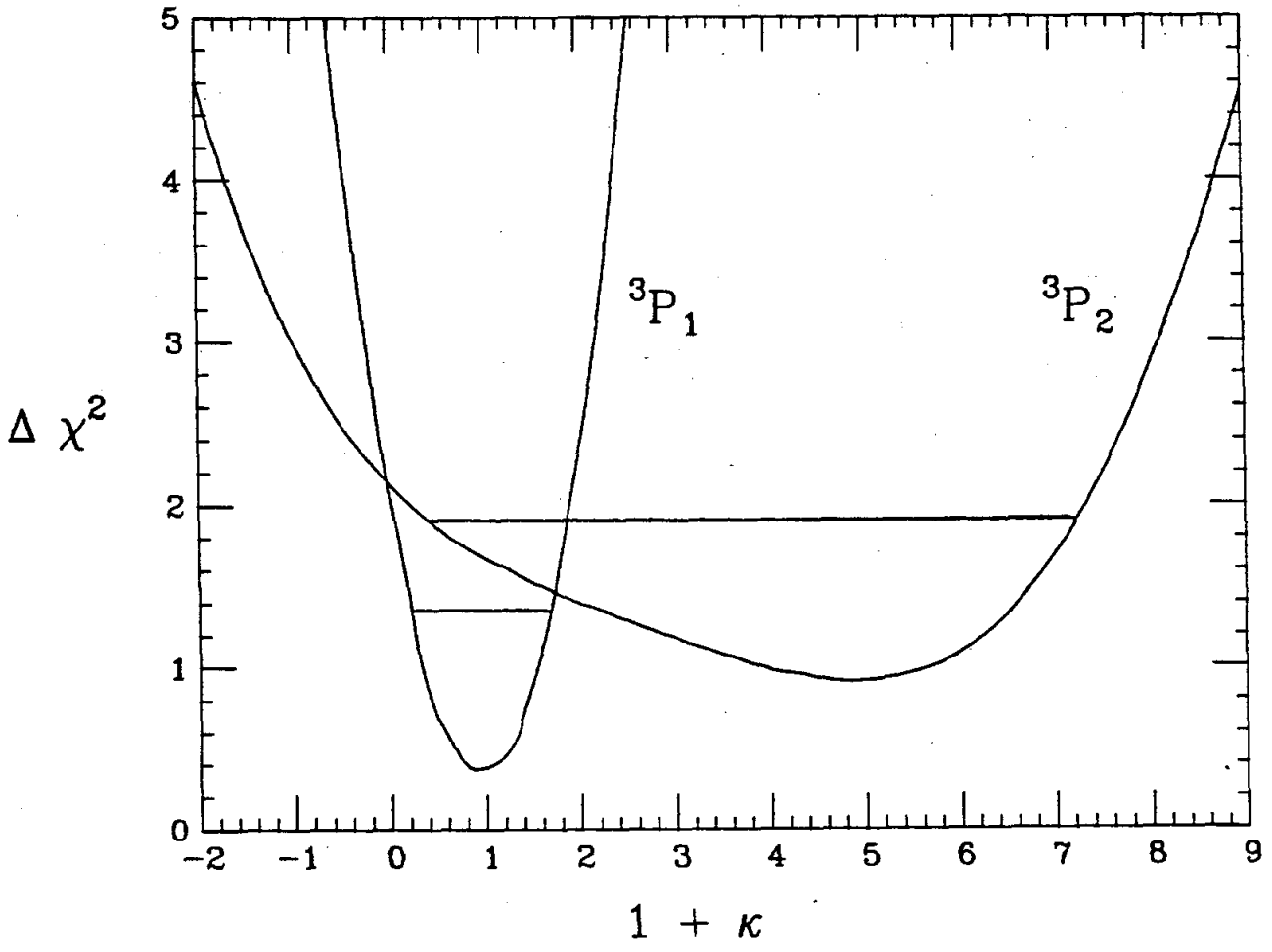

FIG..6-1 Confidence level for fit of x data to the Karl, Meshkov, and Rosner formula for the anomalous magnetic moment. Horizontal bars are the one standard deviation zones.

rected formula[84] for κ shown in equation (6-8) still suffers uncertainty due to the ψ'-ψ'' mixing angle θ_m.

$$a_2 \simeq \xi\epsilon \begin{bmatrix}\sqrt{9/5}\\ 1\end{bmatrix} \frac{(1+\kappa) \pm A \begin{bmatrix}1+2\kappa\\ 1+4\kappa\end{bmatrix}}{1 \pm \xi\epsilon(\alpha+\kappa)+\begin{bmatrix}-1\\ 5\end{bmatrix}A} \qquad (6\text{-}8)$$

$$\text{for } J = \begin{bmatrix}2\\ 1\end{bmatrix}, \quad \epsilon = \frac{E_\gamma}{4m}, \quad A = \frac{\sqrt{2}}{10}\tan\theta_m \frac{\langle 1P|r|1D\rangle}{\langle 1P|r|2S\rangle}$$

In the above formula the spin interaction potential is characterized by α, which assumes the value -1 for a scalar potential, +1 for a pure Coulombic potential, and +3 for a pure Coulombic potential with exchange of transverse gluons (see McClary and Byers). Using a "global" fit to the charmonium rates, a value of θ_m=-1.7° is obtained in reference 77, although an upper limit on the magnitude of 23° has been reported.[85] The ratio of overlap integrals in (6-8) is of order unity; therefore, a plausible limit on the magnitude of A can be placed at $A<0.02$, implying about a 30% overall uncertainty on the value of $1+\kappa$ obtained using (6-6). Within the uncertainties, at least a loose bound on κ is realized. Mixing effects of the ψ'' are most pronounced in the rates for $\psi'\to\gamma\chi$, so that an eventual determination of the mixing angle is possible.

---

[85] H. Yamamoto et al., Prog. Theor. Phys. 58, 374 (1977), and 59, 2151 (1978).

6.3 TRANSITION RATES

Electric dipole transition rates are given by

$$\Gamma(^3S_1 \to ^3P_j) = \frac{4}{27}(2J_f+1)\left(\frac{2}{3}\right)^2 \alpha E_\gamma^3 \int_0^\infty r^2 \Psi_i(r)\Psi_f(r)\, dr \qquad (6\text{-}9)$$

There are several corrections to this formula: 1) Retardation effects incurred by approximating $j_0(kr)=1$ are on the order of $(kr)^2/40$ -- less than 4%; 2) There is mixing of the charmonium wave functions (coupling of channels) -- this correction, which reduces the widths, has been calculated for the ^3S-^3P decays; 3) The gluon distributions in the initial and final states differ, thereby reducing the value of the overlap integral[86] ; 4) Relativistic (recoil) effects are as large as 20%[87] ; 5) The Richardson wave functions have not been used to compute the overlap integrals -- since his potential is softer than $1/r$ near the origin, $|\Psi(0)|_r < |\Psi(0)|$ and $|\Psi'(0)|_r > |\Psi'(0)|$.

Rates calculated using the E1 integral are therefore uncertain within a factor of about 1.5. The coupled channel corrections for the initial rates are[88] 43:34:24 KeV for 1^3P_{012}, compared to measured widths in the range of 11 to 30 KeV.[89] Such measured values agree with the E1 predictions within the estimated 50% uncertainty.

---

[86] T. Appelquist et al., Ann. Rev. Nucl. Part. Sci. 28, (1978).

[87] M. Krammer and H. Krasemann, preprint DESY 79/20 (DESY) (1979).

[88] Reference 77

[89] These widths, as determined from the inclusive photon spectrum, are measured differently for various assumptions about the shape of the background. Work on this problem continues.

This experiment can be used to compare the predictions for ALF $\equiv \Gamma(2^3S_1 \rightarrow \gamma 1^3P_j) \cdot \Gamma(1^3P_j \rightarrow \gamma 1^3S_1)$ with the measured quantities $BR(2^3S_1 \rightarrow \gamma 1^3P_j \rightarrow \gamma\gamma 1^3S_1) \cdot \Gamma(2^3S_1) \cdot \Gamma(1^3P_j)$. For the ψ' width we use (228±56) KeV[90] ; the χ widths for the 1^3P_2 and 1^3P_1 (upper limit) are measured in this experiment. A width for the 1^3P_0 state of (7±3) MeV as measured in the ψ' inclusive photon spectrum has been reported,[91] although these inclusive studies[92] now support a slightly larger width of about 10 MeV. In Table 6-2 the coupled channel corrected E1 theoretical values for ALF are compared to the values obtained from experiment.

TABLE 6-2

STATE	$\Gamma(X \rightarrow all)$ (KeV)	ALF_{exp} $(KeV)^2 \times 10^2$	ALF_{th}
1^3P_0	~10±3	16±7	56
1^3P_1	<2	<108	87
1^3P_2	4±1	115±41	84

The 1^3P_{12} measured values support the theoretical predictions; however, the 1^3P_0 state appears to have a smaller E1 width than calculated.

Another method for comparing the observed radiative rates with the charmonium model utilizes the dipole sum rules, which have been calcu-

---

[90] V. Lüth et al., Phys. Rev. Lett. 35, 1124 (1975).

[91] T. Burnett at the Conf. on Color, Flavor and Unification, Irvine, California, 1979 (unpublished.)

[92] J. Gaiser, in a private communication.

[93] J. D. Jackson, Phys. Lett. 87B, 106 (1979).

lated for the Breit-Fermi Hamiltonian (6-3) by Jackson.[93] Dipole sum rules, which are derived from the charmonium Hamiltonian by invoking the uncertainty principal $[p,x]=-i$, are of two types; the Thomas-Reiche-Kuhn (TMK) sum rule provides only upper bounds for the E1 rates, while the Wigner-Kirkwood (WK) sum rule can provide both upper and lower bounds, though not in all cases. The sum rules applicable to this experiment are listed in equation (6-10).

$$\text{TRK: } \Gamma(1^3P_j\to\gamma\psi) < \frac{4}{3}\frac{\alpha}{m}\left(\frac{2}{3}\right)^2 E_\gamma^2 \left(1 + \frac{2}{3}x_s\langle\vec{L}\cdot\vec{S}\rangle\right)$$

$$\text{WK: } \Gamma(1^3P_2\to\gamma\psi) > \frac{2\alpha}{5m}\left(\frac{2}{3}\right)^2 E_\gamma^2 \left(1+\frac{12}{5}x_p\right) + \frac{3}{5}\frac{E_\gamma}{E_{\gamma'}}\,\Gamma(\psi'\to\gamma'1^3P_2) \qquad (6\text{-}10)$$

$$\text{where } \langle\vec{L}\cdot\vec{S}\rangle = \begin{bmatrix} 1\,, & J=2 \\ -1\,, & J=1 \\ -2\,, & J=0 \end{bmatrix} \text{ and } x_s(x_p) = \frac{m}{2\hbar^2}\cdot\langle{}^3S({}^3P)\left|r\,\frac{dV}{dr}\right|{}^3S({}^3P)\rangle$$

Uncertainties in the charmonium model affect the sum rules by means of the matrix elements x_s and x_p. These matrix elements have absolute bounds of $0<x_s<0.75$ and $-2.5<x_p<1.25$; however, studies of typical potentials lead to plausible bounds of $0.10<x_s<0.18$ and $0.05<x_p<0.15$. In calculating plausible bounds the values $x_s>0.10$ and $x_p>0$ are used.

The WK sum rule provides a useable lower bound only for J=2. Uncertainties in this rule are minimized by using a value for $\Gamma(2^3S_1\to\gamma1^3P_2)$ derived from experiment; a comfortable lower bound is $0.04\cdot228=9$ KeV, thus $\Gamma(1^3P_2\to\gamma\psi) > 191$ KeV (plausibly). Using $\Gamma(\psi'\to\gamma1^3P_j) < 37$ KeV, one obtains the dipole sum rule results listed in Table 6-3.

TABLE 6-3

STATE	$\Gamma(1^3P_j \to \gamma\psi)$TRK (KeV)		$\Gamma(\psi' \to \gamma 1^3P_j)\cdot\Gamma(1^3P_j \to \gamma\psi)$TRK,WK $(KeV)^2 \cdot 10^2$	
	ABSOLUTE	PLAUSIBLE	PLAUSIBLE	EXPERIMENT
1^3P_2	< 649	< 461	$17 < < 171$	16±7
1^3P_1	< 356	< 332	< 123	< 108
1^3P_0	< 262	< 227	< 84	115±41

6.4 THE η AND π^0 DECAYS

The decays $\psi' \to \eta\psi$ and $\psi' \to \pi^0\psi$ are both observed to be somewhat peculiar in that the former has an unexpectedly high rate and the latter is forbidden by isospin symmetry. To understand why the η rate is too large one must consider the dominant decay $\psi' \to \pi\pi\psi$ which has a branching ratio of 50%, and the gluon coupling assumed to be responsible for the decay, shown in figure 6-2. The measurement of the η decay is described in chapter IV; this measurement gives $\Gamma(\psi' \to \eta\psi)/\Gamma(\psi' \to \pi\pi\psi) = 4\%$. Such a level of η suppression relative to $\pi\pi$ is explainable simply from the phase space factor (the η has only 197 MeV/c momentum) and the angular momentum barrier incurred by the P-wave nature of the decay. However, the $^3S_1$ states are singlet members of a meson nonet, whereas the physical η is about 90% octet. Therefore, one would expect an extra suppression of the η decay by a factor $\sin^2(\theta_{mix})=0.01$; the decay rate thus appears to be about 100 times larger than expected.

Two solutions lend themselves to this dilemma. One can assume that the physical η has a $c\bar{c}$ component, thus avoiding the OZI suppression of the decay. Such models[94] are capable of explaining the large rates for

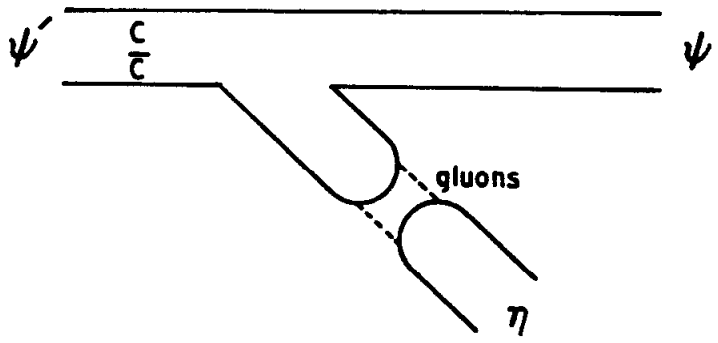

FIG..6-2

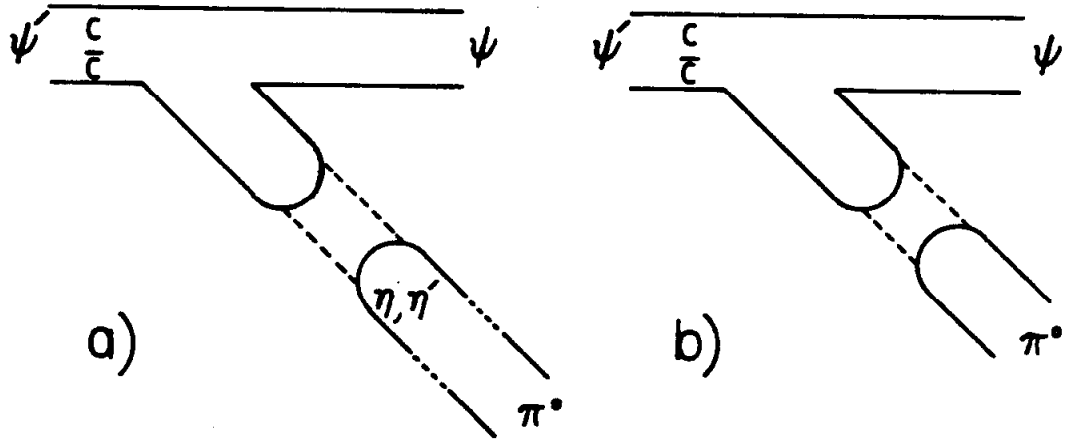

FIG..6-3

$\psi' \to \eta\psi$ and $\psi \to \gamma(\eta/\eta')$. Alternately, Goldberg[95] finds that the η couples strongly to gluons; thus, if the $\pi\pi$ and η decays are indeed of the form $\psi' \to gg\psi$, $gg \to \pi\pi$ or η, the OZI suppression is overcome by the strong gluon couplings. This model is also successful in explaining the $\psi' \to \eta\psi$ and $\psi \to \gamma(\eta/\eta')$ rates.

Citing early evidence (such as the decays $\eta \to 3\pi$) that strong isospin is broken at some level, Segre and Wyers[96] first suggested that the η in figure 6-2 can convert into a physical π^0 by means of π-η mixing (SU(2) breaking), thus permitting the decay $\psi' \to \pi^0\psi$. More recent work has revealed that the decay is augmented by contributions from a virtual η'[97] and a direct π^0 coupling[98]; in the last two years several models for the isospin violating decay have appeared.[99] The most reasonable graphs describing the decay are shown in figure 6-3.

The mixing amplitudes for π^0-η-η' can be derived from constituent

---

[94]H. Harari, Phys. Lett. 60B, 172 (1975); H. Fritzsch and J. D. Jackson, Phys. Lett. 66B, 365 (1977).

[95]H. Goldberg, Phys. Rev. Lett. 44, 363 (1980).

[96]G. Segre and J. Weyers, Phys. Lett. 62B, 91 (1976).

[97]H. Genz, Lett. Nuovo Cim. 21, 270 (1978).

[98]P. Langacker, Phys. Lett. 90B, 447 (1980).

[99]N. Deshpande and E. Ma, Phys. Lett. 69B, 343 (1977); R. Bhandari and L. Wolfenstein, Phys. Rev. D 17, 1852 (1978); N. Isgur et al., Phys. Lett. 89B, 79 (1979); T. Pham, Ecole Polytechnique preprint PRINT 80-0330 (1980);

[100]N. Isgur, Phys. Rev. D12, 3720 (1979); N. Isgur et al., Phys. Lett. 89B, 79 (1979).

quark models,[100] or by considering the u-d quark mass splitting (obtained from a study of baryon mass splittings), the ρ-ω mixing and the decay $\eta \to 3\pi$.[101] To test these models the experimentally observed quantities

$$R \equiv \frac{BR(\psi \to \pi^0 \psi)}{BR(\psi' \to \eta \psi)} = (41 \pm 8) \times 10^{-3} \qquad (6\text{-}11)$$

$$r \equiv \frac{BR(\psi \to \eta' \gamma)}{BR(\psi \to \eta \gamma)} = 5.88 \pm 1.46 \ [102]$$

can be used. The study by Langacker indicates that the direct π^0 coupling is required in order for the theory to compare well with experiment. In his model, $R=(40\pm12)\times10^{-3}$, $r=5.0$, $g_{\eta'}/g_{\eta}=2.5$ and $g_{\pi}/g_{\eta}=0.022$.

A recent work by Ioffe and Shifman[103] uses only the QCD Lagrangian to obtain

$$R = 3\left(\frac{m_d - m_u}{m_d + m_u}\right)^2 \left(\frac{m_\pi}{m_\eta}\right)^4 \left(\frac{p_\pi}{p_\eta}\right)^3 \qquad (6\text{-}12)$$

with a value of 35×10^{-3} when Langacker's u/d quark mass splitting is used. This formula, when compared to the data, clearly implies that m_u cannot be 0.

Figure 6-4 demonstrates how the π^0 decay can occur electromagneti-

---

[101] Reference 98.

[102] R. Partridge et al., Phys. Rev. Lett. 44, 712 (1980).

[103] B.L. Ioffe and M.A. Shifman, preprint ITEP-53 (Moscow) (1980).

[104] D. Sutherland, Phys. Lett. 23, 384 (1966).

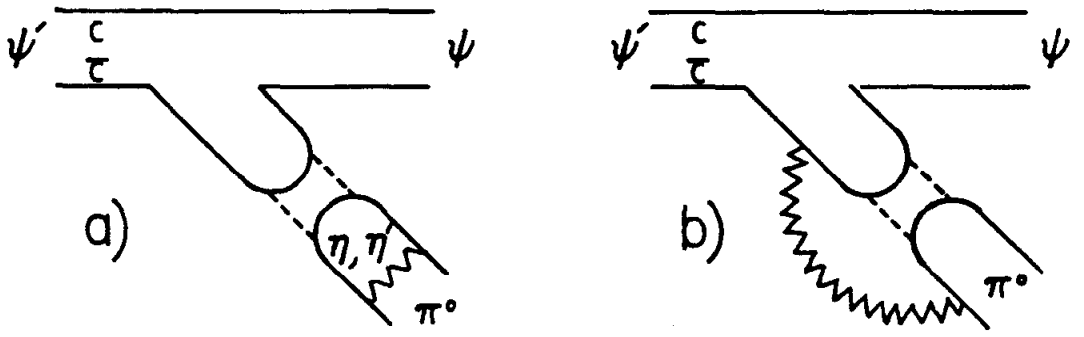

FIG..6-4

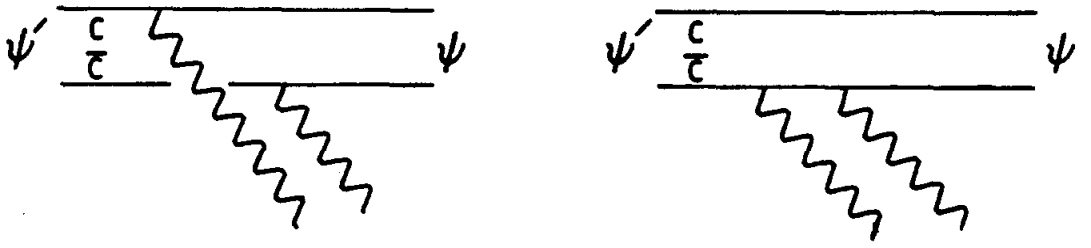

FIG..6-5

cally without violation of isospin symmetry. Using PCAC arguments,[104] graph 6-4a should be of order $\alpha^2(m_\pi/m_\eta)^2$; this argument has been proven in the $\eta\to3\pi$ decays. Contribution to the observed π^o decay from figure 6-4a then gives $R=10^{-4}$, well below the SU(2)-breaking contribution. The process in figure 6-4b violates C-parity and is therefore no problem.

6.5 DIRECT $\psi'\to\gamma\gamma\psi$

The direct decay $\psi'\to\gamma\gamma\psi$ by way of the graphs shown in figure 6-5 has been studied by Pelaquier and Renard.[105] They find that the braching ratio for the direct decay is less than 3×10^{-3}, but give no $\gamma\gamma$ mass structure for the decay. From the $\gamma\gamma\psi$ analysis in chapter IV, there are no events in the $\mu^+\mu^-$ final state Dalitz plot which cannot be attributed to the 1^3P_{012} states or π^o and η decay modes of the ψ'. A 90% C.L. upper limit on the direct decay branching ratio of 2×10^{-3} results for a uniformly distributed Dalitz plot.

---

[105] E. Pelaquier and F. Renard, Nuovo Cim. 32A, 421 (1976).

Appendix A

CONSTRUCTION DETAILS

In order to construct modules of high mechanical strength and to maximize the efficient use of the raw NaI(Tl) material, the individual Crystal Ball modules were rough cut from large (16 inch diameter, 20 inches long) blanks of polycrystalline[106] material. Polyscin blanks were obtained by forcing entire single-crystal NaI(Tl) ingots into a mold at high temperature and pressure; such a blank is referred to as a "fortrusion". The fortrusions were created in the shape of a large hexagonal pyramid from which 13 individual modules could be fashioned. A total of 56 of these blanks was required to construct the 672 necessary crystals used in both the hemispheres, with about 20 additional blanks required for the replacement of inferior or damaged modules. Typically the single-crystal grains in the fortrusions were rendered visible when the material was sanded, and had a boundary dimension of about 1 cm.

---

[106] This refers to the patented Harshaw Chemical Company product known as Polyscin; the fortrusion process used to produce Polyscin was developed by this company.

[107] The machining was performed in a normal environment, so that the crystals formed a layer of hydrate about 0.05 inches thick; the hydrate was removed with a solvent ("Dowenall") just prior to the compensation sanding.

The rough cut modules were milled[107] to provide units of 11 (slightly) different shapes; one such module is shown in figure A-1. Each milled unit was then hand-sanded ("compensated") so that the light received by the phototube at the large end of the crystal would be as independent as possible of the shower position in the module. A one-inch diameter area on the large end of the crystals was optically polished to permit inspection of the crystal's interior. Pieces of white reflector paper were then fit against each face of each crystal, followed by a sheath of aluminized material for the purpose of optically isolating each crystal from its neighbors. The wrapping scheme is depicted in figure A-2. Standard household aluminum foil was used to sheath crystals in the first hemisphere; however, it proved to wrinkle and tear easily. For this reason 0.003 inch thick aluminized mylar was employed during preparation of the crystals for the second hemisphere.

During construction each crystal was inspected for cracks, chipping, and internal impurities (occlusions or flock). Units having cracks extending more than 0.5 inches into the crystal were usually rejected; however, smaller cracks of typically 0.25 inches were impossible to avoid and did not impair the performance. Because of the polycrystalline nature of Polyscin, cracks of a smaller dimension than the grain size tended not to propagate further into the crystal. After the visual inspection, each wrapped crystal was placed on a test jig which approximated the air-gap/phototube arrangement. Resolution for the 0.66 MeV line from ^{137}Cs was then measured and required to be less than 15% (FWHM) for all crystals except the specially trimmed crystals used near

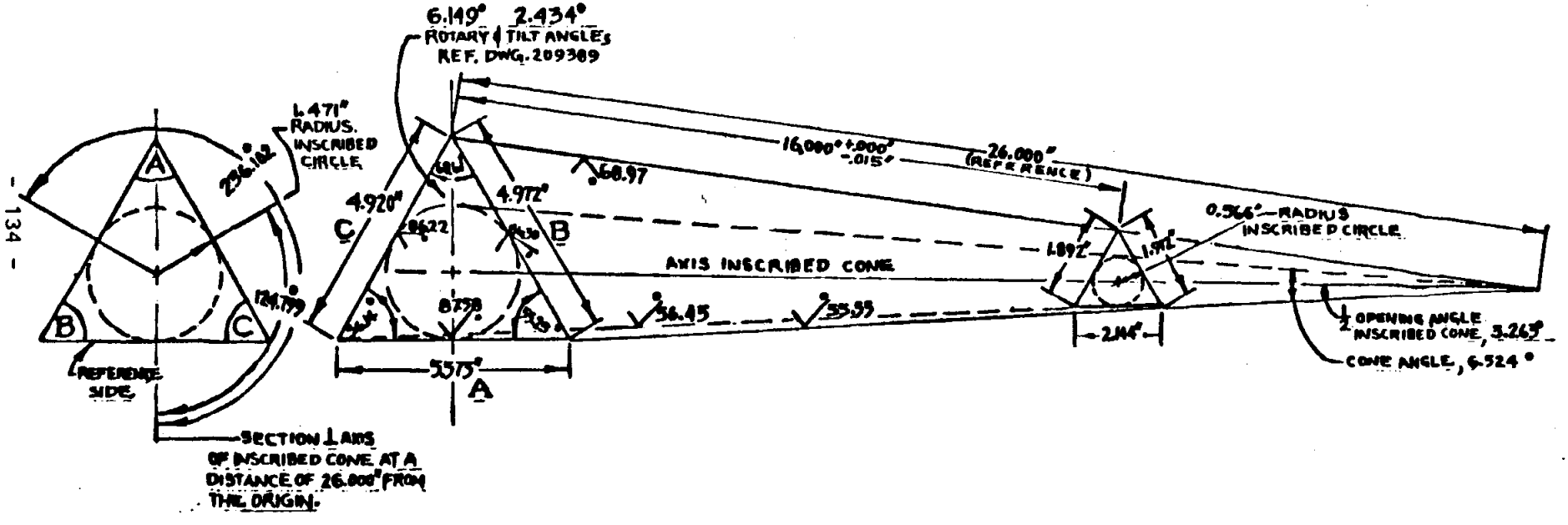

FIG..A-1 Dimensions of a typical ("A") module.

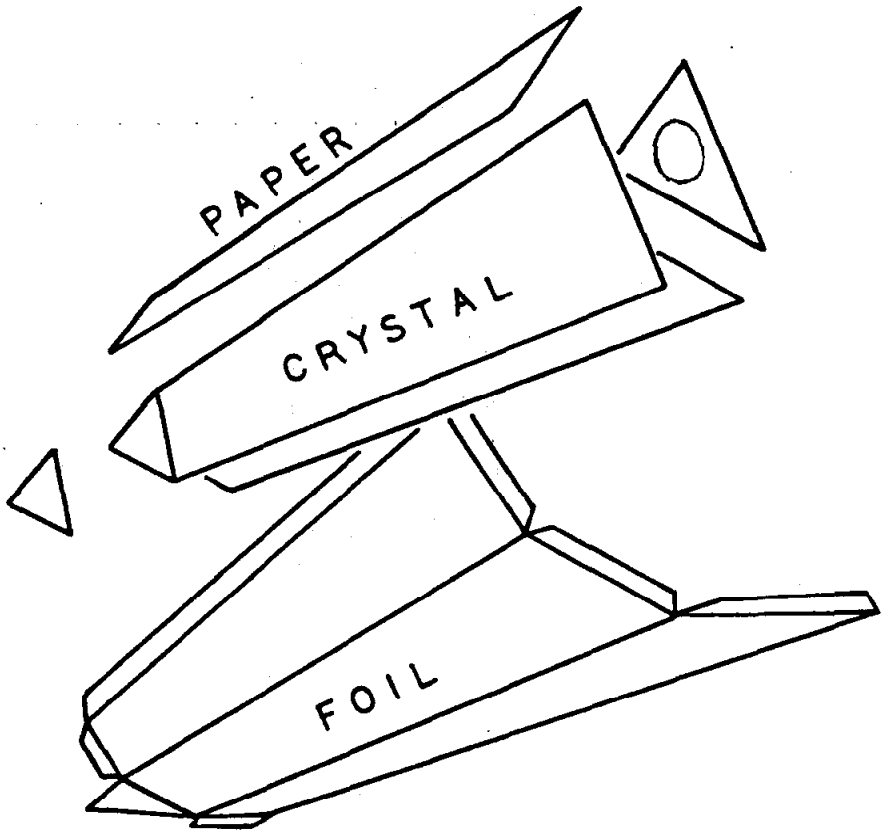

FIG..A-2 Wrapping technique.

the tunnel and washer regions of the can,[108] for which the limit was increased to 20%. A typical Cs spectrum taken with the test jig is shown in figure A-3; the Compton edge in the spectrum is somewhat enhanced for a crystal in the stack. Compensation of the crystal faces was measured by moving the Cs source along each crystal side[109] at 1 inch radial intervals -- this is shown in figure A-4a. Two compensation ranges were investigated; in the first 5 inches from the large end the pulse height could not vary by more than ±2%, while a uniformity of ±4% was required over the first 13 inches. These limits were increased to ±3.5% and ±6%, respectively, for the specially trimmed modules. In addition, the pulse height was not permitted to vary more than ±1.5% for a source applied to each of the crystal sides at a given compensation radius. Units not meeting the uniformity requirements were unwrapped and re-sanded until acceptable performance was achieved, or rejected if necessary. Large cracks sometimes developed in crystals after they had been stacked. Such cracks were detected during routine inspection of the crystals and required unstacking and replacement of the faulty crystal. The effect of a large crack on the uniformity is shown in figure A-4b. After stacking the resolutions of the crystals was again measured, this time using an air-gap/phototube device which was attached to the large end crystal faces by means of suction. For isolated crystals tested on the HCC test jig (it had no air gap near the phototube) the distribution of resolu-

---

[108]Each of the hermetically sealed hemispherical containers was called a "can"; the term "washer" refers to the thin stainless-steel sheet which formed the bottom of each can.

[109]The test was performed routinely using only one side when it became clear that side-to-side uniformity was easily achieved.

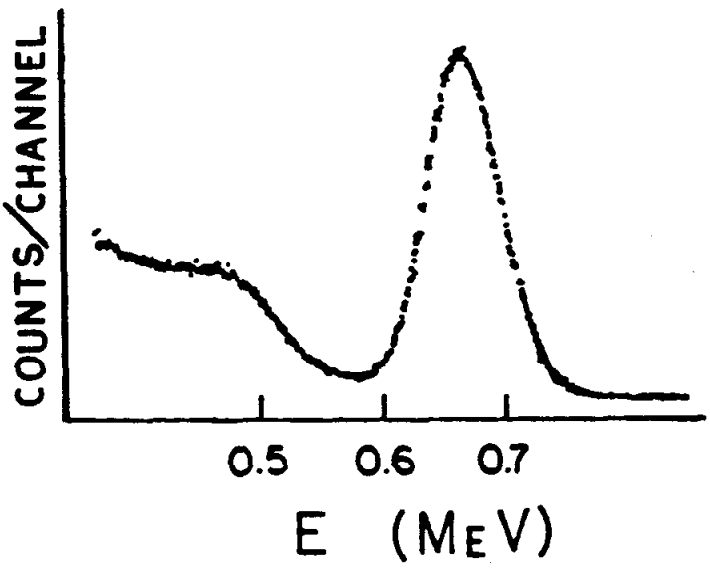

FIG..A-3 ^{137}Cs spectrum for an isolated crystal.

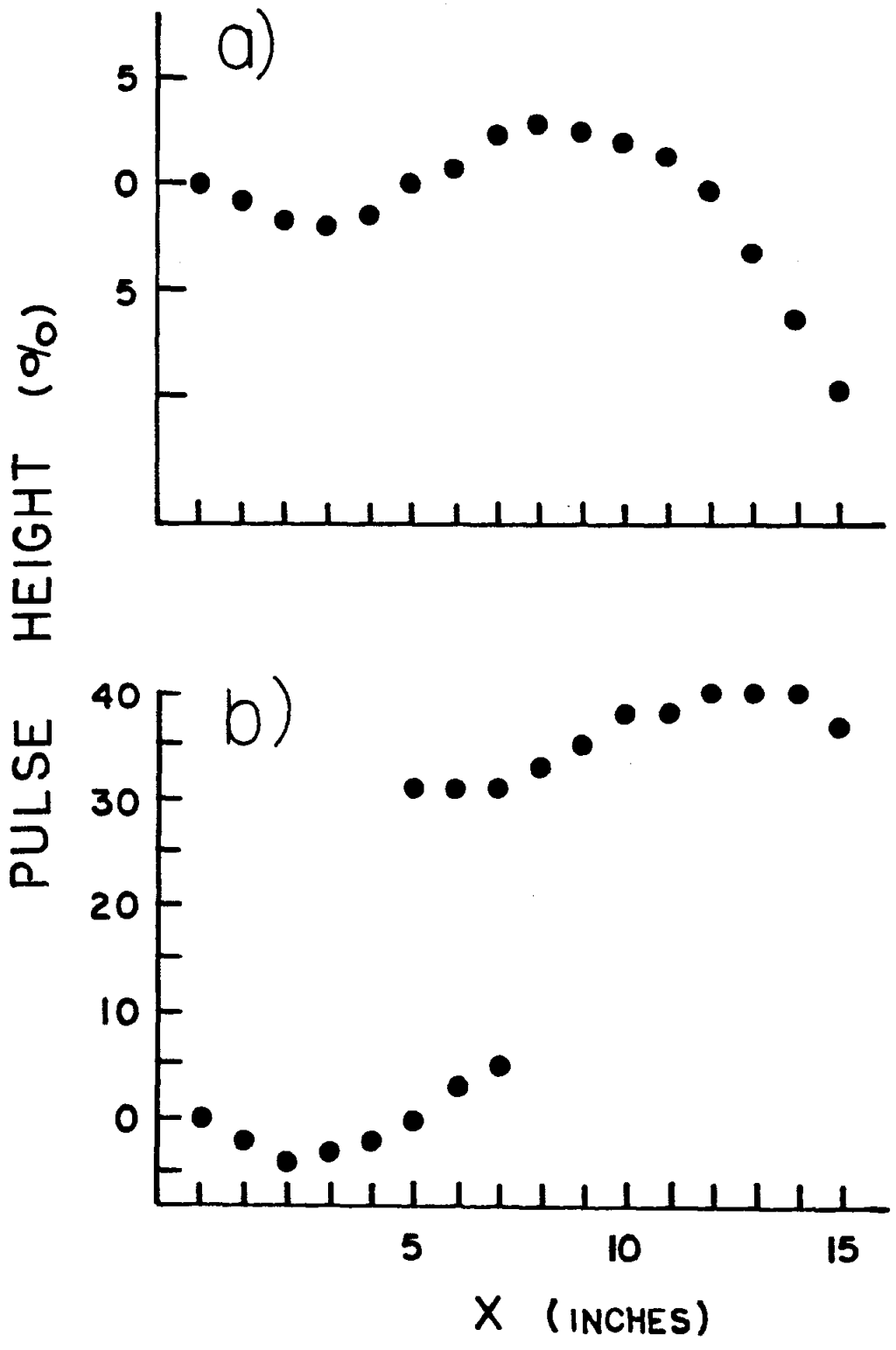

FIG..A-4 Compensation curves for normal (a) and fractured (b) crystals. X is measured from the large end.

tions for Cs, as well as the uniformity measured along one side, is shown in figure A-5.

As has already been discussed in chapter I, the crystals were stacked in the manner of a geodesic dome forming two hemispheres. In order to achieve the nearly spherical shape the individual crystals were machined so that the vertices of the large ends would lie on a sphere of radius 26 inches, while those of the small ends lie on a sphere of radius 10 inches -- this meant that the large ends were not perpendicular to the axis of the inscribed cone for any crystal. Eleven different shapes were required to achieve the spherical structure; they are illustrated in figure A-6 and described in Table A-1.

TABLE A-1

MODULE WEIGHTS AND NUMBERS

Module Type	Weight (Kg)	Number/hemisphere	
A	5.54	28	
B	5.54	28	(mirror image of A)
C	5.38	28	
D	5.38	28	(mirror image of C)
E	5.19	28	
F	5.19	28	(mirror image of E)
G	5.61	26	
H	6.25	28	
I	6.57	54	
J	5.38	30	
K	5.03	30	
	1890.10 Kg	336	
	(2.08 tons)		

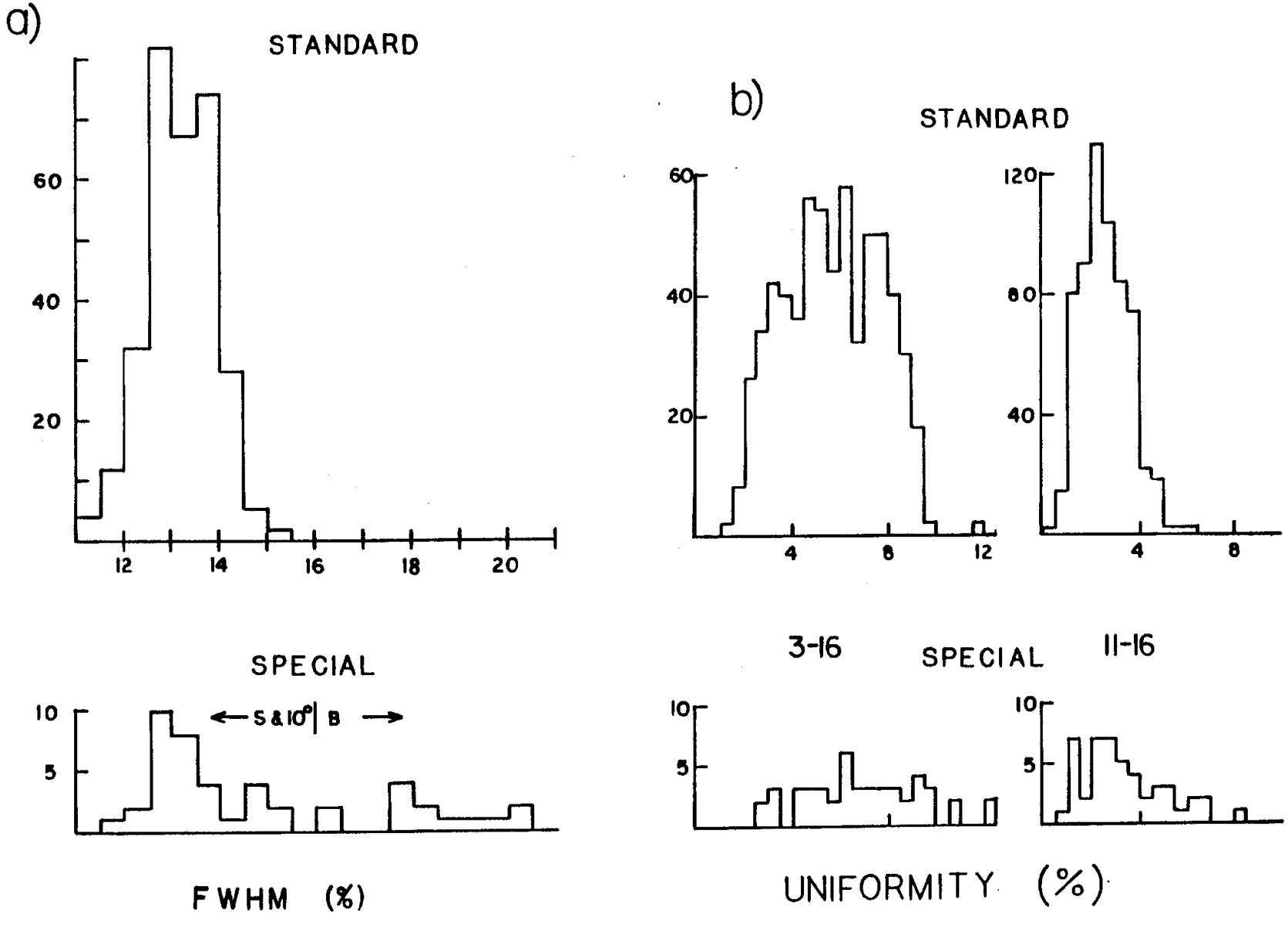

FIG..A-5 Resolution and compensation distributions for the modules.

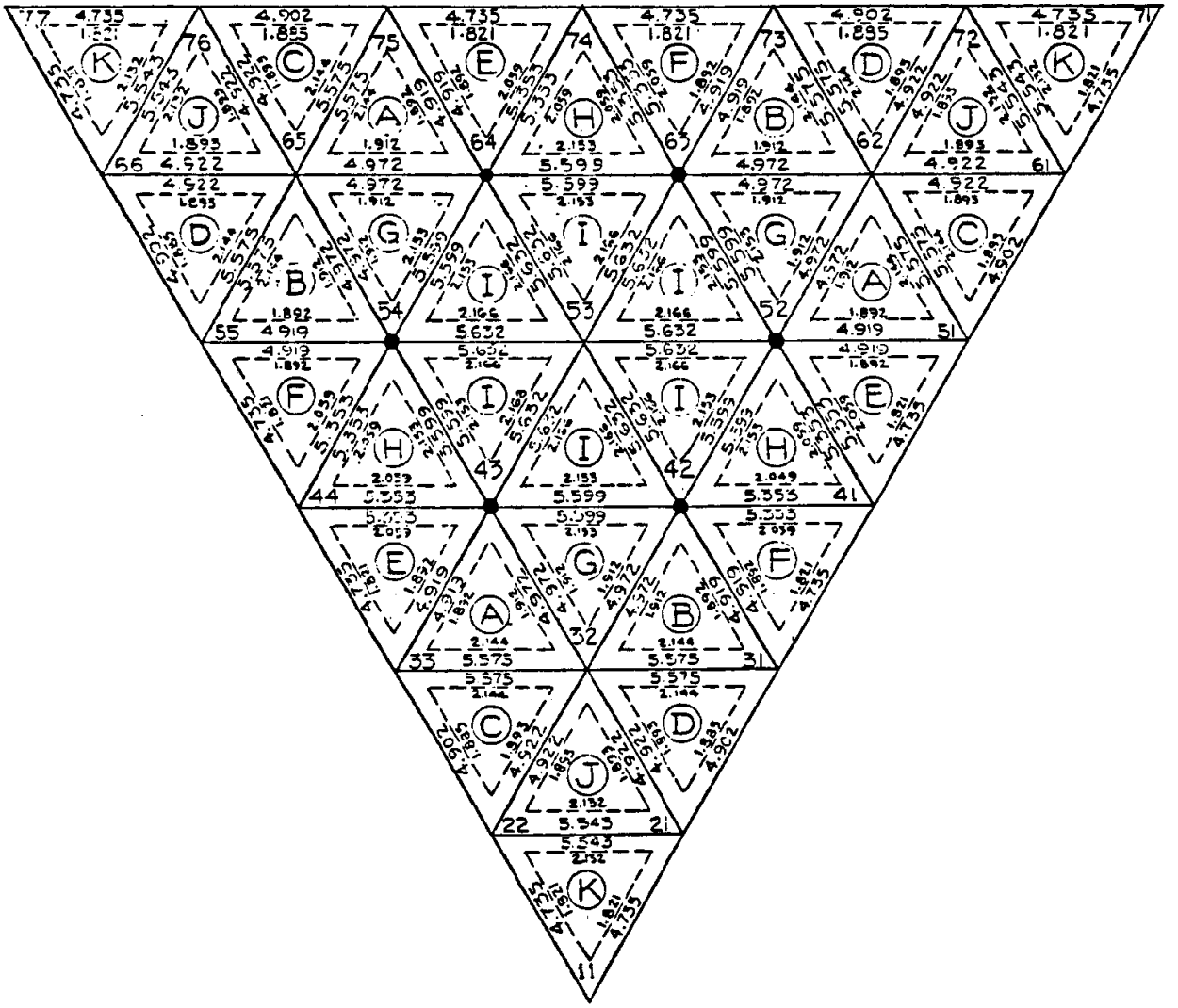

FIG..A-6 Pattern of crystal shapes in a major triangle. The dots denote the location of tensioning cables.

Accurate stacking of the hemispheres required that the crystal dimensions be extremely uniform; these tolerances are shown in Table A-2.

TABLE A-2

CRYSTAL MACHINING TOLERANCES

DIMENSION	TOLERANCE
longitudinal dimension	+0.000 , -0.015 inches
diameter of the large end inscribed circle	+0.000 , -0.005 inches
flatness of the sides	+0.000 , -0.005 inches
radius of all edges	<0.015 inches
angle of the inscribed cone	±0.3 mrad
angle between the end-face planes and the cone axis	±8.7 mrad
dihedral angle (angle between longitudinal edges)	±0.7 mrad

Additional trimming of some of the standard crystals was necessary to accomodate their position near the tunnel regions of the cans (figure A-7) or around the tensioned cables. In the former case the more severe B-cuts degraded the uniformity and resolution of the crystals by a small amount. Near the cables 0.03 inches was trimmed from the adjacent crystal edges. Crystals resting on the bottom surface of the can experienced the forces of all the upper-level crystals and were therefore

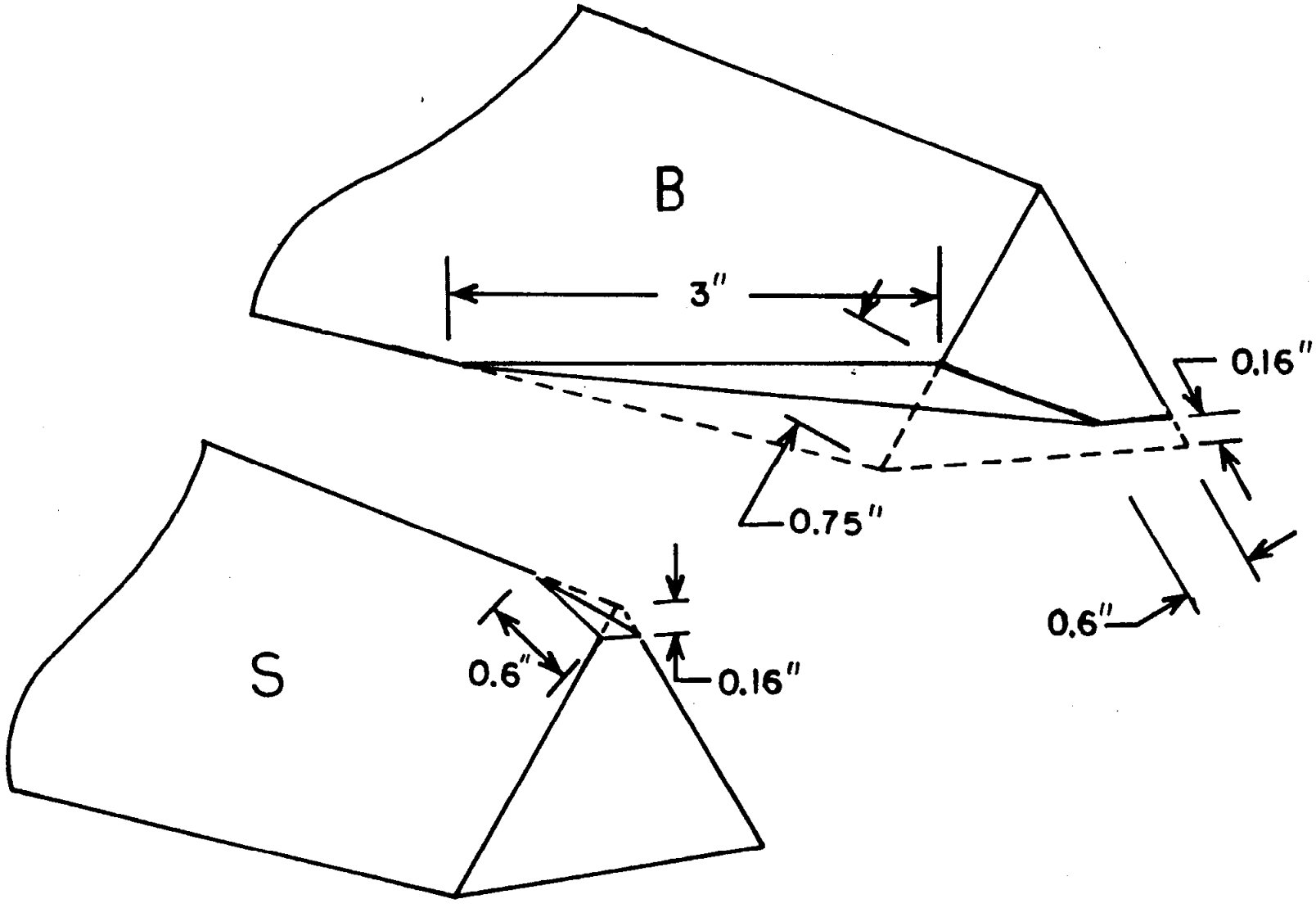

FIG..A-7 Special crystal cuts.

trimmed so that the large ends had a polar angle of 10° (5° in the case of the second hemisphere), where the x-y plane defines the bottom can surface. This trim created room for supports which prevented radial motion of the crystals and caused the pusher-plates to exert an upward force on the crystals.

The construction of the cans is shown in figure A-8. Principal elements are a 0.875 inch thick hemispherical aluminum outer dome of inner radius 26.687 inches, a 0.063 inch thick stainless-steel (304) inner dome, a 0.063 inch thick stainless-steel annulus ("washer") welded to the inner dome and forming the bottom surface of the can, and two half-hexagonal tunnel regions.

An exploded view of one crystal module positioned in one of the hermetically sealed hemispheres is offered in figure A-9. The extremely brittle crystals were protected from motions of the can and neighboring crystals by three means: a) an inner (small end) shim of polyurethane foam about 0.06 inches thick when compressed, followed by a stack of teflon shims; b) the reflector-paper/foil sheath, having a total thickness of 0.036 inches between the crystal surfaces; c) an adjustable pusher-plate/masking plate assembly secured to the outer dome -- this secured the large end faces of the crystals and compressed the crystals longitudinally, thereby increasing their tensile strength. The teflon shims consisted of 1 inch diameter discs of various thicknesses so that the radial position of each crystal could be adjusted during the stacking process. Less than 0.03 L_{rad} of shim material was located in front of the crystal in the most extreme case (about 0.5 inches of teflon shim).

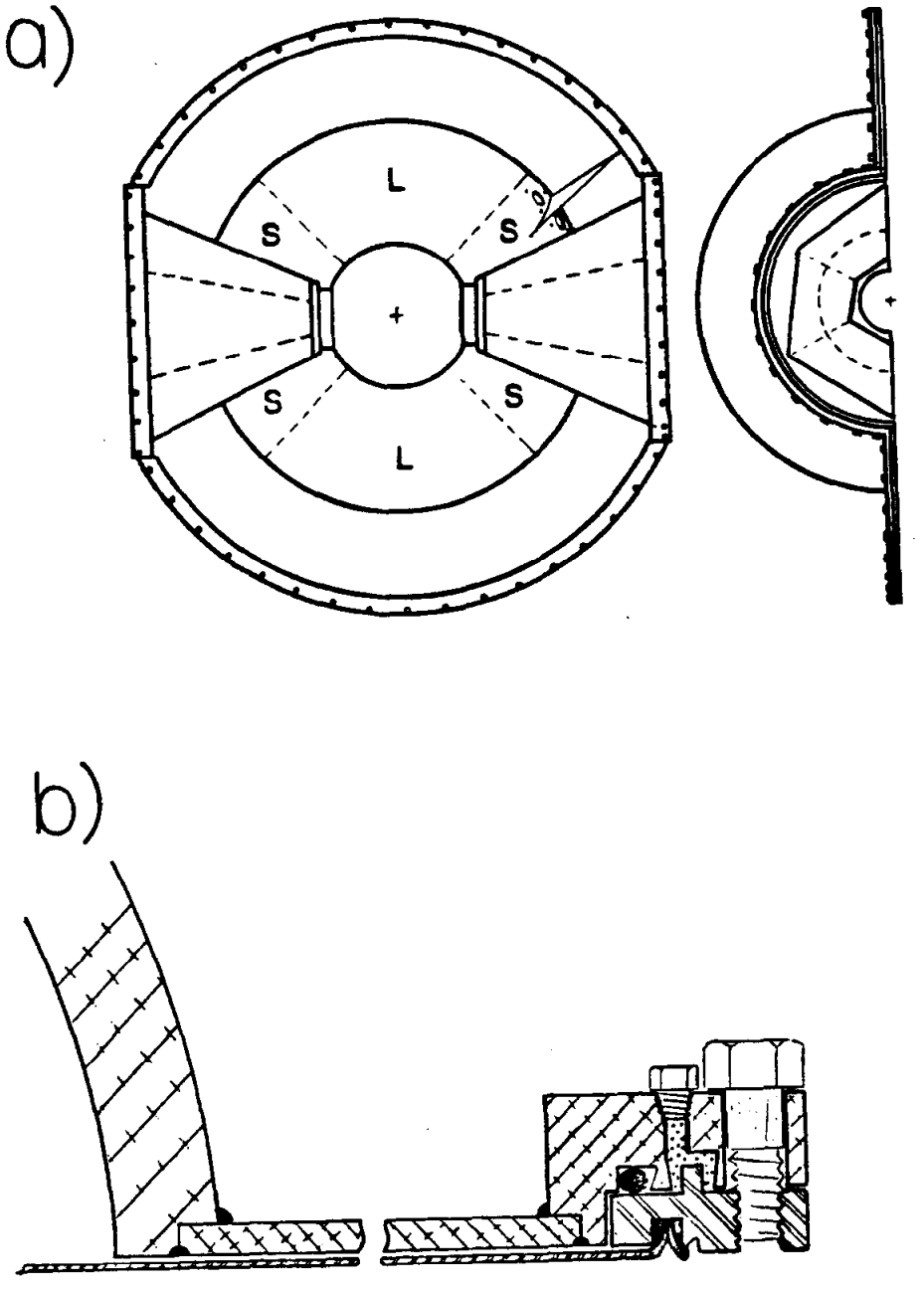

FIG..A-8 Details of the housing. In a) S and L refer to 0.125 and 0.010 inch thick shims, respectively.

c)

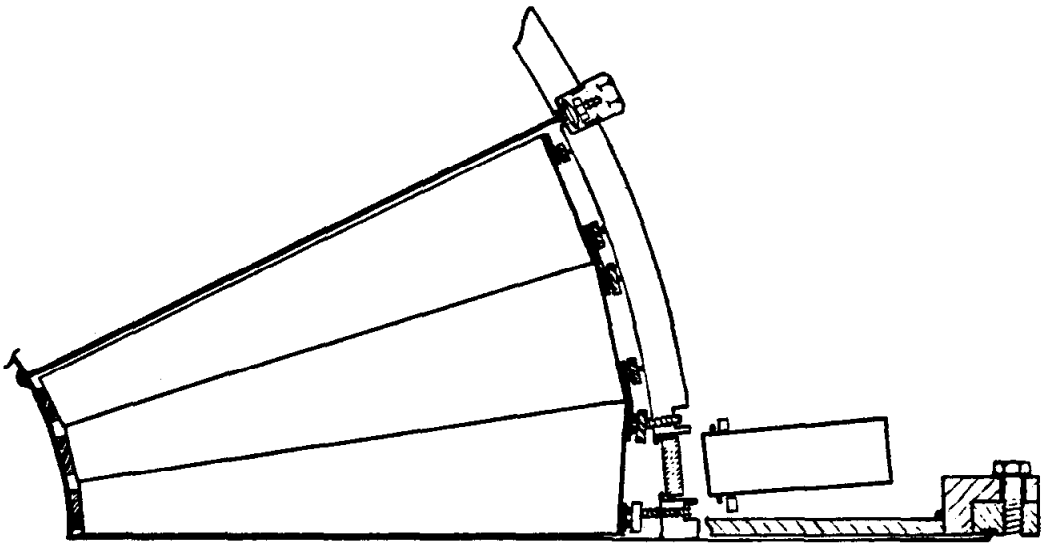

d)

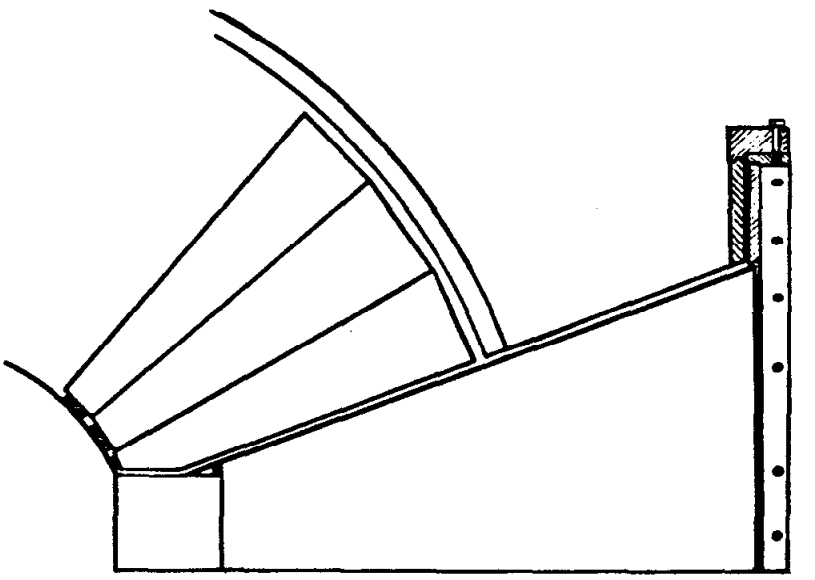

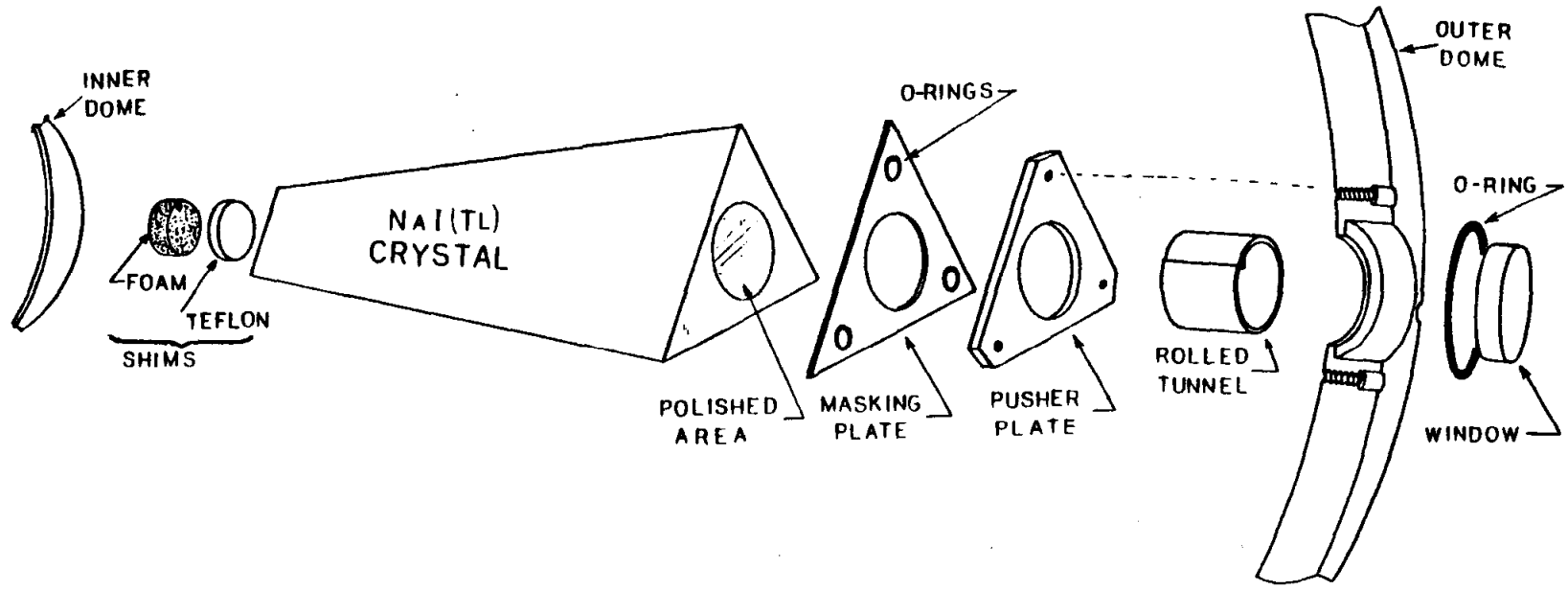

FIG..A-9 Exploded view of one crystal in the housing.

Wedge shaped shims were placed on various crystal sides as required to correct for the cumulative effect of the machining errors and stacking errors. The shims were cast using Dow-Corning Silgard 184 epoxy and had a wedge angle of 1 mrad and a minimum thickness of 0.010 inches. A total of 60 shims was used, but only in the second hemisphere. When fully assembled the inner and outer domes were bonded by tensioned cables running from one dome to the other, and by lowering the internal pressure of the can relative to the atmospheric pressure. Three pressure and two humidity sensors were mounted on each outer dome to monitor the crystal environment. The large, thin washer was not terribly rigid and had the tendency to ripple (an oil can effect), thus causing the breakage of two bottom layer crystals. To prevent further damage from the oil can effect, a resilient shim was placed directly on the washer, as shown in figure A-8a. Under the eight crystals near the tunnel regions the shims had a nominal thicknes of 0.125 inches,[110] while the central area was typically 0.010 inches thick. Viton rubber sheet was used to form the shim for the first hemishere; cast Silgard 184 epoxy, employed in the second can, provided a more level surface on which to begin the stacking of crystals.

A special theodolite-like apparatus (dubbed the super survey tool, or SST) was constructed in order to survey the positions of the crystals and provide a stable basis for the stacking of crystals; the device is shown in figure A-10. The washer of the can being stacked was secured

---

[110]These crystals were slightly undercut so as to avoid the welds near the tunnel seams.

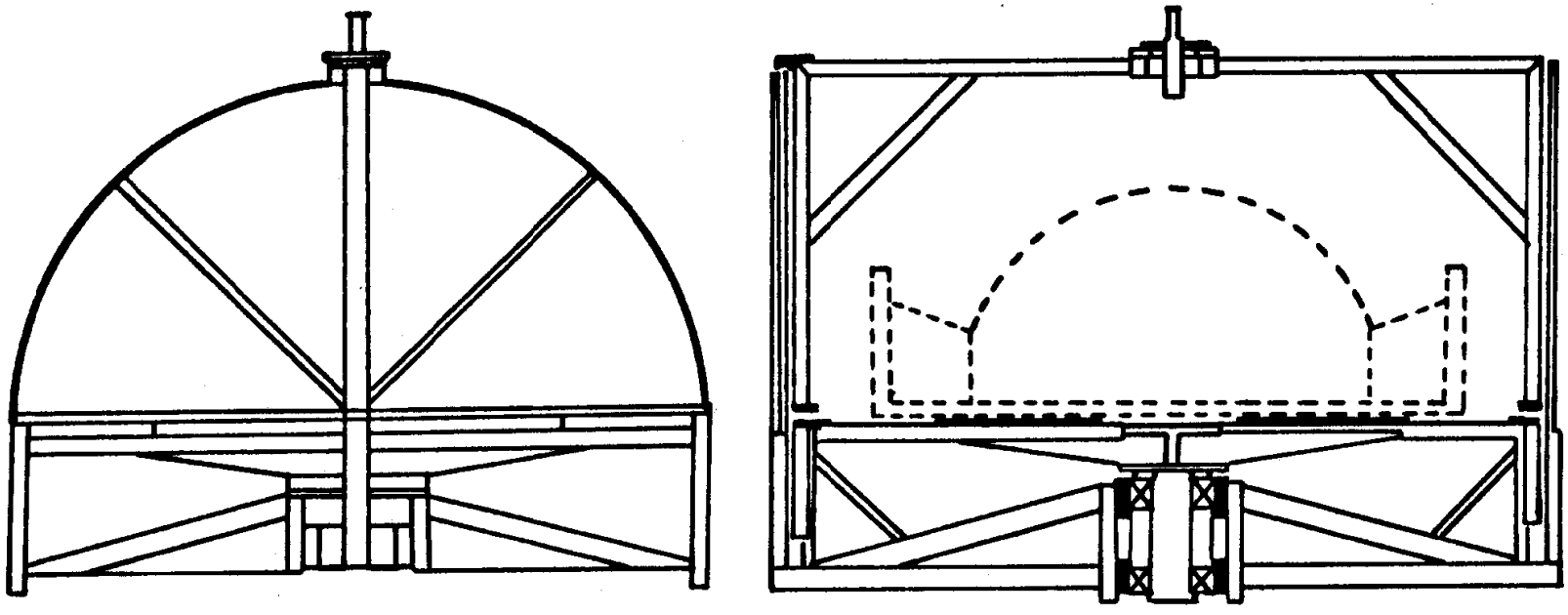

FIG..A-10 The SST (Super Survey Tool).

to the SST base by suction from a vacuum pump which was regulated to simulate the weight of the full load of the crystals upon the washer. For the second hemisphere the vacuum was varied as each new layer of crystals was stacked, and served to minimize the occurence of oil can ripples. The crystal positions were initially measured for only those crystals having an upward (thus accessible) vertex. For these crystals, the azimuth and polar angles of the top vertex edge were sighted with the theodolite arm of the SST. After a complete row had been stacked, marks were scribed on the large end faces prior to placement of the downward-vertex crystals of the row; the scribe marks were then monitored periodically during the stacking process. Support bars were initially fastened to the washer to counteract the radial force exerted by the upper crystals on those in the bottom row. The temporary supports were later replaced by small retaining blocks which were permanently cemented to the washer (figure A-11). Despite these retaining blocks some crystals in the completed stack did shift position after about 24 hours, with an extreme radial motion of about 0.125 inches. This shift was corrected by the action of the pusher-plates once the outer dome was secured to the washer; a systematic hand tightening of the pusher-plates, proceeding systematically from bottom to top, approximately re-created the original stack positions. However, the outer dome obscured the scribe marks so that only a radial position survey was possible after securing the outer dome. The cables were tensioned so as to induce a 0.005 inch shift in the radial position of an adjacent crystal, followed by a final radial-position survey of all the crystals. These final surveys yielded positions accordant with the machining and stacking errors,

giving a net uncertainty of 5 mrad in the position of the crystal axes -- this error is much less than the resolution for reconstruction of showering particles.

Light produced by a given crystal reached the phototube by way of two air gaps, each approximately 1 inch long. The gaps were separated by a 0.5 inch thick window which served as part of the hermetic seal; the light-transmission properties for these windows is shown in figure A-12. The absorbtion of light by the windows impaired the photon signal by 14%. An aluminized tunnel of rolled metal was used to guide the light through the first air gap. After the outer dome had been secured and the pressure plates had been adjusted, optical isolation of the modules was achieved by stuffing aluminium foil into the region between the large ends and the inner dome surface, followed by insertion of the rolled-tunnels; the tunnels were then trimmed to fit flush against the crystal surface. Aluminized plexiglass tunnels were integral parts of the photo-tube assembly and served to guide photons in the second air gap. In addition, one green LED and a fiber-optic cable were imbedded in the plastic tunnel; these were used to test linearity and stability of the calibration. Compared to a direct (greased) optical coupling, a 60% loss of photons was realized with the air-gap arrangement.[111]

---

[111]The inner gap resulted in a 50% light loss, degrading the resolution (FWHM) on Cs from 10% to 12%, while the second gap lost 20% of the light, further degrading the resolution to 14%.

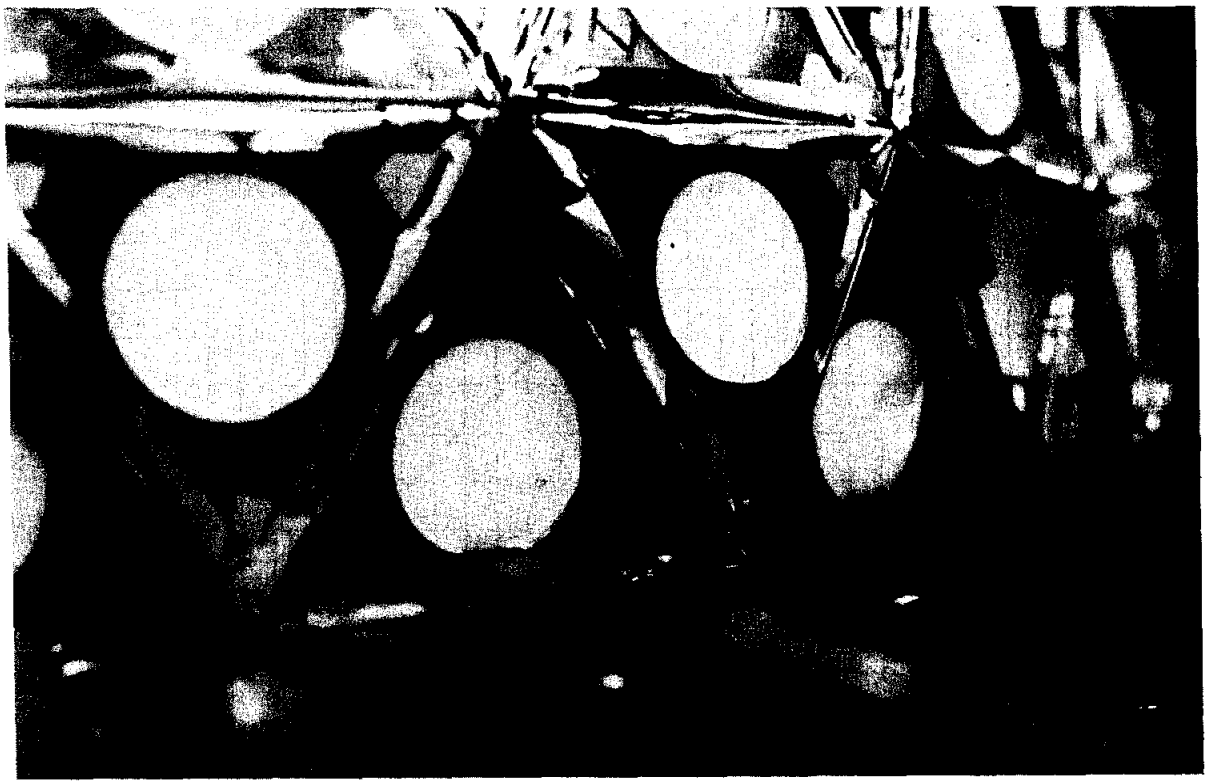

FIG..A-11 Photograph showing the retaining blocks.

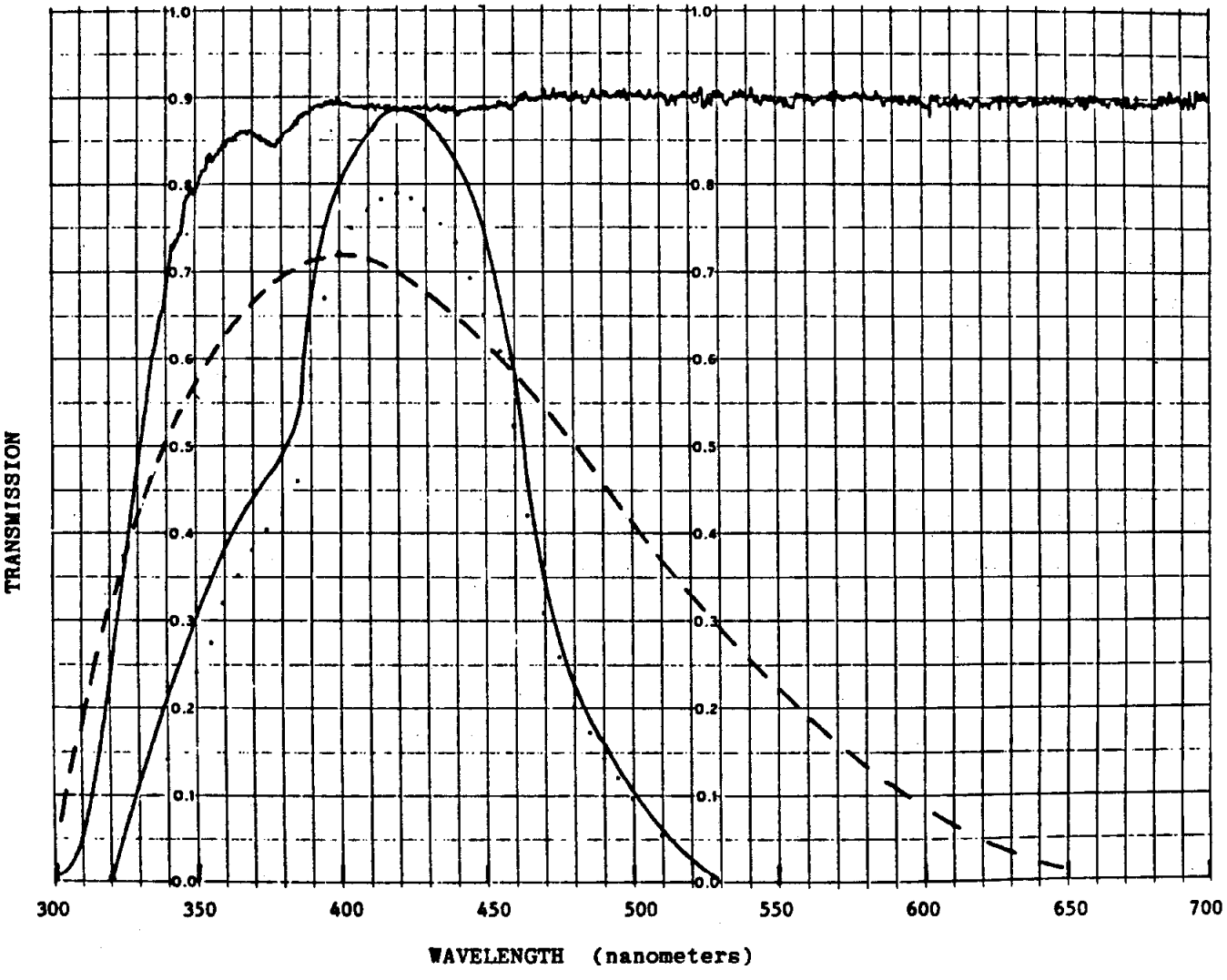

FIG..A-12 Light transmission for the windows (upper solid line), the NaI(Tl) spectrum (lower solid line), the folding of the solid lines (dotted), and the phototube spectral response (dashed).

The hermetic seals along the edges of the can are illustrated in figure A-8b. Resilient Ecco-bond epoxy was forced into a groove about the outer rim of the washers to provide the main seals and to seal all other joints in the cans. The other joints included the tensioned-cable bolts, the humidity and pressure gauge ports, the pressure-plate screw holes, and the window seals. Windows, when inserted into the outer dome, were surrounded by one silicone rubber O-ring; epoxy was then injected around the window, followed by the insertion of another O-ring to retain the fluid epoxy. Upon curing of the seal the second O-rings were removed to permit insertion of the phototube assemblies. Development of the stacking process for the second can is shown in figure A-13.

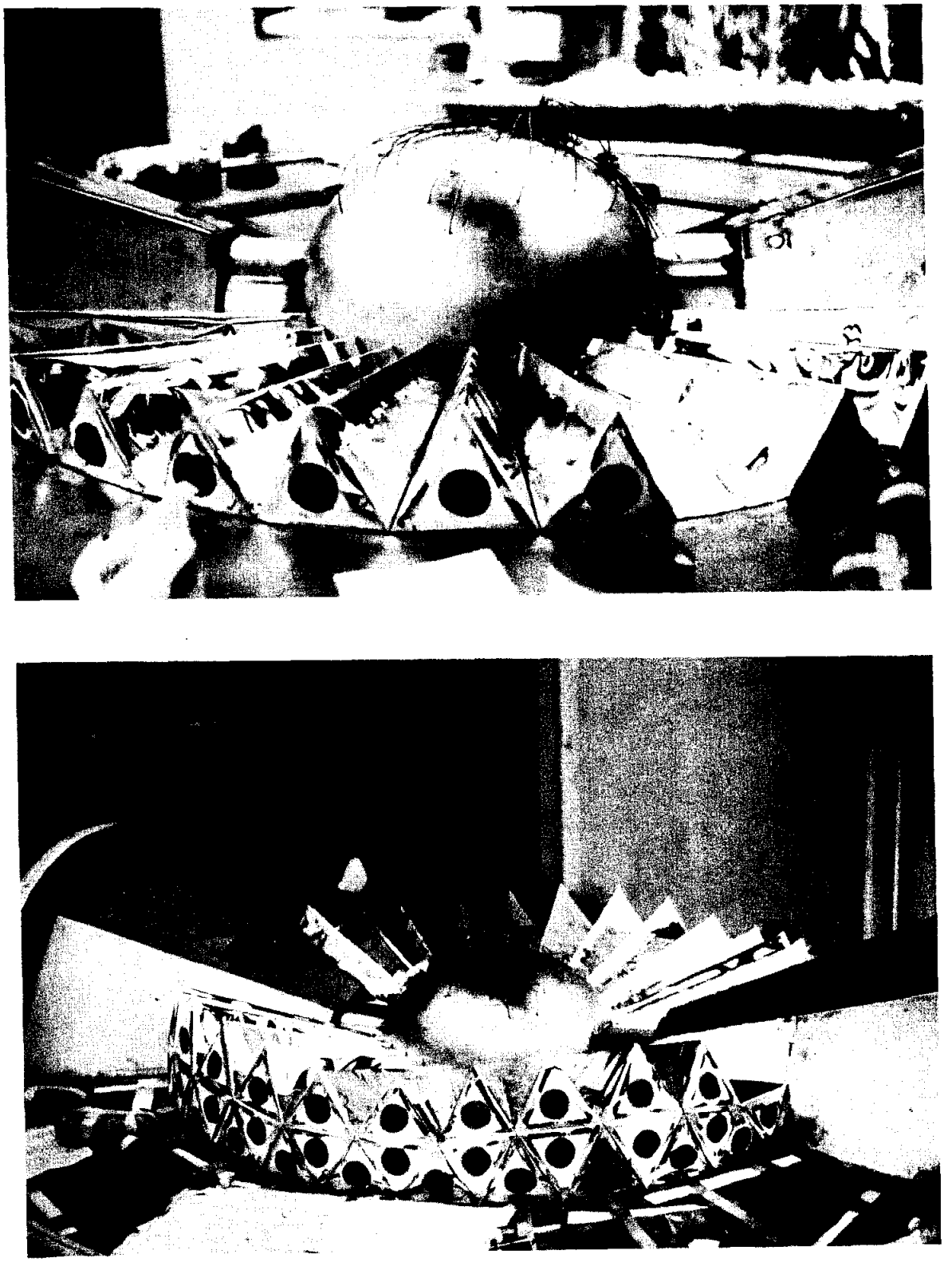

FIG..A-13 Photographs of the second hemisphere stacking sequence.

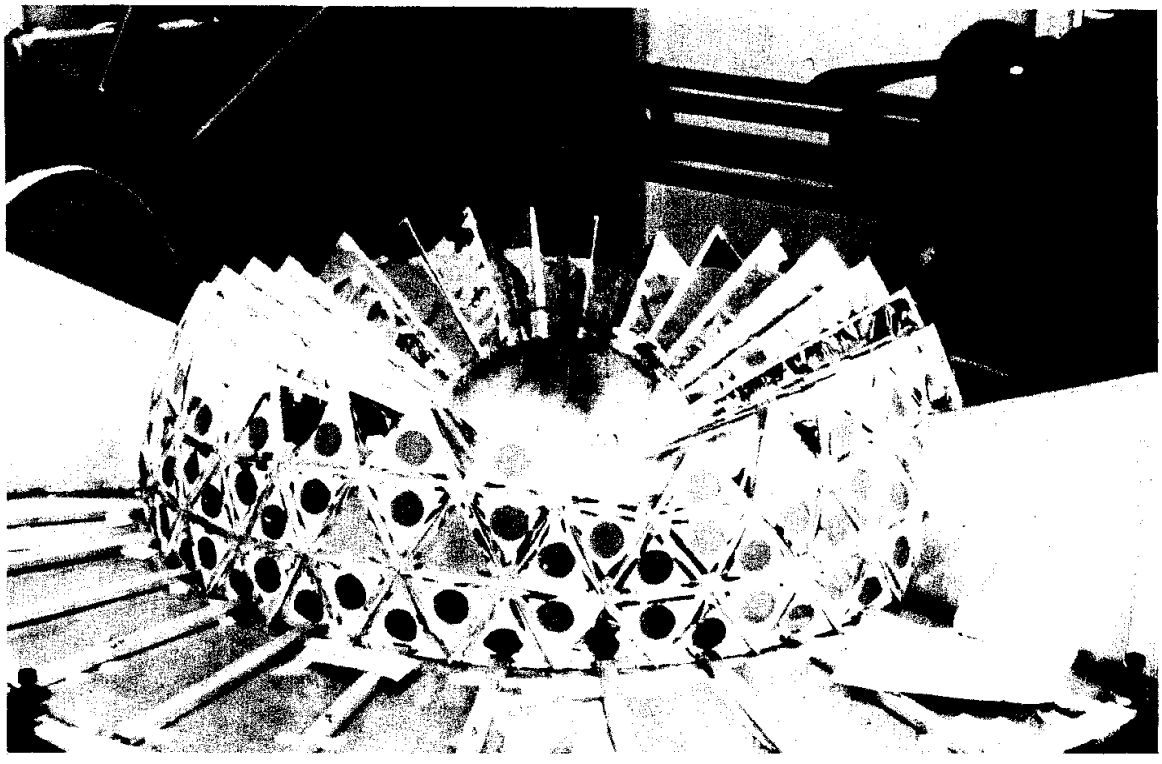

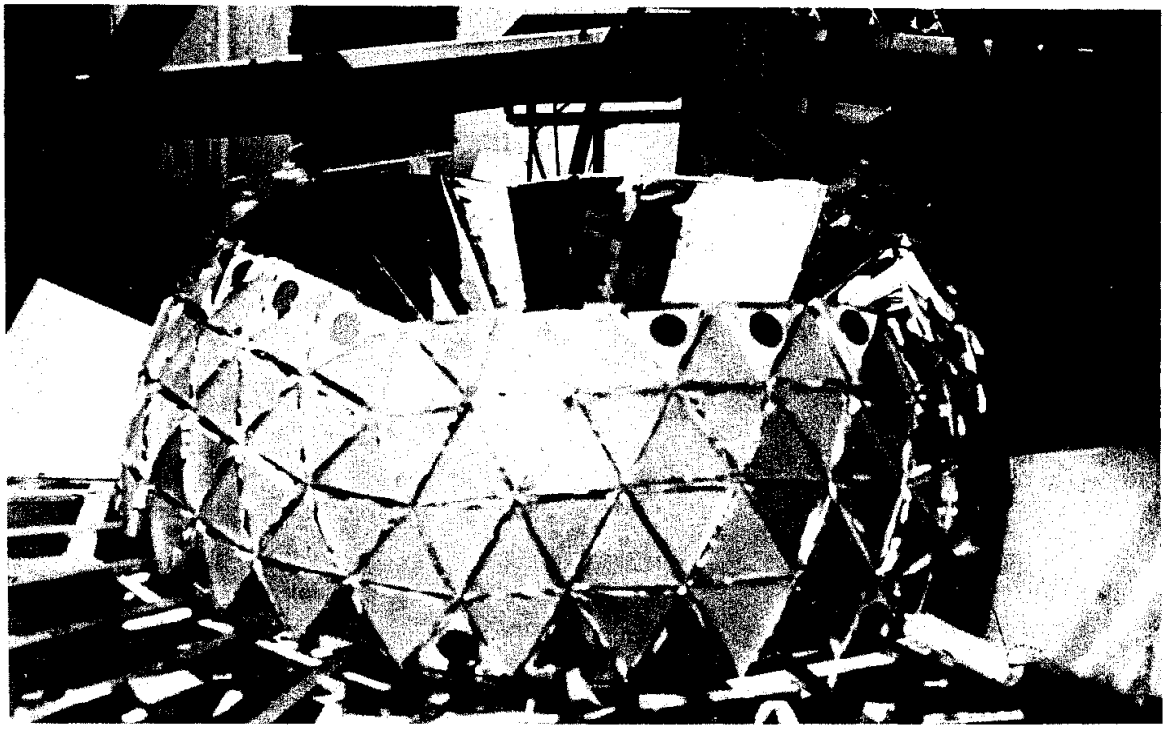

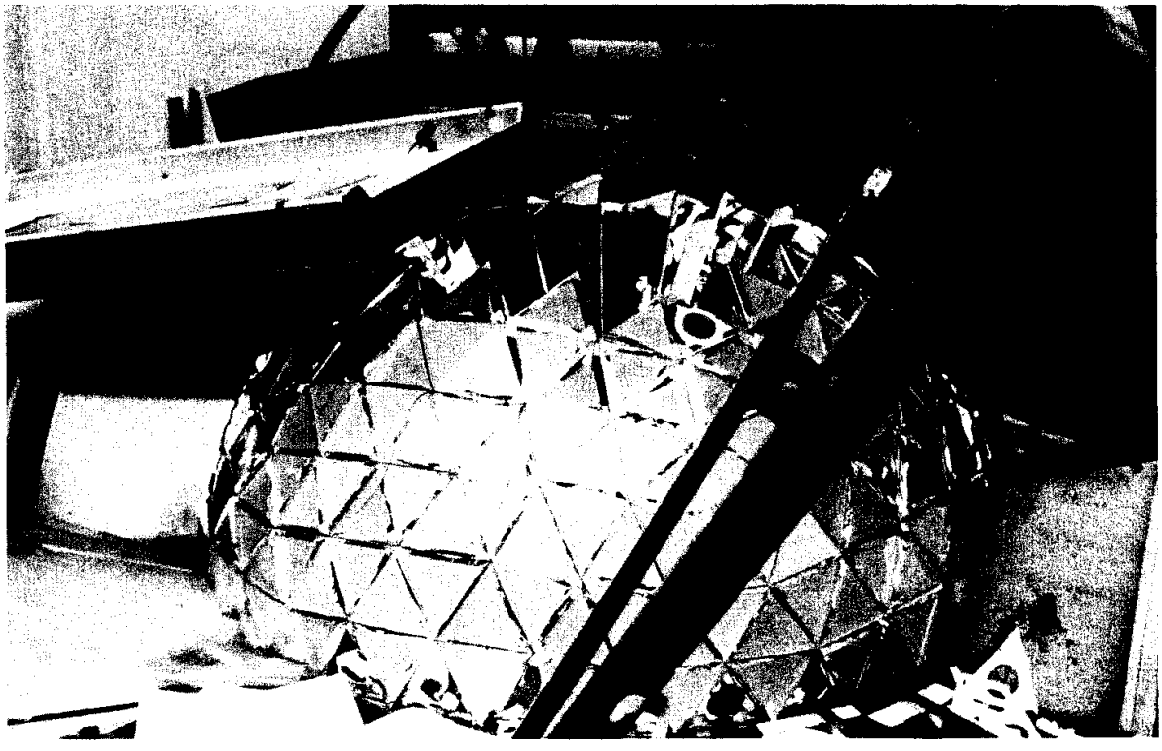

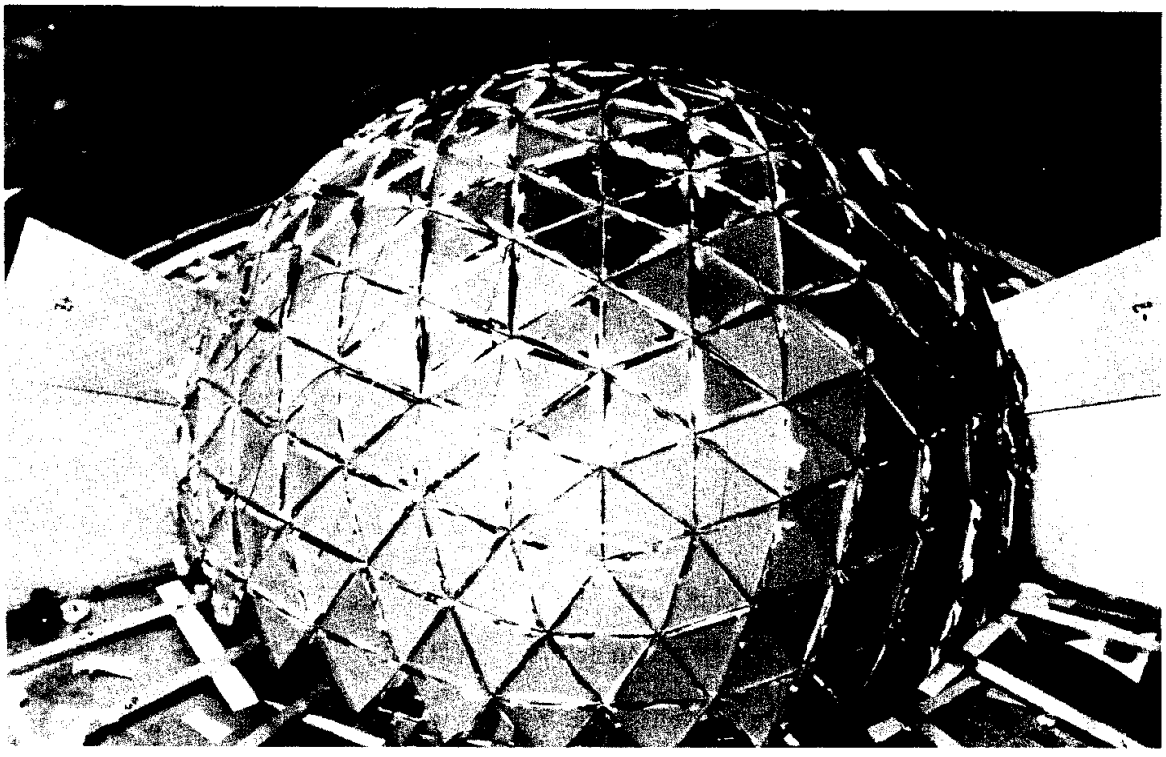

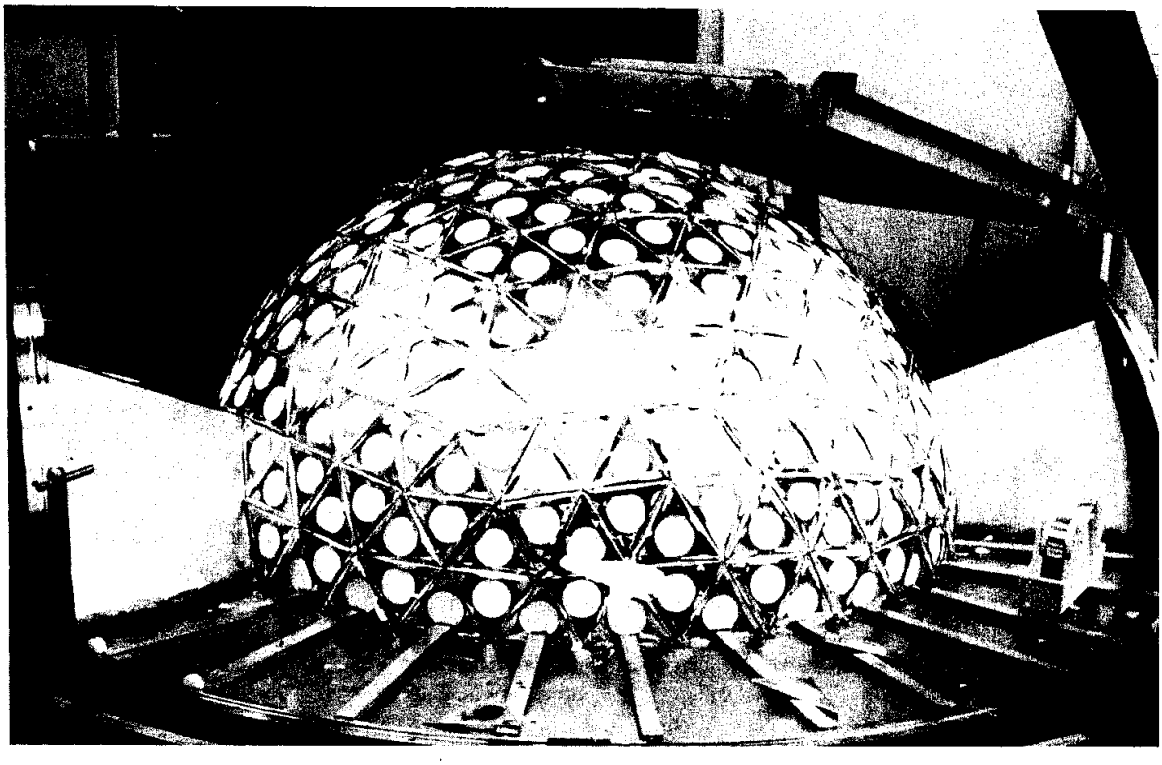

Appendix B

TRIGGERS

The analog sum of the nine crytals in each minor triangle was available for triggering purposes, with a minor triangle calibration of about 1mV/9.6MeV. Owing to variation in the signal cable lengths, the summed signal had a somewhat larger width than that for a single NaI(Tl) channel; it also reflected a ±10% variation in the gains of the phototube bases. The minor triangle signals were attenuated by 75% to prevent saturation of the active electronic addition networks, and were then summed in Lecroy 428F fan-ins to provide the analog signals for each major trangle, the top and bottom hemispheres, and the full ball proper. The addition logic is shown in figure B-1a.

The separate signals from each hemisphere were routed through threshold discriminators permanently set at 144 MeV (60 mV), corresponding to the lower edge in the energy distribution of minimum ionizing particles which traverse the ball radially. The two signals had to be received within 20 ns of each other; this condition appears as the first coincidence in figure B-1b. Also considered in the coincidence was the full ball signal which provided the main signal for energy discrimination, generally at a threshold of 650 MeV. To prevent slewing of the full ball timing signal a constant-fraction discriminator (CFD) was employed. This

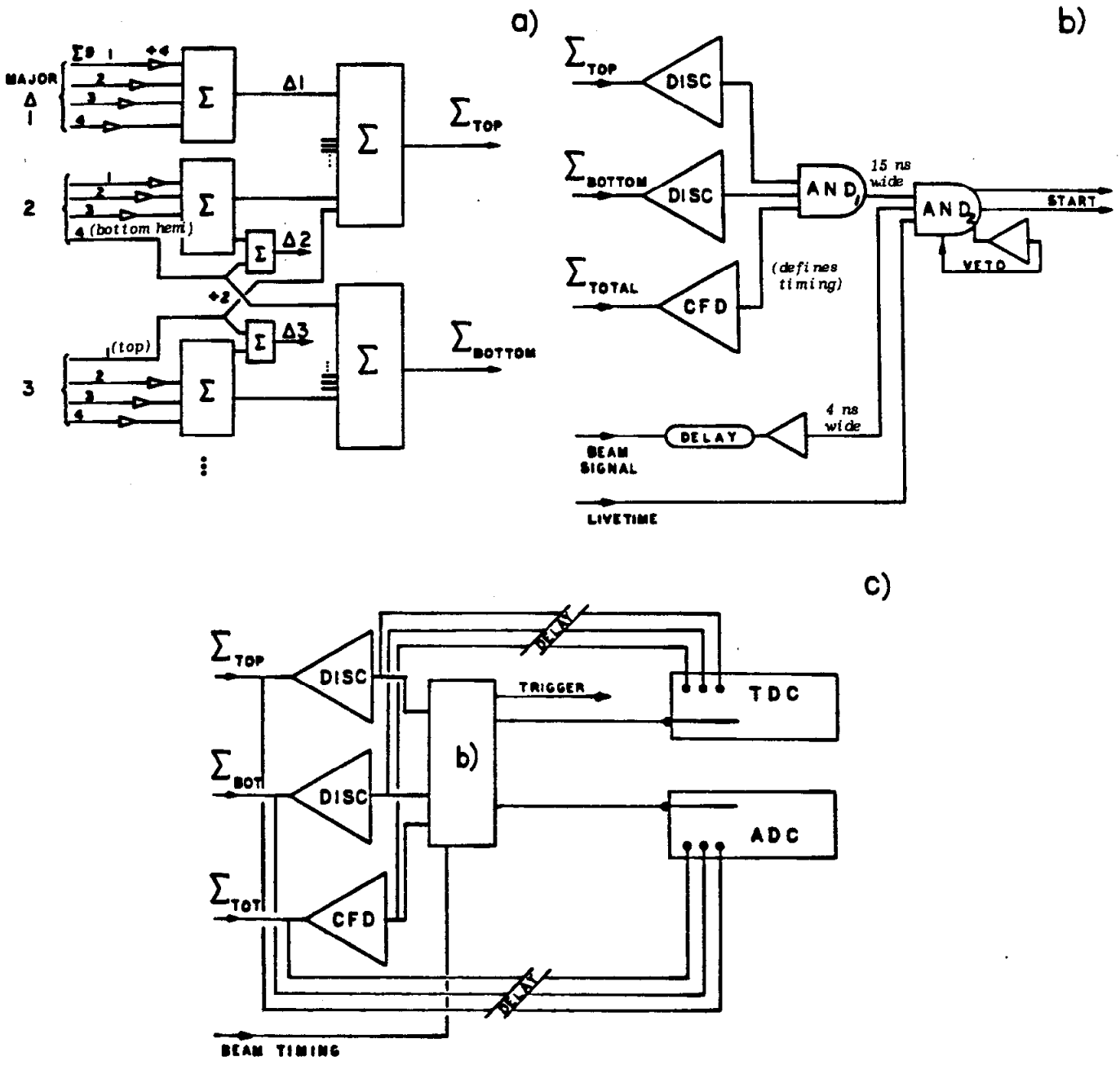

FIG..B-1 Fast trigger schematic.

device added the main signal, delayed by 64 ns, to the inverted and 80%-attenuated main signal, as shown in figure B-2a. From this sum resulted a bipolar signal which crossed the zero-point when 20% of the maximum pulse height was attained. NaI(Tl) signals undergoing this process are shown in figure B-2b; here it is apparent that the zero-cross point occurs at a fixed time after the start of the NaI(Tl) pulse, with less than 250 ps of jitter.

A second coincidence requirement was formed using the full ball signal, the beam-crossing signal from SPEAR, and the livetime signal from the data acquistion network. Here the full ball signal was required to occur within ±8 ns of the beam-cross. If the coincidences were achieved a trigger pulse and a delayed quenching pulse were generated. In addition, start signals defined by the leading edge of the beam-cross pulse were sent to a battery of ADCs and TDCs to record the pulse height in each major triangle and the timing for the top, bottom, and combined hemispheres; this network is shown in figure B-1c.

Timing distributions of the full ball signal are shown in figure B-3 for colliding beam and separated beam configurations. In the latter case the distribution shows the characteristic plateau due to randomly distributed cosmic ray triggers. The large peak at the extreme right hand edge of the plot is an artifact arising from very late NaI(Tl) pulses which defined the timing start; the phenomenon is illustrated in figure B-4. During normal running a large proportion of events in the peak usually indicated a background caused when poor-quality beams caused large random backgrounds.

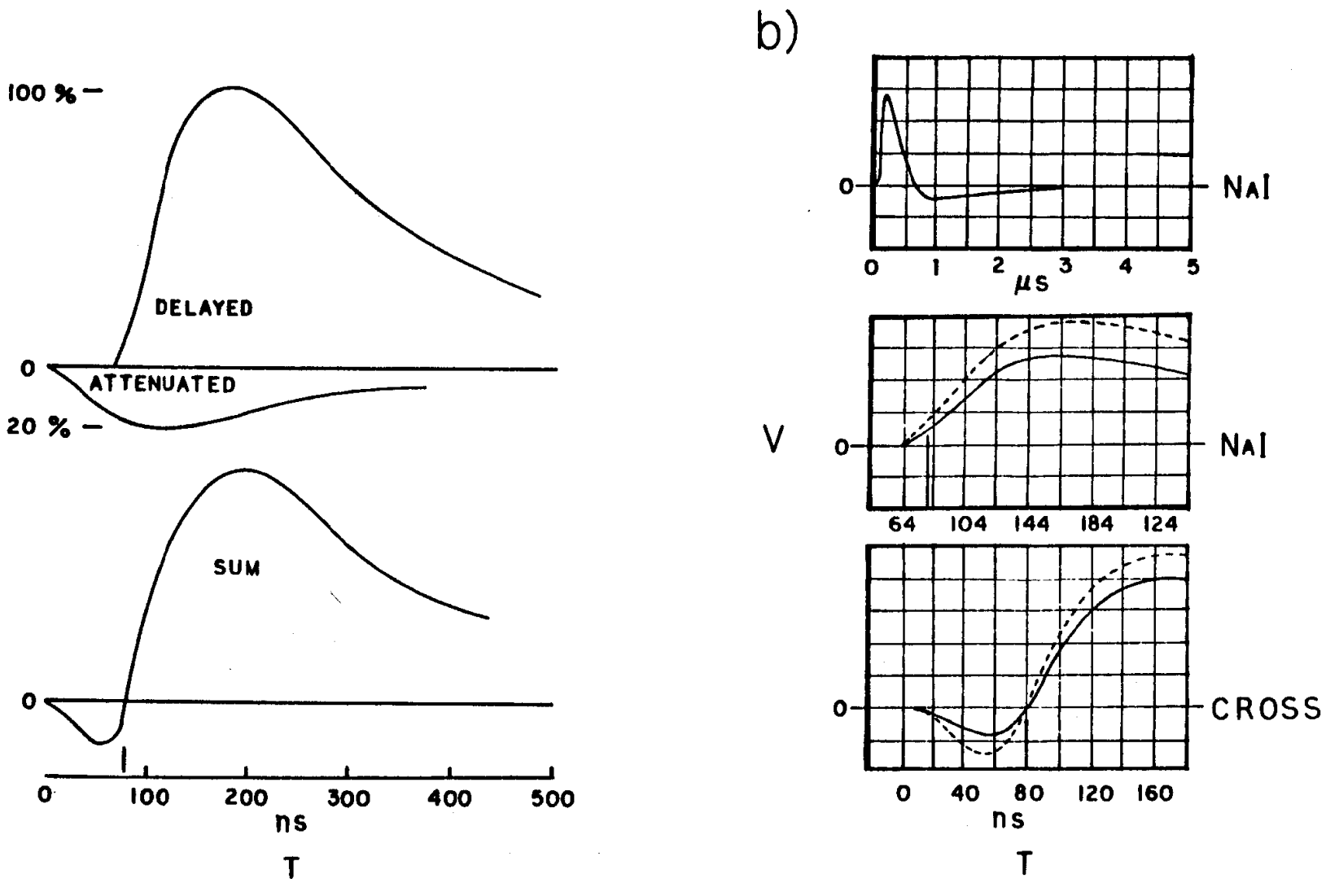

FIG..B-2 Principal of the Constant Fraction Discriminator.

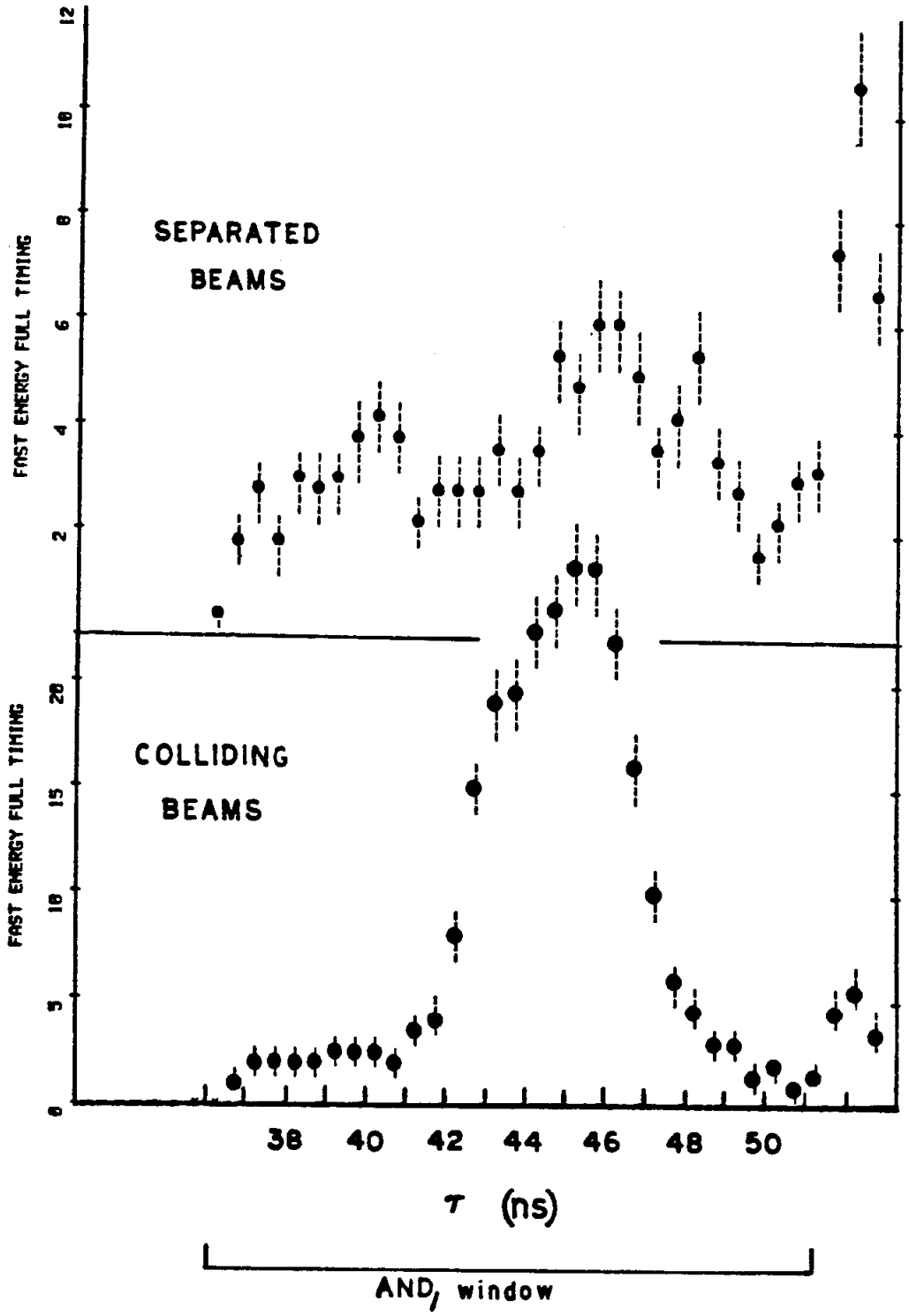

FIG..B-3 Fast trigger timing distributions from the TDC.

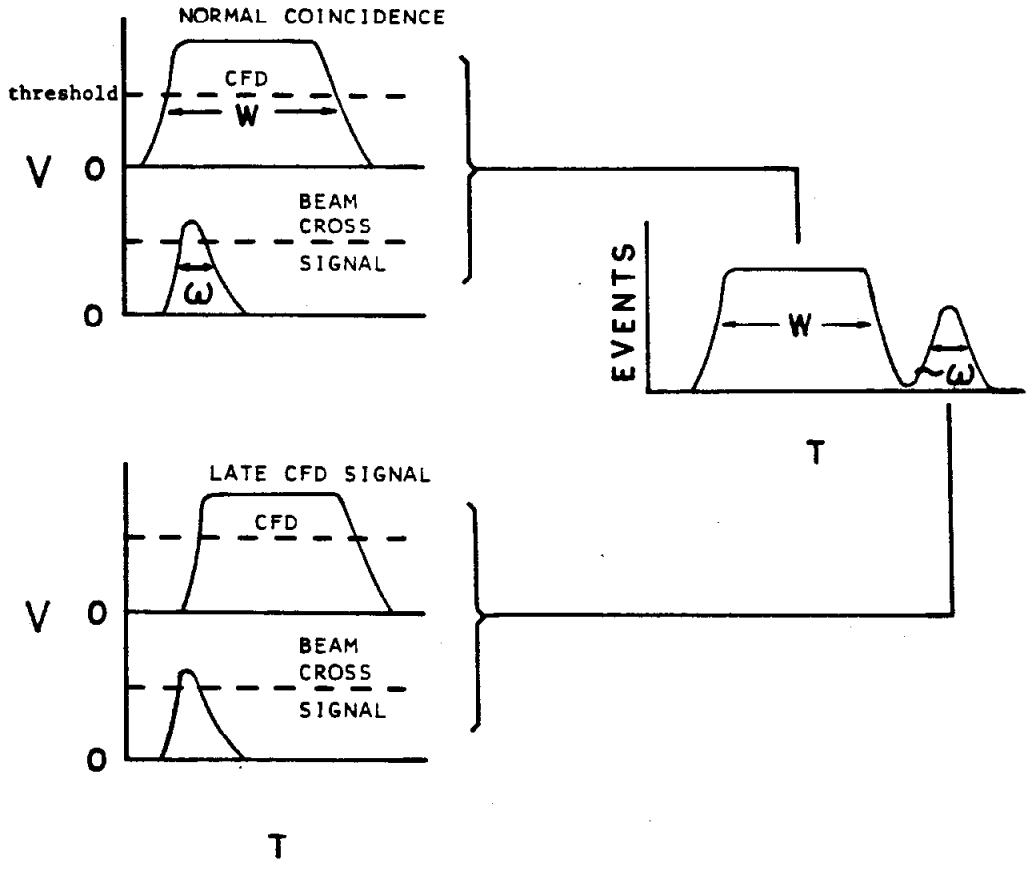

FIG..B-4 Leading edge effect.

Cosmic rays which triggered the apparatus travel about one meter between the hemispheres; hence, there should be a 3 ns timing difference between the top and bottom hemispheres. As seen in figure B-5, the timing signals were too wide to be used in eliminating cosmic-ray events.

Setting of the main Fast Trigger threshold was dictated by the limits on a trigger rate which could be considered tolerable. Cosmic rays traversed the ball approximately radially (i.e., they intersected the central cavity) at a rate of 200 Hz, or 10 Hz during the 40 ns Tower[112] trigger gate about the beam-cross signal. In contrast, ψ' particles were produced at about 0.6 Hz. The total rates due to the Fast Trigger alone and due to the Tower are shown in figure B-6; the tunnel modules were included in the Fast Trigger but not in the Tower, and therefore Fast Trigger saw many more Bhabha electrons and beam-gas events. At the ψ' energy and at a current of 12 ma, the Fast Trigger typically contributed 1.2 Hz to the total trigger rate of 3.5 Hz.

The principal elements of the Tower trigger were a total energy trigger (discussed in chapter I), and a trigger based on more complicated event topologies -- the Multiplicity trigger. Major triangle energies formed from analog signals from the Integrate-and-hold modules[113] were routed to the Tower trigger module,[114] where they were converted to

---

[112]"Tower" refers to all the trigger elements excepting the Fast trigger.

[113]G. Godfrey, Crystal Ball memo CB-NOTE 121 (1976).

[114]G. Godfrey, Crystal Ball memo CB-NOTE 131 (1978).

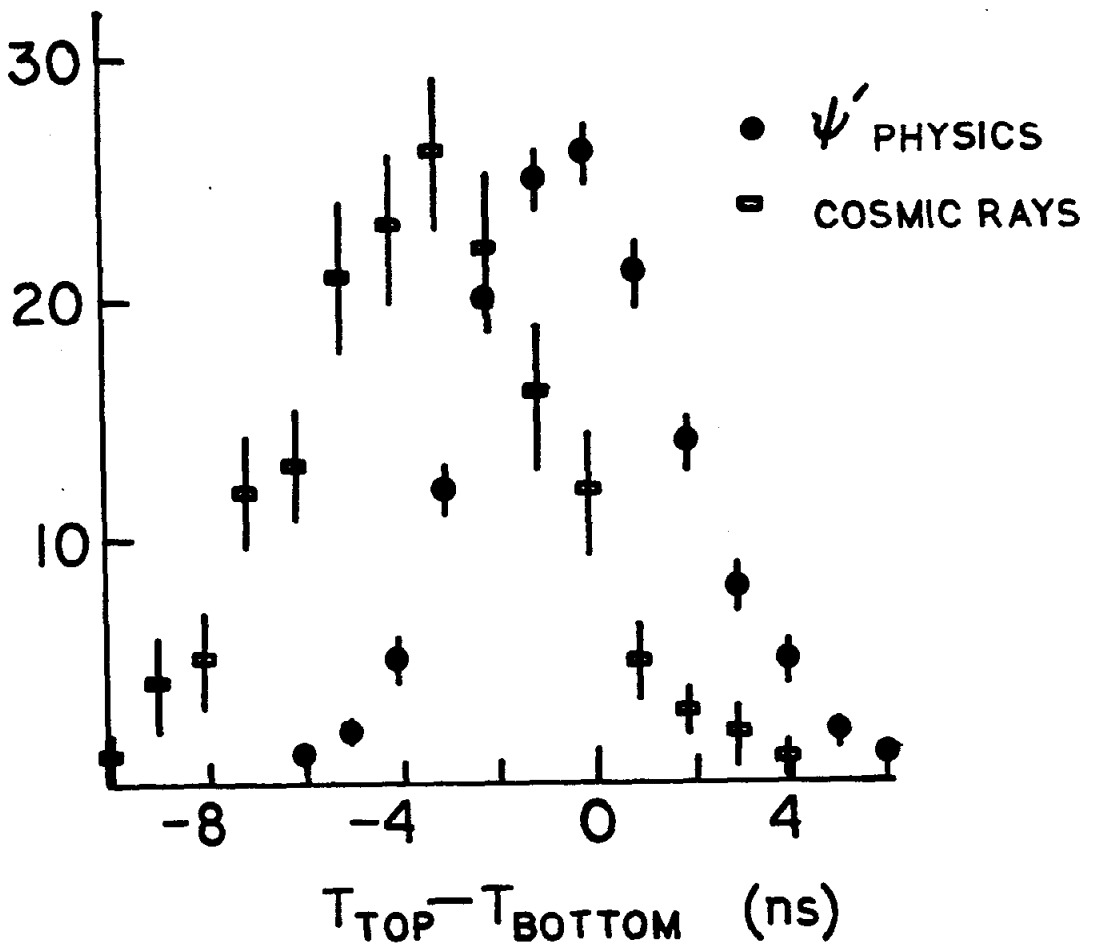

FIG..B-5 Fast trigger top/bottom hemisphere timing.

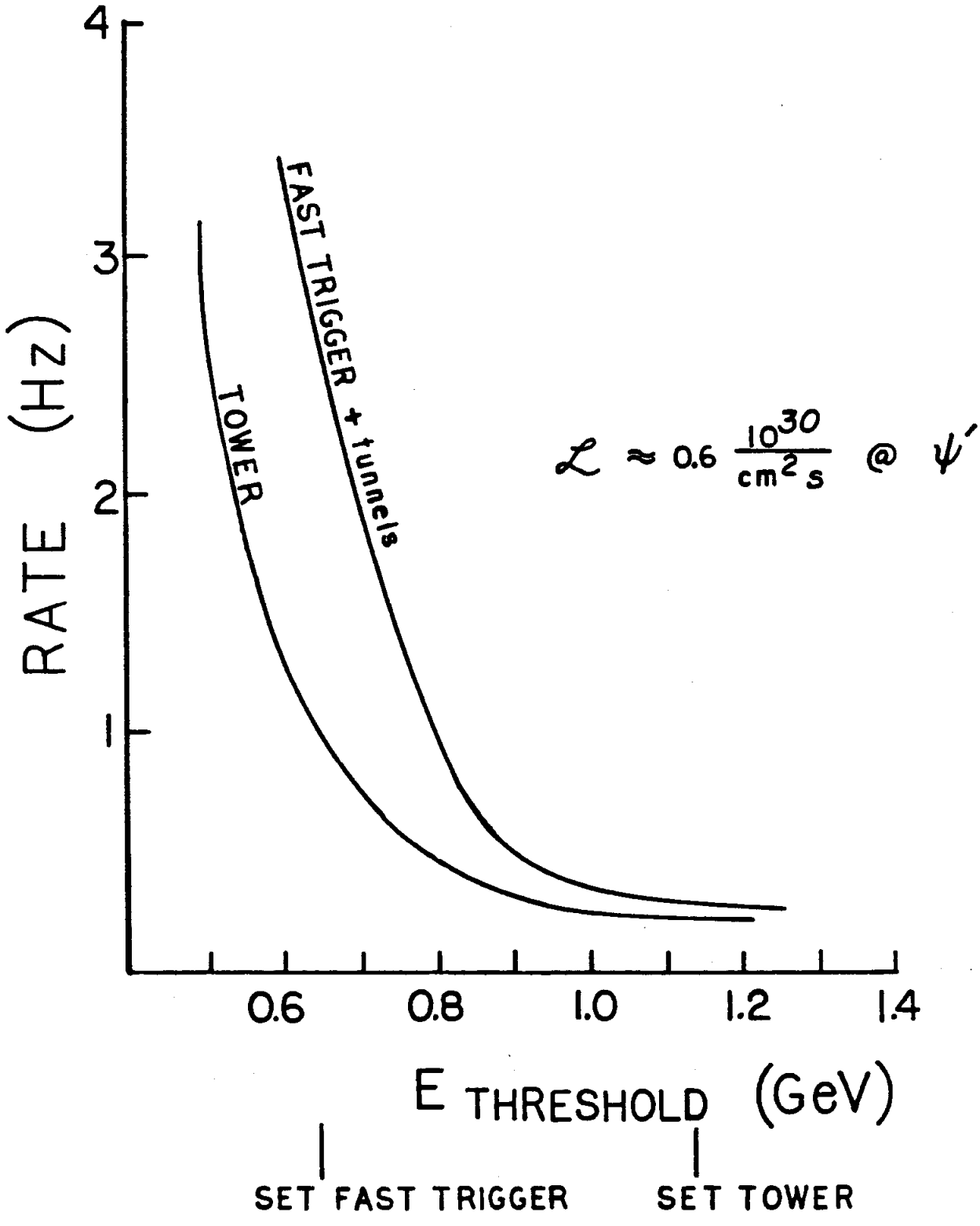

FIG..B-6 Trigger rates for Fast trigger and the Tower (which did not include the tunnel modules). The Tower set point refers to the total energy part of the Tower.

logic pulses in discriminators set to have a threshold of 140 MeV (figure B-7). A decoder then formed logic signals corresponding to 0, 1, 2, 3, or ≥4 major triangles (MT) meeting the discriminator threshold; the ≥4 MT signal caused a trigger without further conditions.

Information from the 2 MT and 3 MT signals was considered only in conjunction with information from the multiwire proportional chambers. Groups of 8 wires from the inner and outer chambers were ORed together to form 18 fixed "segments" in each chamber. Each segment from the inner chamber was then ANDed with the corresponding (i.e., same ϕ value) segment in the outer chamber; if the AND was asserted a charged particle hit was identified. Figure B-8 shows how the 18 segment pairs were all ORed together to determine if there had been one or more hits in the chamber. The grand OR (dubbed Fast OR) was sent to the Tower trigger module, where it was ANDed with both the 2 MT and 3 MT signals. A successful AND with either of the two signals permitted a trigger.

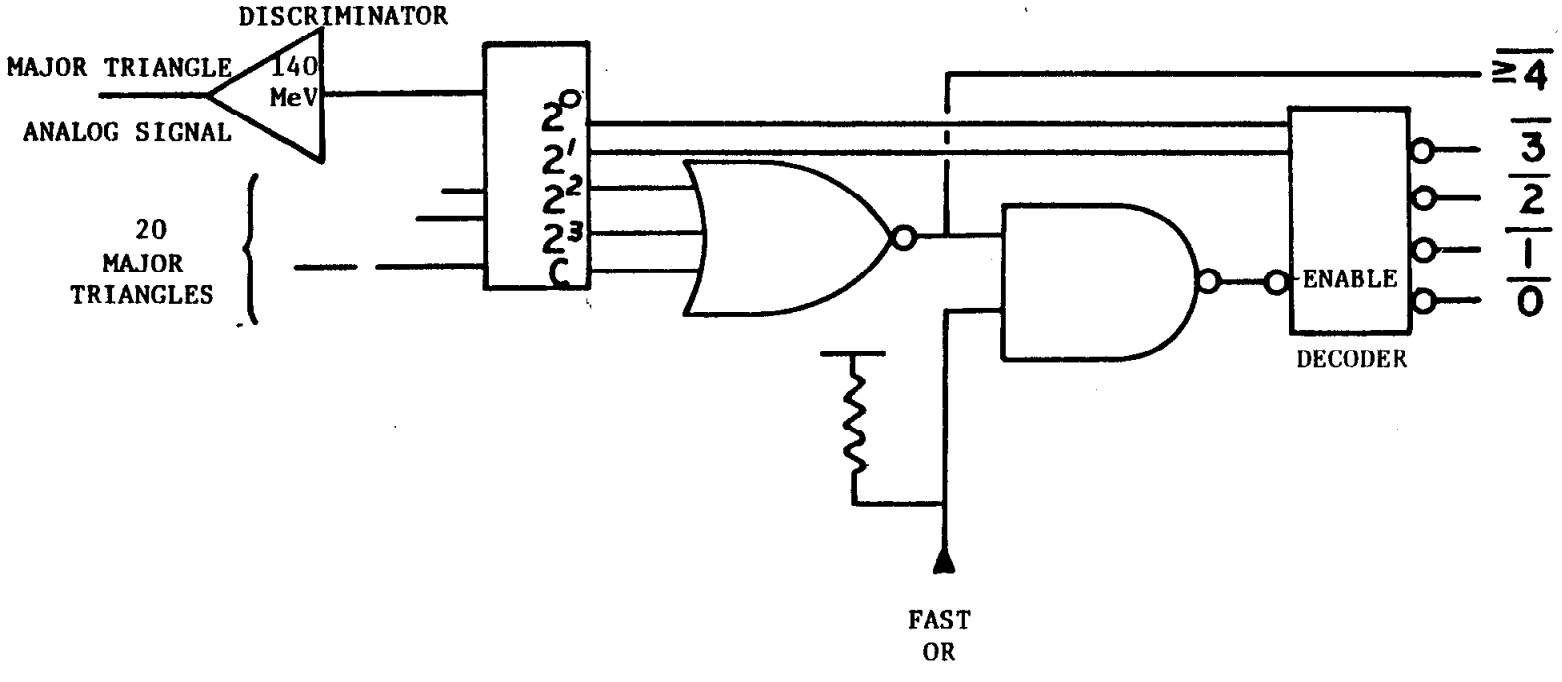

FIG..B-7 Multiplicity trigger logic. The outputs are such that the assertion of the hypothesis means that the wire is at 0 volts.

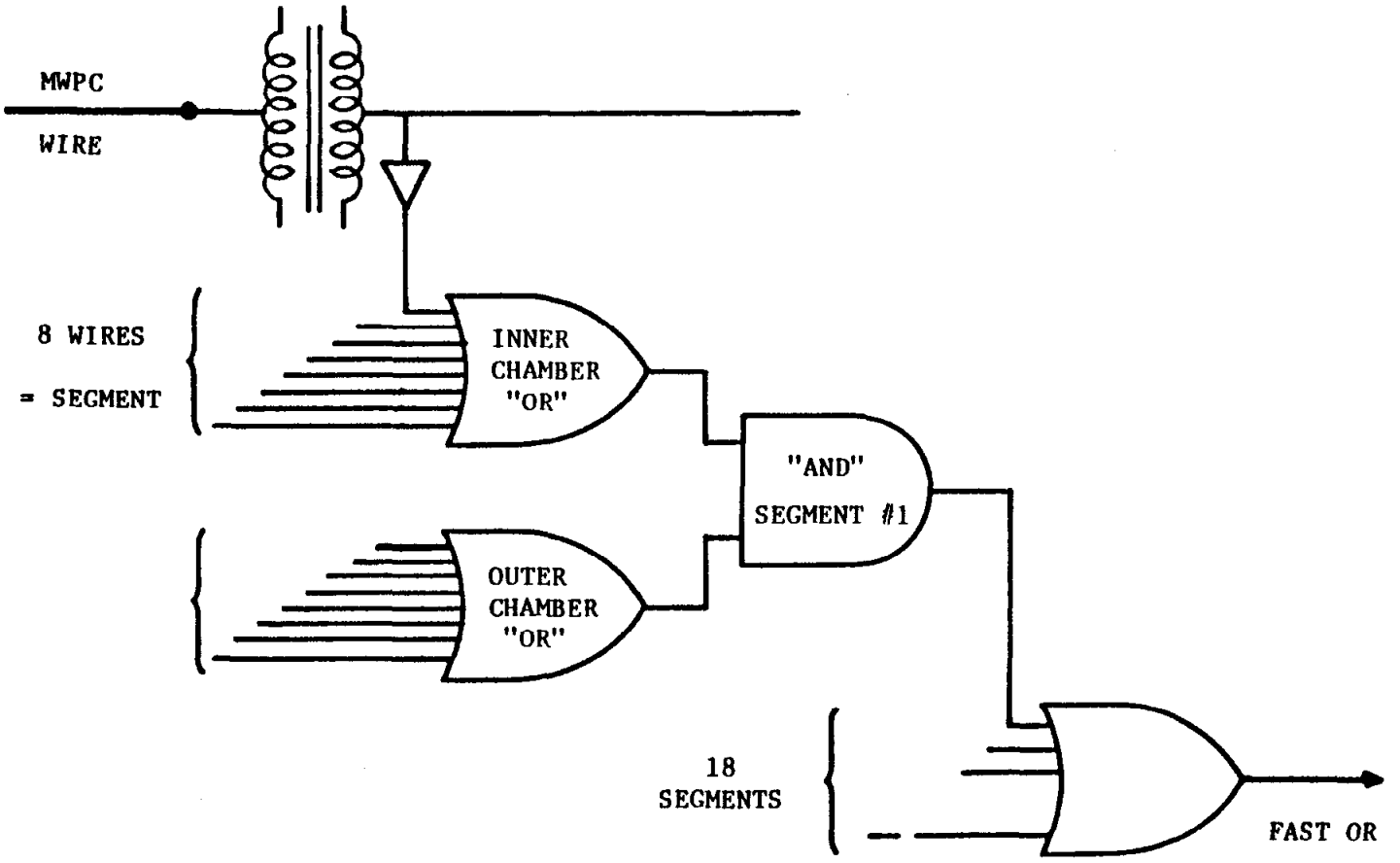

FIG..B-8 Fast "OR" logic.

Appendix C

REJECTED EVENTS

Data acquired in the early part of fall, 1978, when the Crystal Ball detector was still in its infancy, were not considered in this analysis. This early data sample corresponds to about 60 nb^{-1} -- all runs prior to 1037. From this point onwards, selected runs were rejected if the SPEAR operating conditions or performance of the charged-tracking chambers were suspect (mostly the latter). Table C-1 lists these runs and the amount of data they produced.

TABLE C-1

REJECTED RUNS

REJECTED RUN	SIZE (nb^{-1})	REJECTED RUN	SIZE
1051	0.08	1069	0.36
1071	3.76	1099	4.26
1119	0.00	1135	0.00
1905	1.58	1935	4.75
1936	4.33	1926	4.60
2320	4.87	2338	0.00
2458	0.01		
2628	0.17	2719	3.74
2775-2781	16.27	2787	0.38
2855	4.11		

In addition to rejecting runs, several events in the final data sample were rejected after a hand scan (see chapter IV). The event maps for these events are presented in the remainder of this appendix.

TABLE C-2

REJECTED EVENTS

RUN	EVENT	M($\gamma\psi$) high	M($\gamma\psi$) low	M($\gamma\gamma$) (MeV/c^2)
1059	4973	3433	3333	503
2454	4786	3440	3355	244
2460	1140	3412	3387	196
1885	4555	3435	3348	379
2699	5994	3409	3380	322
2703	5971	3628	3155	183
2808	41	3469	3330	95
2815	2287	3461	3341	101
1149	1053	3466	3324	298
2364	5819	3449	3315	514
2670	5956	3459	3323	380
2768	7043	3454	3310	515

RUN # 1059 EVENT # 4973 ETØT= 1092 ECM= 3684

#	CR	TRK	T
1	223	160	C
2	419	185	C
3	185	250	N
4	160	483	N

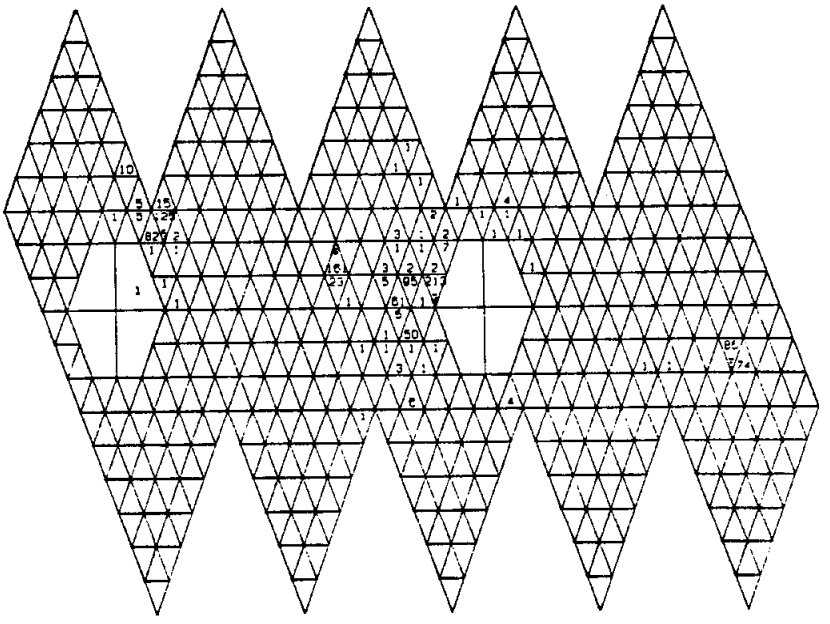

RUN # 2454 EVENT # 4786 ETØT= 1129 ECM= 3684

#	CR	TRK	T
1	181	181	C
2	460	475	N
3	208	255	N
4	211	211	C

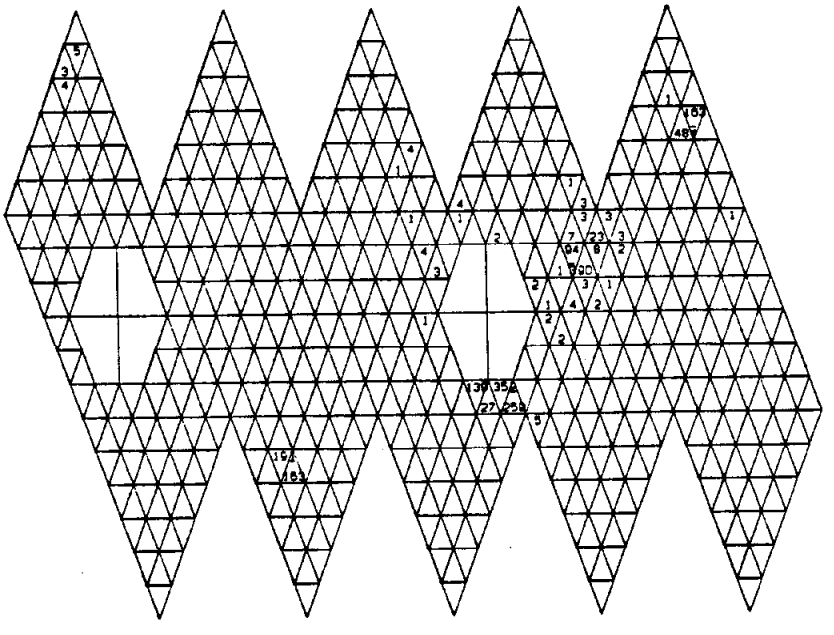

RUN # 2460 EVENT # 1140 ETØT= 3598 ECM= 3684

#	CR	TRK	T
1	218	0	C
2	1373	1696	C
3	232	232	N
4	1629	1421	C
5		253	N

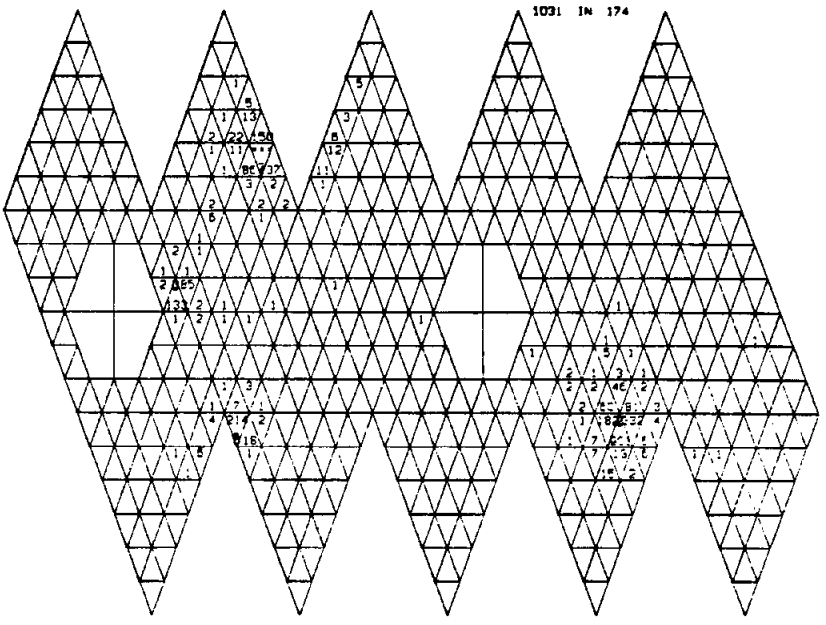

RUN # 1885 EVENT # 4555 ETØT= 1007 ECM= 3683

#	CR	TRK	T
1	282	238	C
2	208	208	C
3	217	306	N
4	238	230	N

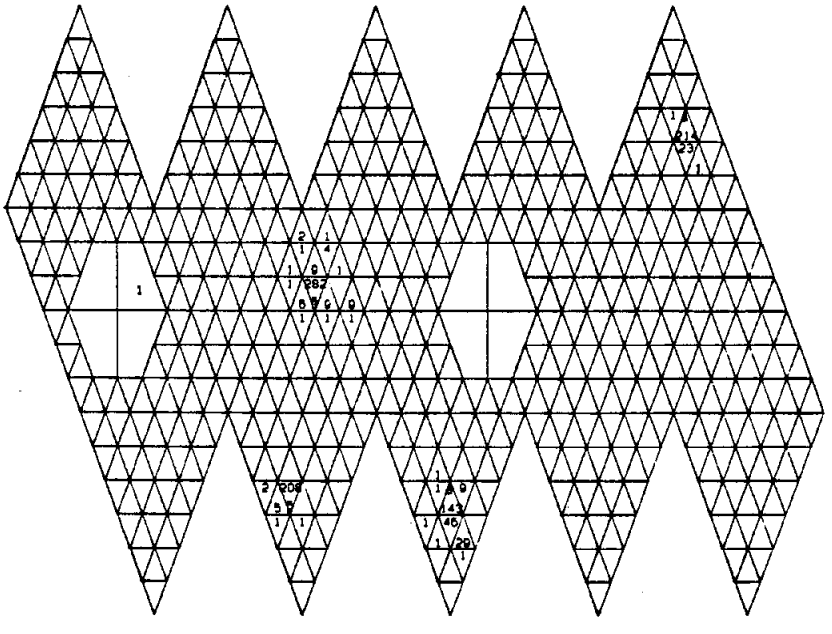

RUN # 2699 EVENT # 5994 ETØT= 962 ECM= 3684

#	CR	TRK	T
1	240	199	C
2	264	211	C
3	211	260	N
4	199	291	N

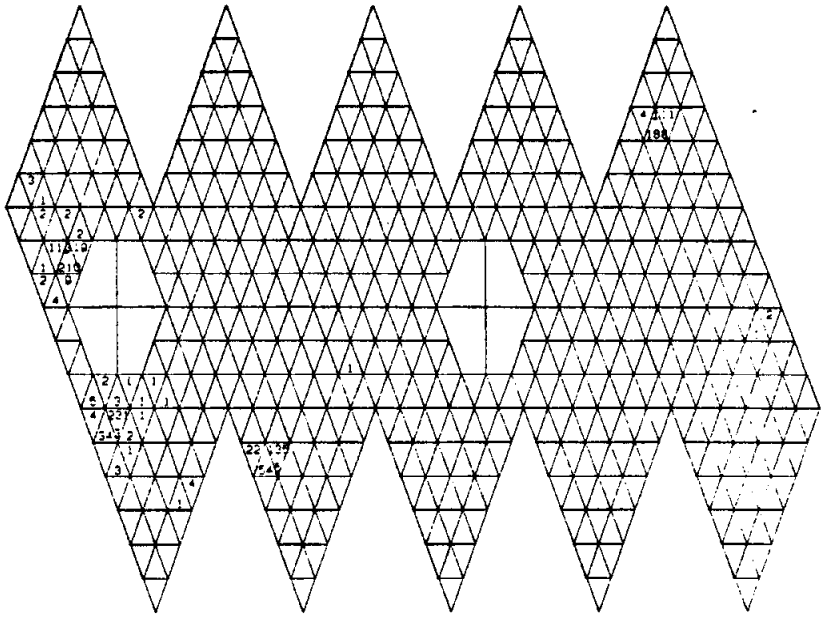

RUN # 2703 EVENT # 5971 ETØT= 3602 ECM= 3684

#	CR	TRK	T
1	1555	1624	C
2	1401	1451	C
3	38	58	N
4	444	473	N

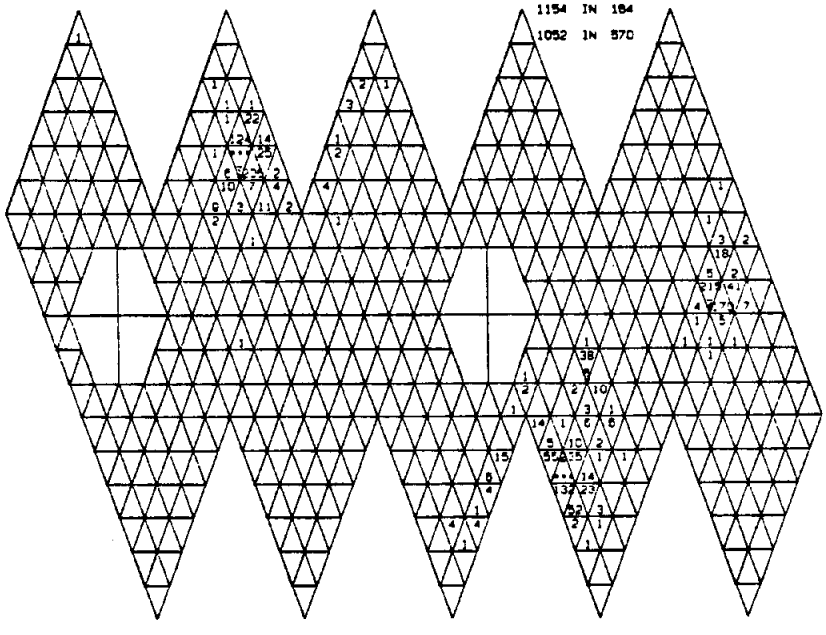

RUN # 2808 EVENT # 41 ETØT= 871 ECM= 3684

#	CR	TRK	T
1	190	189	C
2	455	190	C
3	189	306	N
4		200	N

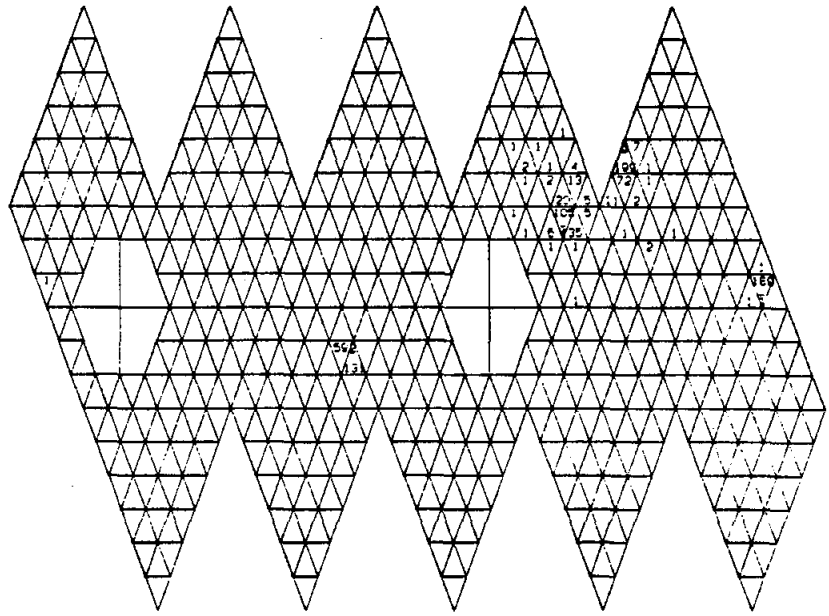

RUN # 2815 EVENT # 2287 ETØT= 887 ECM= 3684

#	CR	TRK	T
1	153	205	C
2	205	153	C
3	184	204	N
4	295	313	N

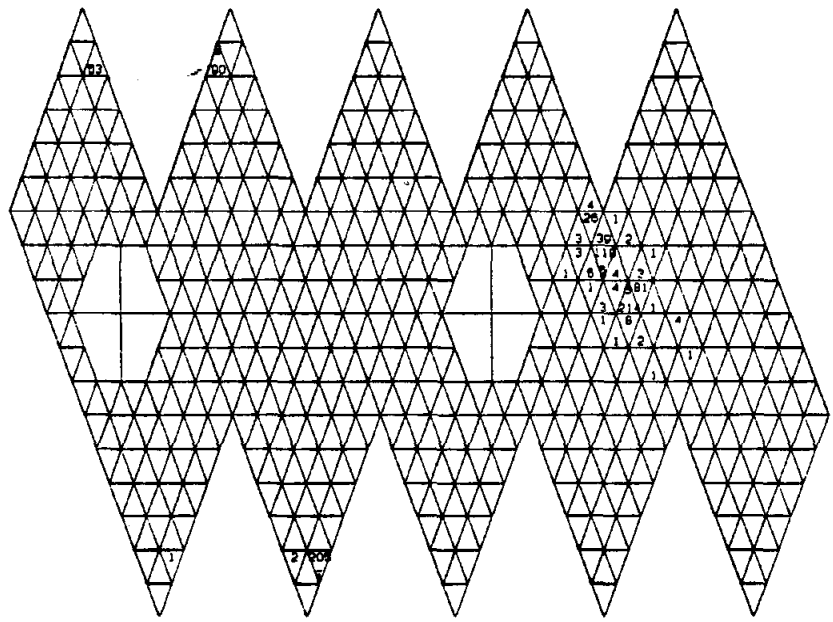

RUN # 1149 EVENT # 1053 ETØT= 3600 ECM= 3684

#	CR	TRK	T
1	1326	1379	C
2	1633	1674	C
3	133	202	N
4	303	323	N

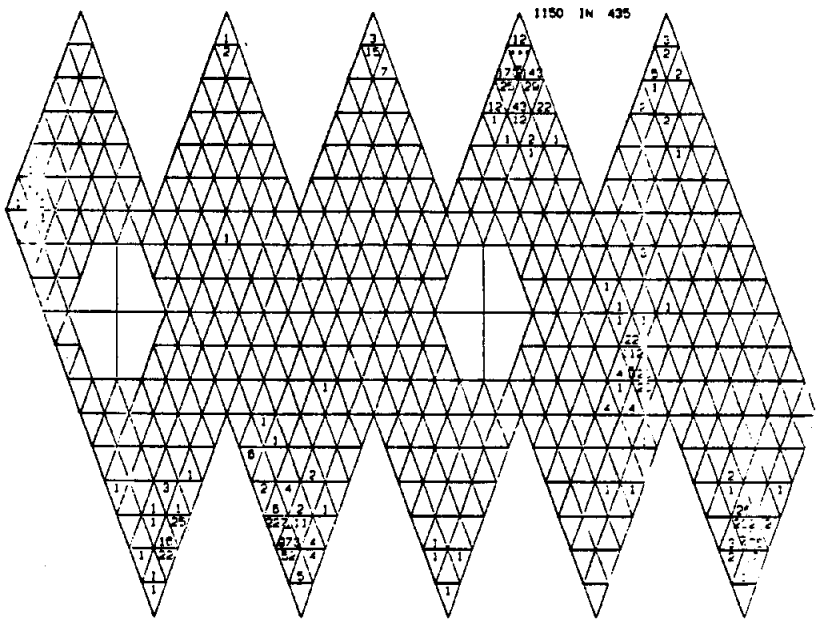

RUN # 2364 EVENT # 5819 ETØT= 3524 ECM= 3684

#	CR	TRK	T
1	1434	1515	C
2	309	1449	C
3	20	329	N
4	1378	20	C
5	191	211	N

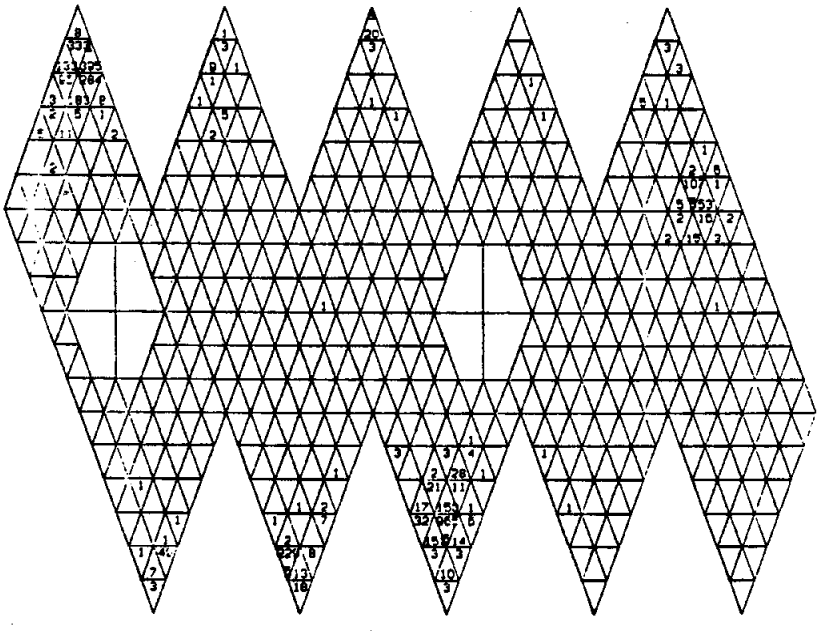

RUN # 2670 EVENT # 5956 ETØT= 3531 ECM= 3683

#	CR	TRK	T
1	308	1477	C
2	1424	319	N
3	1477	1518	C
4	196	220	N

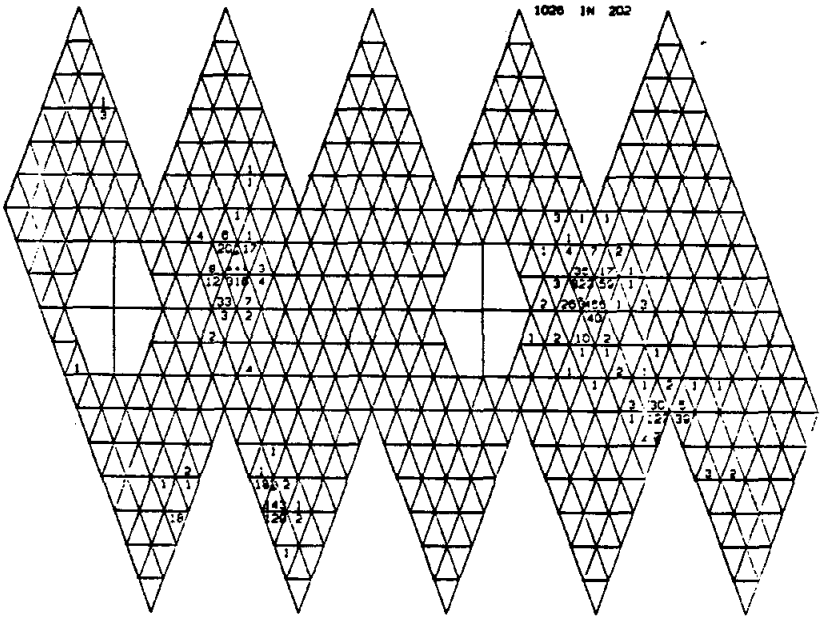

RUN # 2768 EVENT # 7043 ETØT= 3587 ECM= 3684

#	CR	TRK	T
1	1473	1526	C
2	195	1520	C
3	1472	207	N
4	319	336	N

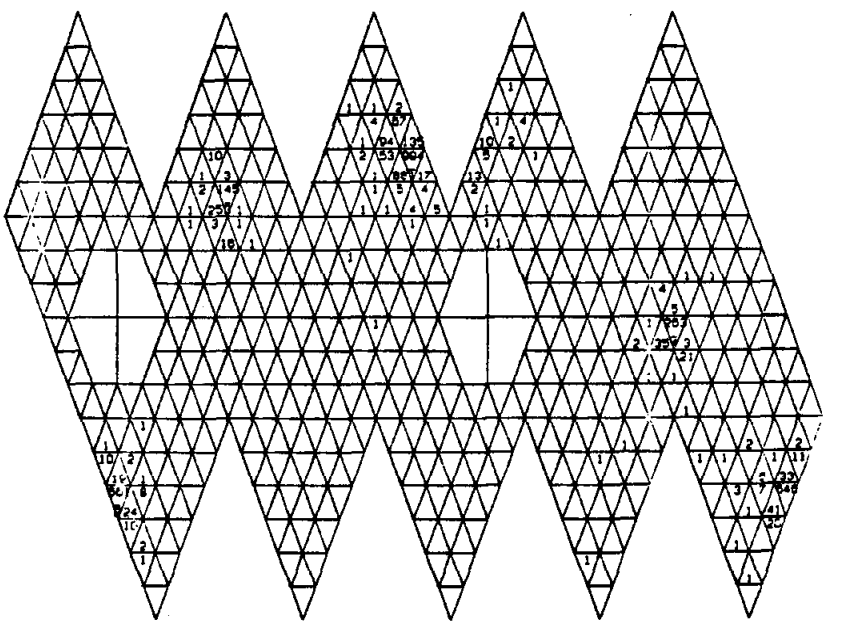

Appendix D

CALIBRATION

Calibration[115] of the NaI(Tl) modules in the Crystal Ball was a three-step process. An initial calibration was performed weekly using the 0.66 MeV ^{137}Cs source to determine the energy/channel slopes, while pedestals were logged as empty target runs while the system was triggered by a pulser. This information was stored on disc and recorded onto the beginning of each data tape. Every two weeks 6.13 MeV Van de Graaff data were acquired in a manner similar[116] to that for normal data and recorded onto tape for analysis at the IBM Triplex. There the data were converted to energy format using the initial ^{137}Cs calibration so that very conservative quality cuts could be imposed during the second-stage calibration: E_c and E_{13} (the energies in the central module and in the $\sum 13$ cluster respectively) for each Van de Graaff calibration event had to exceed 3 MeV, and the ratio E_c/E_{13} had to be greater than 0.5. The latter cut assured that the track was not located near the borders of the central module, for E_{13} was not reliable when this was

---

[115] B.L. Beron et al., Crystal Ball memo CB-NOTE 226 (1977); G.I. Kirkbride et al., IEEE Trans. Nucl. Part. Sci., Vol. NS-26 No. 1, 1537 (1979).

[116] The system operated in the calibration mode -- only triggers from a particular minor triangle were accepted, as during the Cs calibrations.

the case. The low channel pedestals were re-measured prior to an iterative processing of the calibration constants.

For each calibration event:

a) E_c of the maximum crystal was determined

b) E_{13} was computed

c) the event was rejected if $E_c/E_{13} < 0.6$

d) E_{13} for each central crystal i was histogrammed

Then:

f) the deviation of $\langle E_{13} \rangle$ from 6.13 MeV was determined

g) the slope for crystal i was corrected accordingly

i) the sequence a) to g) was repeated
using the new slope values

After three iterations of the above process a final set of constants for each biweekly run period was determined. The high channel/low channel ratios were determined from the data on the condense tapes by examining crystals having the appropriate energy (0-200 MeV) to register in both channels (the low channel had been calibrated by this time). The final set of high channel and low channel pedestals was also determined from the condense tape data. The iterative procedure assumed that the high channel/low channel ratio was independent of energy. The ratio was measured using a calibrated NaI(Tl)-pulse generator and found to remain constant within 2%. By using two light sources (one full strength and the other attenuated) the linearity of the phototubes was measured to be better than 2% ; the results of the study are shown in figure D-1. Ap-

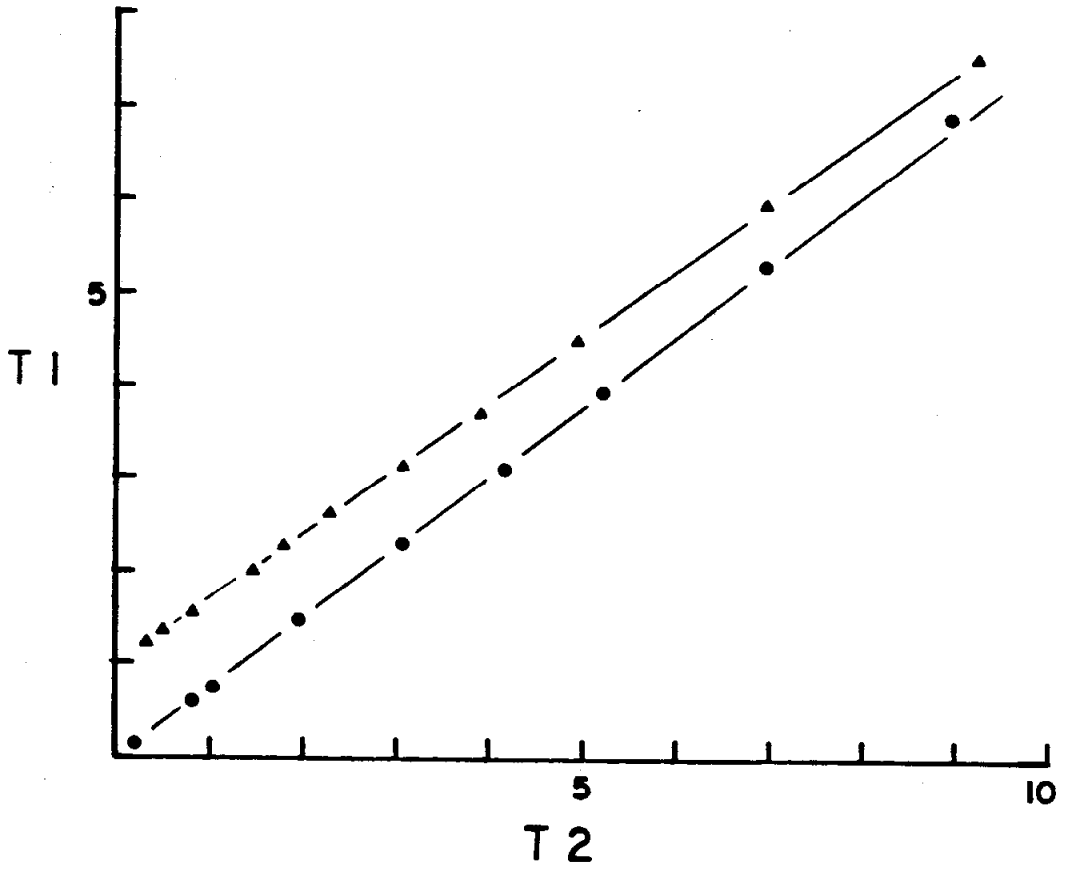

FIG..D-1 Phototube linearity. T1 and T2 refer to two tubes which view the same light pulse, but T2's path is attenuated. Triangles denote the low channel test (~300 MeV max.) and dots denote the high channel test (~3.2 GeV max. into T1) light. The axes show the channel numbers divided by 1000 (100) for T1 (T2); 10^3 is added to T1 in the first case.

parent in the figure is a 1.5% superlinearity at a high channel corresponding to the deposition of 3 GeV into a single module.

Another biweekly adjustment to the calibration constants was made using the Bhabha data acquired during normal running, in a manner similar to that for the 6.13 MeV data. Existing calibration files were not altered during the Bhabha iteration; rather, an independent set of correction factors was formulated and stored on disc together with the final slopes, ratios, and pedestals. For the Bhabha calibration events an upper level cut of 0.83 was imposed on the E_c/E_{13} ratio in order to guard against bias from tunnel modules (for which a large portion of E_{13} was missing).

A shortcoming of the calibration scheme stems from the fairly strong reliance on the initial ^{137}Cs calibration. A significant fraction of the calibration events deposit almost all of the shower energy in a single crystal only for energies on the order of that for Cs. The higher energy calibration points therefore suffer from the intercalibration degradation associated with a summed energy measurement. Poor crystals, or ones which may have drifted a bit, were sometimes excluded from the secondary calibrating process by the cuts on E_c/E_{13}. About 4 to 10 crystals suffered at various times from this problem. For most crystals the calibration stability was quite good and the Bhabha fine tuning was not large (about 5%) -- this is shown in figure D-2. The spectrum for Bhabha events at each stage of the calibration is shown in figure 3-1. Apparent in figure 3-1 is the long low-energy tail which characterizes

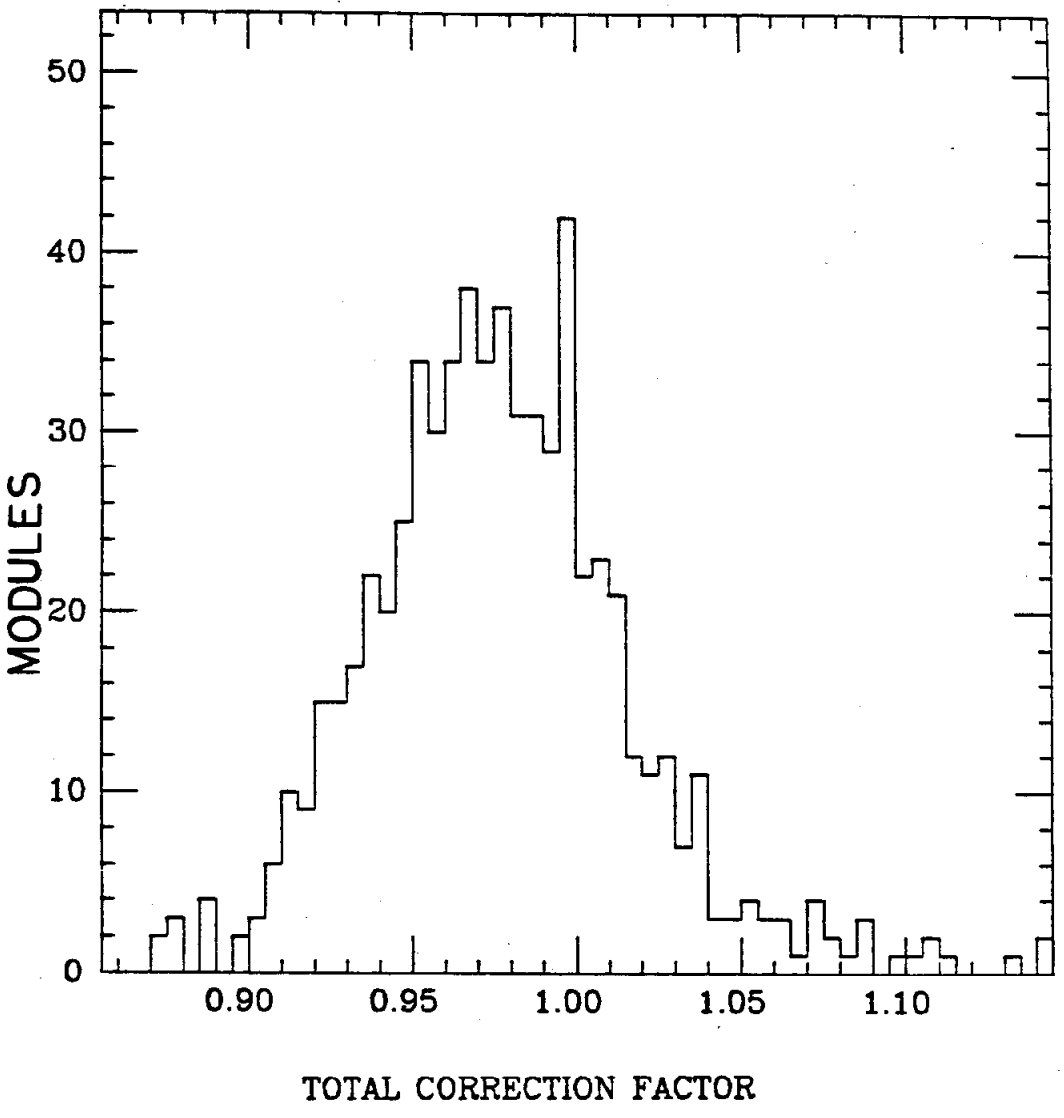

FIG..D-2 Bhabha calibration correction factors.

the NaI(Tl)-measured energy line shape. While no explicit model exists to describe the shape of this tail, the line shape is found to be fit well by the formula:

$$N(E) = \begin{cases} e^{-(E-E_0)^2/(2\sigma^2)} & , E-E_0 > -1.8\,\sigma \\ [1.7\sigma - (E-E_0)]^{-3.5} & , E-E_0 < -1.8\,\sigma \end{cases} \qquad (D-1)$$

By comparing the constants obtained from successive ^{137}Cs calibrations it was determined[117] that these calibrations are accurate to 2%. Changes in the module gains have been monitored continuously and were found to degrade by about 1.4% per year, although a few problem modules near the tunnels had a value up to 12 times larger. The scatter on the crystal degradation measurement is five times larger than the mean, therefore there is no solid evidence for a general deterioration. No visual damage of the NaI(Tl) is apparent, though such damage from radiation or hydration would have to be larger than 20% before becoming discernable. Concerning the tunnel modules, a remeasurement of their compensation curves (see appendix A) along with those for crystals on the equator shows no change within the 2% level. This measurement indicates that the tunnel crystals are not at fault. A possible explanation for the tunnel module degradation is that the phototubes on these modules draw higher currents, owing to the high occupancy of the modules -- a deterioration of the photocathodes would result in a loss of gain.

---

[117] I. Kirkbride, Crystal Ball memo CB-MA TE 248 (1979).

A study of the E_{13} energy as a function of the ratio E_c/E_{13} for Bhabha events is shown in figure D-3. The correlation indicated here represents a dependence of E_{13} on the position of a track within the central module; E_c/E_{13} ($\equiv R$) is simply a measure of this position. A correction for this effect was made to the data by multiplying E_{13} by the factor c:

$$\begin{aligned} c &= 1.055 , && R < 0.40 \\ c &= 0.898 + 0.125\,R , && 0.40 < R < 0.80 \\ c &= 1 , && 0.80 < R \end{aligned} \qquad \text{(D-2)}$$

As the energy of the incident showering particle varies, the energy measurement resolution of NaI(Tl) is found to vary as

$$\sigma(E) = \sigma_0 \; E^{3/4} , \qquad \text{(D-3)}$$

for E in GeV. The Crystal Ball prototype was used to check this behavior in a modular NaI(Tl) array; the results, shown in figure D-4, support the $E^{3/4}$ law. Furthermore, the expected variation was witnessed for Bhabha electrons and $\psi' \to \gamma\chi(3.51)$ photons in the Crystal Ball apparatus. All of the calibration sources from 0.66 to 6.13 MeV yielded a resolution (σ_0) of about 1.5% -- one half of that observed for the higher energy lines, suggesting that there is an energy dependent intercalibration error which bifurcates in the 10-100 MeV region. It should be pointed out that all the low energy calibrations are accomplished in a matter of hours, while the Bhabha samples are accumulated over a full week; this makes the latter more prone to intercalibration effects. Studies of the effect of crystal compensation on resolution at high energy, and the variation of the curves for compensation-vs.-distance into

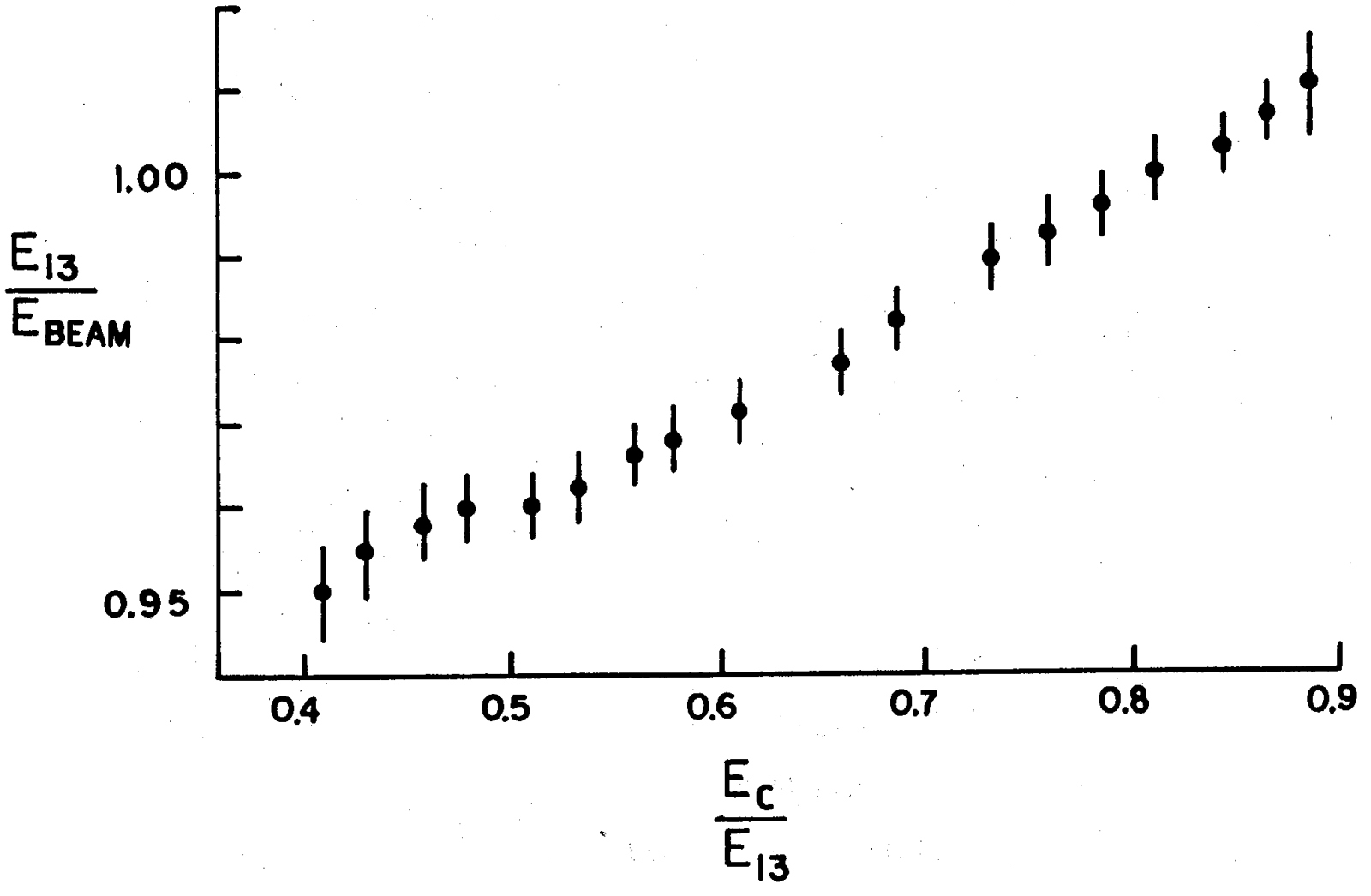

FIG..D-3 Position dependent correction factor.

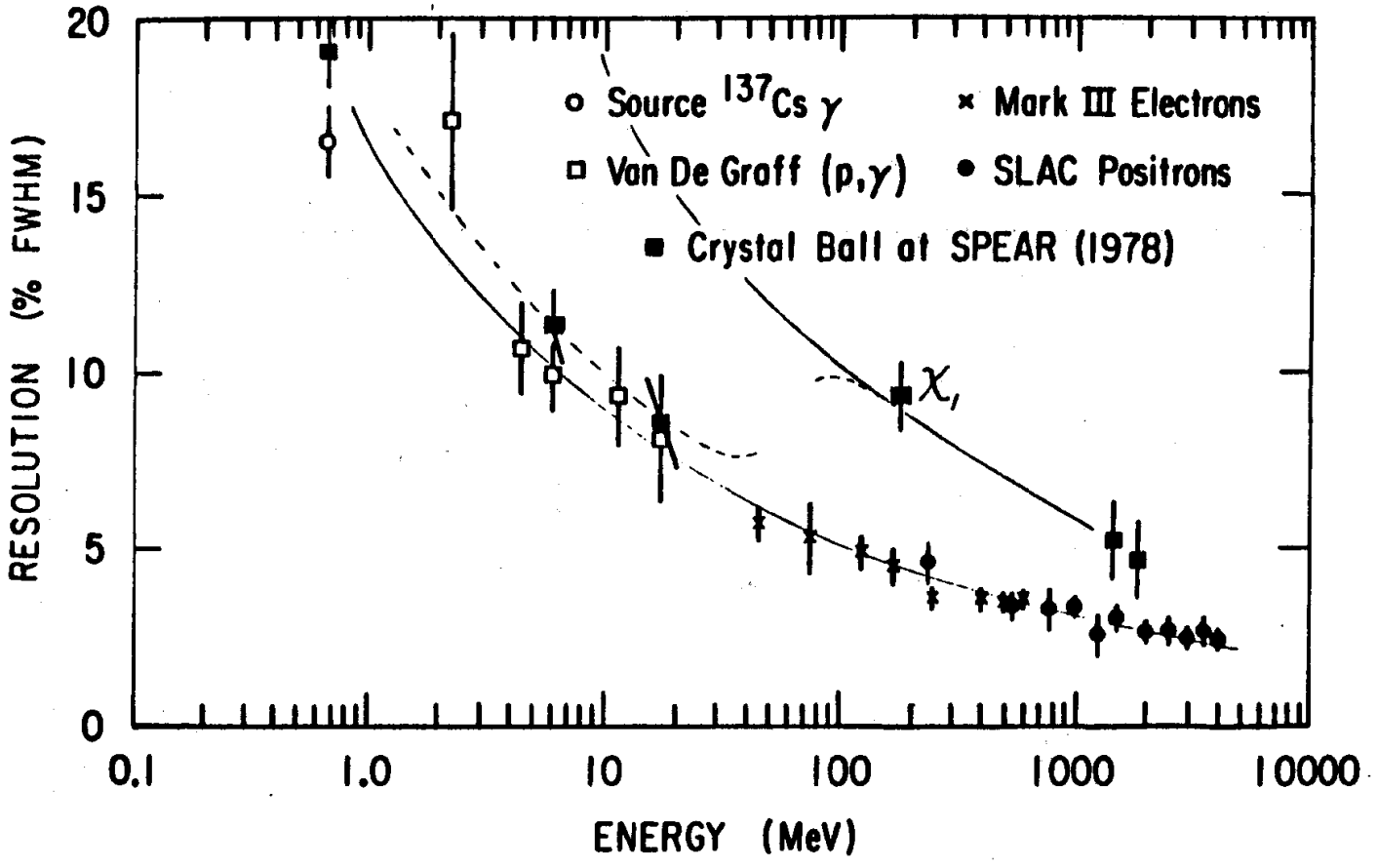

FIG..D-4 Resolution achieved for this apparatus and for an earlier prototype version.

the crystal, find an additional 3% degradation in the resolution due to the compensation variation. The compensation effect represents a form of intercalibration error. Another 2% resolution degradation results from the calibration stability; the high channel/low channel correspondence also contributes 2%. Combining these effects in quadrature gives a total resolution of 5% at 1 GeV, leaving a component of 4% to 5% which is unaccounted for, but could well arise from an intrinsic intercalibration error or from other fluctuations.

Appendix E

ELECTROMAGNETIC SHOWERS AND NEUTRAL TRACKING

When an electron emits bremsstrahlung in a material the resulting photon can produce an e^+e^- pair, which in turn radiate, thus initiating an electron-photon shower.[118] The exponentially increasing proliferation of daughter particles as the material is penetrated is quenched by ionization energy loss of the electrons:

$$-dE/dx\big|_{ion} = 307\ \text{KeV}\ \text{cm}^2\text{g}^{-1}\ \rho Z A^{-1}\ \ln(2mv^2\gamma^2 I^{-1} - 1) \qquad \text{(E-1)}$$

where I is the effective ionization potential (approximately given by 10 eV · Z), $\langle Z\rangle$=32, $\langle A\rangle$=75, and ρ=3.67 g cm^{-3} for NaI. Since the radiation loss in the shower is given by:

$$-dE/dx\big|_{rad} = 1.4\times10^{-3} Z^2 A^{-1} \text{cm}^2\text{g}^{-1}\ \rho E\ \ln(183\ Z^{-1/3}) \ , \qquad \text{(E-2)}$$

it is clear that the energy release in the shower is quenched when the ionization loss equals the radiation loss; this occurs when E is diminished to the level of the critical energy E_c (equal to 17.4 MeV for NaI). In this approximation the shower maximum occurs at a distance of $\log_2(E_0/E_c)$ radiation lengths (L_{rad}=2.59 cm for NaI) into the material, where E_0 is the incident particle's initial energy. A maximum of about E_0/E_c daughter particles is produced during the shower evolution, so

---

[118] B. Rossi, High Energy Particles, Prentice-Hall, Englewood Cliffs, New Jersey, (1952).

that the resolution of shower-measured energy would scale as $\sqrt{E_0}$ on the basis of statistics alone.

Only about 10% of the shower energy is converted into measureable light in NaI(Tl), a 1 GeV/c^2 photon producing about 10^6 photons in the 320 to 530 nm band. The shower generated light has an intensity which varies exponentially in time, with a rise time of about 50 ns and about a 250 ns time constant for the decay. Since the optically isolated modules are of a smaller dimension than the transverse shower extent, the measured energy resolution suffers from intercalibration effects in addition to the photostatistics. One finds that the resolution on NaI(Tl)-measured energies scales as $E^{3/4}$; however, no cogent model has been devised to account for this scaling.[119]

Approximations of the analytic expressions for shower development are not necessary if the Monte Carlo technique is employed to study the shower evolution. Such studies of showers in lead glass[120] have successfully simulated the observed behavior, and a reliable electron-gamma shower Monte Carlo (EGS)[121] has been developed at SLAC; the latter has been used extensively in developing the Crystal Ball analysis programs. Radial (i.e., transverse to the incident-particle trajectory) shower development has been found[122] to behave as:

---

[119]There is some explanation of the scaling in the work by R. Carrington et al., Nucl. Inst. Meth. 163, 203 (1979).

[120]E. Longo and I. Sestili, Nucl. Inst. Meth. 128, 283 (1975).

[121]R. Ford and W. Nelson, report SLAC REPORT 210 (Stanford) (1978).

[122]F. Bulos and A. Liberman, Crystal Ball memo CB-NOTE 127 (1977).

$$\frac{df(\phi)}{d(\cos\phi)} = \frac{0.151\ e^{-70(1-\cos\phi)}}{1 - \cos\phi + 0.0021} \qquad \text{(E-3)}$$

where $f(\phi)$ is the energy fraction in a unit area and ϕ is the angle between the incident particle trajectory and the point being considered. This function has proven valuable in reconstructing tracks by using the energies measured in a cluster of NaI(Tl) crystals.

A Crystal Ball prototype[123] was used in an electron test beam at SLAC to study the behavior of high energy shower evolution. In figure E-1 are shown several examples of the shower profiles as the test beam was aimed at different locations on the front surface of the target crystal (the central module). By continuing this procedure with the target point running along a line from a vertex to the midpoint of the flat edge of the central module, all possible shower configurations for the detector were generated. The plot of energy measured by the central module as a function of the target position is shown in figure E-2; the central module measures 50% or more of the incident particle energy 85% of the time. As mentioned in chapter III, the most convenient method for measuring energies from showering particles consists of forming the sum of the energies in the central crystal and its 12 nearest neighbors. There is only minor improvement in the resolution when larger clusters are used to sum the energy. A comparison of the E_{13} energy with that for a cluster of all concatonated illuminated crystals is shown in figure E-3. From the figure, which depicts the energies for Bhabha electrons, it is

---

[123] Y. Chan et al., IEEE Trans. Nucl. Part. Sci., Vol. NS-25, No.1, 333 (1978).

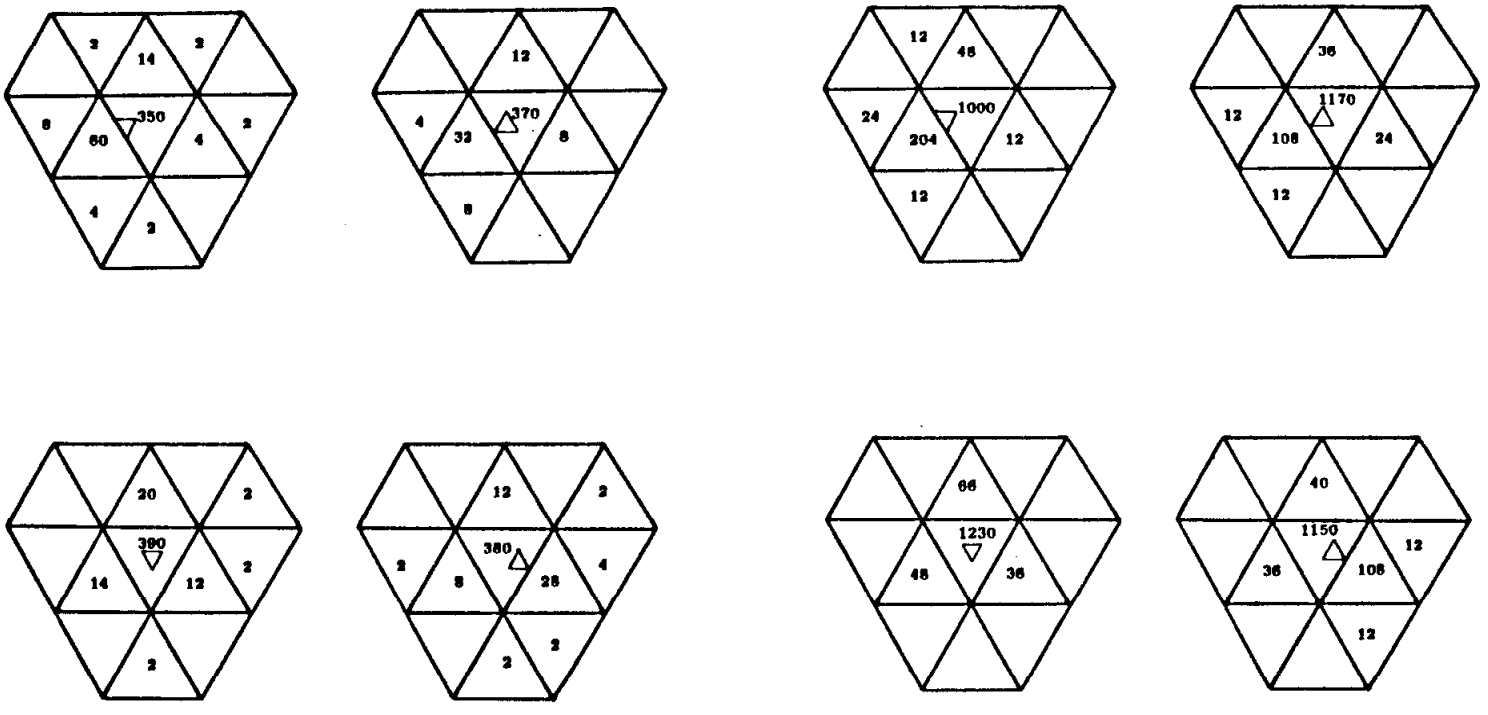

E = 526 MeV

E = 1505 MeV

FIG..E-1 Shower profiles.

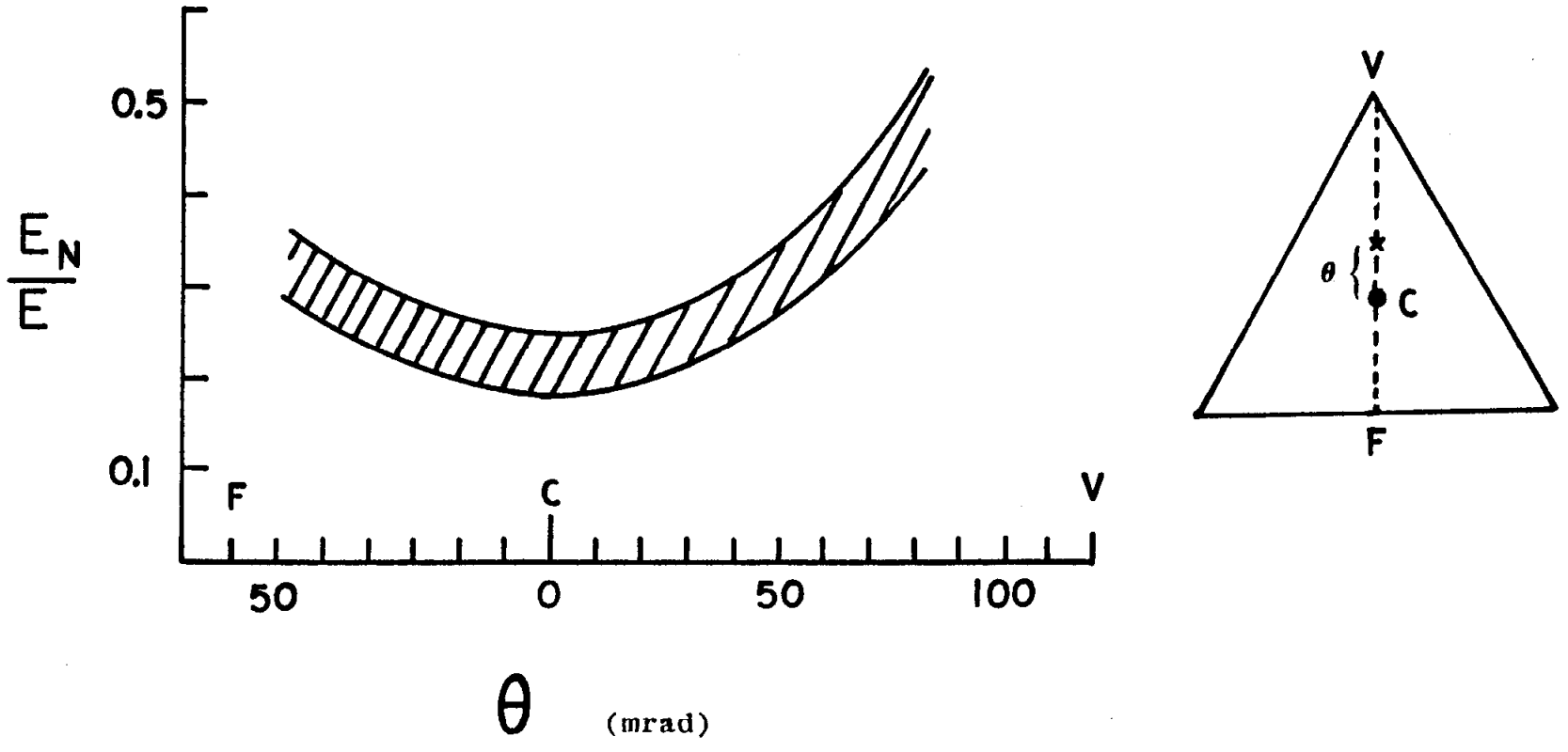

FIG..E-2 Percentage of energy in the neighbor crystals (E_n) as a function of the photon position in the central module. E covers the range 100 to 2000 MeV.

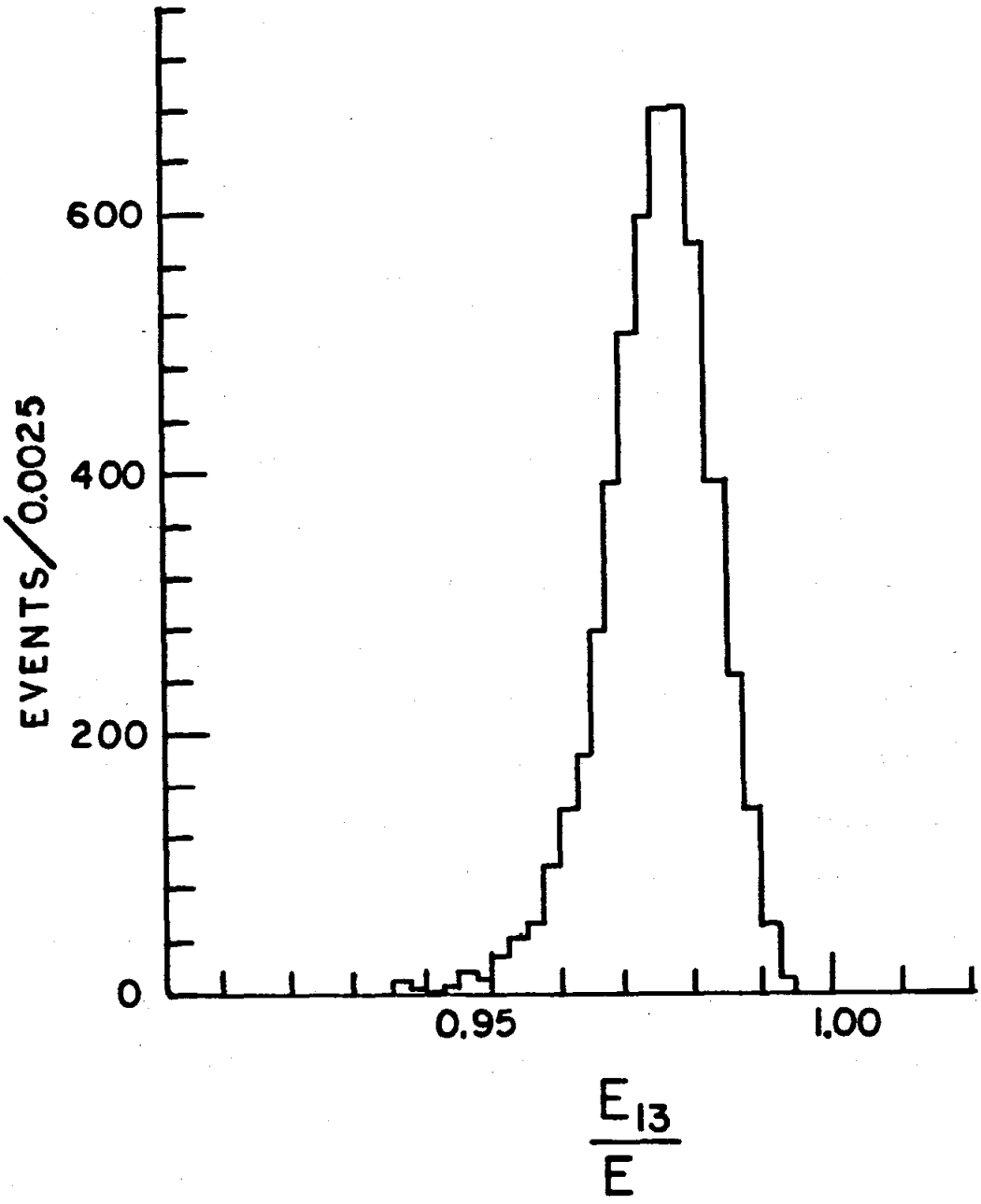

FIG..E-3 E_{13} distribution for 1.8 GeV electrons.

apparent that the $\sum 13$ energy represents 97.5% of the full energy of a showering particle.

An attempt was made to reconstruct the trajectory of the test beam by forming the energy-weighted sum of the centroid vectors for all crystals comprising the $\sum 13$ cluster; however, this center of gravity technique proved to be unreliable for trajectories near the vertices of the central module. A much more rigorous approach consisted of comparing the measured shower profile with that predicted for various target positions in the central module. The predictions were made using the radial shower evolution function given in (E-3), and then the best trial position was chosen by minimizing χ^2. For the trial target positions, the central module was subdivided into 16 imaginary submodules; the test beam was assumed to be aimed at the centroid of each submodule, examples of which are shown in figure E-1. After the optimal submodule trajectory was determined, the actual trajectory was taken to be a vector from the vertex to a point randomly smeared over the front surface of the submodule. This method proved to be far superior to the simple weighted-centroid technique. For the actual Crystal Ball apparatus, the tracking accuracy and its energy dependence for trajectories originating from the z=0 origin are shown in figure E-4; the resolutions needed to optimize the kinematic fitting program for real data support the resolutions obtained from the Monte Carlo study. The energy scaling apparent in figure E-4b is actually quite similar to the $E^{3/4}$ behavior of the energy resolution scaling.

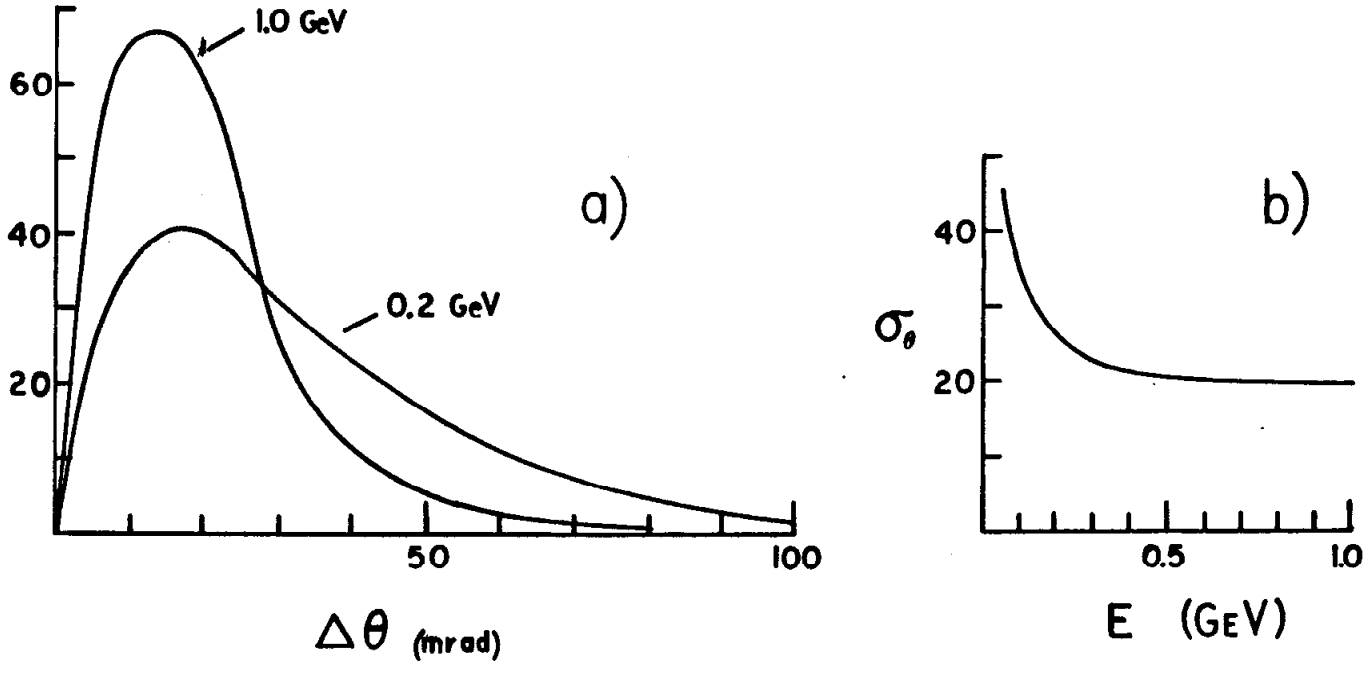

FIG..E-4 Neutral tracking for z=0 (from experiment). a) shows the distribution for the reconstruction angle; b) shows its deviation.

For track origins which have $z \neq 0$, the reconstruction accuracy degrades rather rapidly; this is shown on figure E-5. Fortunately, the standard deviation of the interaction region at SPEAR is only 2.6 cm, thus the average tracking resolution is quite similar to that shown in figure E-4.

In practice there were many tracks to be reconstructed in a single event -- a method was required for sorting out the separate tracks and testing if they were real tracks or just fluctuations in the evolution of a large shower. The sorting process was accomplished in two logical steps. First, the regions of concatenated (and illuminated) crystals were identified, though such a "connected region" may actually result from the coalescing of several incident particles. In order to discriminate against shower fluctuations and "spray" (very low energy scattering from particles striking other parts of the apparatus) a threshold of 10 MeV was chosen to define a crystal as "illuminated". If the threshold was much higher, single tracks of energy less than 20 MeV were lost. Conversely, if the threshold was lower, normal shower fluctuations for higher energy photons tended to create too many connected regions. From this argument the optimal definition of a connected region was determined to be:

CR = a set of contiguous crystals, each
displaying an energy greater than 10 MeV.

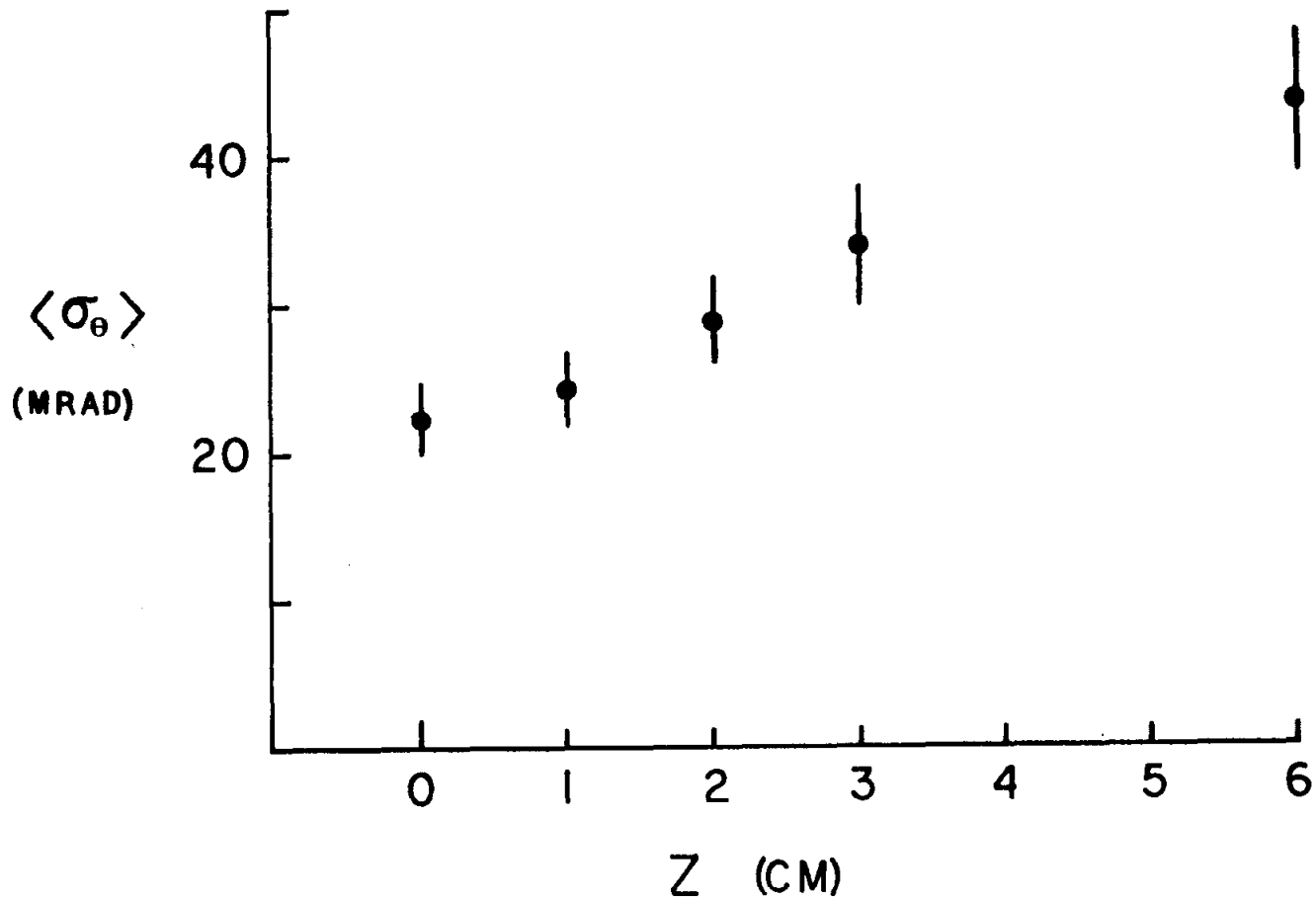

FIG..E-5 Deviation of reconstructed neutral tracking angle as a function of vertex (from a Monte Carlo simulation).

At this point the sets of energy clusters, each the result of an interaction by one or more particles, have been separated. The next step is to scan the energy topology of the connected region in order to determine the number of particles involved, as well as their interaction positions. Crystals in a given connected region were first energy-ordered, the highest assumed to contain the interaction maximum of one particle (a "bump"). Comparing the remaining crystals to the bump module, one next endeavored to determine if the crystal in question had an energy which could not have resulted from a shower fluctuation of the previous bump module. If this was the case another bump had been found, and the process continued for all crystals in the connected region. The bump criterion alluded to took the form of a function (the Bump Discriminator)[124] of the energy ratio and the difference angle (ϕ) of the crystal under test (i) and the existing bump module (b):

$$f(\phi) = \begin{cases} .72\ \exp(-9.4\cdot(1-\cos\phi)) & , \ 12° < \phi < 45° \\ 1 & , \ \phi < 12° \\ 0 & , \ 45° < \phi \end{cases}$$

$$f(E_i, E_b, \phi) = (E_i/E_b) - f(\phi) \ . \qquad \text{(E-4)}$$

The module under test constituted another bump if $f(E_i, E_b, \phi)$ was positive. Essentially having the same form as that describing the electromagnetic shower development (E-3), the Bump Discriminator must necessar-

---

[124] R. Partridge, Crystal Ball memo CB-NOTE 6 (1979).

ily fall more gradually with ϕ, as it describes shower fluctuation development. A scatterplot of energy ratio vs ϕ for events at E_{cm} = 3684 MeV was used to decide on the parameters entering the discriminator function; it is shown in figure E-6. The region of the scatterplot which must fail the ratio test consists of the relatively constant-density region in the lower portion of the plot. The stripped behavior apparent in the figure results from the discrete nature of the neutral track finding algorithm (i.e., the smallest angle is that describing a sub-module).

For the clean electromagnetic and minimum ionizing tracks in $\gamma\gamma l^+l^-$ events the function has proven itself entirely reliable. Overlap of tracks with an opening angle less than 26°, even though separated by the Bump Discriminator, prove difficult to measure accurately, as the neutral tracking is invalidated by confusion of the two shower patterns. For this reason, events with a track pair initially found to have an opening angle less than 26° were not included in the final data sample.

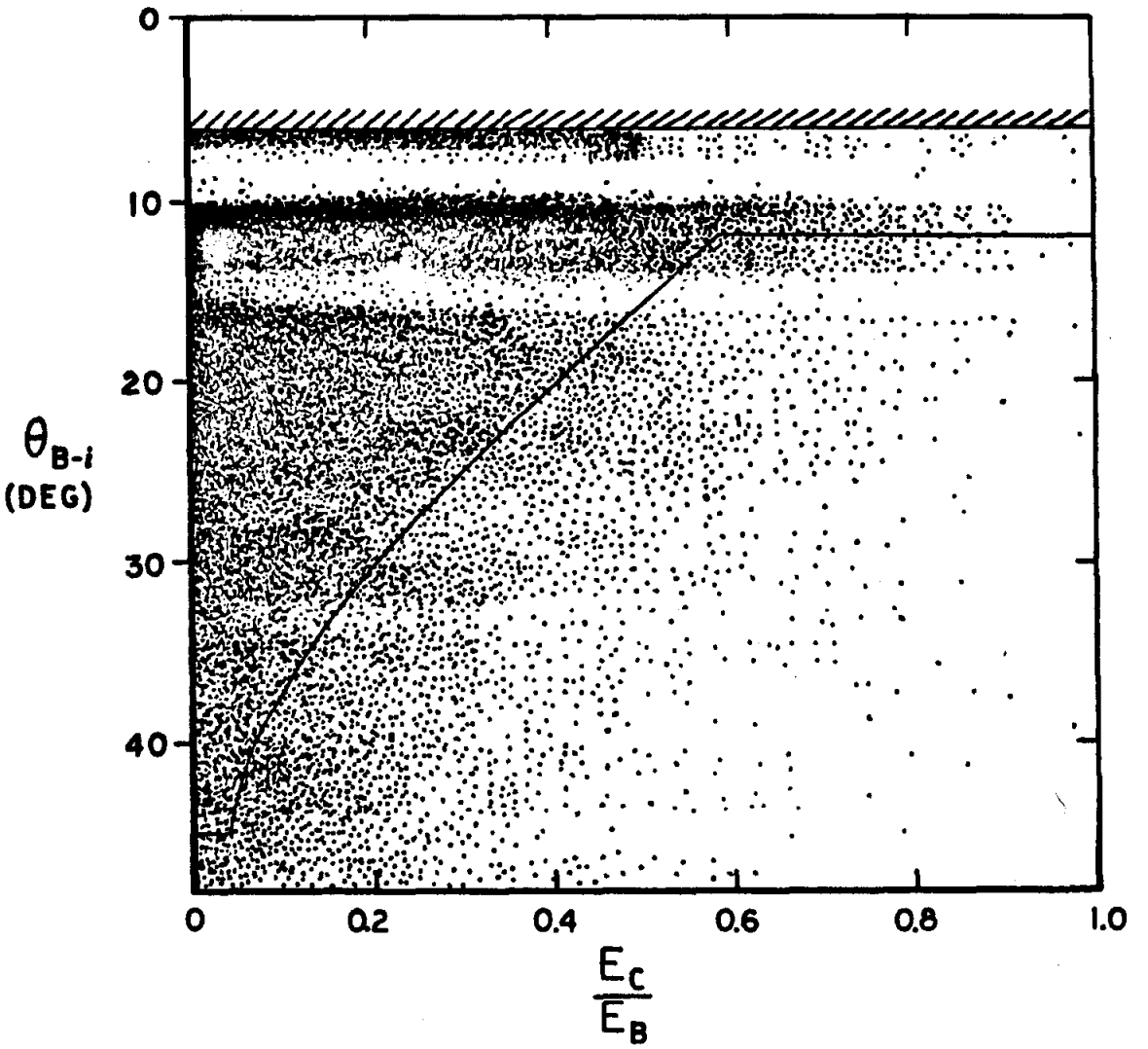

FIG..E-6 Scatterplot for Bump Discriminator Function (see text).

Appendix F

CHARGED TRACKING AND TAGGING

Because of their much finer spatial accuracy, only the inner and outer spark chambers were used in reconstructing charged tracks. In practice the ϕ and z spatial positions of each track were fit independently using the straight and crossed planes. A primary assumption in making these fits was that both the x and y positions of the actual interaction point were zero, an assumption which was verified post hoc. After such a measure of the interaction position z was computed for each track, a better measure of z was obtained from a weighted average of the vertices determined by each track, followed by re-fitting using this final vertex position.

The flow-chart in figure F-1 outlines the track finding procedure. Minimal requirements for reconstructing a track were that at least one straight plane and one crossed plane in each chamber had registered a spark. Two passes were made over the spark data, the first requiring that a "pair" be found in at least one of the two chambers. A "pair" is defined as a correlated hit in each of the two (outer) crossed planes of a chamber, "correlated" implying that, assuming both cross-hits are associated with the same value of ϕ, a line intersecting both hits passes reasonably near z=0. Relaxing this restriction in the second pass, the

SPARK CHAMBERS: FIRST PASS ALGORITHM

FOR Track candidate i :

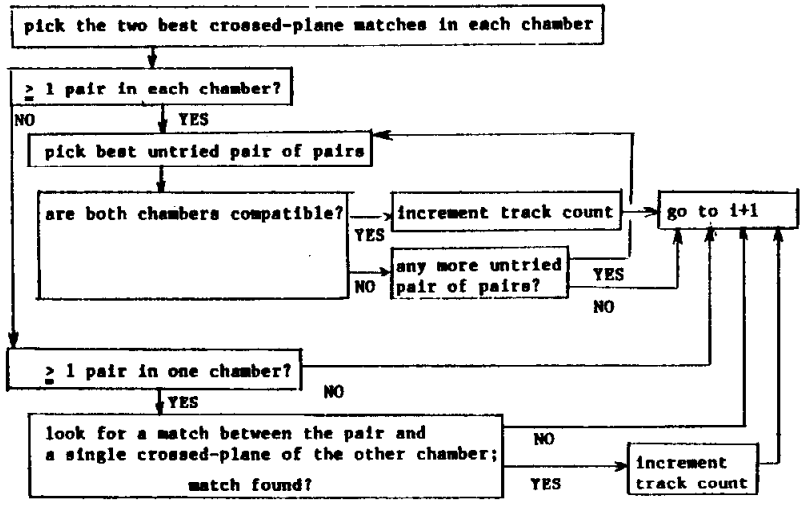

RETRY PASS ALGORITHM

MUST HAVE ≥ 1 STRAIGHT HIT IN EACH CHAMBER :

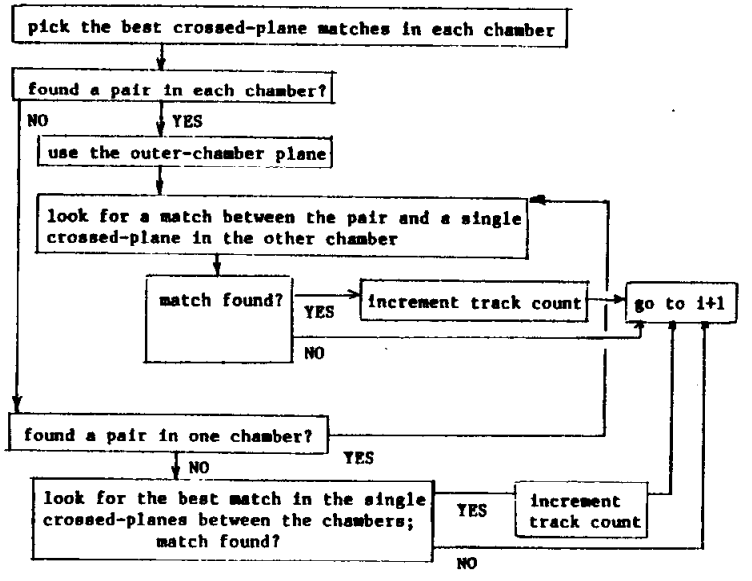

FIG..F-1 Charged tracking algorithm.

minimal criterion for assigning a track was the existence of a hit in a single cross-plane of each chamber, again correlating with a trajectory near the origin. This, of course, was in addition to the fundamental requirement of a straight-plane hit in each chamber, which served to define ϕ.

Bhabha events had the virtue of providing easily identifiable back-to-back electrons, and so were invaluble for testing the chambers and the charged tracking algorithm. Figure F-2a shows a scatterplot of the deviation of the Bhabha opening angle from 180° as a function of the azimuthal angle ϕ, where the polar axis is defined by the positron direction. The clear sinusoidal variation is indicative of an interaction vertex which is displaced from the origin in the x-y plane. A displacment of about -1 mm in x and -2 mm in y was incorporated in the fitting routine to obtain the smooth scatterplot seen in figure F-2b. Uniformity in ϕ is demonstrated in figure F-2c. In figure F-3 the chamber reconstructed trajectories are compared with those obtained from the neutral tracking program. The results of this study for the NaI(Tl)-reconstructed tracks agree well with the Monte Carlo for neutral tracking, and the 2° peak in figure F-3a is simply due to phase space. The spike effect apparent in figure F-3d is due to the granularity of the neutral tracking algorithm.

The Bhabha events were also used to check the single plane spark efficiency, and found it to average 0.94; the equivalent efficiency for the multiwire proportional chambers was 0.96 per plane per track. This

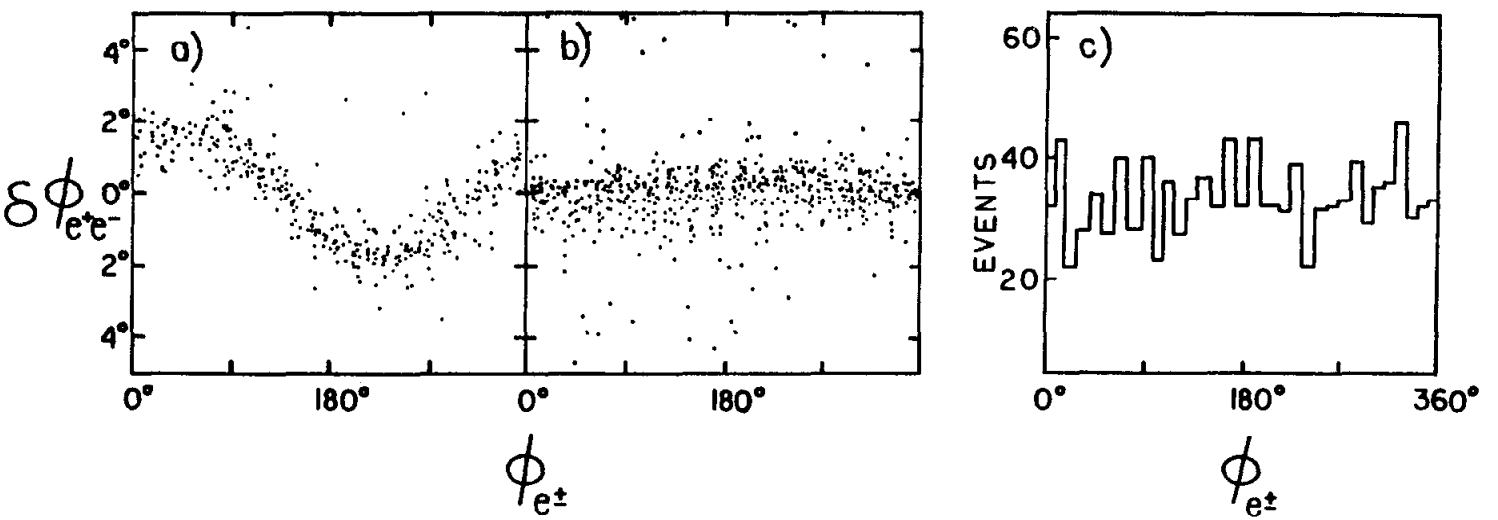

FIG..F-2 Bhabha pair opening angle (minus 180°) as a function of the azimuth. a) chambers off center; b) chamber location corrected in software. Resulting uniformity over azimuth is shown in c).

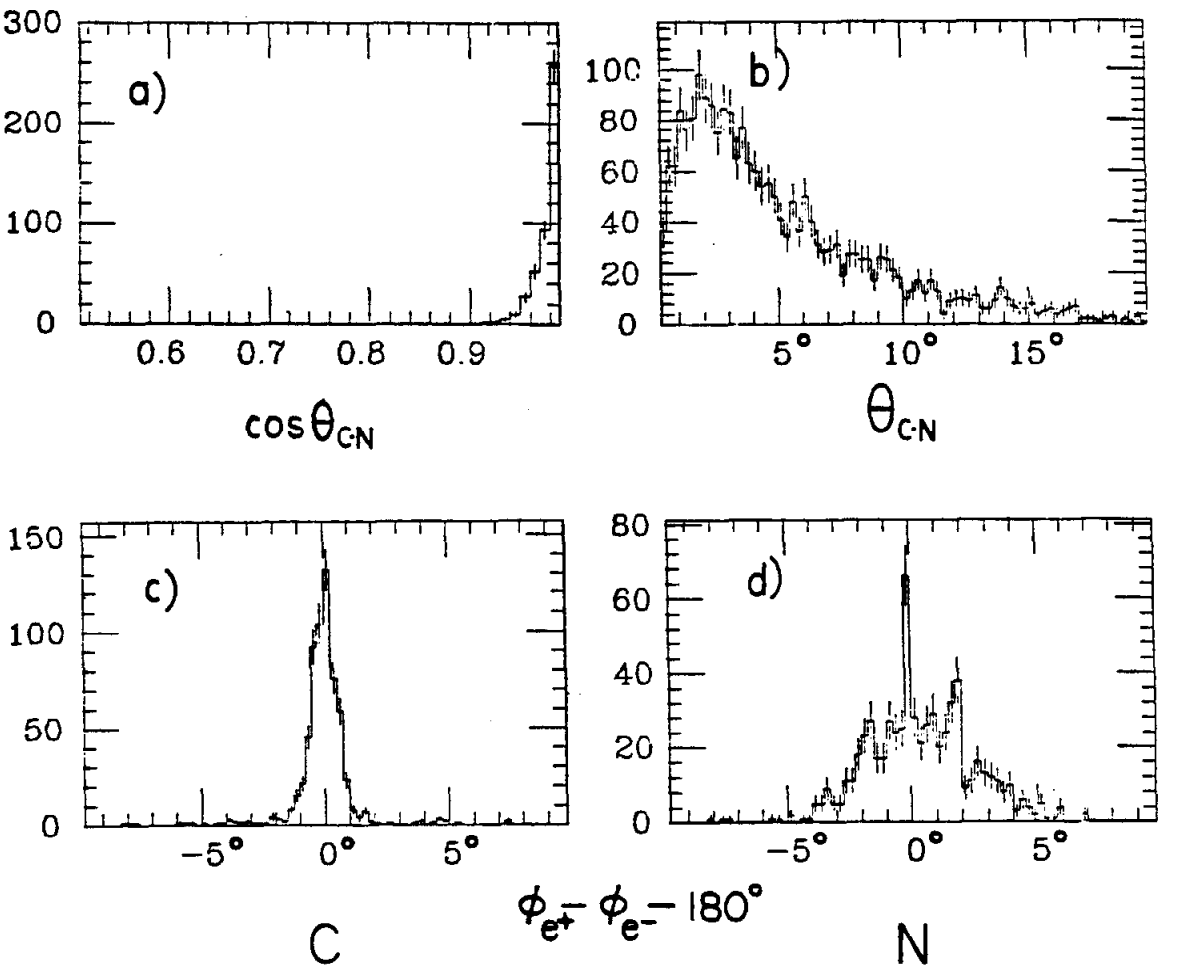

FIG..F-3 Comparison of Bhabha electron trajectories reconstructed using the spark chambers (C) and the neutral tracking (N). θ_{cn} is the difference between the C and N trajectories. The Bhabha opening angles are shown in c) and d).

efficiency was computed for tracks which had already been determined by information from other planes, and therefore is only approximately correct as it neglects possible correlations in efficiencies among the planes. The value of the spark plane efficiency corresponds to a probability of 98% for reconstruction of a Bhabha track.

When there were unassigned sparks after the completion of the second tracking pass, a correlation of the leftovers, as well as of the multiwire proportional chamber information, with the NaI(Tl)-reconstructed tracks was sought. A charge assignment based on this scheme was dubbed a "tag" since the chambers were not used to reconstruct the track. After all the NaI(Tl)-reconstructed tracks were reduced by correlating them with the chamber reconstructed tracks, each of the 8 spark and 4 multiwire proportional chamber planes was examined for a hit near the trajectory predicted by the NaI(Tl)-tracking. The physical zone over which a chamber hit was associated with the NaI(Tl) track varied with the plane in question (this being the result of an optimization study), but was generally of the order 150-200 mrad. This is to be compared with the apex half-angle of 58 mrad (3.3°) for the cone inscribed in a typical NaI(Tl) crystal. Each plane has been assigned a weight (from 0.8 to 1.7, listed in Table F-1) on the basis of tests designed to minimize over-tagging without significantly impairing the ability to tag a charged particle. The weighted sum of planes which had track-correlated hits was then required to exceed unity if the particle was expected to register in either the inner spark or the multiwire proportional chambers, or exceed two if it was expected to trigger all three chambers.

TABLE F-1

TAG ALGORITHM WEIGHTS

PLANE	ORIENTATION	ϕ ACCEPTANCE ZONE	WEIGHT	
1	-30°	300 mrad	1.0	
2	straight	200 mrad	1.3	INNER
3	straight	200 mrad	1.1	MS
4	+30°	250 mrad	.95	
5	-45°	250 mrad	.97	
6	straight	150 mrad	1.2	OUTER
7	straight	150 mrad	1.6	MS
8	+45°	250 mrad	1.0	
9	62°	400 mrad	1.0	
10	straight	180 mrad	1.7	MWPC
11	straight	180 mrad	1.6	
12	90°	2.4 cm (z)	.80	

The weighted plane test essentially meant that 2 or more planes must have registered hits in the vicinity of the NaI(Tl)-reconstructed track. If this test was passed, it was also required that at least one of the planes that fired was straight and at least one was a cross-plane.

Most controversial, perhaps, of the empirical parameters described above is the acceptance zone for correlating a hit with the NaI(Tl)-reconstructed track. The spacing between straight-plane wires in the multiwire proportional chambers corresponds to approximately 88 mrad and is the coarsest structure in the chamber system. Alternate tagging routines requiring only that ϕ of the NaI(Tl)-reconstructed track be within either 88 or 100 mrad of a multiwire proportional chamber hit gave no significantly different results from the much more restrictive algorithm described above.

Because of plane-correlations, multi-track event efficiencies differed from the appropriate power of the single-track efficiency. Thus it was important to determine the overall efficiency, as well as the dependence on cosθ and z, for the 2-charged/2-neutral final state to which this experiment addresses itself. Such an efficiency study was accomplished by using the decay $\psi' \to \gamma\chi(3.51) \to \gamma\gamma\psi \to \gamma\gamma e^+e^-$, a final state easily identified on a Dalitz plot even when the leptons are not required to be tagged. By examining Dalitz plots with 0, 1 and 2 tagged or chamber tracked leptons, a tagging/charged-tracking efficiency of 0.96 per event was determined. The angular dependence for tagging/charged-tracking shown in figure 3-8 was also obtained using the χ cascades.

Appendix G

MONTE CARLO SIMULATION

Although shower development in NaI is accurately simulated by the EGS program, the CPU expenditure is large -- a 200 MeV photon initiated shower requires 0.5 CPU seconds, increasing linearly with energy up to about 2 GeV. Since the computer simulation of the complex angular correlations for the cascade reactions also uses much CPU time, EGS was not used directly in the Monte Carlo event simulator. Rather, it was observed that the simulation of a large number of events smooths over the shower fluctuations so that the shower distribution functions (E-3) could be used in place of EGS. This approximation was further justified by the choice of cuts used to define the acceptance region for events and the acceptable minimum angle (26°) between any two tracks. Therefore, the bump discriminator function (E-4) was used to determine if any two showering tracks could be resolved by the apparatus or if they would merge into one track.

The measurements for all quantities were smeared according to the resolution of the apparatus. In particular, measured energies of showering particles were smeared with the NaI(Tl) line shape described in equation (D-1), while the angles were smeared in a gaussian manner with a resolution behaving as $E^{3/4}$ for neutral-tracked trajectories. Vertices for the

events were distributed gaussianly, with σ=2.6 cm; additionally, there was a measurement error of 1 mm.

In addition to the opening angle cuts, Monte Carlo events were required to pass all the cuts applied to the real data. The endcap region was defined as $|\hat{n}_z| < 0.935$, $|\hat{n}_y| > 0.02$, for tracks along the direction $\hat{n}$; less than 8 MeV had to be deposited in this region. Any tracks having an energy less than 20 MeV were considered to be unobservable, with the exception that the energy could contribute to the total energy measured in the endcaps. Exactly four tracks, each having an energy in excess of 40 MeV, were required in the $|\hat{n}_z| < 0.90$ region and any track observed in the remaining ball region defined by $0.90 < |\hat{n}_z| < 0.935$ constituted a reason for rejecting the event.

Charged particles (the leptons) were assumed to be tagged with 100% efficiency if they traversed the multiwire-proportional chambers. For lepton trajectories having $|\hat{n}_z|$ in the range 0.84 to 0.90 the tagging efficiency was assumed to fall as shown in figure 3-8. An overall tagging efficiency factor of 0.96 was then applied to the efficiencies returned from the Monte Carlo simulations at a later stage of the analysis.

Cascade events were generated according to the angular distribution described in equation (5-5), with the multipole coefficients treated as variable parameters. The sequence for the generation of cascade events was:

1) decay $\psi' \to \gamma' \chi$ uniformly in the ψ' frame

2) decay $\chi \to \gamma\psi$ uniformly in the χ frame

3) boost γ,ψ to the ψ' frame along $\vec{\chi}$

4) rotate γ,ψ from the χ helicity frame to the lab coordinates (G-1)

5) decay $\psi \to l^+l^-$ uniformly in the ψ frame

6) boost l^+l^- to the ψ' frame along $\vec{\psi}$

7) rotate l^+l^- to the lab coordinates

8) compute $W(\theta',\phi',\theta_{\gamma\gamma},\theta,\phi)$ -- reject if greater than $W_{max}\cdot$(random[0,1])

Similarly, the η (or π^0) decays were generated in the following manner:

1) decay $\psi' \to \eta\psi$ as $1+\cos^2\theta$ in the ψ' frame

2) decay $\eta \to \gamma\gamma$ uniformly in the η frame

3) boost $\gamma\gamma$ to the ψ' frame along $\vec{\eta}$ (G-2)

4) rotate $\gamma\gamma$ to the lab coordinates

5) steps 5 to 7 in (G-1)

Generation of background from the decays $\psi' \to \pi^0\pi^0\psi$ followed the sequence:

1) decay $\psi' \to M\psi$ uniformly in the ψ' frame, with M having the mass distribution shown in figure 4-3

2) decay $M \to \pi^0\pi^0$ uniformly in the M frame

3) boost π^0s to the ψ' frame along $\vec{M}$

4) rotate π^0s to the lab coordinates (G-3)

5) decay $\pi^0 \to \gamma\gamma$ uniformly in the π^0 frame

6) boost $\gamma\gamma$ to the ψ' frame along $\vec{\pi^0}$

7) rotate γs to the lab coordinates

8) steps 5 - 7 in (G-1)

In the last example, tests were made to see if any of the four photons would merge with any of the other particles or escape the detector. Thereafter, if there were not exactly two observeable photons in the event, the event was rejected. The preliminary cuts $|n_z| < 0.9$, opening angle $\theta > 26°$, and $E_\gamma > 40$ MeV were applied to the Monte Carlo simulated tracks for a $\pi^0\pi^0$ dataset equal to that produced in the experiment; about 1500 of the initial 18000 events survived these cuts. Application of the $E_{neutral} > 490$ MeV cut reduced the number to 140 background events, none of which had a diphoton mass less than 200 MeV/c^2.

Events surviving the cuts were run through the kinematic fitting program. In the case of the $\pi^0\pi^0$ decays, 117 of the 140 events survived the fit; however, only 7 events had an associated confidence level greater than 0.005. Of these 7 surviving events, 5 had $m_{\gamma\gamma}$ exceeding 525 MeV/c^2. A comparison of the fitted Monte Carlo events with real data is presented in figure G-1, where an excellent agreement is observed. Further agreement is obtained in a comparison of background $\pi^0\pi^0$ events observed in the early stages of the analysis -- fitting of the real data, together with the C.L. cut, removed about 180 events.

Efficiences resulting from the Monte Carlo studies are listed in Table G-1. The systematic errors shown in the table are estimates obtained by varying the parameters in the bump discriminator function, chamber efficiency function, and the vertex distribution. These errors are dominated by the statistical error from the number of Monte Carlo events that could be generated in a reasonable time.

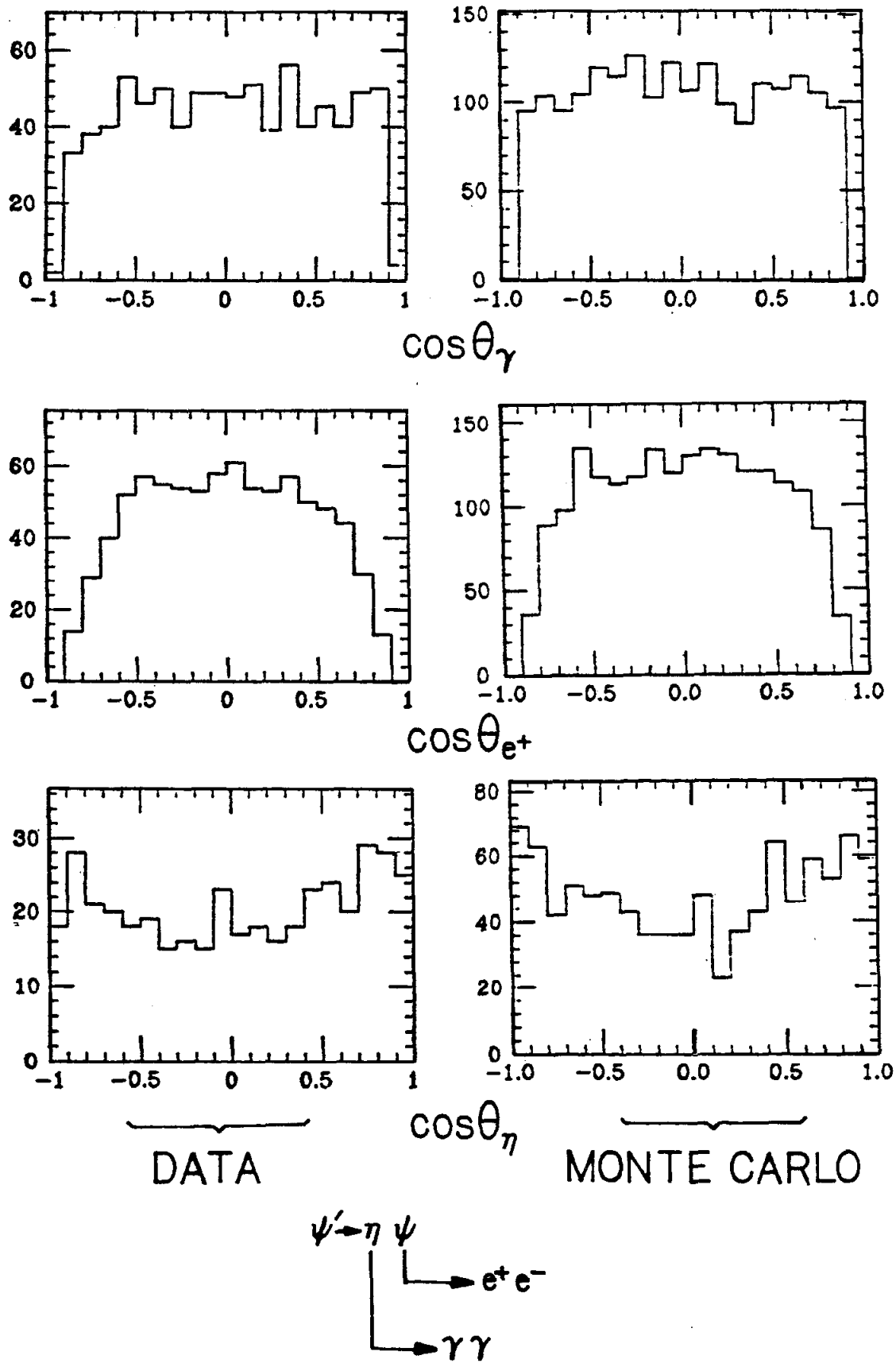

FIG..G-1 Comparison of data and the Monte Carlo simulator on the event class $\psi' \to \eta\psi$. θ is the polar angle of the final state particle indicated.

TABLE G-1

STATE		EFFICIENCY	SYSTEMATIC ERROR
$\chi(3.55)$	e^+e^-	0.370	0.015
	$\mu^+\mu^-$	0.408	0.016
$\chi(3.51)$	e^+e^-	0.387	0.011
	$\mu^+\mu^-$	0.425	0.012
$\chi(3.41)$	e^+e^-	0.295	0.007
	$\mu^+\mu^-$	0.333	0.008
"$\chi(3.591)$"		0.324	0.008
"$\chi(3.455)$"		0.358	0.009
η	e^+e^-	0.455	0.010
	$\mu^+\mu^-$	0.497	0.011
π^0	e^+e^-	0.254	0.007
	$\mu^+\mu^-$	0.276	0.007

In obtaining the values for Table G-1, additional cuts were applied to some states; a $m_{\gamma\gamma} < 525$ MeV/c^2 η cut was applied to the χ states and the complimentary cut was imposed on the η mode. For the π^0 mode efficiency, χ states were removed by the cuts $|m_{\gamma\gamma}-135| < 25$ MeV/c^2, and $|M_{\gamma\psi}-3530| > 60$ MeV/c^2, $|M_{\gamma\psi}-3410| > 5$ MeV/c^2. Spin-parity of 0^- and pure E1 multipolarity were assumed in generating the $\chi(3.591)$ and $\chi(3.455)$ events.

Appendix H

KINEMATIC FITTING

Excepting the particle masses, a four-particle final state is described by N_p=13 parameters: the energy, polar and azimuthal angles of each particle, as well as the z-position of the event vertex. All thirteen parameters were measured for the $\gamma\gamma e^+e^-$ final states; however, the two muon energies remained unknown in the $\gamma\gamma\mu^+\mu^-$ final states. The 13 or 11 measured quantities N_m are denoted by the vector $\underset{\sim}{x}$, while $\underset{\sim}{\sigma}$ describes their measurement uncertainties. Since the reactions of interest here all have leptons which result from the decay of the ψ, it is possible to use a knowledge of the ψ and ψ' masses and the conservation principal for energy and momentum to apply N_c=5 constraints to the data to obtain a set of optimized parameters $\underset{\sim}{x}_f$:

$$F_1(x) = M' - \sum_{i=1}^{4} E_i = 0$$

$$F_{234}(x) = \sum_{i=1}^{4} p_j(i) = 0 \ , \ j=x,y,z \qquad \text{(H-1)}$$

$$F_5(x) = M^2 - 2[\ E^+E^- - \vec{p}^+\cdot\vec{p}^- + m(l\pm)\ ] = 0$$

where M' = 3684 MeV/c^2, M = 3095 MeV/c^2, and i indicates which particle is being considered. The number of independent variables is $N_{ind}=N_p-N_c=8$, so that the number of degrees of freedom in the problem is $NDF=N_m-N_{ind}$= 5(3) for $e^+e^-(\mu^+\mu^-)$ final states. The NDF describe the constraint class (5C or 3C) of the fit, for

$$\chi^2 = \sum [(x_i - x_{fi})^2 \sigma_i^{-2}]$$

is distributed as $\chi^2(NDF)$.

To obtain the optimized data, minimization of χ^2 is coupled with the constraint functions by means of Lagrange multipliers $\underset{\sim}{\alpha}$:

$$\chi^2 = \sum_{i=1}^{N_p} [(x_i - x_{fi})^2 \sigma_i^{-2}] - \sum_{l=1}^{N_c} \alpha_l F_l(x) \qquad \text{(H-2)}$$

$$\frac{d\chi^2}{dx_i} = \frac{d\chi^2}{d\alpha_l} = 0$$

Minimization[125] is accomplished by incrementing the solution $\underset{\sim}{x}_{fn}$ at iteration n by $\Delta\underset{\sim}{x}$, and then by linearizing the constraint functions:

$$F_l(\underset{\sim}{x}_{fn+1}) = F_l(\underset{\sim}{x}_{fn}) + \Delta\underset{\sim}{x} \frac{dF_l(\underset{\sim}{x}_{fn})}{dx_i}$$

$$\frac{\Delta x_i}{\sigma_i} + \frac{(x_{fi} - x_i)}{\sigma_i} + \alpha_l \frac{dF_l(x_{fn})}{dx_i} = 0 \qquad \text{(H-3)}$$

$$\Delta x_i \frac{dF_l(\underset{\sim}{x}_{fn})}{dx_i} + F_l(\underset{\sim}{x}_{fn}) = 0$$

The iterations described by (H-3) were continued as long as the norm of $F(\underset{\sim}{x}_f)$ exceeded 1 MeV. Much computation time was saved by altering the step size in cases where convergence was proceeding slowly.[126] Distribution of the iterations for the final data sample is shown in figure H-1. Events failing to converge after 30 iterations were assumed to contradict the $\gamma\gamma l^+ l^-$ final state hypothesis and were therefore rejected.

---

[125] J. Berge, F. Solmitz and H. Taft, Rev. Sci. Instr. 32, 538 (1961).

[126] J. Park, report SLAC-REPORT 150 (Stanford) (1972).

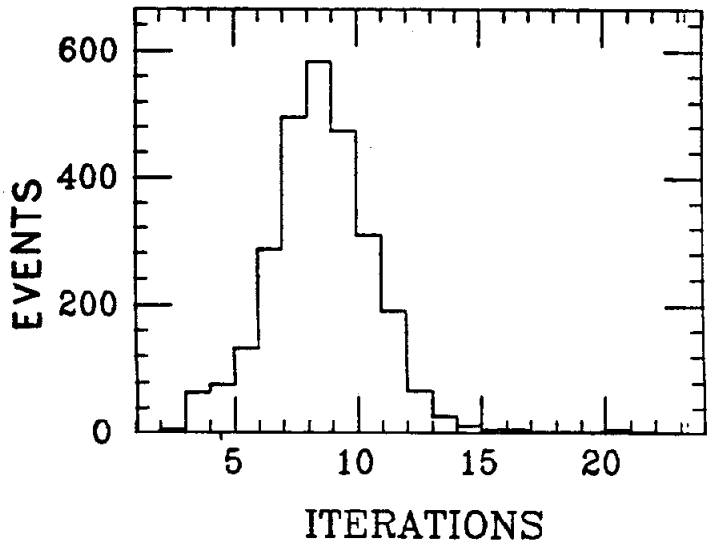

FIG..H-1 Distribution of kinematic fitting iterations for events surviving the fitting.

If equation (H-2) is to be rigorous there can be no correlation between the x_i. Furthermore, the σ_i must be nearly gaussianly distributed or else the resulting $\underset{\sim}{x}_f$ will be biased. To decouple the z-vertex from cosθ (see figure H-2) a new variable was used in the fitting program; it describes the vector from the z=0 origin to the shower maximum in the central crystal. Independence and suitability of the fitting variables can be measured by the distribution of pulls S_i:

$$S_i = \frac{(x_{fi}-x_i)}{\langle x_{fi}-x_i\rangle_{rms}} \qquad (H\text{-}4)$$

which should be distributed as gaussians of null mean and unit deviation. The distributions for the final data sample are shown in figure H-3 and the confidence level distributions are shown in figure H-4; the energy pulls are slightly skewed by the non-gaussian line shape of NaI(Tl). By fitting Monte Carlo events which were generated with the NaI(Tl) line shape described in appendix D, accurate simulation of the data was achieved (figure H-5). Events with no vertex information had z set to zero, and its variance was set to that describing the distribution of e^+e^- vertices ($2.6^2 cm^2$).

Masses obtained from the fitted data suffer errors arising from the uncertainty in the NaI(Tl) line shape and from the parameters M and M′ used in the fit. Since the distribution of fitted masses is nearly gaussian while that for unfitted masses exhibits the NaI(Tl) line shape, a Monte Carlo simulation was used to correct the masses M_{1s} extracted from the optimized data. Shifts (M_0-M_{1s}) of $(-0.6\pm0.3):(+0.5\pm0.3):(-0.8\pm0.3)$ MeV/c^2 were obtained for the $\chi(3.51):\eta:\pi^0$ masses respectively, where the

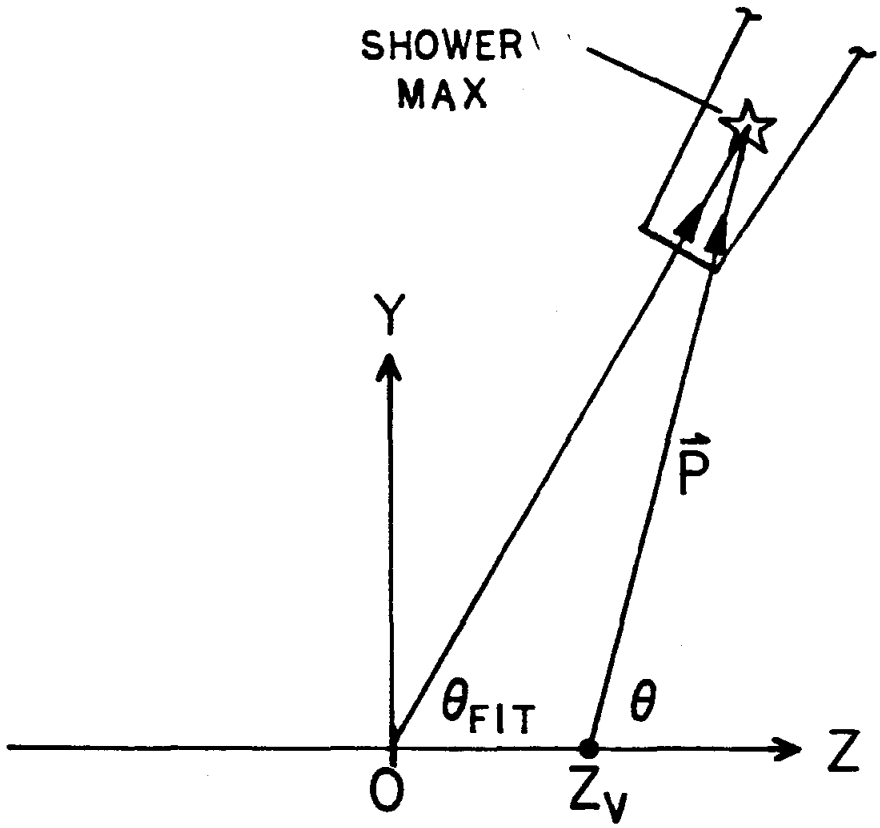

FIG..H-2 Definition of the fitting varible θ_f, which is decoupled from the vertex measurement.

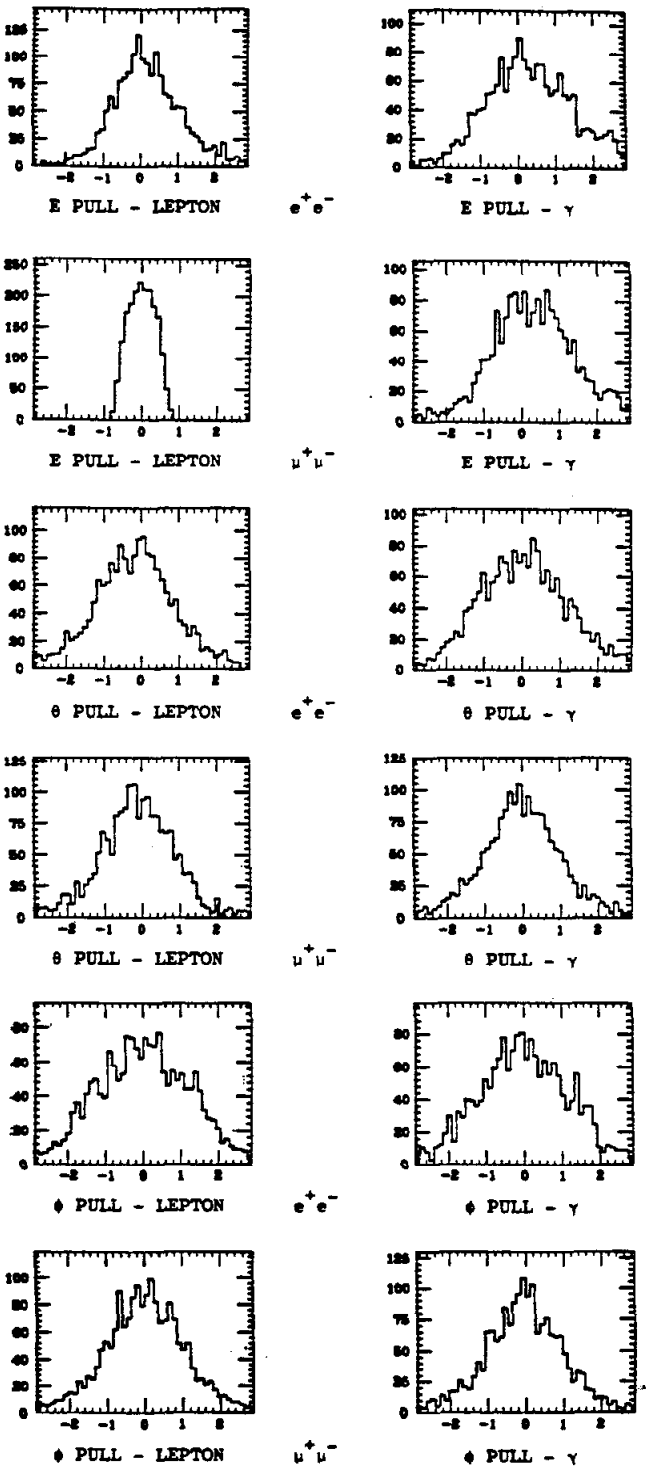

FIG..H-3 Distribution of all pulls for the final event sample.

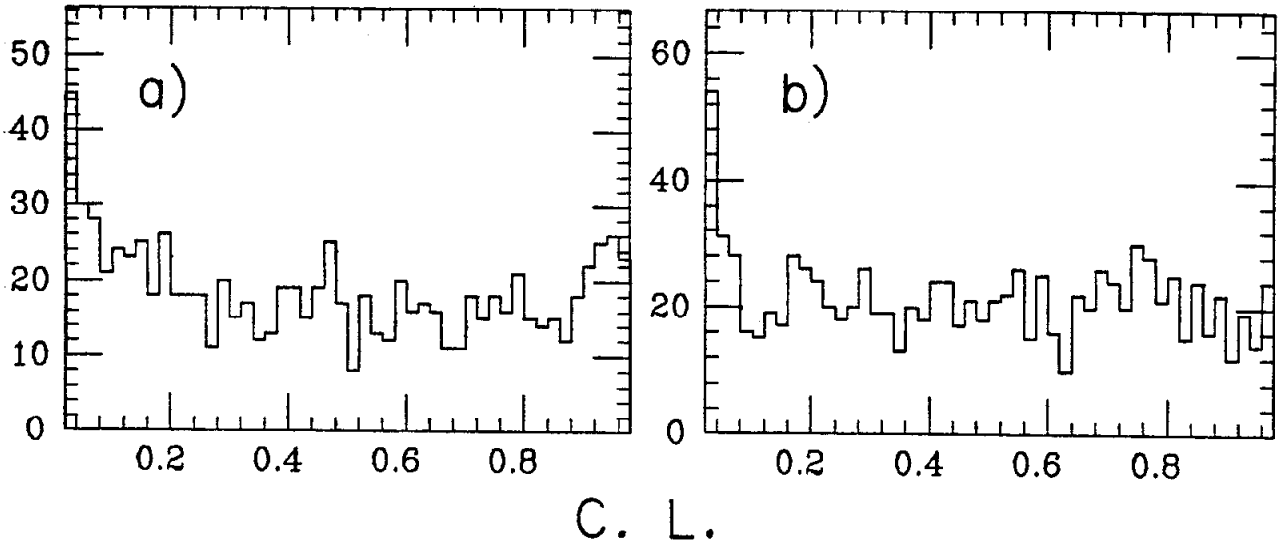

FIG..H-4 Confidence level distribution from the kinematic fitting. a) shown e^+e^- events and b) showns $\mu^+\mu^-$.

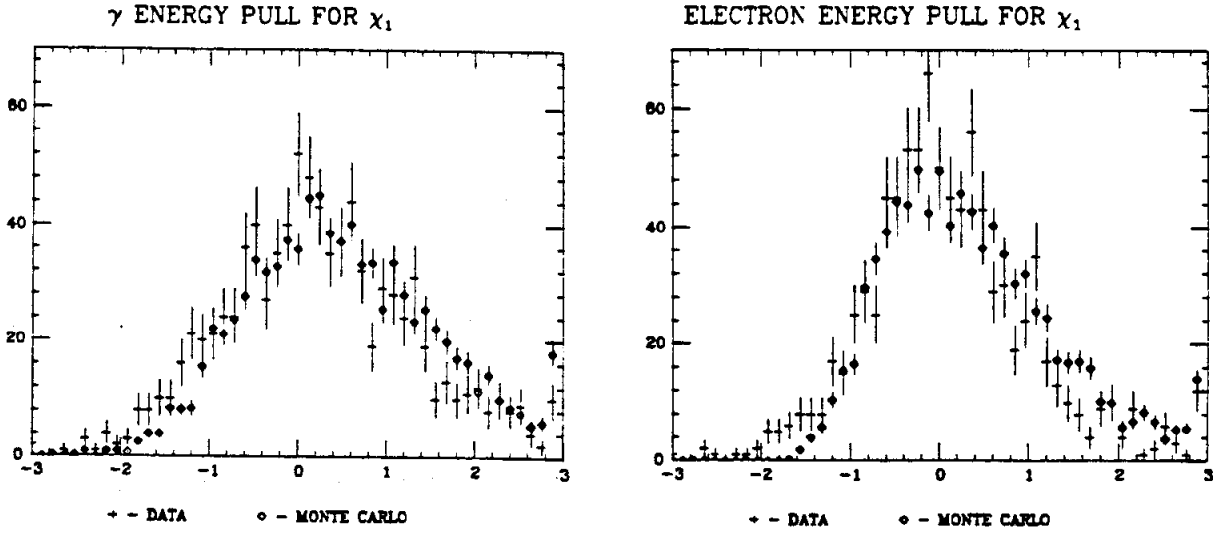

FIG..H-5 Pulls in the energy of photons and electrons after kinematic fitting. The asymmetry arises from the NaI(Tl) line shape.

error was obtained from Monte Carlo studies using extreme deviations in the assumed NaI(Tl) line shapes. Because it has a broad natural width (see chapter IV) the $\chi(3.55)$ exhibits a more symmetrical line shape, with no shift in the fitted mass; the 0.3 MeV/c^2 uncertainty in the line shape effect also applies to this state.

The effect of the kinematic fitting parameters M and M′ can be approximated by writing the masses in terms of the constrained variables:

$$M^2_\chi = \frac{M'^2 + M^2 rX}{1 + rX} \qquad \text{(H-5a)}$$

$$M^2_\eta = D^2 - \frac{(M + D)}{M}\left[(E_1+E_2)^2 - 2E_1E_2(1-\cos\theta_{\gamma\gamma})\right] \qquad \text{(H-5b)}$$

where:

$$D \equiv M' - M\ , \quad r \equiv E_1/E_2\ , \quad X \equiv 1 - E_1 M'^{-1}(1 - \cos\theta_{\gamma\gamma})$$

In (H-5a) the energies essentially enter only as the ratio E_1/E_2 and the calibration error drops out; the photon opening angle dominates in the determination of the η mass. Systematic errors contributed by the fitting parameters are given by:

$$dM_\chi = \frac{2M'^3(1+rX)-(D^2+2DM)rE_1(1-\cos\theta_{\gamma\gamma})}{(1+rX)^2\,M'^2}\,dD + \frac{2M'^2(1+rX)+(D^2+2DM)r(1-X)}{(1+rX)^2\,M'}\,dM \qquad \text{(H-6)}$$

$$dM_\eta = \frac{D}{M_\eta}\,dD$$

These errors, along with the additional line shape uncertainty, are to be added in quadrature.

Appendix I

STATISTICAL METHODS

For a binned histogram describing the measurements $\underset{\sim}{x}$ there exists a normalized probability function $f(\underset{\sim}{x},\underset{\sim}{p})$ for the population of the bins, assuming that the parameters $\underset{\sim}{p}$ fully describe the physics of the distribution. Consider first the one-dimensional histogram having NB bins for which the x_i (i=1,NB) are not correlated. The likelihood function for a fit to the data using the parameters p (e.g., the numbers of counts under resonance peaks) is given by

$$L = \prod_{i=1}^{NB} f(x_i,\underset{\sim}{p}) = \prod_{i=1}^{NB} \frac{e^{-m_i} m_i^{x_i}}{x_i!} \qquad (I-1)$$

The explicit form of L given above describes a Poisson distribution, with $\underset{\sim}{p}$ predicting m_i counts in bin i. Of special interest here is the fit to a branching ratio (BR), which must reflect errors both in the number of counts observed and in the normalization factors (i.e., n′, the number of ψ' produced, and ϵ, the efficiency for observing the decay mode). The number of counts expected in the spectrum is

$$m_i = l_i \cdot n \ , \qquad (I-2)$$

where l_i is the normalized line-shape and n is the total number of counts expected in the peak

$$n = n' \cdot BR \cdot \epsilon + Bk \ . \qquad (I-3)$$

The background is described by the last term above. Now, the m_i have a probability distribution which is centered about the correct value, m_{oi}, and is generally gaussian. The correct form of L is therefore

$$L = \prod_{i=1}^{NB} \int \frac{e^{-m_i} \; m_i^{x_i}}{x_i!} \; e^{-(m_i - m_{oi})^2/(2s_i^2)} \; dm_i \quad ; \tag{I-4}$$

the normalization factor is not included above. The smearing factor s is just the quadrature-sum of the individual errors:

$$s_i^2 = (BR \cdot \epsilon \cdot l_i \cdot \sigma[n'])^2 + (BR \cdot l_i \cdot n' \cdot \sigma[\epsilon])^2 + (\sigma[Bk])^2 \; . \tag{I-5}$$

It has been shown[127] that the integration in (I-4) can be performed analytically to obtain:

$$f(x_i,p) = \frac{(2)^{(x_i-2)/2} \; s_i^{\,x_i} \; e^{(s_i^2 - 2m_{oi})/2}}{\sqrt{\pi}\,(1 + \mathrm{erf}\left(\frac{m_{oi}}{\sqrt{2}s_i}\right))\, x_i!} \sum_{j=0}^{x_i} \binom{x_i}{j} (-D)^j \, I_j$$

$$D \equiv -(s_i^2 - m_{oi}) \cdot (2\, s_i)^{-1}$$

$$a \equiv (x_i - j + 1)/2 \tag{I-6}$$

$$I_j = \begin{cases} \Gamma(a, D^2) \; , & D > 0 \\ \Gamma(a) + (-)^{x_i - j} \, [\Gamma(a) - \Gamma(a, D^2)] \; , & D < 0 \end{cases} \; ,$$

which is properly normalized. Note that the quantity D is dimensionally correct since $\underset{\sim}{m}$ is dimensionless. When determining the 90% confidence level upper limit on the branching ratio for an unobserved state, L is plotted as a function of BR and then integrated numerically to obtain the value of BR where 90% of the total area is attained.

---

[127] D. Coyne, Crystal Ball memo CB-NOTE 404 (1979).

Multidimensional histograms often prove too CPU-intensive for the rigorous method just presented. In such cases the total population of the histogram is held fixed, thus removing one degree of freedom from the problem and neccessitating a binomial probability distribution:

$$L = n!\, n^{-n} \prod_{i=1}^{NB} \frac{m_i^{x_i}}{x_i!} \qquad \text{(I-7)}$$

The logarithm of this likelihood function is equal to that for the Poisson statistics when Sterling's approximation ($\ln n! = n \cdot \ln(n) - n$) is made. One obtains the best measurement for the parameters by maximizing $L[m(\underset{\sim}{p})]$.

Confidence in the optimized fit can be measured in several ways, all of them rigorous only in the limit $x_i \to \infty$. The standard Pearson χ^2 test is one such example which is not valid for the small bin populations in this analysis. A much better measure of the fit is afforded by the likelihood ratio test,[128] which compares the maximum value of L with one obtained using the approximation that the data precisely describes the real distribution $(\underset{\sim}{p})$. From such a procedure one obtains the test statistic

$$t = -2 \ln \left[n^{n} \prod_{i=1}^{NB} (m_i/x_i)^{x_i} \right] \qquad \text{(I-8)}$$

which is distributed as $\chi^2(NB-1)$ for $n \to \infty$. This test statistic is valid for histograms in which about 70% to 80% of the bins contain more than two counts.

---

[128] W. Eadie et al., Statistical Methods in Experimental Physics, North-Holland, Amsterdam (1971).